

Grand-Design Warps in Galactic Disks

Dissertation

zur

Erlangung des Doktorgrades (Dr. rer. nat.)

der

Mathematisch–Naturwissenschaftlichen Fakultät

der

Rheinischen Friedrich–Wilhelms–Universität

Bonn

vorgelegt von

Gyula István Géza Józsa

aus Bonn

Bonn, Dezember 2005

Angefertigt mit Genehmigung
der Mathematisch–Naturwissenschaftlichen Fakultät
der Rheinischen Friedrich–Wilhelms–Universität Bonn

1. Referent: Prof. Dr. Ulrich Klein
2. Referent: Prof. Dr. Peter Schneider

Tag der Promotion: 8. März 2006

Erscheinungsjahr: 2006

Diese Dissertation ist auf dem Hochschulschriftenserver der ULB Bonn
http://hss.ulb.uni-bonn.de/diss_online
elektronisch publiziert.

This dissertation is electronically published at the Hochschulschriftenserver of
the ULB Bonn:
http://hss.ulb.uni-bonn.de/diss_online

Contents

Contents	3
1 Introduction	1
2 Dark Matter and the kinematics of galactic disks	5
2.1 Cosmology and dynamics of disk galaxies	5
2.2 The spherical Dark Matter distribution and rotation curves	6
2.2.1 Basic principles of rotation curve analyses	7
2.2.2 Symmetric disks and spheres in spiral galaxies	8
2.2.3 Parametrisation of the stellar component	10
2.2.4 The interstellar medium	12
2.2.5 Derivation of rotation curves and the tilted-ring model	13
2.2.6 The controversy of Dark Matter profiles	18
2.3 Warps in disk galaxies	22
2.3.1 Basic warp description	23
2.3.2 Warp shapes	25
2.3.3 Rules for the behaviour of warps and their direct implications	27
2.3.4 Warp formation: theories	33
3 A new method to fit tilted rings to datacubes	47
3.1 Introduction	47
3.2 Tifific layout	49
3.2.1 Tilted-ring model	49
3.2.2 Chi-square evaluation	52
3.2.3 Chi-square minimisation	53
3.3 Beam smearing and smoothing in velocity-fields	57
3.4 Tifific tests	60
3.4.1 “Beam smearing” in tifific	60

3.4.2	An edge-on rotation curve	62
3.4.3	An edge-over warp	62
3.4.4	Tirific performance and the user interface	66
3.5	Graphics and analysis output	66
3.6	Results and discussion	67
4	New rules for the behaviour of warps	71
4.1	Introduction	71
4.2	The examined galaxies	77
4.3	HI observations and data reduction	78
4.4	Tilted-ring modelling	83
4.5	Global features in the tilted-ring models	99
4.6	Non-circular motions and their possible influence on the results	104
4.7	Discussion and summary of the results	109
4.8	Supplementary figures and tables	113
5	The warped Spindle NGC 2685	137
5.1	Introduction	137
5.2	Observations and data reduction	141
5.2.1	Optical observations and data reduction	141
5.3	Observations and the warped structure of NGC 2685	143
5.4	The environment of the Spindle	145
5.5	The stellar and gaseous components of NGC 2685	148
5.6	The warped structure of the gas disk of NGC 2685	149
5.7	Tilted-ring modelling	153
5.8	Global features in the tilted-ring models	159
5.9	Non-circular motions	161
5.10	Summary of the results and discussion	163
5.11	Supplementary figures and tables	164

6 Final remarks	173
6.1 Summary	173
6.2 Outlook	176
A Acknowledgments	179
References	181
List of Figures	193
List of Tables	205

1 Introduction

Warps are a basic feature of disk galaxies. At least half of all galaxies show a systematic bending of the outer disk when they are observed with high sensitivity in the optical bands. Usually the phenomenon occurs at large radii, where the stellar disk is dim. In the neutral gaseous disk, which usually exceeds the observable stellar disk by a factor of two up to three, the tilt of the disk with respect to its inner part is evident in nearly all observed disks of “normal” spiral galaxies.

Astronomers became aware of their high frequency of occurrence rather late in the 1970s, when spectroscopic imaging with radio interferometers became a regularly applied observation technique. With the resulting raise of sensitivity and spatial resolution the structure of HI disks in external galaxies could be resolved. Radio astronomers proved unambiguously that the dominant fraction of mass in disk galaxies is either unseen or that the gravitational laws must be rewritten. At the same time warps were discovered to be present in almost all bright spiral galaxies.

Warps are common and furthermore they seem to show systematics in their appearance. Because of that any picture that is drawn about structure and formation of disk galaxies should include an explanation for the the frequency and the structure of warps. In turn, this observed structure can then serve as an important tool to reveal the true structure of a galaxy, including invisible components.

Unfortunately, a satisfactory uniform theory of warps has not been found within the thirty years since they got the attention of astronomers, for a manifold of reasons:

Warps are hard to observe. Classical warps occur at the edges of the disks. Their structure can be observed up to a certain radius employing the HI emission line, but even such observations are limited by sensitivity. The HI disk is not detectable anymore, but usually it has no well-defined edge. It fades away with rising distance from the galactic centre, suggesting that a faint HI disk is still present. Thus, it is not known how a warp develops towards the real end of the galaxy (if there is any well-defined one). Indeed, as it will be shown in this thesis, pushing the detection limits may reveal surprises.

Warps are not easy to parametrise. A warp is a three-dimensional structure, which we see only in projection. To parametrise its structure and kinematics implies a de-projection from the observable two or three dimensions to six dimensions in phase-space. In the best case, such a parametrisation should be independent of the global orientation of the galaxy towards the observer. While the method to parametrise warped disks by a so-called “tilted-ring model” is nearly as old as the first observation of a gaseous warp in an external galaxy, up to now the applications to produce such a model had the flaw of being subject

to incalculable systematics that were connected with the galaxy orientation or bearing a tantalising amount of work to produce such a model. Thus, parametrisations of warps and their kinematics, especially rotation curves, had always to be treated with the caveat that an interpretation may be biased.

Warps have individual appearances. As human beings differ slightly from each other in every respect, so do disk galaxies. While everyone agrees that a nose, for example, will always be recognisable as a nose, it is at the same time evident that individual noses look quite different but can at the same time be classified into schemes: stub noses, even noses, hooknoses. One can classify two major types of warps, and a third one for galaxies exhibiting an even mixture of the major types, all named after their appearance. Regarding the names given to the warps in this classification scheme, one has to keep in mind that galaxies are transparent in the HI component, while our eyes are naturally accustomed to look at largely opaque sources. So, mostly, these names are results of a trial to describe a shining thing that shows a behaviour like a campfire as an opaque thing that only reflects and absorbs light. The first one is the “grand-design”, “S-shaped”, or “integral-signed” warp (beautiful even noses). A galaxy with an S-shaped warp is point-symmetric with respect to the galactic centre and if seen edge-on the galaxy appears as an integral sign. The second class is the “U-shaped” or bowl-shaped warp (say, a snub nose). A galaxy with an U-shaped warp is axisymmetric with respect to the projected angular-momentum axis of the inner disk, and seen edge-on it appears as a U. A galaxy with a U-shaped warp can be fancied as a bowl with a flat bottom. The last class of warps is the “L-shaped” warps (the hooked nose of boxers). If seen edge-on and from the right viewing-angle, galaxies with an L-shaped warp show a bending of the disk on one side, but not on the other side. Thus, they don’t show a clear symmetry, but are suspected to be a mixture of the first two classes of warps. Among warps, the S-shaped type seems to be the one with the highest frequency of occurrence, although this is a matter of discussion among observers. The frequency of the shapes found depends slightly on the galaxy environment. It is not clear whether all warps have the same origin, each warp is to some degree individual, and the disk shows individual appearances in the reach of the warp. It is therefore a task to filter the common features that belong to the warping phenomenon from other, maybe local, features. It may well be that the structure of a galaxy is disturbed by recent tidal interaction. Even if tidal interactions originate warps, the individual effect on the structure of the galaxy has to be separated from the general structure that a warp has (due to interaction or not).

All these difficulties resulted in a situation, where some characteristics of warps are known, reproduced to some degree by a number of competing warp formation models. Most models fail to globally explain the warping phenomenon in the context of cosmological scenarios. For example, it is possible to explain warps by tidal interaction with satellites, but if this is a mechanism to excite warps, there

must be another one that produces similar warps without satellites, because it is known that a large number of isolated galaxies possess warps. The second – not so beautiful – alternative is that every galaxy has at least one undetected satellite of noteworthy size. It is unknown whether the different kinds of warps are the results of the same formation mechanism or if several mechanisms are at work at the same time. If there are competing mechanisms, they maybe leave a signature in the kinematics of disks that provides a clue in which way a warp originated.

Galaxy warps influence cosmological studies also in a less direct way. Rotation curve analyses of galaxies test whether predicted rotation curves from certain cosmologies match the measured rotation curves. Hence, the derivation of rotation curves is an important tool in cosmology. But the estimation of true rotation curves depends highly on the assumed geometry of the galactic disks. If the geometry is not known the derived rotation velocities of the orbiting material contain an unknown systematic error that is due to a wrong estimation of the inclination of the disk towards the observer. For this kind of analysis, warps are highly disturbing. Not only the orientation of the disk as a whole has to be measured, but also its change with radius. As the measure of the galaxy kinematics and geometry is far from being perfect up to now (see above), observers have a real problem to show that the “core catastrophe”, the failure of the standard cosmological theory to predict the observed rotation curves, is not just an observational catastrophe in that observers simply produce wrong rotation curves.

It is therefore necessary to attack the warping problem from the observational side again. Analysis methods and observational sensitivity have to be improved in dedicated studies of warps in order to provide more insight in their structure to provide tests and inspiration for theory. The underlying work of this thesis was dedicated to serve for these two issues.

The main goal was to provide new observational insights in the structure and kinematics of warps. As said above, it is unknown, whether all warps have the same origin. It was therefore decided to first concentrate on one type, namely the S-shaped or grand-design warp. This is in a way the simplest form and by far the best-studied one, observationally and theoretically. Because of its symmetry a disk with an S-shaped warp can be viewed as a set of infinitesimally thin rings, which are inclined with respect to each other, but have the same centre. If these infinitesimally thin rings are substituted with many very thin circular rings of a finite number, one reaches an approximation of that ideal view, the so-called tilted-ring model. The core problem of the analytic work was to create a method that fits such a tilted-ring model to the observed data in a quality that matches that of the data. With a trustful model at hand one can then analyse and compare the structure of the observed warps and search for features that they have in common. Apart from the symmetry, another criterion was applied when the small group of galaxies was selected that build the core of the examined

systems presented in this thesis. A few of them should have large warps. If there are common features to S-shaped warps, then they should stand out in systems that contain this feature with a high amplitude.

Four galaxies were observed in the HI line employing the WSRT (Westerbork Synthesis Radio Telescope, The Netherlands) and in the near infrared with the INT (Isaac Newton Telescope, La Palma, Spain). Two of them have a large warp. An analysis software to derive tilted-ring models and rotation curves has been developed in order to parametrise the observed systems. The analysis method was applied in order to parametrise the HI disks of the four warped galaxies. The resulting models and obtained data were compared. This thesis is a summary of the outcome of this work.

The structure of the thesis is as follows: The second chapter is a summary of underlying theoretical concepts for warp formation and the structure of DM halos, briefly contrasting theory with current observational facts. The third chapter describes the developed analysis software. The following two chapters describe the observations and the parametrisation of the sample galaxies. Chapter 6 is a summary of the insights gained.

2 Dark Matter and the kinematics of galactic disks

In the recent decade it has become possible to simulate structure formation for various cosmological settings with the aid of computers. Given the right physics and initial conditions, which are known from other studies, today's structure of the universe down to sub-scales of galaxies can be predicted. These predictions of the distribution and kinematics of the baryonic and dark component in galaxies can be tested against observations and can be contrasted with analytic studies of galaxy dynamics. Spectroscopy of kinematical tracers in galaxies thus became a tool to test cosmology. This chapter contains a summary of the picture of galaxy structure in the nearby universe as found from computer simulations in contrast with analytic studies and observational facts. Theories about warps and warp formation are reviewed and set in a framework of today's cosmology. The focus of this chapter lies in testable predictions that can be addressed employing conventional spectroscopic measurements. In some detail, analysis techniques and their limitations are discussed to show the care with which such analyses have to be approached. While not expressively relevant for the further elaboration of this work, rotation curve analyses are discussed to some detail in order to illustrate the importance of proper kinematic modelling of disk galaxies.

2.1 Cosmology and dynamics of disk galaxies

In the recent decade much effort has been put into constraining our cosmological view of the universe (see e.g. Lahav & Liddle in Eidelman et al., 2004, for a review). Cosmological parameters have been fixed to establish the paradigm of a Λ CDM universe, the so-called "concordance model", in which the bulk of the matter is in a form of only weakly and gravitationally or only gravitationally interacting heavy particles (the Dark Matter, DM). Only about six percent of the matter is baryonic. Both, baryonic and Dark Matter make only about thirty percent of the critical mass of the universe. Nevertheless, the universe is (close to) flat, for which an inflationary period in its very early evolutionary stages is made responsible. The missing mass or energy density is provided by a component called "Dark Energy" with an amount leading to a nearly precisely flat universe. The nature of the Dark Energy is even more enigmatic than that of the Dark Matter, for which Physics provides a number of possible weakly interacting hypothetical particles.

The structure observed today is due to the evolution of statistical density fluctuations in the very early stages of the universe. After being initially seeded in an inflationary stage such density fluctuations start to evolve as soon as the Horizon at an evolutionary stage is large enough: One end of a density wave can get into physical contact with the other end. Cavities start to grow and over-densities

start to contract until this process is reversed because of internal pressure. Such a process is mainly possible because of the tight coupling of photons and baryons. At that stage, light can impose a substantial amount of pressure on baryons. The density fluctuations are primarily observable after the photon decoupling through observations of the CMB, where structure formation has already evolved. After this decoupling another phase is reached. Photons can float away freely and an important restoring force is lost. That means that the baryons start to clump and structure formation in the universe is initiated.

Structure formation in a Λ CDM universe has occurred bottom-up: It first turned up at small scales (dwarf galaxies), then progressing to larger scales (larger galaxies, galaxy clusters and superclusters). The form in which the universe presents itself today is a result of interaction of physical processes. Knowing the initial conditions and the physical processes and forces at work one can in principle predict what is seen today, and in turn use the observations as a test of the parameters used in a prediction. Since the middle of the 90's (e.g. Navarro et al., 1995, 1996, 1997; Moore et al., 1998) theorists have been performing computer simulations of structure formation in the universe with rising subtlety (Abadi et al., 2003a,b; Meza et al., 2003), providing observational astronomy with testable predictions of observable phenomena down to sub-scales of galaxies.

While on galaxy scale Dark Energy does not play a role, Dark Matter is supposed to be one of the major constituents that determine galaxy dynamics. The observation and parametrisation of the kinematics of disk galaxies and the comparison with computer models on the basis of cosmological models is therefore a test of the validity of the applied models. Any distinct deviations from the predictions made by computer simulations will enforce a re-examination of the methods used to perform the simulations and, if this is not successful, a recapitulation of our cosmological views. Today's computer- and technical power are sufficient to deliver both, a reliable modelling of the dynamics and morphology of various types of disk galaxies expected in hypothetical cosmological scenarios, as well as the parametrisation of observed disk galaxies on the observational side.

Despite the fact that the dynamics of disk galaxies has been studied excessively, some crucial questions remain unanswered or ambiguous. Studies of various aspects of disk galaxies remain a demanding and exciting task.

2.2 The spherical Dark Matter distribution and rotation curves

It is known for a long time from observations (Rubin & Ford, 1970; Bosma, 1978; Rubin et al., 1980), that the behaviour of galaxies is different from what would be observed if only self-gravity of the observed luminous matter would determine their dynamics. The favoured answer to this phenomenon is that galaxies are

surrounded by halos of Dark Matter, which account for the bulk of the mass, in agreement with the predictions of today’s theoretical simulations. The main reason to introduce a *thick (hot) or spherical* component, a halo, as an unseen component in a galaxy even before they became the *result* of simulations stems from early times: It prevents the formation of unrealistic disk instabilities like heavy bars in simulations of disk galaxies (James & Sellwood, 1978) for which then a halo became an input assumption. In recent simulations also the impact of the luminous matter and its mutual (gravitational) interactions with the halo are taken into account. Λ CDM simulations predict a shape (the three-dimensional density distribution) of the halo, as well as the dynamical behaviour and distribution of the luminous matter (see e.g. Abadi et al., 2003a,b; Meza et al., 2003). Because by definition the DM halo cannot be observed directly to determine its shape, this has to be done via observations of the luminous matter as a tracer of the most extended component of a galaxy. Galaxies with rotationally supported (gaseous and/or stellar) disks are the preferred laboratories with which the task of determining their composition is performed. Their luminous components consist of stars and gas (and, as a minor component, of course dust) on stable or quasi-stable orbits on a surface, the “disk” (as shown below, in some cases the term disk is stressed a bit, it will be used nevertheless), with a sufficiently well defined centre of symmetry. Spectroscopy of gas and stars (H II regions) may be used to examine the tangential velocity of test particles in well defined orbits within a given hypothetic gravitational potential. This is not possible in other types of galaxies for which only statistical approaches are feasible. Surface photometry of the examined objects is an additional need. Here, the mass distribution of the luminous matter can be extracted in order to identify one unknown component, the DM halo (or any unseen matter).

2.2.1 Basic principles of rotation curve analyses

For many spiral galaxies it is considered a valid approximation to treat the DM halo as a spherically symmetric density distribution $\rho_{DM}(r)$, where r is the distance from the centre. Also, in a zeroth-order treatment, the orbits of stars and gas in the disks of well-behaved spirals can be regarded as circular about a common centre, and hence, the corresponding potential as being axisymmetric. Certainly, deviations from these symmetries have to be taken into account and the validity of these approximations has to be checked in individual cases. On the other hand, analysis approaches that take into account deviations from circular symmetry of orbits soon get very complicated and do not allow a stationary approach or rely on other simplifying assumptions (e.g. Schoenmakers et al., 1997). Such a treatment makes a test of hypothetical DM distributions possible, including those that stem from Λ CDM simulations.

For a test particle on a circular orbit in the symmetry plane of an axisymmetric

potential ϕ the rotation velocity v_c as a function of the radius r calculates with

$$v_c^2(r) = r \left(\frac{\partial \phi}{\partial r} \right) \quad , \quad (2.1)$$

hence, as $\phi = \sum_i \phi_i$

$$v_c^2(r) = \sum_i v_i^2(r) \quad , \quad (2.2)$$

where v_i is the rotational velocity in an orbit about the i 'th single constituent (DM halo, gaseous disk, stellar disk, bulge) of the galaxy with the potential ϕ_i . As from photometric measurements the luminous density distribution, as well as from spectroscopy (HI, H α , CO line) the rotation curve $v_{\text{true}}(r)$ can be figured out, a least squares fit can be performed to test the goodness of fit of hypothetical radial density distributions of the DM component. Having extremely well known rotation curves at hand, eq. 2.1 can be inverted. One has to quadratically subtract the contributions of the luminous matter from the global rotation curve, a task for which the density profiles of the luminous components have to be known very well. Then, taking into account the Poisson's equation for a spherical potential produced by the Dark Matter halo the potential can be derived:

$$\Delta \phi_{\text{DM}} = 4\pi G \cdot \rho_{\text{DM}} = \frac{v_{\text{DM}}^2}{r} + 2 \cdot \frac{v_{\text{DM}}}{r} \frac{\partial v_{\text{DM}}}{\partial r} \quad . \quad (2.3)$$

A critical issue using eq. 2.3 is that one has to use the derivative of the (baryon-subtracted!) rotation curve. While it is hard to argue that a derived rotation curve is reliable, the reliability of the gradient in the very same rotation curve is by right a matter of discussion. This means that with a few exceptions (Salucci et al., 2003; Weldrake et al., 2003), the usual way to fit a rotation curve is to parametrise competitive spherical DM distributions and to see which one fits best in eq. 2.2.

2.2.2 Symmetric disks and spheres in spiral galaxies

The matter in galaxies within this simplification consists of axisymmetric components, as well as of disk-like components. For the disk-like components with an axisymmetric mass density given by

$$\rho(x, y, z) = \rho(r, z) \quad , \quad (2.4)$$

where r denotes the radius and z the distance from the symmetry plane, the radial force in the symmetry plane $F_{rd} = -\frac{\partial \phi}{\partial r}|_{z=0}$ reduces to (Casertano, 1983)

$$F_{rd}(r) = 4\pi G \int_0^\infty u du \int_0^\infty d\zeta \frac{2\sqrt{u}}{\pi\sqrt{r\rho}} (\mathcal{H}(p) - \mathcal{E}(p)) \frac{\partial}{\partial u} \rho(u, \zeta) \quad (2.5)$$

with

$$p = p(x) = x - \sqrt{x^2 - 1} \quad \text{and} \quad x = \frac{r^2 + u^2 + z^2}{2ru} \quad (2.6)$$

and \mathcal{K} and \mathcal{E} are the complete elliptic integrals (Binney & Tremaine, 1987, Formulae 1C-15)

$$\mathcal{K} = \int_0^1 \frac{dt}{\sqrt{(1-t^2)(1-k^2t^2)}} \quad (2.7)$$

$$\mathcal{E} = \int_0^1 dt \sqrt{\frac{1-k^2t^2}{1-t^2}}$$

for whose calculation effective numerical methods exist (Press et al., 1986, Chap. 6.7).

The mass density $\rho(r, z)$ can be measured (indirectly) for the luminous components. Remarkably, the simplifying assumption that

$$\rho(r, z) = \rho_0(r)f(r, z) \quad \text{or} \quad \rho(r, z) = \rho_0(r)f(z) \quad (2.8)$$

works quite well for galactic stellar disk (van der Kruit & Searle, 1981b,a).

For a spherically symmetric component with a mass density $\rho(r)$ the radial force simply calculates as

$$\frac{\partial}{\partial r} = \frac{GM(r)}{r^2} \quad , \quad (2.9)$$

$M(r)$ being the mass inside the sphere of the radius r

$$M(r) = \int_0^r 4\pi s^2 \rho(s) ds \quad . \quad (2.10)$$

Because of the assumed symmetry the mass density is given by (Binney & Merrifield, 1998, Chap. 4.2.3)

$$\rho(r) = -\frac{1}{\pi} \int_r^\infty \frac{d\sigma(r')}{dr'} \frac{1}{\sqrt{r'^2 - r^2}} dr' \quad , \quad (2.11)$$

where $\sigma(r)$ is the projected surface density of the spheroid that for a luminous bulge component is related to a measurable surface brightness or intensity (eq. 2.15). Both expressions can be combined (Kent, 1986) to

$$M(r) = \int_0^r 2\pi r' \sigma(r') dr' + \int_r^\infty 4(\sin^{-1}(r/r') - r(r'^2 - r^2)^{-1/2}) s \sigma(r') dr' \quad . \quad (2.12)$$

2.2.3 Parametrisation of the stellar component

An example for a parametrisation of the disk component of a spiral galaxy is the so-called truncated exponential stellar disk

$$\rho(r, z) = \rho_s(r) (\text{sech}(z/z_0))^2$$

$$\rho_s(r) = \begin{cases} \rho_0 e^{-r/h} & r \leq R \\ \rho_0 e^{-R/h} (1 - \frac{r-R}{\delta}) & R \leq r \leq R + \delta \\ 0 & R + \delta \leq r \end{cases}, \quad (2.13)$$

a theoretically motivated (Spitzer, 1942; Freeman, 1978) density-law that resembles a truncated Freeman-disk (Freeman, 1970)

$$\sigma(r) = \sigma_0 e^{-r/r_h} \begin{cases} \sigma_0 e^{-r/h} & r \leq R \\ \sigma_0 e^{-R/h} (1 - \frac{r-R}{\delta}) & R \leq r \leq R + \delta \\ 0 & R + \delta \leq r \end{cases}, \quad (2.14)$$

where σ is the face-on surface density of a galactic disk. For a disk, surface density σ and surface brightness Σ are coupled by the stellar mass-to-light ratio M/L or Υ with a non-trivial relation:

$$\sigma(r) = M/L \cdot \Sigma = \Upsilon(I_1, I_2, \dots) \cdot \Sigma, \quad (2.15)$$

where I_1, I_2, \dots are colour indices and Σ the face-on surface brightness. Usually the simplification is applied that Υ is a constant for a given stellar component like disk or bulge. Van der Kruit & Searle (1981b; 1981a; 1982) fitted successfully the disk in a sample of spiral galaxies with eq. 2.14. While the existence of a cutoff and the actual best-fitting function for the vertical distribution are a matter of debate (Barteldrees & Dettmar, 1994; Binney & Merrifield, 1998; Wainscoat et al., 1989), eq. 2.14 is a widely accepted description for a stellar disk. The parametrisations vary by the existence of a cutoff radius and the scaleheight law. Instead of a *sech*² distribution, also pure exponential distributions have been applied. More careful analyses have to take into account the coexistence of various distinguishable disk components with varying thickness (e.g. Wainscoat et al., 1989), also an outcome from today's numerical simulations (Abadi et al., 2003b). The usual approach to model a rotation velocity from the light distribution of a stellar disk is either to use a disk parametrisation like eq. 2.13, for which the rotation velocity is calculated employing eq. 2.5, or to measure the surface brightness directly, to assume a law for the vertical density distribution, and to interpolate in-between the measured data points with a differentiable function.

The light distribution Σ of most stellar bulges and elliptical galaxies can be represented by a Sersic-law (Sersic, 1968):

$$\Sigma(r) = \Sigma_0 e^{-k(r/r_e)^{\frac{1}{n}}} . \quad (2.16)$$

For a value of $n > 1$, analytic expressions for the corresponding three-dimensional light distribution solving eq. 2.12 are given in Simonneau & Prada (2004). Again, for a rotation-curve analysis, a measured light profile can be used to solve eq. 2.12 numerically.

While a mass-decomposition does not heavily depend on the actual form of the details of the assumed stellar density law, three difficulties enter the estimation of the stellar mass-distribution in disk galaxies that might well lead to systematical errors in the results. The first is the internal dust obscuration, which has to be estimated. For that, either a measurement of the colours in the galaxy is necessary to estimate dust extinction, or the galaxy has to be observed in very red bands, where attenuation by dust is mitigated or even negligible. The best solution would be to do both and not to choose galaxies seen edge-on, where the dust contamination is difficult to estimate.

Second, the light profiles, even the photometric images of earlier type galaxies stem from both, the bulge and the disk component. Both differ in colour but are not easily disentangled. Several methods for a disk-bulge decomposition have been proposed. An accurate decomposition is very difficult and requires photometric information in several colours (Prieto et al., 2001). Hence, the chosen target objects for special purpose mass-decompositions for which the accuracy in the innermost regions is important are usually late-type spiral galaxies without a significant bulge component. In the presence of a bulge, a parametrisation of the luminosity-profiles is inevitable before a mass decomposition can be performed.

The third difficulty concerns the stellar mass-to-light ratio Υ . To derive the surface mass density, today usually observations in one red band are employed, based on the assumption that Υ is constant throughout the galaxy. This is essentially wrong. Spiral galaxies show a colour-gradient with radius in the disk. This means that the underlying stellar population changes and, as a consequence, also the ratio of emitted light per stellar mass unit, making Υ a function of the *colour* at a certain radius (and also azimuth). The dependence of Υ was considered to be at least weak in red bands, as colour gradients in spiral galaxies are low and furthermore stellar population models indicated that, using photometry in the redder bands, Υ should not depend dramatically on the colour (de Jong, 1996), at least when employing NIR photometry. Recent theoretical studies by Bell & de Jong (e.g. 2001) showed that these variations can be substantial for a galaxy even when using red filters. The only possible way out of this misery would be to employ measurements of colours. Within their analysis Bell & de Jong (2001) and Bell et al. (2003) provide a technique to track the relative variation of Υ with radius using a colour-based relation and thus to estimate the surface mass density much more accurate. The uncertainty of the colour-based technique is the underlying initial mass-function, causing an offset of the zero-point. This zero-point is fixed by the rotation curve analysis itself, as it is in any case common practice

to fit or estimate even a constant Υ in eq. 2.2. To the author’s knowledge, this technique has never been applied.

2.2.4 The interstellar medium

The estimated mass contents of the observable interstellar medium in disk galaxies is mostly low compared to the contribution of the stars. The visible gas contributes to about 10 percent of the luminous mass for late-type spiral galaxies, although even 50 percent can be reached for galaxies of the irregular type. The dust mass is usually as low as 1 percent of the total gas mass. Ionised gas is found in the environments of hot stars and star-forming regions or in the form of a “warm” smoothly distributed medium. Usually the total mass of the ionised gas is comparable to that of the dust. It is therefore roughly correct to state that dust and ionised gas are dynamically unimportant, while neutral and molecular gas play some role. The usual approach to account for the contribution of one of the major dynamical constituents of the interstellar medium in a galaxy is roughly as follows: The column density N_{HI} and hence the mass-surface density $\Sigma_{\text{HI,p}}$ of the atomic neutral hydrogen perpendicular to the line-of-sight can be calculated from HI emission line measurements:

$$\begin{aligned} \frac{N_{\text{HI}}}{\text{cm}^{-2}} &= 1.248693 \cdot 10^{24} \cdot \frac{\Omega_{\text{BSA}}}{\text{arsec}^{-2}} \cdot \frac{I_{\text{tot}}}{\frac{\text{Jy}}{\text{beam}}} \\ \frac{\Sigma_{\text{HI}}}{\text{M}_{\odot}/\text{pc}^2} &= 1.00059 \cdot 10^4 \cdot \frac{\Omega_{\text{BSA}}}{\text{arsec}^{-2}} \cdot \frac{I_{\text{tot}}}{\frac{\text{Jy}}{\text{beam}}} \end{aligned} \quad , \quad (2.17)$$

where Ω_{BSA} is the so-called “Beam Solid Angle”, the integral of the spatial filter function (the “beam”; in the optical it would be called the point-spread function) of the observing device (a radio antenna or a radio-interferometer) over the unit sphere, and I_{tot} the total intensity

$$I_{\text{tot}} = \int_{-\infty}^{\infty} I(\nu) d\nu \quad , \quad (2.18)$$

where $I(\nu)$ is the (frequency-dependent) intensity. A face-on mass-surface density for the use in eq. 2.14 can be calculated by dividing the derived Σ_{HI} by $\sin i$, where i is the inclination of the normal of the plane in which the gas resides with respect to the line-of-sight towards the observer. While frequently a parametrisation of the radial HI profile finds its entry in the analysis, more commonly, the HI contribution to the rotation curve is calculated numerically from a measured radial profile, the azimuthal HI distribution being uniform enough in most cases to allow such an approach. The helium distribution is assumed to be coupled to

that of the HI. Hence, it is the common approach to account for the helium contribution to the mass density distribution by accounting a helium mass fraction of 0.4 the HI mass. The third component of the interstellar medium relevant for the mass distribution is the molecular hydrogen. As molecular hydrogen lacks a dipole moment, it is directly detectable only in absorption against background objects. This means that for the estimation of its distribution inside a galaxy, a tracer molecule has to be found, for which a mass scale factor can be established to estimate the distribution of H_2 . The easiest molecule to detect is CO in the emission line of the transition from the first rotationally excited state to the ground state. It is still a matter of debate whether a so-called X-factor

$$X = N_{\text{H}_2}/I_{\text{CO}} \quad (2.19)$$

can be established for extragalactic objects, but $X = (3 \pm 1) \cdot 10^{20} \text{cm}^{-2}/\text{K km s}^{-1}$ is an accepted range for the galaxy. The uncertainty of the X-factor enters directly rotation curve analyses, if the H_2 is taken into account. Moreover, in many cases the distribution of the molecular gas in a galaxy is not azimuthally uniform but concentrated in spiral arms (see e.g. Helfer et al., 2003), making an inclusion of this component in a rotation curve analysis a difficult problem. However, the molecular gas fraction may play a significant role towards the centre, where its mass-fraction can be a few times larger than that of the HI. In these regions the molecular gas is quite often distributed uniformly, such that it can in principle enter a rotation curve analysis like the HI. Due to the lack of measurements, which are time-consuming, this has but not been applied frequently.

2.2.5 Derivation of rotation curves and the tilted-ring model

Besides the correct estimation of the mass distribution of the luminous mass in disk galaxies, it is equally important to derive reliable rotation curves. For this purpose, spectroscopy of the gaseous components of galaxies is employed. While in some cases stellar absorption lines are analysed, one usually measures prominent emission lines, namely the HI, CO, and $\text{H}\alpha$ emission lines. The intensity distribution in dependence of the frequency I_ν or the wavelength is related to the intensity distribution in dependence of recession velocity via the Doppler shift. Hence, the one-dimensional rotation curve can be deduced from an observed intensity distribution that is a function in three dimensions (referred to also as a datacube) in case of an integral spectroscopy like HI synthesis observations, and in two dimensions where spectra are taken along some pre-defined line along a galaxy as is the case for long-slit spectroscopy.

Consider a flat disk on which the material moves in circular orbits about a common centre (x_0, y_0) , the y axis pointing towards North. The centre moves with a systemic velocity v_0 away from the observer. An orbit at a projected radius r is

seen as an ellipse, divided into two parts by its minor axis. At the receding side the material has a greater recession velocity than the systemic velocity, at the approaching side the recession velocity is lower than the systemic velocity. This ellipse and hence the three-dimensional orientation of the orbit is usually determined by two parameters, the inclination i , which is the tilt of the spin vector with respect to the line-of-sight, and the position angle pa , which describes the orientation of the ellipse on the sky. Various definitions of the position angle exist. It is common to define it by either the orientation of the major or the minor axis of the projected ellipse with respect to the North pole, the y-axis. One can adopt the definition that pa is the angle between the two straight lines from the centre towards the north and from the centre towards the descending node, where the recession velocity changes from being higher than the systemic velocity to being lower than the systemic velocity, measured anticlockwise from North. This angle is also referred to as the “node angle”, in short the angle between the minor axis and the Northern direction. The recession velocity with respect to the observer v_{obs} at a certain position (x,y) along the ellipse then calculates as

$$v_{\text{obs}}(x,y) = v_{\text{sys}} + v_{\text{rot}} \frac{(x - x_0) \cos(pa) + (y - y_0) \sin(pa)}{r} \sin i \quad . \quad (2.20)$$

If one can assign the correct recession velocity to one point at a given radius, then, given that the orientation, the central position, and the systemic velocity are known, this simple equation can be solved for the rotation velocity. Of course neither of these requirements are fulfilled in practice, making the estimation of a rotation curve a complex problem. Galaxy disks are warped, making inclination and position angle a function of the radius, in which case the above model becomes a so-called “tilted-ring model”. The rotation velocity and the geometrical parameters have to be derived simultaneously. Circular orbits are an assumption that is definitely violated in the presence of bars and other systematic errors (see below) enter such an analysis. Two principal ways to extract rotation curves from a measured intensity distribution exist in the context of a tilted-ring modelling.

One way is to assign a recession velocity to the measured spectra at given positions on the sky. With a number of such derived velocities, a velocity map or so-called “velocity-field” of the galaxy is constructed. In the case of a long-slit spectrum, this map can be carried out only along one line. Depending on the number and geometry of the measured points, it is then possible to derive simultaneously the parameters that describe the disk geometry, the position of the centre, the systemic velocity, and the rotation velocity for a given radius r . Depending on the quality of the measurement, varying numbers of assumptions are necessary. In the ideal case of a two-dimensional perfect velocity-field of a galaxy that is neither seen face-on nor edge-on, and for which the centre and the systemic velocity is approximately the same at all radii, in principle no assumptions are required and the geometry is a result of the tilted-ring analysis, used by Rogstad et al.

(1974) for the first time. While at that time, the model fitting was done by hand, today various computer codes exist that allow an automated least-squares fit to the velocity-field (van Albada et al., 1985; Begemann, 1987). If, however, the number of independent data points decreases, more and more assumptions will be necessary to derive the rotation velocity. In the cases, where data along one cut through the velocity-field are analysed, the geometry of the galaxy has to be estimated as an input, e.g. by analysing the photometric information available. Usually, a fitting strategy is necessary, in which it is assumed that the galaxy possesses a common centre and a common systemic velocity for all radii. For very low radii, the assumption of a coplanar disk is also reasonable in most cases. These global properties can be evaluated in a first run in order to then solve for the galaxy geometry in a second run and finally, possibly after a number of steps fixing more and more parameters, for a rotation velocity. Examples for such strategies can be found in Verheijen (1997) and Gentile (2003). The velocity-field method has several drawbacks. The derivation of a proper recession velocity is a non-trivial problem. Pointing on a position of the galaxy, a measured spectrum contains always the contribution of a volume in the galaxy. Firstly, the galaxy itself is not perfectly flat but has a certain thickness, such that the line-of-sight crosses a range of radii and azimuthal positions in the galaxy. Secondly, the measured spectra are the convolution of the true intensity distribution with the instrumental function, the beam. This means that pointing to a position on the sky, the measured spectrum is a weighted mean of the true intensity over a certain area, additionally broadened by an instrumental spectral function (the width of which is called “instrumental dispersion”). Thirdly, the orbiting material contains additional random motions that broaden them. The volume becomes the larger the more inclined a galaxy is with respect to the observer. It is not desirable to observe galaxies too face-on, because the error of a derived rotation velocity goes as $(\sin i)^{-1}$. Therefore, a velocity profile (spectrum), from which the rotation velocity has to be derived, has a complex structure that depends on the intrinsic properties of the galaxy, some of which are the subject of the measurement. Measured spectra are asymmetric due to this effect, such that simple techniques as assigning a weighted mean of the spectra (the so-called first moment) or fitting Gaussians would lead to an underestimation of the rotation velocity. The incalculable effect of “beam smearing” has thus become the major issue in the discussion of mass-decompositions. It leads usually to a damping of the curvature of the derived rotation curve. The next drawback of the method becomes obvious, when the case of a warped disk is considered. It is known that in principle every galaxy disk is warped to some degree (see below), which leads occasionally to the situation that the line-of-sight crosses the galaxy disk twice or several times. In such a case it is even impossible to assign a single recession velocity to a point in the galaxy. Trials to circumvent the problem can lead to a wrong estimation of the disk geometry, and hence, the rotation velocity (see e.g. Schinnerer & Scoville, 2002, and Chap. 5).

Another way to find a rotation curve, that is not hampered by these systematic effects, is to artificially reproduce a spectral observation of the observed material and to compare it with the true observation in order to improve the model datacube or long-slit spectrum. While in principle this technique is applicable by means of a least-squares fit, most probably due to the missing computational power, a direct model-fitting has been used scarcely. Least-squares fitting routines for long-slit observations have been developed and applied by Simard & Pritchett (1999) and Böhm et al. (2004) for several galaxies, while the direct fit of the tilted-ring model to the much larger datacubes has been applied only once (Corbelli & Schneider, 1997) and is one of the major topics of this thesis. Model datacubes have been used to check the results of a fit to the velocity-field (Gentile et al., 2004) or to analyse more complex disk structures (Fraternali et al., 2001). A direct fit has the obvious advantage that systematic errors are reduced and moreover the number of independent data points is increased. The bill is an increase in the fit parameters. It is necessary to include a model description for the surface brightness distribution, which is simply not possible if fitting to velocity-fields. To the first order the surface brightness distribution can be assumed to be azimuthally uniform and can then be fixed at a series of radii.

However, both methods have their shortcomings in the real structure of galaxy disks. One of the basic assumptions is the circularity of orbits. Thus, especially in the presence of motions along bars, a tilted-ring model gets unreliable. Hence, either the relevance of non-circular motions has to be excluded in a separate test, or non-circular motions have to be included in the fitting procedure (see e.g. Schoenmakers et al., 1997; Simon et al., 2003). The other assumption is the homogeneity of the observed disk material. Cavities on short scales enter the derivation of velocity-fields, while on large scales (compared to the radius of a ring) they will affect a direct fit to the datacube.

The perfect tracer for a rotation curve lies in a very flat homogeneous disk and emits line-radiation at very short wavelengths (making a high resolution possible), is un-obscured by dust, translucent, and detectable to the outermost radii in the disk. None of these requirements are fulfilled by the kinematical tracers of disk galaxies. The $H\alpha$ recombination line of hydrogen is usually the strongest optical emission line that is produced in warm ionised regions, while – depending on the bandwidth of an observation – other (forbidden) lines can be used for an analysis, too. In a galaxy disk, this emission stems mostly from H II (star forming) regions. The obvious advantage of this tracer is the high spatial resolution that can be reached. However, this tracer has the drawback that while usually it is found in the plane, it is easily expelled vertically from the disk, because it is thin gas. Hence, the kinematical information from H II regions has to be examined with care. Furthermore, dust obscuration and scattering of light by dust plays a big role in this spectral regime, when a galaxy is observed edge-on (Baes et al., 2003). Star formation is restricted to the centres of galaxies and to spiral arms.

Thus, optical emission lines are at least restricted to lie in the stellar disk. The kinematics at large radii cannot be traced with optical emission lines. The same accounts for CO emission lines from rotational transitions in the mm- or the sub-mm regime. CO can be found in cold clumps of molecular material that are the birth-sites of stars. Seen from a larger distance, such clumps form a more or less continuous distribution of molecular gas on larger scales, clouds and cloud complexes. As already mentioned above, the distribution of these complexes is not necessarily homogeneous. These emission lines bear a larger observational beam, but the cloud material is not easily subject to local disturbances. Single clumps span a mass distribution that starts at $1M_{\odot}$. Any supernova explosion or stellar wind is more likely to destroy a cloud than to expel it from the disk, as would likely be the case for the warm medium in the disk. Thus, CO as a tracer of kinematics has the large advantage that one can trust in the emission originating in the thin galactic disk. The only tracer that can be employed to trace the kinematics on large scales is the neutral hydrogen, because at the largest radii, the visible disk consists of this material only. Hence, for a complete determination of the galaxy kinematics, the HI emission line cannot be omitted. Most of the HI is fairly tied to a somewhat thicker disk (but see e.g. Swaters et al., 1997; Fraternali et al., 2001) and azimuthally distributed rather uniformly (but see e.g. Boomsma et al., 2002). The drawbacks of this tracer are that it emits at a rather low wavelength and frequently shows a lack in the galaxy centre. As HI observations are thus highly affected by beam smearing and frequently do not trace the central kinematics of a galaxy, usually for a rotation curve analysis one or both of the other common tracers are used to trace the central kinematics.

The last, and maybe most important point to be discussed in this section is that of assigned error bars. It is possible to derive statistical errors of a rotation curve in a formal way when fitting to velocity-fields or to the entire datacube. Such error bars, which are derived under the assumption of a uniform statistical error of the data, are far too low. Firstly, often the exact statistical uncertainty that has to be assigned to a data point in a cube or a velocity-field is poorly known. Secondly, and most important, the internal structure of galaxy disks and hence the disk in which the various tracers reside, plays a major role in the derivation of rotation curves. Galactic disks are not uniformly filled with the tracer material but show inhomogeneities and furthermore can locally not even represent an orbital motion, as shown above. Such inhomogeneities enter a rotation curve as an incalculable systematic error. Hence, other methods have to be found to derive “proper” error bars to rotation curves. A commonly accepted way has still to be found (cf. Blais-Ouellette et al., 2004) and it is in principle necessary to inspect closely available data in order to judge the reliability of derived data points. A way to determine error bars is to fit independently two sides of a galaxy with a fixed centre and to estimate an error from the difference of the fit results (e.g. Gentile et al., 2004), while recently more complex methods found their way

into the analysis (Simon et al., 2005). It has but to be emphasised that there is no way around the close inspection of the data in order to distinguish between features that are due to an erratic fit as e.g. can occur due to outflow motions and real features of the rotation curves. As this is a partly subjective issue, the error bars and the reliability of rotation curves are a matter of debate. As this debate dominates the discussion of mass-decompositions, it is important to take highest care in the derivation of rotation curves, and, if possible, to use analysis techniques that do not introduce systematic errors in addition to those that are present anyway.

2.2.6 The controversy of Dark Matter profiles

In the 90's computers became available with which it was possible to perform computer simulations of structure formation in the universe. The accuracy of these simulations was claimed to be high enough in order to simulate the structure of Dark Matter halos down to a sub-galaxy scale. One of the outcomes of these simulations is that the structure of Dark Matter in the universe is self-similar from the scales of clusters down to sub-scales of dwarf galaxies.

The radial density profile of CDM halos is assumed to be expressible analytically, depending on only a few parameters, and similar for clusters, galaxies and dwarf galaxies. Usually, the radial dependence of a Dark Matter density profile $\rho(r)$ (including those that do not stem from simulations) can be expressed analytically as

$$\rho(r) = \frac{\rho_0}{f(r/r_s)} \quad , \quad (2.21)$$

where ρ_0 is a characteristic density, and r_s a characteristic scale. With the assumption of spherical symmetry the mass $M(r)$ included in a sphere of radius r can be calculated (eq. 2.10), and hence with eq. 2.9 and eq. 2.1 the rotation velocity $v(r)$.

For cosmologically motivated profiles, some definitions shall be explained here. Usually, the characteristic density is related to the critical energy density ρ_c at which the universe becomes flat

$$\rho_c = \frac{3H^2}{8\pi G} \quad , \quad (2.22)$$

H being the Hubble constant and G the gravitational constant, via the dimensionless characteristic density scale

$$\rho_0 = \delta_c \rho_c \quad . \quad (2.23)$$

Cosmological simulations provide the mean over-density ρ_{vir} at which an object virialises at a given redshift. The virial over-density ρ_{vir} is usually defined as a

dimensionless quantity Δ_v in units of ρ_c

$$\rho_{\text{vir}} = \Delta_v \rho_c \quad . \quad (2.24)$$

In an Einstein-de Sitter universe with the total mass- and matter density of $\Omega = \Omega_m = 1$, Δ_v accounts to $178 \approx 180 \approx 200$, for a concordance model with $\Omega = 1$ and $\Omega_m = 0.3$ Δ_v becomes 337. For analytic expressions to calculate Δ_v see Bryan & Norman (1998) or Kitayama & Suto (1996). The virial radius r_{vir} is defined as the radius at which the mean density is a factor Δ times ρ_c

$$\bar{\rho}(r_{\text{vir}}) = \frac{GM(r_{\text{vir}})}{4/3\pi r_{\text{vir}}^3} = \Delta\rho_c \quad , \quad (2.25)$$

where usually Δ is of the order of Δ_v but not necessarily identical. In the first publication of an analytic density profile from simulations in an Einstein-de Sitter universe (Navarro et al., 1996), a Δ of 200 was used and kept by the authors from thereon (see Navarro et al., 1997). $M_{\text{vir}} = M(r_{\text{vir}})$ is called the virial mass. The virial velocity $v_{\text{vir}} = v(r_{\text{vir}})$ is coupled with the virial radius via

$$\frac{r_{\text{vir}}}{v_{\text{vir}}} = \sqrt{4/3\pi G\Delta\rho_c} \quad . \quad (2.26)$$

With the definition of the concentration parameter

$$c = \frac{r_{\text{vir}}}{r_s} \quad , \quad (2.27)$$

the rotation velocity of semi-analytic density profiles is conventionally given in dependence of the concentration and the virial velocity, while for other (completely empirical) profiles it is given in terms of the characteristic density and the characteristic scalelength, while a variety of possible parameter pairs exists. Eqs. 2.23 and 2.27 define for example δ_c . Tab. 2.1 gives an overview of used velocity profiles and corresponding rotation velocities. The major difference of the CDM density profiles of older origin is that the predicted mass density rises towards the centre with a gradient $-\alpha$ steeper than -1, they are said to have a ‘‘cusp’’. In contrast, purely empirical Dark Matter density profiles have a constant density ‘‘core’’ towards the centre with $\alpha = 0$.

Prime candidates to test the fitting quality of different Dark Matter halo profiles are naturally those which are dominated by their Dark Matter component or for which at least the influence of the luminous component on the dynamics is remote: dwarf-, low-luminosity-, and low-surface brightness (LSB) galaxies (Carignan & Freeman, 1988; Persic et al., 1996; de Blok & McGaugh, 1997; Pickering et al., 1997). For a mass decomposition of these, the unknown introduced with the stellar mass-to-light ratio enters the analysis less severe. Intriguingly, the cuspy Λ CDM halos appeared not to be compatible with rotation curves of dwarf spiral

Profile name	analytic form	resulting squared rotation velocity
NFW ¹⁾	$\frac{\delta_c \rho_c}{(r/r_s)(1+r/r_s)^2}$	$v_{\text{vir}}^2 \frac{(1+c)(1+cx)\ln(1+cx)-cx(1+c)}{x(1+cx)(1+c)\ln(1+c)-c(1+cx)}, x = \frac{r}{r_{\text{vir}}}$
Moore ²⁾	$\frac{\delta_c \rho_c}{(r/r_s)^{1.5}(1+(r/r_s)^{1.5})}$	$v_{\text{vir}}^2 \frac{\ln(1+(cx)^{1.5})}{\ln(1+c^{1.5})}, x = \frac{r}{r_{\text{vir}}}$
Generalised NFW ³⁾	$\frac{\delta_c \rho_c}{(r/r_s)^\alpha(1+r/r_s)^{3-\alpha}}$	$v_{\text{vir}}^2 \frac{\int_0^{cx} y^{(2-\alpha)}(1+y)^{\alpha-3} dy}{\int_0^c y^{(2-\alpha)}(1+y)^{\alpha-3} dy}, x = \frac{r}{r_{\text{vir}}}$
Navarro ⁴⁾	$\rho_{-2} \exp(-\frac{2}{\alpha}(\frac{r}{r_{-2}})^\alpha - 1)$	$\frac{4\pi G \rho_{-2} e^{2/\alpha}}{\alpha r} (\frac{2}{\alpha r_{-2}^\alpha})^{-3/\alpha} \Gamma(\frac{3}{\alpha}) \gamma[\frac{3}{\alpha}, \frac{2}{\alpha}(\frac{r}{r_{-2}})^\alpha]$
Pseudoisothermal ⁵⁾	$\frac{\rho_0}{1+(\frac{r}{r_0})^2}$	$4\pi G \rho_0 (1 - \frac{r_0}{r} \arctan(\frac{r}{r_0}))$
Burkert ⁶⁾	$\frac{\rho_0 r_0^3}{(r+r_0)(r^2+r_0)^2}$	$\frac{4\pi G \rho_0 r_0^3}{2r} (\ln(\frac{r+r_0}{r_0}) + \frac{1}{2} \ln(\frac{r^2+r_0^2}{r_0^2}) - \arctan(\frac{r}{r_0}))$
URC ⁷⁾	$\frac{\rho_0}{1+(\frac{r}{r_0})^2} \frac{r^2+3r_0^2}{3r^2+3r_0^2}$	$v^2(r_{\text{opt}})(1 + (\frac{r_0}{r_{\text{opt}}})^2) \frac{r^2}{r^2+r_0^2}$

Tab. 2.1: *Common spherical density profiles of Dark Matter halos.* 1) Navarro et al. (1997), 2) Moore et al. (1998), 3) de Blok et al. (2001), 4) Navarro et al. (2004); Simon et al. (2005), r_{-2} and ρ_{-2} are the radius and the density where the logarithmic slope of the density profile equals -2 , Γ is the complete Gamma function, and γ the lower incomplete Gamma function, 5) Bahcall et al. (1982), 6) Burkert (1995), 7) “Universal Rotation Curve” (Persic & Salucci, 1995), cf. Gentile (2003), r_{opt} is the radius at which 83 percent of the optical light is encompassed, which defines the core radius r_0 .

galaxies. This discrepancy was first realised by Flores & Primack (1994) and Moore (1994), even before the first analytic form of a CDM density profile was published by Navarro et al. (1996). In subsequent studies, various authors claimed to be able to confirm these findings (Burkert, 1995; Blais-Ouellette et al., 1999; Salucci & Burkert, 2000; de Blok et al., 2001; Borriello & Salucci, 2001; de Blok & Bosma, 2002; Salucci et al., 2003; Welldrake et al., 2003; Simon et al., 2003; Gentile et al., 2004). Simulations using different codes with higher accuracy and cosmological parameters better adapted to today’s standard CDM cosmology confirmed the major result of Navarro et al. (1996) that a Dark Matter density

profile should have a slope of less than -1 towards the centre (Navarro et al., 1997; Kravtsov et al., 1998; Moore et al., 1999b; Navarro & Steinmetz, 2000; Ghigna et al., 2000; Hayashi et al., 2004; Navarro et al., 2004; Reed et al., 2005), while the existence of an asymptotic power-law, as proposed e.g. by Navarro et al. (1996) or Moore et al. (1999c) has become a matter of discussion (Navarro et al., 2004). Navarro et al. (2004) and Reed et al. (2005) claim their findings to be reliable down to central radii of $0.005 - 0.01 r_{\text{vir}}$. For a galaxy of the size of the Milky Way this corresponds to at least 1 kpc , below which rotation curves cannot be used to test any cosmological prediction. If the data analysis and the techniques used in the numerous mass decompositions of Dark Matter dominated galaxies are reliable, this suffices to impose a problem (beneath others) on the current standard cosmological view on galaxy scales.

However, some objections to these findings can be made. Recently, the question has been risen, how well a rotation curve represents the underlying potential. Some authors claimed that in presence of a bar or a net triaxial potential – as is a general outcome from CDM simulations – a rotation curve derived under the assumption of circular orbits is biased towards a shallower underlying Dark Matter potential. If the potential in disk galaxies is generally triaxial or not axisymmetric in the plane of the galaxy disk, rotation curves thus suggest a cored density distribution, if naively treated as a tracer of an axisymmetric potential. This problem can but be dealt with observationally. If there is a significant deviation of the orbits in a galaxy from circularity, it can be detected by a modified tilted-ring analysis, allowing for harmonic changes of the rotation velocities along the rings. Such analyses, first used by Franx et al. (1994), have been performed excessively by Schoenmakers et al. (1997). They came to the conclusion that in the absence of a visible bar, the ellipticity of the potential in the plane of the disk is less than 0.1 . This means that in general an observer can trust a rotation curve derived from observations of unbarred galaxies. Simon et al. (2003) and Simon et al. (2005) include a harmonic analysis in their rotation curve analysis of five Dark Matter dominated galaxies. They detect an orbital ellipticity in all cases, but they also show that these are small enough to justify a mass-decomposition with the derived rotation curves. In a very extensive analysis including a colour-based estimation of Υ , they find that while the rotation curves are well fitted with a pseudoisothermal profile in one case, they are well fitted with an NFW profile in one other case, the central slope of the mass profile having a large spread. This is in conflict with both, halo profiles stemming from simulations, as well as with the assumption of DM halos having a core. Unfortunately, their analysis is based not only on analyses of velocity-fields, but they also employ a rather crude technique (full Gaussian-fitting) in order to calculate their velocity-field. Furthermore, the gaseous components of the galaxy are not taken into account in the mass-decompositions, making their results vulnerable.

An unresolved issue is, how pressure-supported the disk material in the central

regions of galaxies is. If the dispersion of the material is high, a rotation velocity of a perfectly cold disk would be significantly higher than the measured one. In order to calculate a rotation curve for which eq. 2.1 is valid, the measured one has to be corrected upwards. The result would be a better fit of cuspy Dark Matter profiles.

Nearly all authors claiming to be able to rule out cuspy Dark Matter profiles in disk galaxies, use analyses of velocity fields. van den Bosch et al. (2000) pointed out that by doing that, due to beam smearing effects, analyses even of LSB galaxies do not provide the required accuracy. Van den Bosch & Swaters (2001) and Swaters (2001) come to the same conclusion, as well as Swaters et al. (2003) employing mock-observations of galaxies: Even the combination of optical and HI rotation curves cannot give a definite answer to the problem, due to various effects that enter the analysis as an unaccounted systematical error, the thickness of the disk, leading to ambiguities of velocities along the line-of-sight, spatial resolution (beam smearing), especially in case of HI spectroscopy, and absorption effects in H α observations. Other authors do not agree: Using observations and simulations, de Blok & Bosma (2002) and de Blok et al. (2003) tried to show that these arguments are not valid for LSB galaxies. Rotation curves of LSB galaxies rise very slowly and are therefore not as affected by beam smearing and other observational effects as other galaxies. If a CDM density profile is fitted to the rotation curves of these galaxies, the mean concentration of the halos is far too low to be realistic in a CDM scenario.

As controversial results exist the question of the influence of the beam smearing on rotation curve analyses must be regarded unresolved, and hence the question whether rotation curves of disk galaxies impose a problem on the CDM paradigm. Analysis techniques that mitigate the unwarranted effects of a line-of-sight crowding by a finite thickness of the disk and beam smearing are thus a welcome tool to get a better answer to the question whether halo profiles that the commonly favoured theory predicts are the ones to be observed in nature.

2.3 Warps in disk galaxies

For many disk galaxies the optical disks containing the stars are flat to a first order approximation, the orbits of the stars lying in one (thickened) plane. Because of that, before the fine-structure of neutral gaseous disks of galaxies could be explored, a bending of a galaxy disk – a warp – was considered an extraordinary phenomenon (e.g. Pease 1917, Sandage 1961, Arp 1966, cf. Sancisi 1976). Warps were not treated as being an important feature. With the discovery of the warp in the HI disk of the Milky Way (Burke, 1957; Kerr, 1957), this view started to change, although authors hesitated to associate the features that identify a warp in the velocity-field and the total HI maps of external galaxies with

their origin (Shobbrook & Robinson, 1967; Lewis, 1968; Gordon, 1971; Bottinelli & Gougenheim, 1973). Wright et al. (1972) were the first to realise that M33 is a heavily warped galaxy and that the warp can be used to explain every “extraordinary” feature in the kinematics and the distribution of its outer HI disk. Shortly after, Rogstad et al. (1974) deciphered their HI synthesis maps of M83 with their newly developed tilted-ring model in order to show that this galaxy shows the same phenomenon and Rogstad et al. (1976) confirmed the results of Wright et al. (1972) with synthesis observations and tilted-ring modelling. Sancisi (1976), who observed five edge-on galaxies, in which warps are directly evident from the integrated HI maps, put evidence to the fact that warping is a common phenomenon in disk galaxies: Four galaxies of his sample were warped beyond the optical disk. Finally Albert Bosma’s (Bosma, 1981a,b) famous work did not only show that the rotation curves of disk galaxies cannot be accounted for by the gravitational field of the baryonic disk and assuming Newtonian dynamics, but also confirmed that warping is a basic feature found in a large number of disk galaxies. In a sample of 35 nearby galaxies he identified 12 galaxies as being undoubtedly warped while his criteria to distinguish a warp from non-circular motions in a plane were strictly in favour of “oval” distortions and asymmetric distortions of the kinematics in the plane of the disk.

Studies of warps had become exciting. Warps could no longer be regarded as peculiarities occurring in a few special cases. They have to be taken into account, if one wants to explain structure and formation of galaxies.

2.3.1 Basic warp description

Two prototypes of warps exist and can be observed, while usually a warp can be viewed as a mixture of both leading to an asymmetric appearance. S-shaped warps can be considered as a continuous tilting of the disk while retaining a common centre. In projection they resemble an integral sign or the letter “S” when seen edge-on. U- or bowl-shaped warps are a displacement of the disk in vertical direction while the spin normal vector stays the same. This leads to an appearance of a “U” when seen edge-on. An expressively asymmetric warp is sometimes referred to as “L-shaped”. Fig. 2.1 shows prototype warped galaxies.

Frequently, in theoretical and observational works, warps are described in terms of a tilted-ring model. The mid-plane surface of the disk \mathbf{S} parametrised by radius r and azimuth φ calculates then as

$$\mathbf{S}(r, \varphi) = r \begin{pmatrix} \cos pa(r) \cos \varphi - \sin pa(r) \cos i(r) \sin \varphi \\ \sin pa(r) \cos \varphi + \cos pa(r) \cos i(r) \sin \varphi \\ \sin i(r) \sin \varphi \end{pmatrix} + s(r) \mathbf{n} \quad , \quad (2.28)$$

the orientation of the disk at radius r being described by the inclination i and the position angle pa and s being the displacement of the disk in the direction of the

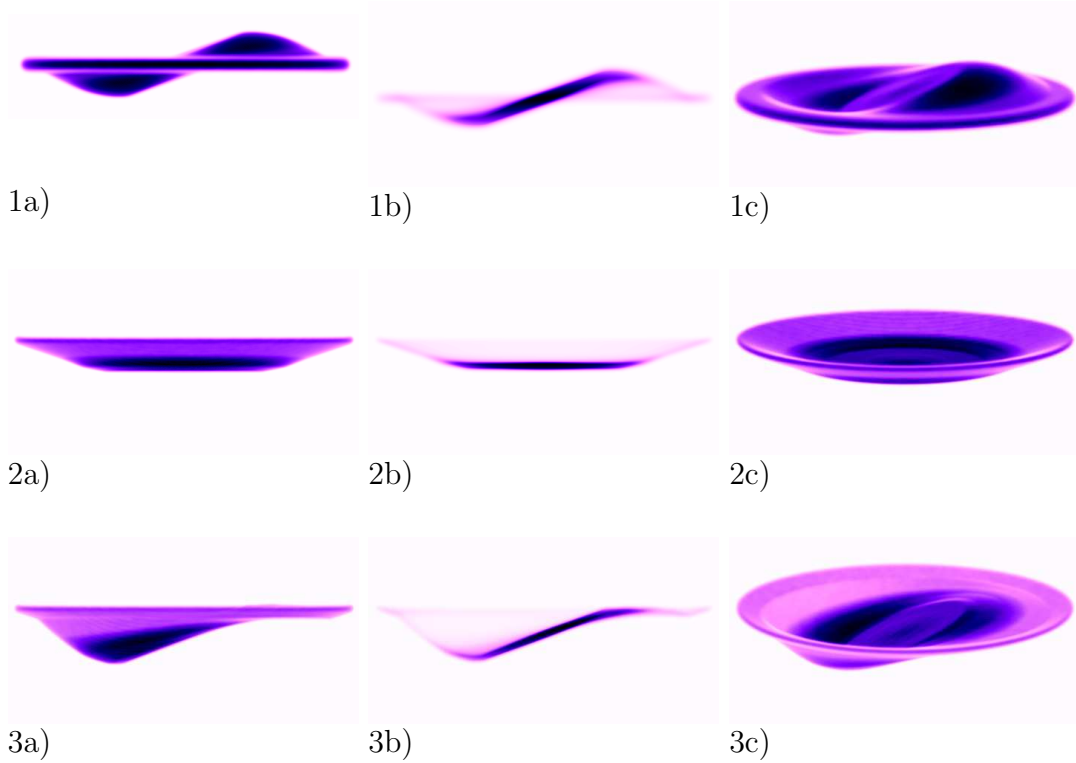


Fig. 2.1: Various warp shapes, generated using a tilted-ring model. a) edge-on view opaque, b) edge-on view transparent (as seen in observations), c) inclined view opaque. 1) S- or integral-shaped warp, 2) U- or bowl-shaped warp, 3) Mixed, asymmetric or L-shaped warp.

constant normal vector \mathbf{n} . In case of an S-shaped warp s is a constant, while in case of a U-shaped warp i and pa are constants and \mathbf{n} is the normal vector of the disk determined by i and pa . In order to resemble a (usually observed) projected shape of a U or an S, i , pa , and s and their derivatives should be monotonic functions. Regarding only central displacements in the z-direction, $s(r) = z_0(r)$, $\mathbf{n} = (0, 0, 1)$, with i staying small, and substituting φ with $\varphi - pa = \varphi - \varphi_1$, eq. 2.28 can be written as

$$\mathbf{S}(r, \varphi) = (r \cos \varphi, r \sin \varphi, z_0(r) + z_1(r) \sin(\varphi - \varphi_1(r))) \quad , \quad (2.29)$$

with $z_1(r) = r \cdot pa(r)$. This, in turn, is a special case of a perturbation formalism to describe the mid-plane surface

$$\mathbf{S}(r, \varphi) = (r \cos \varphi, r \sin \varphi, \sum_{m=0}^{\infty} z_m(r) \sin(m \cdot \varphi - \varphi_m(r))) \quad . \quad (2.30)$$

U-shaped warps are thus sometimes referred to as an $m = 0$ azimuthal perturbation in vertical direction, while S-shaped warps are referred to as an $m = 1$

perturbation with respect to a flat disk, the so-called trivial mode being a tilt and shift of the whole disk

$$\begin{aligned} z_0(r) &= \zeta \\ z_1(r) &= \alpha r \\ \varphi_1(r) &= \beta \end{aligned} \quad , \quad (2.31)$$

ζ , α , and β being constants. In the following sections a galactic disk is called warped when the disk geometry can be described with sufficient precision by eq. 2.28 or eq. 2.29. Also, the definition of S- U- and L- shaped warps as given above will be used.

2.3.2 Warp shapes

Warps may have different origins. At least the various appearances of warps occurring at various scales suggest that the warp of one galaxy may well be considered as a mixture of different single warping structures generated by different mechanisms or the same temporary mechanism but at different stages of evolution. Such warping structures, while clearly distinguishable if occurring solely in a single galaxy, are in general not easily distinguished if occurring in the same galaxy. An observer who wants to categorise warps and to measure their properties is thus confronted with a difficult situation, which is but not hopeless as different warp types may well be distinguished. Unfortunately, the terminology in terms of warp classification is not well developed and in statistical works usually restricted to a categorisation of a warp of belonging to the S-, U-, or L-shaped class and a quantification of the warp amplitude and the asymmetry for projections of galaxies.

On scales well inside galactic stellar disks warping is a common phenomenon with a frequency of occurrence up to 100 percent, depending on the threshold one sets in order to identify a disk as being warped (Schwarzkopf & Dettmar, 2001). Usually the warps reach only a maximum height of a few percent of the radius at which they occur. Quite frequently, a moderate tilt of the very central disk (or an indistinguishable bar) with respect to the mean plane is observed (Schwarzkopf & Dettmar, 2001), a feature also present in our own galaxy (Liszt & Burton, 1980). Warping of a low amplitude inside the stellar disk will furtherly be called a a “small-scale warping” or “corrugation”.

Optical studies of edge-on galaxies show that usually a substantial warping of stellar disks develops at their edges or at least at larger radii (Sánchez-Saavedra et al., 1990a,b; Reshetnikov & Combes, 1998; Schwarzkopf & Dettmar, 2001; Sánchez-Saavedra et al., 2003), their shapes possibly being distributed uniformly between U-,S-, and L-shaped warps. Regarding the frequency of warp shapes, results are quite diverse, obviously due to selection-effects and the subjective

nature of the classification. Reshetnikov & Combes (1998), who distinguish only between S- and U-shaped warps, find a total of 35 percent U-shaped- and 34 percent S-shaped warps in a sample of 540 galaxies. Schwarzkopf & Dettmar (2001) find 19 percent U-shaped, 24 percent S-shaped and 20 percent L-shaped warps in an analysis of 108 galaxies. This stands in contrast to the findings of Sánchez-Saavedra et al. (2003) studying a sample of 150 galaxies. They determine a fraction of 52 percent S-shaped warps and only 5 percent U-shaped and 4 percent L-shaped warps in their sample. These studies roughly agree, however, in the total number of 60-70 percent of observed warps occurring at the edges of the optical disks in edge-on galaxies. Estimating the number of warps missed in such studies due to an orientation bias, Reshetnikov & Combes (1998) estimate the total percentage of galaxies with a U- or S- shaped warp to 86 percent, meaning that practically all galaxies do show a warp occurring at the edges of the optical disk. Here, warps observed in optical disks that have the highest amplitude at their edges shall be called “optical warps”.

Usually, warping becomes substantial at large radii, where the light from stars is dim. Hence, warps are observed best and show the largest amplitudes in the HI component of a galaxy, simply due to the fact that an optical warp is restricted to the detectable extent of the optical disk. If a galaxy is observed in its gaseous component, usually the warp in the gas is an extension of and optical warp and evolves to a larger amplitude. A U-, S-, or L-shaped warp that is seen in the gaseous component shall be called a gaseous warp. Gaseous warps are usually S- or L-shaped (García-Ruiz et al., 2002b). In general, a warp that is seen in the stars and/or the gas with a large amplitude at large radii (not necessarily evolving at the edge of the disk) shall be called a large-scale warp. If such large scale warps are integral-signed with a high degree of symmetry, they are generally called “grand-design warps”, the most examined warp type in the literature. Quite often, grand-design warps are thus simply called warps, their nature induced from the context. Most warp studies of individual galaxies, are aimed at galaxies with a grand-design warp, as is also the case in the present work. Therefore this terminology will be kept and a grand-design warp be called simply a warp, if the context does not allow for ambiguities.

A quite common warping phenomenon is that of a “knee” or a “wobbling” at intermediate up to larger radii. The mid-plane of the galactic disk changes its orientation or position either in the manner of a U-shaped or an S-shaped warp and then turns back towards the orientation or position of the central disk. In terms of eq. 2.28 and below, i and pa are not monotonic in case of an point-symmetric wobbling (S-warps), but reach a local extremum and then turn back to their initial values or become monotonic functions of r . The same accounts for z_0 when a U-type wobbling is observed. The large-scale warp evolves with radius oppositely to the direction of the initial warp. Examples for an S-type wobbling are UGC 7321 (Uson & Matthews, 2003) or ESO 121-G6 (Józsa, 2002),

and possibly the Milky Way with Gould's belt (e.g. Frogel & Stothers, 1977). U-type wobbling is found e.g. in UGC 1281 (García-Ruiz, 2001).

2.3.3 Rules for the behaviour of warps and their direct implications

Detailed structural HI studies of grand-design warps of rather isolated galaxies and the relation of their warp structure to intrinsic galaxy parameters lead to a set of rules that warps follow in general. Nearly no rule is a hard law, as clearly counter-examples can be found (pointing to the fact that, while grand-design warps have a common origin, other mechanisms to excite warps play a role in individual cases). But they have been established as a general trend. The most extensive work was carried out by Briggs (1990), who compared tilted-ring models of a sample of 12 galaxies generated from (at that time) high-quality HI synthesis data. He found that the warps in the sample follow basically four rules:

Rule 1: The HI layer is planar within the blue optical radius R_{25} , but warping becomes detectable within the Holmberg radius $R_{H0} = R_{26.5}$.

Rule 2: The kinematical minor axis (the line connecting the single nodes in a tilted-ring model) in the plane defined by the inner flat disk is straight inside a transition radius $R_{tr} \approx R_{H0}$.

Rule 3: Outside R_{tr} the kinematical minor axis in the plane defined by the inner flat disk advances in the direction of galaxy rotation for successively larger radii.

Rule 4: A unique reference frame exists, in which the kinematical minor axis exhibits two straight regimes, one inside R_{tr} , one outside R_{tr} .

A deeper understanding of these rules can be achieved realising that a warp makes the galactic disk a system of coupled gyros. At two different radii the disk exchanges a mutual torque determined by the mass density and the mutual inclination of the disk with itself at the different radii. This leads to a precession of the disk, with an a priori different precession rate at different radii determined by the differential angular momentum $\partial \mathbf{m} / \partial r(r)$ and the net torque T imposed on the disk at the given radius, including a possible external torque. If the local torque is adjusted such that the precession frequency does not vary much (or not at all) throughout the disk, the disk will precess as one unit, representing a frozen long-lived warp structure. It can be shown that in presence of an external torque such solutions exist (e.g. Sparke & Casertano, 1988). It is now obvious that the pattern of the node-line – the kinematical minor axis – is a frozen-in structure in the presence of co-precession. A winding kinematical minor axis can thus be interpreted as a breach of co-precession.

Rules 1 and 2 thus imply that the self-gravity of the disk is important for warp formation. A tilt of the disk is maintained at a certain value in regions where the disk is massive, single test-particles being forced to fall on the common plane. In other words, the torque mutually imposed on the galaxy material orbiting at different radii leads to a strong coupling of the inner disk. This coupling still enforces at larger radii a co-precession. Without a co-precession, the kinematical minor axis would be expected to wind up in the inner plane of the galaxy. Rule 3 implies that the coupling becomes weak enough to allow the outer disk to precess at a differing precession rate with respect to the inner disk at radii larger than R_{tr} . If one assumes a retrograde precession with respect to the direction of rotation (a behaviour similar to that of a gyro), Rule 3 further implies that the precession rate decreases with radius beyond R_{tr} .

While rules 1-3 are generally accepted as describing by large and large the structure of grand-design warps, one year after its publication rule 4 was put down by Briggs & Hamphuis (1991) to “be a restatement of the fact that the LON (kinematical minor axis) rotate with increasing radius”, because the special reference frame quoted would simply be one in which this rotation becomes a gentle arc, easily approximated by a straight line. However, taken seriously, this rule could also imply that the transition radius divides two regions which co-precess independently from each other. One of the main results of this work is a different interpretation of this rule, with the implication of a co-precessing disk beyond R_{tr} .

In the framework of his mass-decompositions to reveal the structure of the DM halos in which the galaxies reside, Bosma (1991) found a connection between the halo properties and the likeliness of a galaxy to show a warp, at the same time emphasising the global importance of the warping phenomenon:

Rule 5: Warps are ubiquitous: In at least half of all galaxies warps are detected.

Rule 6: A weak correlation between the halo core radius (of a pseudoisothermal halo) derived from mass-decompositions and the probability to detect a warp exists. Galaxies with smaller core radii (with respect to the optical radius of the disk) are less likely to be warped.

Rule 6 implies that the Dark Matter halo plays a significant role for the formation and evolution of warps.

Several statistical studies of warp properties exist. Among those optical studies are the most frequent and the highest number of galaxies is analysed (Sánchez-Saavedra et al., 1990a,b; Reshetnikov & Combes, 1998; Schwarzkopf & Dettmar, 2001; Sánchez-Saavedra et al., 2003). As already hinted at, such studies suffer from the fact that warps usually occur at the edges of optical disks and their

properties are not easily determined. HI studies (Briggs, 1990; García-Ruiz et al., 2002b) give a much better insight in the properties of warps. First, the observed material traces the warp out to much larger radii, second one can use the additional spectroscopic information in order to derive a three-dimensional warp shape as has been done by Briggs (1990). Optical studies have to be treated with the caveat that for those indeed warp properties are derived from a two-dimensional projection of a galaxy. Usually, such studies are carried out using edge-on galaxies (as determined by the projected axis ratio), in which a warp shape can be identified better than in galaxies with an orientation towards face-on. However, with such a selection an observational bias is introduced, which is poorly understood, an approach tried by Reshetnikov & Combes (1998) by simulation of galaxy observations. Large warps for example may lead to a thickening of the projected disk, hence a decrease of the axis ratio, and they are thus naturally deselected in a sample of edge-on galaxies. It is thus not astonishing that in the HI study of García-Ruiz et al. (2002b) the frequency of detected warps is much larger than in optical studies. In order to estimate the errors inherent to optical studies, García-Ruiz et al. (2002b) compared their results for 9 cases that were studied also by Sánchez-Saavedra et al. (1990a). In two of four cases, where Sánchez-Saavedra et al. (1990a) detected no warp in the nine galaxies, they found a warp to be present, in two cases of detected warps they found an opposite orientation. The reason for this was a misinterpreted wobbling and dust features in the optical images. The optical images were not sensitive enough to show the large-scale structure of the warps.

Sánchez-Saavedra et al. (1990a), Reshetnikov & Combes (1998), Reshetnikov & Combes (1999), and Sánchez-Saavedra et al. (2003) use by large and large the same quantities in order to quantify a warp, as shown in Fig. 2.2. The warp angles α_e and α_w are the angles between the central major axis of the galaxy and the line drawn from the centre of the galaxy to the outermost point identified as belonging to the galaxy projection. The beta angles β_e and β_w are the angles between the galaxy major axis and the line drawn from the point where the warp starts to evolve to the outermost point identified as belonging to the galaxy projection. With the terminal radii along the major axis $r_{t,e}$ and $r_{t,w}$ and the warp radii $r_{w,e}$ and $r_{w,w}$ (see Fig. 2.2), both angles are connected via

$$\tan(\alpha_{e/w}) = \tan(\beta_{e/w})(r_{l,e/w} - r_{w,e/w})/r_{l,e/w} \quad . \quad (2.32)$$

The global warp angle for the galaxy and the global beta angle are the mean of the values found for both sides. In order to quantify the difference for both sides, either the difference of the warp angles (García-Ruiz et al., 2002b) or the difference of the warp angles normalised with the sum of the warp angles is in use and called the “asymmetry index” α_s .

It is clear that such definitions are not entirely satisfactory. Especially the use of the warp angle in order to quantify the amplitude of a warp is a critical issue at

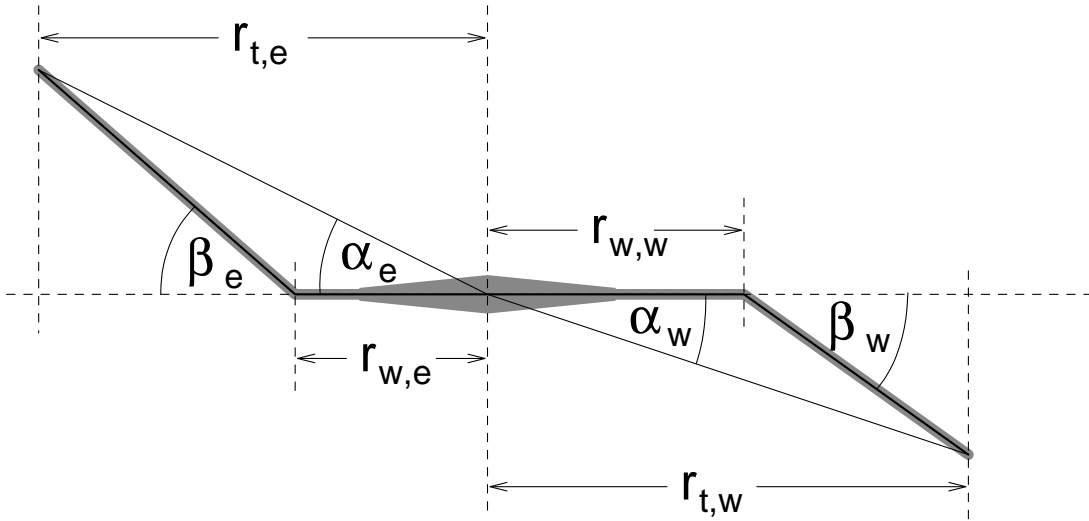


Fig. 2.2: Definition of warp angles α_e and α_w and beta angles β_e and β_w for a schematic edge-on warp. $r_{w,w/e}$ and $r_{t,w/e}$ are the warp starting radius and the projected distance along the major axis to the last measured point respectively.

least in the case of optical studies. It depends delicately on the sensitivity of the observations analysed. It is thus not astonishing that in the HI study of García-Ruiz et al. (2002b) the mean warp angle is larger than that found in optical studies. For a *perfect edge-on* warp, a “true” warp angle must lie in-between the measured α and β , provided the warp orientation parameters are monotonic functions of the radius (as given for a grand-design warp). The evaluation of the beta angle depends critically on the estimation of r_w . Bearing in mind that usually a galaxy will have an arbitrary orientation to the observer, this radius is hard to determine given the small amplitudes of optical warps with a peak of the distribution of α of a few degrees ($\alpha_{\text{peak}} = 3^\circ$ in the study of Reshetnikov & Combes, 1998).

In a discussion of the – sometimes contradictory – results of the statistical studies of warps these caveats have to be kept in mind. All statistical studies agree in detecting warps in such a high number of galaxies that it seems probable that every galaxy with a large enough disk is warped, a fact that is already stated in Rule 5.

The fraction of U-, S-, and L-shaped warps among all warped galaxies is controversial as discussed above. A statement in form of a rule will thus not be given here.

The most studies agree that the warp amplitude, quantified by the warp angle, is independent of the galaxy type and also the frequency of observed warps (e.g. Reshetnikov & Combes, 1998, 1999; Sánchez-Saavedra et al., 2003), although Sánchez-Saavedra et al. (2003) report a *non-detection* of warps in lenticular galax-

ies, an intriguing result, that should but be treated with the caveat of the subjectivity of the optical studies. Counterexamples are known (e.g. Oosterloo et al., 2002). Bosma (1991) found an underrepresentation of warps in galaxies of earlier type, but his results were based on a sample of a rather small number of galaxies. Despite the contradictions in the literature, weighing up the arguments, one may be allowed to formulate a rule.

Rule 7: The warp amplitude and the detection frequency is independent of the galaxy type.

An agreement among observers exist that the environment of the galaxies has an influence on the structure of warps. In optical studies, warps are more often detected in dense environments, while García-Ruiz et al. (2002b) find warps in all galaxies of their sample, which have an HI disk that extends the optical disk. In their sample, warps in a dense environment show a higher amplitude and tend towards a higher asymmetry. The spread of this correlation is but large and rather isolated galaxies with large warp amplitudes exist (NGC 5055 or NGC 755: Bosma, 1981a; Battaglia et al., 2005; Kenn, 2005).

Rule 8: On average warps are more asymmetric and have a higher amplitude in dense environments.

This points towards the fact that at least two mechanisms exist that excite or maintain warping. One common for all galaxies and one that is connected with interaction with the surrounding medium. With respect to the warp type in dependence of environment, results are contradictory. Reshetnikov & Combes (1998) report a higher frequency of S-shaped warps for galaxies that are interacting or have close companions, while Schwarzkopf & Dettmar (2001) find that the frequency of U-shaped warps is higher in denser environments.

Among the correlation studies given by Castro-Rodríguez et al. (2002), based on the sample of Sánchez-Saavedra et al. (2003), one result shall be emphasised here. Employing spectroscopic measurements, they evaluate at the same time the total mass and the luminosity of their sample galaxies, and hence can roughly estimate the ratio of stellar light and total mass, which is a rough measure of the ratio of stellar mass and halo mass. They find that the amplitude of warps is independent of that ratio. In contradiction to the interpretation of Rule 6 given here, they conclude that the Dark Matter halo does not play the major role in the warp formation process. Even if the absence of the correlation would still hold in a large study of HI warps, this conclusion is daring, as shown below. Nevertheless, these findings shall be fixed as

Rule 9: No clear correlation of the warp amplitude and the ratio of the stellar light and the total mass of a galaxy seems to exist in the optical regime.

Of great interest is the connection of optical and gaseous warps. If one detects a difference in both warps, this would immediately allow to conclude that the warp of a galaxy is generated by interaction of the galactic gaseous component with the extragalactic environment, a likely scenario for galaxies in a denser environment like clusters. Another hint towards formation scenarios in which the interstellar medium is the sole component that reacts to some force would be a difference of a warping amplitude in different observing bands. The blue light of galaxies traces young stars which recently formed from the gas in the galaxy, while in redder bands older stars are traced. If a warp has been generated rather recently in the gaseous component, then the younger bluer stars that form in a warped structure, should show a more pronounced warping than the redder stars in the galaxy. Sánchez-Saavedra et al. (1990a) pointed out that they detect more warps if the galaxy is observed in a bluer band, but already stated that this might simply be due to the fact that spiral galaxies become bluer towards their edges. Hence, as warps occur mostly at the edges of galaxies, their result might be biased.

Sasaki (1987) reported a departure of the projected optical and the HI warp in NGC 5907, but concluded that this might be a projection effect as the radial distribution of the stars and the HI in this galaxy differs. This result was confirmed by Florido et al. (1992). Florido et al. (1991), however found a “clear dependence of the warp curve on wavelength” for three galaxies. In order to check whether such departures are visible for other galaxies, Cox et al. (1996) explored the stellar- and the HI distribution in the edge-on galaxy UGC 7170 and did not find any deviation of the HI disk from the optical disk. Since then, no dedicated follow-up studies of colour dependency of the warp have been made, meaning that if present, the effect is so weak that it is not an obvious feature of warps. Here, the approach is adopted that the colour-dependence of warps is an unresolved issue, that but usually such deviations of gaseous and optical disk or of the stellar disk viewed in different colours are not detectable or very weak.

Rule 2 connects the appearance of a warp with the surface density of the disk material. A warp occurs where the stellar disk becomes dim. A higher precision of that statement seemingly could not be reached. A connection to a true drop of the surface density in the stellar disk, if such a drop can be found at all (see Sect. 2.2.3), with the position of the warp radius has not been found yet. For the HI disk this is different. García-Ruiz et al. (2002b) studied the global surface density profiles of the HI disks in their galaxy sample. They found, that while in the inner part of the disks, morphologies could be rather different in individual cases, galaxies show a rather sharp drop of the HI surface density at some radius where the stellar disk becomes dim. This drop, as a rule, is always near to the warp radius. Towards larger radii beyond the drop, the HI surface density is only slightly decreasing or even constant. So, while in the stellar disk no feature is connected to the warp radius, in the HI disk it is.

Rule 10: The HI disks of galaxies exhibit a sharp drop in surface brightness at some large radius. Beyond the drop-radius, the HI surface density is decreasing only slowly with radius. The warp radius, where the warp starts to evolve, is in the range of the drop radius.

Hence, there seems to be a mechanism that smoothes out the HI distribution at large radii. Either the smooth low-level distribution of the hydrogen (in connection with a dim stellar disk) enables the occurrence of the warp, possibly because the gravitational coupling of the disk becomes weak enough, or the same phenomenon that is responsible for the warping cares to smooth out the HI distribution. Possibly both happens at the same time. Except on an observational basis in García-Ruiz et al. (2002b), the HI drop has but not yet been explicitly discussed at all in connection with the warping phenomenon.

2.3.4 Warp formation: theories

Warps are ubiquitous. Hence, they must be excited frequently, or they have to be long-lived structures. Both can be true. Warp formation can in principle happen via different channels, an individual warp may be generated from different processes and a single warp structure may be stable while others are not. The fact that a correlation exists between the density of the galaxy environment and their amplitude and shape immediately leads to the conclusion that warp formation mechanisms exist that are connected with an interaction with the surroundings of galaxies. If warps are sufficiently long-lived, but warps in isolated galaxies have been excited in a period in which the galaxy had the chance to interact with the visible environment in its past, it would be expected that warps of isolated galaxies have not only on average but always rather small warps, which is not the case. It follows that in order to explain warps in isolated galaxies one has either to assume that warps are excited by interaction with invisible material that has a higher abundance in dense regions, or, as stated above, as an evidence towards the co-existence of at least two processes that ignite or maintain warps. Several possibilities for warp formation have been proposed, some of which shall be discussed here.

Free precession, bending modes, and Dark Matter As already mentioned above, a galaxy disk can be viewed as a set of an infinitesimal number of heavy rings, on which the galactic material orbits. As these rings may not lie in a plane by default, they impose torques on each other and thus become a system of coupled gyros. In such a more or less complicated system, it is not directly evident whether an equilibrium stationary state may exist in which a warp is “frozen in”, possibly sustained by the action of an external force. If such equilibrium states

exist, initial distortions will dissipate into such a configuration, resembling a tuning fork, when being hit. The energy imposed on the tuning fork by bashing it is surely not in the form of a harmonic wave, but is transported into the harmonic oscillation of the device, which keeps on vibrating for a very long time. Long-lived stationary states of precession are called bending modes or warping modes. If bending modes of galactic disks exist, they immediately provide an explanation for the omnipresence of warps, even large ones, in isolated galaxies. They are an extremely attractive explanation for warps as with their presence the quantisation of a warp is a measurement of the matter-distribution in galaxies, as mainly this determines the “eigenfrequencies” of the warp modes. Hence a lot of theoretical studies deal with the possibility of stable solutions for a warped disk. They fail, unfortunately, to be simple, in the sense that it was soon realised that a bending mode of the disk is possible only if ignited and/or maintained by external agents like the Dark Matter halo or some process that even imposes a periodic forcing on a test particle oscillating vertically with respect to the galactic plane.

While for the tuning fork an initial distortion settles very quickly into the stationary state of oscillation, a galaxy is but a different system. Therefore, the settlement of a perturbation into a bending mode can be a time-consuming process and the bulk of observed warps may be not in an equilibrium state but settling towards it. A few studies therefore concentrated not only on the existence of warp modes but also on the behaviour of a disk settling into such a state.

Lynden-Bell (1965) considered the possibility of a systematic precession if the galaxy would show a small misalignment of its symmetry axis and the direction of its angular momentum. In such a system, showing “a wobble as may be observed by throwing a penny in the air spinning almost about its axis”, with differential rotation present, a systematic bending in the disk would be possible, the nutation of the disk potential as a varying force sustaining the warp. His adopted model for the disk’s mass distribution was included in a generalised self-consistent analysis by Hunter & Toomre (1969), who found that such free modes of oscillation can only persist in disks that have a sharp cut-off at their edges as the one used by Lynden-Bell (1965). Graphically, in terms of a tilted-ring model, the self-gravitation couples the rings locally to each other enforcing a co-precession against the tendency to precess differentially in the global potential of the galaxy. If the rings get lightweight over a large range of radii, the coupling force is too weak to prevent the differential precession. The possible bending modes in that case become a continuum. Their conclusion was that such modes would not exist in real galaxies.

With the realisation of the dynamical importance of the Dark Matter halo, the possibility was considered if it could alter the physical conditions in a way that

bending modes would become a possibility again for a galaxy, possibly externally enforcing oscillations. This issue was first addressed by Binney (1978), considering the consequences that an additional, dominating triaxial potential (with a solid-body rotation) would have on the global dynamics of a galaxy disk. He came to the conclusion that for a rotating triaxial halo, inducing a periodic forcing on the disk, a warp might be excited or maintained, in a similar fashion as was previously proposed by Lynden-Bell with a wobbling disk. His work, though, missed a precise prediction of warp structure and amplitude.

Petrou (1980) considered the possibility whether the Dark Matter halo, imposing an external force on the disk could act as a moderator by changing the precession rates in the disk. If the flattening of the halo is not necessarily equal at all radii, the possibility exists that the differential precession of the disk could be stopped by a increasing flattening of the halo towards larger radii. At larger radii the restoring torque would then be greater and thus the precession rate higher, enabling the outer disk to keep up precessing in phase with the inner one. This thought was reconsidered by Sparke (1984). If a halo is oblate and the flattening ϵ of the halo rises faster than linearly with radius, a stable warp mode exists even for a galaxy with a smooth edge. Such a halo must be fairly massive (larger than 20 times the disk mass) and extend to 2 or 3 times the disk radius. Interestingly, she found a possibility to maintain a warp in a configuration where the halo may keep a constant shape, namely if the halo is not oblate (the major axis of the ellipsoid lying in the plane of the galaxy) but prolate. Such a halo would need less mass and a lower extension in order to maintain warps.

Bertin & Mark (1980) and later (Bertin & Casertano, 1982) proposed a different mechanism that could excite warps even in isolated galaxies with the aid of the halo. A vertical displacement of the disk propagating in the medium of the halo due to the galactic rotation causes cavities and over-densities in the medium, which in turn enhance the displacement. Thus, a galactic disk could start to flap like a flag in the wind due to this bending instability if embedded in a non- or slowly rotating DM halo and produce a warp. Unfortunately, their precise prediction of the warp shape did not reproduce the observed warps well. A warp generated via a flapping instability would start at the centre of the galaxy.

Dekel & Shlosman (1983) and Toomre (1983) were the first to propose a tilt of a slightly flattened Dark Matter halo with respect to the disk as a possibility to enable stable bending modes in galactic disks. Such bending modes have a high enough amplitude even if the halo is only slightly flattened. Dekel & Shlosman (1983) found stable modes for a halo increasingly flattened towards larger radii and estimated the time on which disk and halo would align due to dynamical friction large enough in order to ensure the persistence of the warp, already realising that a Dark Matter halo may become intrinsically tilted aligning with the disk in its inner regions. Toomre (1983) considered the simpler model of a

massive ring (of satellites) placed at a large radius and found that a realistic warp could ignite. In such a configuration, the central galaxy would precess in phase, thus keeping a straight kinematical minor axis. Both models had in common that the main bending force did not come from a short distance as would be the case in a halo that keeps the same axis ratio at all radii, but mainly acted in form of a torque ignited at large radii. As a consequence, they produced galaxy warps which showed a flat disk at large radii with a spin axis aligning with the torque.

The possibility of a rigid halo with a constant inclination towards the disk and hence the resulting “modified tilt modes” was further investigated by Sparke & Casertano (1988), Kuijken (1991), and, for the case of bowl shaped warps by Sparke (1995). The three authors found that indeed stable configurations with a shape and an amplitude nearly reproducing galactic warps existed, if the halo would remain inclined and rigid over a large time, giving quantitative descriptions of the warp shape found. Kuijken (1991) already used these in order to determine the halo properties of spiral galaxies.

Unfortunately, all theories invoking a global co-precession of the disk were doomed to fail as a global explanation for warps due to the results of the detailed studies of Briggs (1990). Discovering Rule 3, he could exclude bending modes that generate a straight kinematical minor axis, as would be the result of co-precession. Furthermore, the tilt modes in the presence of a Dark Matter halo had to face a different problem.

Nelson & Tremaine (1995) reopened the question of the role of dynamical friction in the maintenance of warps. Unlike Bertin & Mark (1980), who found that a warp would indeed grow, they took into account the resorting force in the presence of a pressure gradient in the halo. They found that in some special (rather exotic) cases indeed a warp might be excited, in the more general case any warp would but dampen out in a time short compared to a Hubble time (the age of the universe), meaning that a warp would alter significantly after it has been excited. Dubinski & Kuijken (1995) simulated the behaviour of a warped, inclined disk in a “live” (reactive) halo. They found that a disk would rapidly align with the halo and the warp would wash out in a few rotation periods in the disk for unrealistically lightweight disks. For a realistic disk, they found a damping time of only one rotational period in the inner disk. Remarkably, the timescales for the halo to align with the disk were rather large for large radii. This analysis was based on a far too small number of particles in order to simulate the frictional coupling of the disk and the halo. Instead of using a realisation of a disk in particles, Binney et al. (1998) thus chose to represent it as a set of inclined rings. Their results differed from those of Dubinski & Kuijken (1995) in a small detail. While also in their simulation the warp washes out quickly in the inner regions of the galaxy and winds up, the warp amplitude was not damped. Their resulting disk became thicker at the edges. (Binney et al., 1998)

interpreted these results in a remarkable way. They argued that, while bending modes with a rigid halo could be excluded as a possibility for warp maintenance, still the possibility existed that a common bending mode of disk and halo might exist, the characteristics of which would differ completely from that of “modified tilt modes”. In such a common bending mode, the system would rather consist of an inner disk-halo system and an outer inclined halo system. Choosing the initial conditions right, the energy stored in the outer precessing rings would be contained in a long-lived ordered warped structure. This picture got recent support. In a series of high-resolution simulations in a concordance framework, Bailin et al. (2005) examined the settlement of a system containing a galactic disk and a Dark Matter halo. The presence of the disk has an enormous effect on the halo structure, making it considerably rounder. This effect is greatest at small radii, leaving a halo that is increasingly flattened towards larger radii (see also Kazantzidis et al., 2004). This resembles the initial conditions employed by Dekel & Shlosman (1983) in order to produce their steady-state warping. Furthermore Bailin et al. (2005) observe that the (still slightly flattened) triaxial halo tilts at a radius of $0.1r_{\text{vir}}$ and is thus in a state of misalignment with itself. Such a misalignment is reached on an extremely short timescale. While in the inner part being well aligned with the disk, it settles to a random orientation beyond $0.1r_{\text{vir}}$. Bailin et al. (2005) are pessimistic about the existence of such an extended disk in a CDM environment. Nevertheless they note that, if at that radius a baryonic disk component existed, eventually the whole system might settle into a common bending mode that looks similar to the shape found for the Dark Matter halo. Beyond $0.1r_{\text{vir}}$, a gas disk would settle into the preferential plane of the outer halo. As such, the warp maintenance would be due to a misalignment of the outer and the inner halo, very much like the situation proposed by Toomre (1983). In such a system, however, it is to be expected that the inner disk-halo system will precess at a different precession rate than the outer gas-disk halo system, in concordance with Rule 3.

Even before Briggs (1990) showed that at large radii co-precession is not present in the disk anymore, the possibility of a warp as a transient feature with large time-scales was considered.

If discrete bending modes do not exist for a galactic disk, still an initial vertical distortion of a galaxy may be sustained long enough possibly propagating in a galaxy disk in order to be seen as a warp for a long time. This possibility was first considered by Kahn & Woltjer (1959). If an initial perturbation in form of a warp should stay detectable over the lifetime of the galaxy, they concluded that the mass distribution in the disk would have to be far too spherical compared with galaxy models at that time (Schmidt, 1956) in order to maintain the precession frequency low enough in order to provide a warp that is not washed out.

The presence of a galactic halo permitted a re-consideration of the possibility of

warps being transient features that last long enough in order to account for their frequency. Tubbs & Sanders (1979) calculated that a peripheral disturbance in a galaxy might last up to 5 rotational periods due to the fact that for a sufficient cutoff in the disk, due to the presence of the (spherical) Dark Matter halo, the global potential would become spherical enough in order to sufficiently suppress the precession of the disk material in the peripheries of galaxies. This was followed up by May & James (1984) in a computer simulation of a disk in the analytic potential of a spherical massive halo. They showed that in such a setup indeed an initial warp could last for a long time.

The consequence of a transient warping in a non-inclined halo, however, would still be a differential precession at all radii. This is compatible with Rule 3, but not with Rule 2 for the behaviour of grand-design warps. Furthermore in such a setup, a warp would be quickly damped by dynamical friction (Nelson & Tremaine, 1995).

Christodoulou & Tohline (1986) were the first to consider the shape of the kinematical minor axis as an indicator for the underlying mass distribution. Their main conclusion was that a prograde twist (in the direction of the disk rotation) of a warp is generated by an oblate global mass-distribution while a retrograde twist will be caused by prolate density distributions, as may be caused when a prolate halo becomes the dominant contributor to the potential. This is an interesting notion in the light of Rule 3. Seemingly, if not in any state of equilibrium, Dark Matter halos are oblate. Realising that realistic warps do not maintain a straight kinematical minor axis, Hofner & Sparke (1994) simulated the time evolution of a corrugation in a galaxy with an inclined Dark matter halo. The result was a corrugation wave propagating outwards in the galaxy, leaving a warped disk behind that showed the structure of a modified-tilt mode. The settlement of the wave, however, would take a long time, with the result that the kinematical minor axis in the outer parts of the galactic disk would show the observed leading structure. An interesting side effect from their simulations is the generation of a wobbling structure in their disks, as the corrugation travels outwards in the disk, regardless of the physical existence of a normal mode, allowing to speculate that a wobbling is indeed a transient feature of a bending wave travelling through the disk. Ideta et al. (2000) simulated the behaviour of a disk in inclined rigid halos. They found that while they were not able to generate realistic warps in a configuration where the halo was oblate, they did so using prolate halos. Unfortunately, again, these outcomes are dubious, as they are based on a rigid halo. The works of Nelson & Tremaine (1995) and Dubinski & Kuijken (1995) acted as a razor for a lot of theories as already foreseen by Toomre (1983).

In this unfortunate situation, theorists became desperate. If a conventional normal mode, as well as modified tilt modes were not able to exist in the presence of a dark matter halo, the presence of large warps in isolated galaxies became

a problem. A natural but very inconvenient consequence was to invoke interactions with the environment in order to explain warps. The interaction partners, however, had to be sufficiently invisible in order to explain the high frequency of warps in isolated galaxies. One of the candidates of interaction partners was Dark Matter. In the standard cosmological view, a Dark Matter halo is not an isolated structure, but surrounded by a high number of satellite halos (Moore et al., 1999a) of different size, satellite galaxies being the visible tip of the iceberg. In principle it gains in size and changes structure due to the “cosmic” infall of these lumps of Dark Matter. In hypothetical scenarios the explanation for warps can be sought in that the changes of the halo due to cosmic infall enable warp formation. The merit of this approach is that it at the same time explains the fact that warps are ubiquitous, because cosmic infall is supposed to happen for every galaxy, and that warps are stronger in dense environments, because the density distribution of luminous matter follows that of the dark matter. In a dense environment cosmic infall is thus stronger and the generation or maintenance of warps is more effective. The ugly side is that in this picture not only the Dark Matter halo is invoked as influencing and generating the structure of the warps, but it also needs to be changed by a process of which little is known. The warps produced in model calculations and simulations in which the effects of cosmic infall are included in some or the other way, are the ones that reproduce observed grand design warps best. At the same time the exact understanding of warp formation is shifted to a time in which cosmic infall is well understood. Believing that cosmic infall is the main driver for warp formation, the expectance of warps being able to tell us something about the underlying mass structure (Binney, 1992) has to be somewhat muted.

Binney (1992) and Ostriker & Binney (1989), who foresaw the upcoming problems of warp modes, proposed the accretion of angular momentum by cosmic infall as a solution to the problem. They gave qualitative arguments how the accretion of misaligned angular momentum that continuously changes the spin orientation of the Dark Matter halo could explain both, the shape of the Milky Way warp and at the same time the central tilt of the Milky Way disk. This qualitative reflections were followed up by a number of computer simulations. Jiang & Binney (1999) simulated the behaviour of a galactic disk consisting of flat rings embedded in a flattened halo represented by particles with an initial alignment of the symmetry axes of both components. Cosmic infall was simulated by injecting halo particles into a slightly inclined torus at large radii, thus simulating both the slewing of the halo mass distribution and its angular momentum. They found that under certain assumptions for the injection rate, a warp in the halo forms. This warp is closely traced by the disk material, which is completely aligned with the halo. The final warp shape, however, was not compatible with observations as the disk (and the halo) found did not show any flat region, except for the halo in the outermost parts at radii, where the disk was not present anymore. Instead of taking into account

the reorientation of the halos spin axis and the change of its shape, Debattista & Sellwood (1999) discussed the effect of an ab initio differing orientation of the spin axes of halo and disk in order to explore whether the mutual torque imposed on both components would suffice to produce a warp. They simulated the time-evolution of a disk embedded in a nearly spherical halo with differing spin axes. All components in their simulation were realised by particles. They found that a warp with a realistic amplitude develops, that resembles the rules for the behaviour of warps. In this model, the strength lies in the coupling of the disk and the halo by dynamical friction, which enables the warp to be excited. The torque is strongest in the central region as both components are densest there. Hence, the warp is in fact a tilt of the inner disk as long as the frictional forces are large enough. Debattistas approach stands in contrast with the findings of Bailin et al. (2005) who find from their simulations that in a standard cosmological setup any misalignment of disk and halo seems to happen extremely fast. Their work thus bears the question whether a misalignment of the spin axes can indeed be maintained long enough in order to ensure the observation of a warp in every disk galaxy.

Bailin & Steinmetz (2003) stressed the point that in a standard CDM cosmological environment at a given time the disk is exposed to a variety of tidal torques. Firstly, the Dark Matter halo is sufficiently in touch with its environment in order to show a misalignment of its principal axes with respect to the spin vector of the disk (see also Sharma & Steinmetz, 2005, and citations therein). They analyse CDM simulations in which they calculate these torques, which are growing towards the centre of the galaxy, and consequently simulated the behaviour of an N-body galactic disk, embedded in a statical and spherical potential but under the influence of the calculated differential torque. A major shortcoming of this approach is the neglect of frictional processes between halo and disk. However, after one Gyr, the disk shows a structure that remarkably resembles that of observed warps. Due to gravitational coupling, the inner disk is tilted as one unit, while in the outer regions the galaxy disk retains its original orientation, the torquing being weakest at these radii. With respect to the inner disk, the warp is the transition from the inner flat region to an outer flat part of the galaxy. This finding is not in a large conflict with observations.

All simulations of warping processes in cosmological environments under the assumption of warps being frequently excited by infall processes reorientating the Dark Matter halo suffer from partly grave simplifications, but nevertheless provide the models that most realistically resemble the structure of grand-design warps.

Satellite interaction The detection of the Milky Way warp by Burke (1957) and Kerr (1957) immediately bore the question whether it could be excited by a

gravitational interaction with the Large Magellanic Cloud (LMC). The structure of the Milky Way warp leads any observer to that suggestion, as the largest height above the inner plane of the Galaxy is reached in the direction towards the LMC. Both authors, however, already noted that the deviation expected would be two orders of magnitude smaller than observed. Later on the issue was picked up by Elwert & Hablick (1965) and Avner & King (1967), who in a simplified analysis were more optimistic about the LMC as the generator of the Milky Way warp. Especially Avner & King (1967) pointed out that the secular evolution of the perturbation imposed from the LMC in its passage through its orbit would have to be taken into account. Hunter & Toomre (1969) could show that, including the self-gravity of the disk and the response of the disk itself to its vertical perturbations, the LMC would only come into a discussion as the originator of the warp if it had a past pericentric passage at a galactocentric distance of 20kpc and a total mass of $2 \cdot 10^{10} M_{\odot}$, which is two or three times more than assumed by Avner & King (1967). This possibility was finally excluded by Murai & Fujimoto (1980) and Lin & Lynden-Bell (1982) showing that the LMC is close to its perigalacticon at a distance of about 50kpc.

Nevertheless, tidal interaction with companion galaxies as the originator of warps remained an attractive explanation. If warps might be generated via tidal interactions with small companions, this mechanism could be a possible explanation for the observed facts if galaxies would often have unseen companions. Observations of stellar rings obviously stemming from a debris of a companion galaxy as in the case of NGC 5907 (Shang et al., 1998), a galaxy long thought of as being the prime example for an isolated galaxy with a large warp (Sancisi, 1976; Sasaki, 1987), and the fact that in a standard cosmology indeed a number of small companions of each big galaxy is expected to be present, stirred the suspicion that such companions might be able to be responsible for a galaxy to become warped.

If satellite galaxies should be responsible for warps, their impact has to be amplified in some way. One – maybe daring, but enduring – way to enhance the influence of a satellite galaxy at large radii is to modify the dynamics. Indeed, since MOND (Modified Newtonian Dynamics, Milgrom, 1983) has been invented in order to explain rotation curves of spiral galaxies, it has stayed a persistent alternative to Dark Matter advocated by a non-negligible minority of astronomers against the concordance model. Brada & Milgrom (2000) showed in a simplified simulation that, employing MONDian physics, in which the gravitational force gets more attractive with respect to Newtonian dynamics at large distances, a warp in the Milky Way could be due to an interaction with the LMC. They found the warp generated in their simulation to have the right amplitude and orientation.

Another way to generate larger warps by small companions was proposed by Weinberg (1998), invoking the Dark Matter halo of a galaxy as an agent to effi-

ciently transport a disturbance of the potential at large distances into the region where it could effectively influence the structure of the disk (see also Lynden-Bell in the discussion in Sparke, 1985). Satellites could induce a resonant feature in the halo of the galaxy, a so-called wake, that has a structure in the reach of the disk. Hence, a perturbation in the potential caused by a satellite at larger distances, would be carried inside the disk and could possibly cause a warp. As in such a scenario, the largest warp would be produced for a polar orbit of the satellite, the LMC (which has a nearly polar orbit) would be an optimal candidate for the formation of a warp in the galaxy. As a follow-up to Weinberg (1998), whose calculations were not fully self-consistent, García-Ruiz et al. (2002a) simulated the behaviour of a galaxy disk consisting of a set of rigid rings in the potential of a “live” (responsive) Dark Matter halo perturbed by a satellite, still but under some simplifying assumptions. They found that neither the amplitude nor the direction of the warp ignited by this process could be brought into accordance with the observations of the Milky-Way-LMC system, the warp angle of the generated warp being less than 1° , and the tip of the warp pointing into a direction perpendicular to the orbit plane of the satellite galaxy. Furthermore, they found that a warp generated by tidal interaction with an LMC-like companion would have a severe winding problem, the kinematical minor axis winding into a tight spiral, inconsistent with the observations of grand-design warps. Consequently, a simple but strong argument against the LMC as the originator of the Milky Way warp was given by Bailin (2003). If a warp is ignited by a satellite, the warp excitation is a transfer of angular momentum from the satellite orbiting the centre of the Milky Way to the disk. At some radius, where a warp is to be seen, the resulting angular momentum of the disk is then simply the sum of the transferred portion of angular momentum and that of the disk. As a consequence, a configuration in which the tip of the warp points in the direction of the satellite’s orbit is unphysical. So, a galaxy that should be able to generate the Milky Way’s warp should have a polar orbit in a plane perpendicular to the direction of the warp. Bailin (2003) found a candidate in the Sagittarius Dwarf galaxy, a small satellite galaxy of the Milky Way currently in the process of tidal disruption (Ibata et al., 1994). The still remaining question whether a warp like the Milky Way warp could be produced by tidal interaction with a small companion was addressed by Bailin & Steinmetz (2004a) in a fully self-consistent computer simulation. They found that indeed in a disk-halo-satellite system resembling that of the Milky Way and the Sgr dwarf galaxy a warp-like structure would be ignited frequently shortly after every perigalactic passage of the satellite. A bending wave would then propagate outwards in the disk and reach the rim of the galaxy shortly before the next passage of the satellite galaxy. While a quantitative analysis and comparison is missing in their study, (Bailin & Steinmetz, 2004a) conclude that indeed many warps could be due to tidal interaction. The warps found, however, are dynamical, meaning that they are short-lived. Further investigations of the observable properties of such warps in terms of their amplitude and shape were not reported.

One might well assume that as the warps ignited are transient features, they will not or only temporarily resemble the appearance of a grand-design warp and will thus be well distinguishable from those.

Interactions with the intergalactic medium As warps are primarily seen in the neutral gas disks of galaxies, the possibility has been regarded that the driving force that ignites and maintains warps could be imposed from external sources on the gaseous disks of spiral galaxies only. Candidates for interaction partners that would react with the gas in the disk are intergalactic matter in form of gas or the intergalactic magnetic fields. Evidence for the gaseous disk being the prime target for the warping force has been sought in observations of colour dependent warping amplitudes (Florido et al., 1991, see above) and the alignment of warps of neighbouring galaxies. The latter was claimed to be visible for a number of nearby galaxies and for the members of the local group by Battaner et al. (1990a, 1991). While an alignment of warps is hard to explain by other proposed warping mechanisms, intergalactic magnetic fields driving the warping of the disk would impose no major difficulties with an alignment.

One of the oldest suggestions for warp formation is that a galaxy, subject to an extragalactic wind would develop a warp due to pressure gradients in the galactic corona, which in turn are produced by the passage through a dense medium. Kahn & Woltjer (1959) pushed forward this idea, driven by the belief that the Dark Matter preventing the Local Group to become dynamically unbound was provided by a large cloud of ionised gas in which the members of the Local Group reside. Already Hunter & Toomre (1969) dismissed this idea. They argued that the pressure gradients implied also a vertical forcing of the disk, with a resulting mixing of an $m = 0$ and $m = 1$ vertical distortion in the Galactic disk. The Milky Way warp should have at least an asymmetric warp with a difference in amplitude on both sides with a ratio of 3:2. Furthermore, up-to-date estimates of the gas density in the local group and small groups of galaxies (Murali, 2000; Bureau & Carignan, 2002; Grebel et al., 2003) with $< 10^5 \text{ atoms cm}^{-3}$ are way below $10^4 \text{ atoms cm}^{-3}$ estimated by Kahn & Woltjer (1959). However, the assumption that the force exciting galactic warps and maintaining them by pressure gradients remained. Battaner et al. (1990a) proposed intergalactic magnetic fields as a possibility to provide the external torque on the gaseous disk to excite and maintain warps. Binney (1991) calculated the strength of the intergalactic magnetic field necessary to provide the force in order to generate warps at realistic galactocentric distances to be far too high. Magnetically driven warps require a field-strength of a few μG . These, while not present in the field, however, could be present inside galaxy clusters (Kronberg, 1995). While Battaner & Jimenez-Vicente (1998) calculate a warp shape for magnetically induced warps that is compatible with the structure of S-shaped warps, recently Sánchez-Salcedo (2005) demonstrated in an elaborate work that a warp induced by magnetic fields would have a severe wind-

ing problem, magnetic fields not being able to mute differential precession, even worse accelerating it, giving a wind-up of the kinematical minor axis half-way around the galaxy in 0.32Gyr . Thus, magnetic fields may safely be disregarded as a prime source for warp excitation. Firstly, the intergalactic field strength is generally too low to impose the torque necessary to excite a warp, second, if the field-strength is high enough, the reaction of the disk would be a thickening of the gas layer and not a systematic warp.

For a long time, the idea of a gas infall on the disk being able to produce S-shaped warps was thought of being implausible. Binney (1992) argued that any wind that is blowing onto the disk would rather cause a bowl-shaped warping than an S-shaped warp as the forces acting on the disk would be rather axisymmetric than being able to impose a torque on the disk. López-Corredoira et al. (2002) reopened the issue with a calculation of the torque imposed on the disk when the galaxy moves through the intergalactic medium. Via frictional processes the gas could be stopped in the galactic disk and impose both an axisymmetric force but mainly a torque on the disk. If the galaxy would be inclined to some degree towards the propagation vector of the intergalactic material, the change of the direction of the particle stream in the gravitational field of the galaxy results in a non-symmetric forcing of the disk, and hence a net torque. Neglecting the axisymmetric forces, which they estimated to be low enough, they were able to generate an S-shaped warp employing a tilted-ring model. Sánchez-Salcedo (2004; 2005) reviewed this approach. He calculated the shape of excited warps as always being asymmetric, always containing partially an U-shaped contribution arising from axisymmetric forcing. For his model he adopted a gas inflow with a velocity of 100kms^{-1} and a mean gas density of $6 \cdot 10^{-5}\text{atoms cm}^{-3}$, an extremely generous estimation also used by López-Corredoira et al. (2002) based on the unplausible assumption that the Dark Mass in the local group is made up of lumps of cold gas in form of High Velocity Clouds (López-Corredoira et al., 1999), which in the meantime has proven to be an untenable hypothesis (Pisano et al., 2004; Westmeier et al., 2005). If all the impulse carried by such a wind is directly transferred on the disk without heating it, a warp amplitude comparable to that of the Milky Way is reached. Like Hunter & Toomre (1969) he found that the warp of the Milky Way should carry a 3:2 asymmetry. Furtherly, he noted that generally warps induced by direct gas-infall onto the disk should show the following features: i) S-shaped warps should be asymmetric, ii) S-shaped warps should never curve back to the disk plane, iii) a strong correlation between the HI disk size and the amplitude of the warp is expected, iv) a correlation between the galaxy mass and the warp amplitude is expected. The Milky Way warp thus cannot be ignited by a direct inflow of intergalactic gas on the disk, because the gas density in the Local Group is too low, and the warp of the Milky Way has simply the wrong shape. Inside a radius of $15 - 17\text{kpc}$, it shows a symmetric S-structure without a measurable $m = 0$ contribution, outside that radius it becomes asymmetric but

curving back onto the disk on one side. The gas density required to produce warps of larger amplitude is generally found not to be reached for galaxies in groups or in the field. Beneath that, the degree of asymmetry reached in surveys of warps is too high in order to assume that accretion of intergalactic matter is a major contributor for warp formation.

The main conclusion has to be drawn that the intergalactic medium can play a significant role for warp formation only inside galaxy clusters.

Self-inflicted disk instabilities Nelson & Tremaine (1995) had shown that in the presence of the Dark Matter halo, a warp without a restoring force would dampen out quickly, the halo being an agent to ensure the vertical disk stability. Thus, if such a halo would not exist in a galaxy, a disk instability may be able to grow and a warp might be excited even in isolated galaxies. Pfenniger et al. (1994) and Pfenniger & Combes (1994) proposed that the dark matter in disk galaxies might not be in a form of non-baryonic Dark Matter but provided by a hardly detectable cold gas component in the galactic disk. Revaz & Pfenniger (2004) could show that in such a case or for the presence of a comparably lightweight Dark Matter halo long-lived warps could be the result from bending instabilities. They derive a maximum allowable mass of a dynamically hot Dark Matter halo to be 0.6 of the total mass of the system in the reach of the disk. In simulations they show that indeed in a heavy disk scenario, long lived U-, L- and S- shaped warps can be ignited. For one very long-lived case they followed the time evolution of the warp and studied its structure. Unfortunately, while keeping a straight kinematical minor axis in its inner parts, in the outer parts it formed a trailing spiral thus being not in accordance with Rule 3. Another drawback of the warps that are produced by bending instabilities is that they have an amplitude lower than 5° . This could account for the values found in optical studies, but not for HI warps that can reach very high amplitudes, even if their hosting galaxy is isolated. So, if self-inflicted bending instabilities are a cause for warps, they are not the only one. Nevertheless, they should be regarded as a serious possibility to explain warping in the reach of the stellar disk.

Summarising remarks From the many possibilities that have been discussed in the literature, only a few proposed mechanisms can possibly explain grand-design warps, their global presence and their structure. Tidal interaction with small companion galaxies is a possibility to explain the increase of warp amplitudes in a denser environment but it probably cannot account for the appearance of large symmetric warps of isolated galaxies, unless the Newtonian laws are violated. Interaction with the intergalactic medium may safely be ruled out to be able to originate warps in the most cases. Bending instabilities, while a possibility to account for warps in the reach of the stellar disk, are not a possibility to

explain the high warp amplitudes reached in some cases. Two possibilities remain in order to explain the high frequency of occurrence of warps. Cosmic infall might reorder the halo such that warps are frequently generated or they are maintained even for isolated galaxies. The second, by far most attractive possibility is that of a common bending mode of a slightly flattened halo and the galactic disk. One prediction of this scenario would be the presence of a flat gaseous disk at large radii. Unfortunately, this disk appears in the simplified simulations of cosmic infall, too. The discrimination of one of these possibilities might come from theory. Remarkably, the study of Bailin et al. (2005) imposes a caveat on the outcome from Debattista & Sellwood (1999). An outstanding, but poorly discussed result from Bailin et al. (2005) is the extremely short timescale on which the halo aligns with the disk. Their initial galaxy models were refined versions of galaxy models taken from a larger cosmological simulation. The starting point of the simulation was determined as the time after which no major merger would happen in the larger simulation. They analysed the structure of the simulated galaxy at that point, as well as about 2.2Gyr later and found that no significant evolution in the mutual alignment of disk and halo and the halo structure takes place in that time. In the simulation of Debattista & Sellwood (1999) the maximal warping of the disk was reached after a time of 10 rotational periods at a radius equal to the disk scalelength. That roughly corresponds to 500Myr, taking M31 as a template galaxy with an exponential scale length of $\approx 5\text{kpc}$ and a rotation curve amplitude of 265kms^{-1} . After twice the time, the warp damped out in their model, meaning that halo and disk become aligned on a timescale of 1.5Gyr. The results of Bailin et al. (2005) thus point towards a much tighter coupling between disk and halo, as the alignment seems to happen on a much shorter timescale. A more elaborate comparison between the models of Debattista & Sellwood (1999) and Bailin et al. (2005) could thus maybe serve to rule out one of both possibilities to produce warps, leaving out one theory for warps matching the observations.

3 A new method to fit tilted rings to datacubes

A new software to directly fit a “tilted-ring model” to spectroscopic datacubes is presented. A galaxy disk is parametrised as a set of thick rotating rings with varying surface density and orientation with respect to the observer. The algorithm generates model datacubes from the parametrisation of such a disk, which is automatically adjusted to reach an optimum fit to a data cube from observations via a chi-squared minimisation method. The shortcomings of the currently available programs to produce a tilted-ring model are discussed and it is shown that our method mitigates the well-known problem of beam smearing when performing fits to the velocity-field, and is able to parametrise HI disks of galaxies that are crossed twice or more by the line-of-sight. The program and source-code are publicly available under <http://www.astro.uni-bonn.de/~gjozsa/tirific.html>.

3.1 Introduction

The orbits of the disk material in spiral galaxies have comparably low an ellipticity (e.g. Bosma, 1981b; Schoenmakers et al., 1997), such that it is a good approximation to treat them as being circular. This means that to the first order the kinematics of a galactic disk can be described at a certain galactocentric radius by a set of three parameters, the rotation velocity, and two parameters that describe the local disk orientation with respect to some reference system. Inside r_{25} , the gas disks of spiral galaxies are usually flat (e.g. Briggs, 1990), such that in many cases it is even valid to assume that the orientational parameters do not change with radius but can be assigned to the disk as a whole. This assumption is frequently made in derivations of rotation curves from optical spectroscopic data or from CO synthesis data. With only long-slit observations along the galaxies’ major axes at hand, it is the only possible approximation (e.g. Rubin & Ford, 1970), while it is frequently applied for an analysis of integral-field spectroscopic data (Simon et al., 2005) in order to stabilise fitting processes.

In the 70’s it became evident that galaxy disks do not stay flat at large radii but become warped (Rogstad et al., 1974; Sancisi, 1976). This affects mostly the extended HI component. In order to parametrise the kinematics of such warped disks it is then necessary to vary the orientational parameters with radius. Such a “tilted-ring model” was first constructed for M83 by Rogstad et al. (1974). While being treated as an exception in the past (e.g. Schwarz, 1985), today it is known that quite a number of galaxies exist for which the assumption of a flat central stellar disk is also not valid (Corsini et al., 2003). Thus, in order to derive reliable rotation curves, one has either to apply a tilted-ring modelling, or to show that the assumption of a flat inner disk is valid (as has e.g. been done by Simon et al., 2005).

In some cases the tilted-ring model is still an oversimplification, namely, when the non-circularity of orbits in a galaxy gets severe as in the presence of a bar (e.g. Bosma, 1978; Simon et al., 2003). Nevertheless for many cases it is a good approximation and hence became a standard kinematic model for galaxies. Several routines exist with which it is possible to fit such a model to spectroscopic data, the most excessively used being the ROTCUR routine (van Albada et al., 1985; Begemann, 1987), which was a generalisation of the original fit method of Warner et al. (1973). It is implemented in several reduction packages, e.g. GIPSY (van der Hulst et al., 1992), NEMO (Teuben, 1995) and AIPS (Fomalont, 1981). ROTCUR fits for each radius an inclined rotating ring to a velocity-field, a map in which ideally each point represents the projected velocity of the disk material in the central plane. ROTCUR derivatives and extensions exist. The GIPSY routine RESWRI takes into account that non-axisymmetric potentials leave their characteristic imprint in the velocity-field (Binney, 1978; Teuben, 1991) and allows for an azimuthal variation of the rotation velocity (see also Franx et al., 1994; Schoenmakers et al., 1997). Similarly, RINGFIT (Simon et al., 2003) allows for the same variation, while at the same time only allowing for a flat disk. Simon et al. (2005) use this routine to test the reliability of their rotation curves. ROTCURSHAPE (implemented in NEMO, Teuben, 1995) performs a global fit of the velocity-field, in which the ring parameters are not fitted independently, but “at once”.

All of these routines have in common that they are based on an analysis of the velocity-field, which itself is the result of a previous intermediate reduction step from a datacube to the tilted-ring model. Various methods exist to extract a velocity-field by analysing single spectra in a datacube. They all have their shortcomings. First, for some galaxies with large warps or galaxies seen close to edge-on, the derivation of a single representative velocity-field is impossible, as, even if the disk-geometry is known, the line-of-sight crosses the disk twice or more, such that for one position on the sky more than one velocity has to be assigned. Second, besides possible deviations from the assumed circular symmetry of the orbits, a velocity-field is contaminated by beam smearing effects (see below, also Teuben, 2002). This leads to a situation where, in principle, a tilted-ring model that is a result of a fit to a velocity-field, has to be cross-checked by a comparison of a resulting model datacube as can be produced by the GIPSY routine GALMOD (van der Hulst et al., 1992, originally by T.S. van Albada). Occasionally, a fit of such model datacubes has been performed by adjusting the model parameters and successively improving the model datacube by comparing it “by eye” with the original datacube (Arnaboldi & Galletta, 1993; Swaters, 1999).

The drawbacks of the velocity-field fits lead to the development of a series of analysis software that perform direct fits to the datacube (Irwin & Seaquist, 1991) or a position velocity diagram (Simard & Pritchett, 1999; Takamiya & Sofue, 2002;

Böhm et al., 2004), thus circumventing the beam smearing or smoothing problem. These fit routines that simulate an observation from a model parametrisation fail, however, to allow for an intrinsic change of the orientational parameters and hence are no realisations of the tilted-ring model. Especially for the analysis of HI kinematics, such a routine is most suitable, and has been realised once by Corbelli & Schneider (1997), in the case of a tilted-ring analysis of the spiral galaxy M33. In this case, however, the fit was performed on single spectra from a single-dish observation. Thus, besides not being available publicly, it would not suit to perform a fit to a datacube as comes from synthesis or integral-field spectroscopic observations.

Here, a new, publicly available software called *tirific* (for tilted-ring-fitting-code) is presented that performs an automated fit of a tilted-ring model to a datacube. This software was originally developed to construct tilted-ring models of heavily warped galaxies observed in the HI emission line. It can, however be used for all kind of spectroscopic datacubes of translucent objects that can be approximated by the tilted-ring model. While the software will still be under development for quite some time in order to improve the performance and to allow for extended functionality beyond the tilted-ring model, *tirific* is well usable in its current form and two basic issues can be answered: Does a method to fit a tilted-ring model directly to the datacube lead to more reliable results than a fit to the velocity-field and is it possible with such a software to reach a reasonable fit in a reasonable time.

The chapter is laid out as follows: In Sect. 3.2 the model layout and the fitting procedure are introduced, in Sect. 3.3 the smoothing effect of velocity-field-based fitting algorithms is discussed, in Sect. 3.4 the results of a few simple tests of *tirific* are presented, Sect. 3.5 gives a brief overview of the output and plot facilities of *tirific*. In Sect. 3.6 the results are being summarised and an overview of shortcomings, future implementations, and extensions of *tirific* is given.

3.2 Tirific layout

Tirific (tilted-ring-fitting-code) is a program to automatically fit a tilted-ring model to a datacube via a χ^2 minimisation.

3.2.1 Tilted-ring model

A *tirific* tilted-ring model is specified by a set of parameters at different radii plus a set of global parameters. The number of parameters belonging to the model is then the number of such radii times the number of parameters that change with radius plus the parameters that are independent of radius. The set of parameters

belonging to a given radius shall be called a "ring" in order to stick to the traditional terminology. A model is calculated in a very similar, but not identical way as in the GIPSY routine GALMOD. To calculate a model, a number of "sub-rings" with a user-specified width is created by linear interpolation of the ring-specific parameters. Those sub-rings are then modelled by a Monte-Carlo integration as being rotators on which the material rotates with the same tangential velocity (this is already a differential rotation) with a certain orientation to the observer that is determined by a position angle and an inclination and then projected on a cube the dimensions of which are specified by the input datacube. The orientational parametrisation in this figure is shown in Fig. 3.1. The final step to get a model representing an observation consists of a convolution with a 3d-Gaussian, at once representing the instrumental effect of a finite observing beam or point-spread function and the finite resolution in the frequency regime, as well as the internal dispersion in a galaxy.

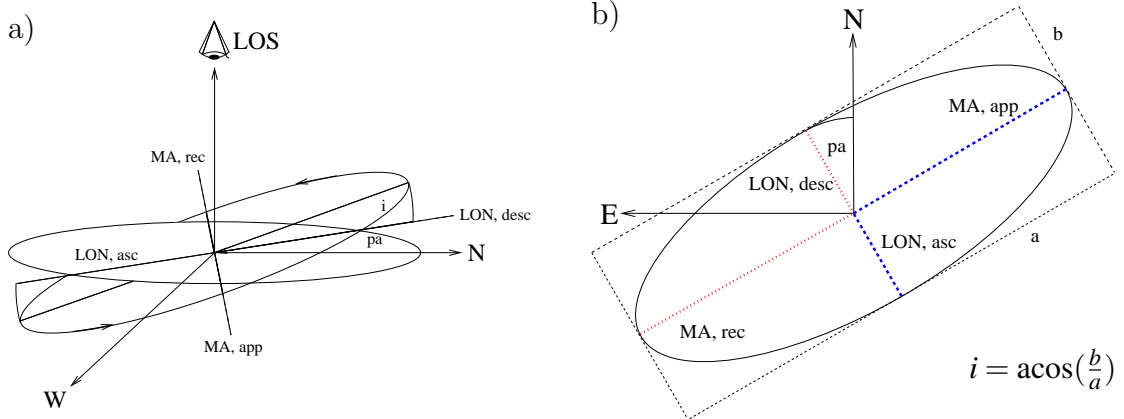


Fig. 3.1: Definition of the orbital orientational parameters inclination i and position angle pa . a) View of a circular orbit of the tracer material from an arbitrary position. A circular orbit appears as an ellipse to the observer as shown in b). The three-dimensional orientation of the orbit circle is parametrised by the position angle enclosed with the N-axis and the "descending" line-of-nodes LON,desc and the inclination. The descending line-of-nodes is the half-minor axis of the projected ellipse defined by the centre of the ellipse and the point where the galaxy material switches from having a higher recession velocity than the systemic velocity to having a lower recession velocity than the systemic velocity, moving anticlockwise along the ellipse. With the inclination being the angle between the celestial plane and the orbital plane, the orientation of the orbit is fixed. LOS is the line-of-sight, MA,app the approaching half-major axis, MA,rec the receding side half-major axis, LON,asc is the ascending line-of-nodes

The user specifies the number of rings and for each ring (see also Fig. 3.1):

- The radius.

- The circular velocity.
- The scaleheight (for the specification of the vertical density distribution see below).
- The surface brightness.
- The inclination.
- The position angle. Contrary to the usual custom (e.g. GALMOD, ROTCUR), the position angle is defined as the angle between the N-axis and the minor axis of each ring from N over E (See Fig. 3.1). In comparison to GALMOD the tirific position angle is 90° larger. The tirific definition is also used by Briggs (1990).
- The Right Ascension of the central positions of the rings, which is allowed to vary from ring to ring.
- The Declination of the central positions of the rings, which is allowed to vary from ring to ring.
- The systemic velocity, which is also allowed to vary from ring. to ring

The user specifies the following global parameters:

- A global isotropic velocity dispersion that includes the instrumental dispersion. It is clear that such a treatment is unphysical, as it is known that the dispersion changes with radius in spiral galaxies and is also not the same in vertical and horizontal direction of the disk. On the other hand, one has to keep in mind that the tilted-ring model itself is in fact an unphysical parametrisation of the galaxy kinematics, that still needs to be interpreted, even if it resembles a lot of the true kinematics in the galaxy. The reason to keep a velocity dispersion as a global parameter is to enhance the computational speed. It gives the possibility to shift the modelling of the dispersion to a convolution instead of a (time-expensive) Monte-Carlo integration. Future realisations of tirific are but planned in which a changing and anisotropic velocity dispersion will be allowed for.
- The second global parameter is the layer type for the vertical density distribution. The user can chose between a Gaussian, *sech*², Exponential, Lorentzian and a Box layer.
- The constant total flux of one point source (a “cloud”). The number of Monte-Carlo point sources is approximately the total flux of the model divided by this number. When calculating the point sources for a subring, however, the cloud flux is changed by a tiny fraction in order to keep the flux of the subring accurate.

After the calculation of a point source model and a gridding of the Monte-Carlo point sources on a model cube (of the dimensions of the input original), the cube will be convolved with a 3d-Gaussian, a product of a 2d-Gaussian in the xy-plane, and a one-dimensional Gaussian determined by the global velocity dispersion. The form of the Gaussian in the x-y-plane is determined by the observational beam of the input cube, which can be redefined by the user.

Here, the following caveat has to be taken into account: Assuming that the original (not the observed) brightness distribution consists of point sources, such that the point source model is in fact a representation of a possible brightness distribution, the actual convolution with this Gaussian would *not* represent an observation. This is due to the fact that the applied form of gridding (a point source is directly gridded to the next neighbouring pixel) is the same as a convolution with a box-function of the size of a pixel. If one then convolves with a Gaussian, the brightness-distribution is convolved twice, once with a box function (which is small compared to the observational beam), once with a Gaussian. If one wants to examine the appearance of an actual point source model in a fake observation this is an error that has to be corrected for. However, when comparing a galaxy HI distribution with a point source model, the mass-function of HI clouds comes as an incalculable error. For tirific, the gaseous distribution is assumed to be smooth (not consisting of point sources at all), justifying a double convolution.

3.2.2 Chi-square evaluation

The convolution routine implemented in tirific is meant to be as fast as possible. The only possibility to reach the required speed is by an fft-convolution, for which the FFTW (Frigo & Johnson, 2005) library is used. It seems to be the most flexible and of the highest quality of all freely available fft libraries.

Tirific calculates the χ^2 and with that, the relative probability of two models. Usually, a χ^2 calculates as

$$\chi^2 = \sum_i \frac{(m_i - o_i)^2}{\sigma_i^2} = \sum_i \frac{(m_i - o_i)^2}{w_i} \quad , \quad (3.1)$$

where i is an index running over all pixels in the cube, m is the model datacube o the original, and σ_i the noise of the original datacube in the i th pixel. If no quantisation noise is assumed, then

$$\sigma_i = \sigma_{\text{rms}} \quad , \quad (3.2)$$

where σ_{rms} is the rms noise in the original datacube. As the model is the result of a Monte-Carlo integration, this assumption is not true. Instead, in tirific the

(significant contribution of the) quantisation noise σ_i^q is regarded with

$$w_i = \sigma_{\text{rms}}^2 + (\sigma_i^q)^2 \quad . \quad (3.3)$$

The quantisation noise $\sigma_i^{q,u}$ of pixel i with n_i point sources of total (cloud-) flux f^c each in the *un-convolved* model cube m^u is given by

$$\sigma_i^{q,u} = \sqrt{n_i} \cdot f^c = \sqrt{\frac{m_i^u}{f^c}} \cdot f^c = \sqrt{m_i^u \cdot f^c} \quad . \quad (3.4)$$

If g is the convolution kernel, then the quantisation noise σ_i^q in the convolved map is given by

$$\sigma_i^q = \sqrt{\sum_j g_j^2 \cdot (\sigma_j^{q,u})^2} = \sqrt{\sum_j g_j^2 \cdot m_i^u \cdot f^c} \quad . \quad (3.5)$$

If the convolution kernel is a Gaussian of width σ_{gauss} , Equation 3.5 is equivalent with a convolution with a Gaussian of width $\sqrt{2} * \sigma_{\text{gauss}}$ in every direction and multiplication with a normalisation factor. Tirific can calculate the weight map

$$w(i) = \sigma_{\text{rms}}^2 + (\sigma_i^q)^2 \quad (3.6)$$

to perform a correct chi-square evaluation. It is, however, a bigger computational effort to do so, and the user might be inclined to modify the goodness-of-fit evaluation. With a “weight parameter” W the weight map is calculated to

$$w_i = \frac{\sigma_{\text{rms}}^2 \cdot W^2 + (\sigma_i^q)^2}{W^2} \quad . \quad (3.7)$$

In case of $W \rightarrow \infty$, the weight map becomes a constant, σ_{rms}^2 , giving tirific the possibility to safe one convolution. If $W = 1$, the noise will be estimated correctly, including the quantisation noise (which can easily exceed the rms noise in the datacube). The parameter is kept continuous to give the user a kind of a weighting scheme at hand. With an increasing weight parameter, the emphasis will be more and more taken away from regions with high quantisation noise (and thus high surface density) towards regions the regions of low surface density.

3.2.3 Chi-square minimisation

With the type of model generation in tirific, the usual χ^2 minimisation algorithms employing derivatives of the fitting function like the Levenberg-Marquardt algorithm (Levenberg, 1944; Marquardt, 1963; Press et al., 1986) are not easily realised, as the fitting function is an unknown. The Monte-Carlo method as a way

to produce a model cube was chosen because an analytic form of the tilted-ring model does not exist. Furtherly, the model itself, for which a Hessian and a gradient would have to be supplied in an analytic form, is the convolved tilted-ring model in three dimensions. While the investigations of the possibilities for optimised fitting algorithms will continue, for tirific the simplest solutions without the need for derivatives were implemented first hand.

Tirific offers two modes to find a best-fit model, a golden-section search algorithm and a Metropolis Monte-Carlo-Markov-chain algorithm. The first is an uneconomic but reliable method to find local χ^2 -minima in parameter space without the necessity to normalise the χ^2 evaluated with tirific, i.e. for this algorithm the knowledge of the rms noise in the analysed datacube does not play a major role. Tirific was tested as shown in Sect. 3.4 and 3.5 using this algorithm. The second can serve for the search of global minima of the chi-square in parameter-space including a very simple functionality to perform a simulated annealing. Furthermore it can in principle provide statistical error bars for the model, provided the noise in the input datacube is Gaussian and well-known (which it is usually not).

Parameter fitting in tirific is rather flexible. The user can specify single parameters to be fitted, or groups of parameters that will be fitted at once as one parameter. As an example, the user has the possibility to fit a changing projected centre from ring to ring as is, e.g., expected for a galaxy disk with a bowl-shaped warp. Such bowl shaped warps result in an asymmetric projected appearance. For rather symmetric galaxies this might not be desirable, in order to keep the number of free parameters low. With tirific the user has the possibility to fit a single centre for all rings, defining the centres of all rings as a group and fitting the value of this group as a whole.

The golden section algorithm The golden section algorithm (Press et al., 1986, Chap. 10.1) is a simple way to find a local minimum in parameter space. Sequentially each specified parameter undergoes a nested intervals process minimising the χ^2 . In a single iteration-process a parameter is first changed by a user-provided step-width and the “trial” χ^2 is calculated. If the trial χ^2 is larger than that of the current best-fit model, the search direction is reversed, if it is smaller, it is maintained and the step width is multiplied by a factor h . This procedure is continued until a (local) χ^2 -minimum is bracketed. Then, gradually reducing the step width, the position of the minimum is located to a user-given precision. The step width is varied by changing the search direction and/or a multiplication with a factor h . Defining

$$s = \frac{3 - \sqrt{5}}{2} \tag{3.8}$$

h is given by

$$h = \begin{cases} \frac{1-s}{s} & \text{enlarging the stepwidth} \\ \frac{s}{1-s} & \text{reducing the stepwidth} \end{cases} . \quad (3.9)$$

The choice of these numbers provides a maximum reliability of the found minimum at the expense of increasing the needed number of iterations. The stopping conditions for a single iteration process are a maximum number of iterations and a minimal reached step width. After each minimisation, tirific checks if the results are satisfactory. They are not, if

- the maximum number of iterations has been reached,
- user provided boundaries for the parameter are exceeded,
- the change of the parameter with respect to the start value is too large

The whole fitting process is stopped, when after a sequential fit of all parameters no unsatisfactory situation has been encountered or a maximum number of sequential fits has been reached.

The drawbacks of this algorithm are obvious. As the algorithm does not calculate a direction of the steepest decent, it may need a long time to find a local minimum in a narrow χ^2 -valley in the parameter space. Furthermore, the minimum that is found will always be a local minimum, such that the fitting process will require the watching eye of the user in order to judge whether a global minimum has been found. The advantage of the method is that a minimum of knowledge about the noise in the datacube is required. A steepest decent method would always have to rely on a good estimation of the noise in the datacube that a model is fitted to, a task that is not simple when using e.g. data from interferometric observations. Such local minimum finder methods will be implemented and tried out in future versions.

Metropolis algorithm and simulated annealing The Metropolis algorithm (Metropolis et al., 1953) and the method of simulated annealing is reviewed by Koonin & Meredith (1990, Chap. 8.1) and Press et al. (1986, Chap. 10.9).

The implemented version works in a very simple way:

1. A first model is calculated, parameters given by the user.
2. A trial model is calculated from the previous model, each parameter is being varied randomly within a user-given interval.

3. If the chi-square χ_{trial}^2 of the trial model is lower than the chi-square χ_{bef}^2 of the previous model and if it is inside a user-specified parameter range, it will be accepted as the next model. If it is not better, the trial model will be accepted as the next model with a probability

$$p = \exp\left(\frac{\chi_{\text{bef}}^2 - \chi_{\text{trial}}^2}{2 \cdot \text{ann}}\right) \quad , \quad (3.10)$$

where the annealing factor *ann* is provided by the user.

4. If the trial model is accepted, it is written to a list and it becomes the previous model in the next step. If it is not accepted, the previous model will stay the previous model in the next iteration and will be written to the list.

It can be shown (Koonin & Meredith, 1990) that after a sufficient number *N* of iterations, this Markov chain converges, and the parameters in the list are distributed like

$$N_e(\mathbf{X}) \propto \exp\left(-\frac{\chi^2(\mathbf{X})}{2 \cdot \text{ann}}\right) \quad , \quad (3.11)$$

where $N_e(\mathbf{X})$ is the number density of the models in the list at the position of the parameter set \mathbf{X} . This means that (with *ann* = 1) after a number of steps this very simple analysis provides a set of models that are distributed following a statistics inferred by the χ^2 (see Press et al., 1986, Chap. 14.1) without having to know the distribution itself. This assumes but the Gaussianity of the errors assigned to the data points, and that the model itself is close to reality.

The implemented algorithm can in principle be used for two purposes. One is to derive a statistically distributed sample of models. With that it is straightforward to derive error bars. The sample of models has to be sorted by probability (the χ^2), and then the variance of the parameters is e.g. fixed by the 68.26 best-fitting percent of the models. Tirific provides the possibility to perform this analysis.

The second possibility that tirific provides is a very simple version of simulated annealing (see Press et al., 1986, Chap. 10.9 for a review). When starting the program, the factor *ann* will be varied linearly within a number of steps. The user has thus the possibility to "cool" his system of models (or to heaten it), while the possibility to vary the energy input is given, too (by variation of the maximum step width). The algorithm can thus be used for a global minimum search. A schedule for such a search would look like this: At the start, set the step width and the annealing factor to higher values. The models will then vary in a wide range in parameter space. With cooling, i.e. reducing the ann factor, and at the same time lowering the energy input, i.e. reducing the step width, the system will be forced to more and more relax at a global minimum.

The functionality of both possibilities, the Metropolis algorithm and the simulated annealing, has not been tested sufficiently and it may be necessary to implement more sophisticated versions with an automated adjustment of the annealing factor and the step widths. Tests with datacubes from HI observations indicate that the estimated error bars are far too low. The reason for that may be that in fact the tilted-ring model is too far from a realisation of the HI kinematics and -distribution in a galaxy and that the (non-Gaussian) local density deviations of the HI distribution are the dominant contribution to the uncertainty of data points. Such an incalculable contribution then leads to an underestimation of the errors. `tirific` is a very slow routine (see below) and hence complete test-series that cover a range of input parameters that influence a fitting process take a lot of time. Such test-series are on the way and will be documented elsewhere. The further documentation will be restricted to the well-tested golden-section algorithm, in order to answer the question whether good fit results are principally possible.

3.3 Beam smearing and smoothing in velocity-fields

An error that arises in all cases when a velocity-field is analysed in order to extract a rotation curve can be demonstrated with a simple experiment shown here. A model datacube is created using `tirific`. A Gaussian beam of a Half-Power-Beam-Width of $12''$ and a (total) velocity dispersion of 10 km s^{-1} was used to produce a low-noise mock observation with $17.6 \cdot 10^6$ point sources of a galaxy in a datacube with a spatial pixel separation of $4''$. For demonstration reasons the rotation curve was chosen to fall off at large radii. The parametrisation of the model is shown in Fig. 3.2 a. For the galaxy, an inclination of 60° was chosen and the position angle was kept fixed at all radii. This is deemed an ideal case for a rotation curve analysis using the GIPSY routine `ROTCUR`.

In order to produce a “perfect” velocity-field, the cube was chosen to have an unrealistic channel separation of about 0.26 km s^{-1} . With this datacube a peak-velocity map was created using the `MOMENTS` task of GIPSY. For a noiseless datacube, such a velocity field is equivalent to a velocity-field created by fitting half-Gaussians to the extreme velocity side (as is e.g. done in García-Ruiz et al., 2002b). For a representative sample of positions this was checked by performing ten of such fits employing the GIPSY task `XGAUPROF` and a comparison with the peak velocity values. The mean deviation of the fitted values from the peak velocity values was found to be $(-0.008 \pm 0.190)\text{ km s}^{-1}$, meaning that the peak velocity map can be thought of being identical with a velocity map using half-Gaussian fitting. Such velocity maps are thought of being of high quality and coming near to the true projected mid-plane velocity. Using the velocity-field, a rotation curve was produced using the GIPSY routine `ROTCUR`, once with a

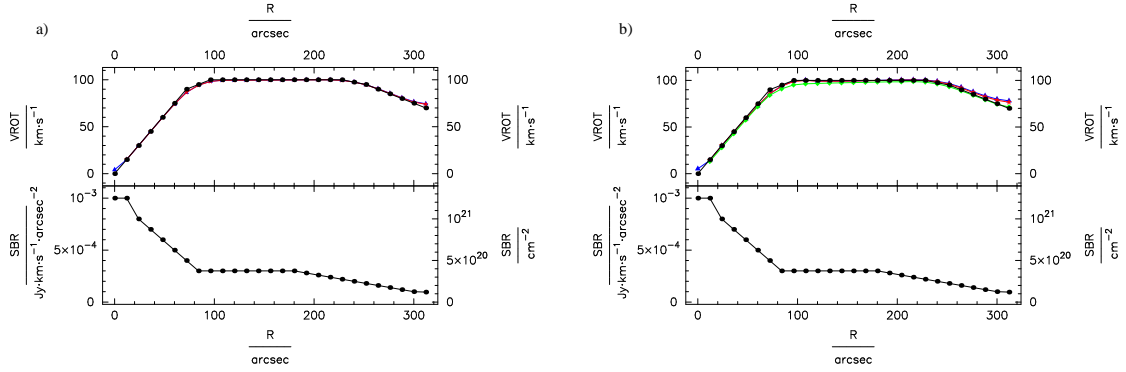


Fig. 3.2: Testing rotation curve extraction from velocity-fields. Black lines and dots show the parametrisation with which two mock observation have been generated. a) Top panel: rotation curve. Bottom panel: HI surface brightness and -density. The galaxy inclination is 60° . b) Same parametrisation as in a) but with an inclination of 75° . A velocity-field was generated as described in the text. Blue lines and blue triangles: Results from a ROTCUR fit with a free-angle of 0° and a uniform weighting. Red line and red stars: Results from a ROTCUR fit with a free-angle of 30° and a cosine weighting. Green line and green diamonds: Results from a cut along the galaxy major axis, corrected for the inclination. Black lines and black filled circles: Results from a tirlific fit.

“uniform” weighting and without a free-angle and once using a “cosine” weighting scheme and a free-angle of 30° . For both fits the central position and the orientational parameters were kept fixed at the known model values and the input rotation curve was identical with the model rotation curve. The nearly identical results of both fits can be seen in 3.2 a) (see also Teuben, 2002).

The fitted rotation velocities are biased following a certain pattern that depends on the shape of the surface brightness profile, which in this test-case is monotonically falling. In the regions where the rotation curve is rising, the rotation velocities are underestimated, and in the regions where the rotation curve is falling, the rotation velocities are overestimated. Hence, the fitted rotation velocity tends to be wrongly estimated in the direction of higher surface brightness. The reason for this lies in the fact that the measured velocity profile at a certain position of the galaxy is a convolution of the observational beam with the true intensity distribution. Thus, if the intensity is not a constant over the beam area, the resulting “smeared” profile gets more contribution from areas with a higher intensity and hence gets asymmetric, even if it would be symmetric using a pencil-beam. The position of its maximum is dragged towards velocities with a higher associated surface brightness. In a second experiment, where the inclination is set a bit higher to a value of 75° (Fig. 3.2 b), the corresponding viewgraph shows that this effect is not localised in a straightforward manner. It

is also visible at radii where both, rotation curve and surface brightness are flat over a large range. This means that “smoothing” affects the rotation curve at all radii. The reason for this lies in the fact that in projection the galaxy gets shortened along the kinematical minor axis. Points in the vicinity of the kinematical minor axis are thus affected by beam smearing to a greater extent. Usually, a section of the velocity-field is thus not regarded (by specification of a “free-angle”) for a rotation curve analysis and a weighting of data points is applied, while the experiment showed that this treatment does not help much for the analysis of the inner regions, but improves matters in the outer regions. An extreme choice for a free-angle would be to only read out the velocities along the major axis of the galaxy and to correct the velocities for the inclination. This is equivalent to an extraction of a rotation curve from a long-slit observation (with a very large point-spread function). The results from such a “fit” are shown in Fig. 3.2 a) for the mock observation with an inclination of 75° . It can be seen that with such a choice the results in the outskirts of the galaxy get slightly better on the expense of far worse results in inner parts of the galaxy.

Even if the maximum deviation from the true rotation curve is not very large (about 3.9 km s^{-1} for $i = 75^\circ$ in this experiment), this variant of beam smearing can introduce a severe misinterpretation of the measurement, as the resulting rotation curve is biased *systematically*. An assignment of a (large) statistical error to compensate for the beam smearing is thus not a solution. Results from mass decompositions in which (unknown) density profiles are fitted to rotation curves derived from velocity-fields are very vulnerable in that aspect. The smoothing effect can lead to a favouritism of density profiles with a lower curvature. The result shown here shows that beam smearing even takes an effect at radial distances by far exceeding the beam size. This means that it is not negligible, even when analysing observations with a very small instrumental beam or point-spread function ($\text{H}\alpha$ or CO observations).

A routine that fits models to datacubes is bound to be slow, and hence, has not been realised before. With rising computational power this is now possible. For such a routine, the effect of the instrumental beam is that of introducing a real statistical error, as it determines the number of independent data points. A bias of the results enters at the level of the (changeable) model, not on the level of the input measurement (See Sect. 3.4). The Figs. 3.1 a) and 3.2 b) also show the results of a fit with tirific to artificial datacubes that are identical with the datacubes used to produce the velocity-fields, except for a worse velocity binning of 2.06 km s^{-1} . As for ROTCUR the first-guess-parameters were identical with the model parameters. Naturally, tirific makes a perfect fit and the resulting model is identical with the input model. It is but noticeable that, in principle, with tirific it is thus possible to produce an artificial observation that can be reproduced by a fitting process over and over. For routines working on the velocity-field this is not the case. First, the surface brightness distribution, which is a free extra output

in tirific, has to be inferred using other information (e.g. by fitting a tilted-ring model to the total intensity map). Second, an artificial datacube will always have to be subject to a convolution with an artificial beam, hence introducing a beam smearing with the result that the artificial cube never reproduces a velocity-field that fits to the tilted-ring model found by the fitting routine.

Even without the corrugation introduced by an instrumental beam or an instrumental velocity dispersion, disk galaxies themselves bear similar effects: the finite thickness of the disk acts similarly. Along a line-of-sight the resulting spectrum will also be a sum over different azimuthal and radial regions in the galaxy. Hence, if the best quality of a resulting rotation curve is warranted, smearing effects are also to be taken into account analysing observations with a small observational beam. It is a better approximation to model a galaxy with a finite thickness in order to compensate for that effect.

3.4 Tirific tests

The first two tests of tirific have already been discussed in 3.3. Tirific is able to perfectly fit a simple model produced by tirific itself. Here, a small number of similar tests with rising difficulty for tirific is shown in order to show the benefits of tirific, as well as its limitations.

3.4.1 “Beam smearing” in tirific

In Sect. 3.3 a very simple test-case for tirific was shown. Here, the reaction of tirific is examined, when envisaged with a more realistic case of a perfect model galaxy that shows substructure below the (variable) sampling resolution used in tirific. For that purpose, a third model was generated doubling the number of parameters or halving the radial sampling of the model parameters to a value of $6''$ (See Fig. 3.3). Tirific was used to fit a model sampled at the HPBW of $12''$, making the “perfect” fit impossible. This reflects the more realistic situation of a fit to a datacube stemming from an observation. Galaxy disks are supposed to have a smooth rotation curve without sharp transitions from one gradient to another.

Only the rotation curve and the surface brightness was fitted, fixing all other parameters to the known model parameters. The results are shown in 3.3 a). Tirific achieves a nearly perfect fit in regions, where the tirific fit model is able to reproduce the mock observation, i.e. in those regions, where the intermediate data points that are not fitted by tirific lie on a straight line in-between the data points that are fitted by tirific. In the regions where this is not the case, tirific

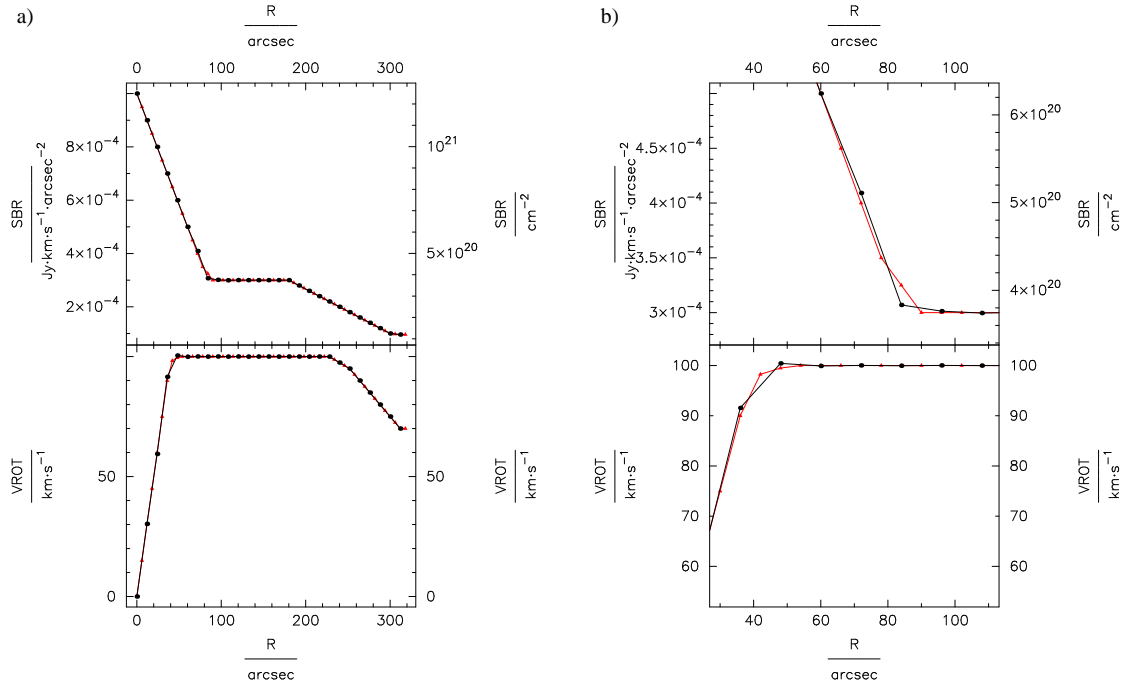


Fig. 3.3: Testing rotation curve extraction with tirific. Red lines and red triangles show the parametrisation with which a mock observation of a flat galaxy with 60° inclination has been generated. The parametrisation for the mock observation is twice as dense as for the fit of the mock observation performed with tirific. At positions where the mock galaxy could not be fitted perfectly by this construction, tirific was forced to interpolate with the result of a model-inherent “beam smearing”. The fitted parameters are represented by black filled circles and black lines. a) Complete parametrisation. b) Zoom-in to show the effect.

has to over- or underestimate some values in order to compensate for deviations from the model inferred by sub-sampling structures.

Tirific behaves as expected, as can be seen best at the turn-over radius of the mock galaxy at about $80''$. In order to compensate for the effect of underestimating the data point in-between $84''$ and $96''$, the rotation velocities are raised in the fitting process by a small amount, optimising the deviation of all three data points from their “real” values in the synthetic galaxy. This is an effect similar to beam smearing. Like for fitting routines working on velocity-fields, it is inferred by the (tilted-ring) model, which is not able to reproduce the “reality” sufficiently. Other than for such fitting routines, in tirific the choice of the model is the *only* factor that influences the systematics, as in principle it is always possible to reduce the sampling distance of the model (at the expense of a higher statistical error). With the choice of the tirific model, the deviations amount to a maximum of $1.6 \text{ km} \cdot \text{s}^{-1}$, which are significantly lower than the deviations of ROTCUR. They

are a result from a search of a best-fit value of the parameters at all radii, not only a single one. A side-effect is that the use of tirific will lead to an overestimation of the curvature at the turn-over radius. Other than other fitting programs, tirific thus favours mass models that lead to higher a curvature of the rotation curve in that region, hence steeper density distributions. If a mass model using a tirific rotation curve would still deliver the usual result favouring cored density profiles, this would have a significantly higher weight.

3.4.2 An edge-on rotation curve

One of the strengths of tirific is supposed to lie in the ability to perform reliable fits, where velocity-field methods are bound to fail by definition. This is expressly the case when the line-of-sight crosses the galaxy disk twice or more often. An extreme case of such a situation is encountered when a galaxy is observed nearly edge-on, as then, the galaxy disk is crossed not only twice but an infinite number of times. A mock galaxy observation was simulated using the rotation curve and the surface brightness profile of Sect. 3.4.1 (oversampling the HPBW), but putting it in an edge-on position. Then, the mock observation was fitted with tirific, taking the input model parameters as a first guess, but leaving the rotation velocity, the surface density profile, and the orientational parameters, inclination and position angle as free parameters. With that, again, tirific reaches a nearly perfect fit, interpolating in the regions where the fit results cannot reproduce the mock observation by construction (See Fig. 3.4 a). Hence, tirific is able to figure out reliable rotation curves for observations of edge-on galaxies. A caveat is that tirific assumes a galaxy to be translucent. Observations of edge-on galaxies suffer significantly at certain wavelengths from self-absorption and scattering processes (e.g. Baes et al., 2003). This has to be taken into account when interpreting tirific results especially when fitting to optical spectroscopic data.

3.4.3 An edge-over warp

Tirific has been constructed to be able to fit to datacubes from observations of warped galaxies, which is the main purpose of the tilted-ring model. In order to construct a case tailored to put tirific to the test and for which no appropriate software exists yet, an edge-over warp was constructed, oversampling again the resolution with which tirific would be run. The galaxy orientation was chosen to flip over to a different orientation at an intermediate radius of $180''$ in order to reach a final orientation at $228''$. The inclination was chosen to flip from 75° over 90° to reach a value of 110° . The position angle was chosen to change from -10° to 11° . This represents a strongly warped galaxy with an outer disk that is inclined with an amplitude of 40.6° with respect to its inner counterpart. In a

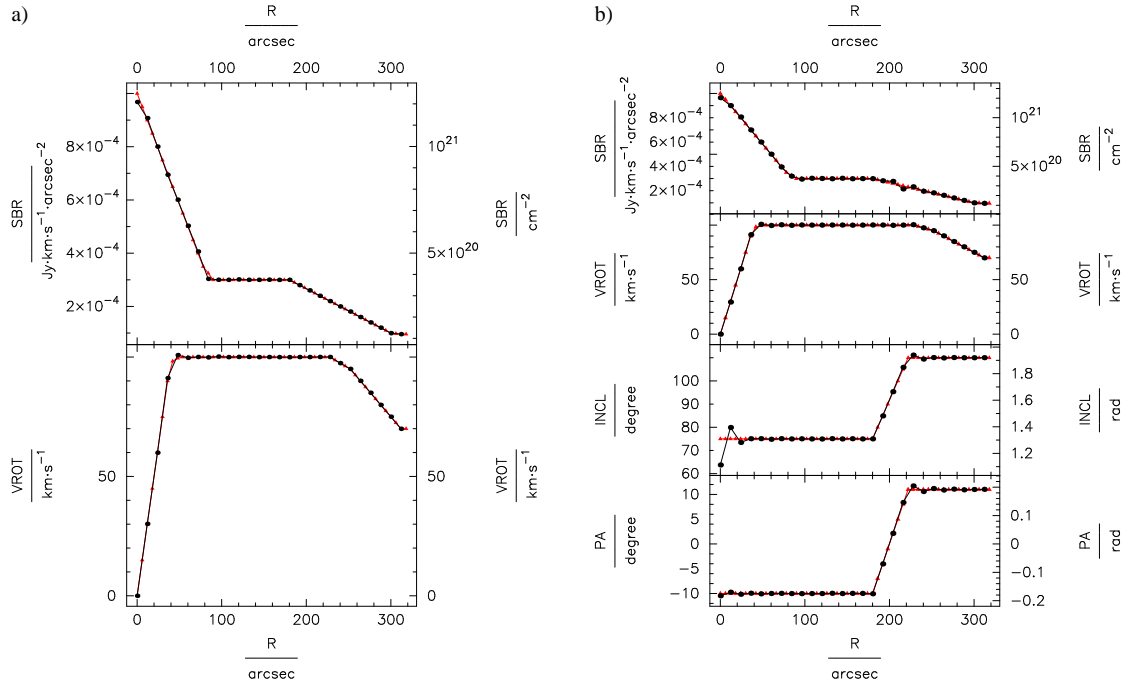


Fig. 3.4: a) Testing rotation curve extraction with tirific. Red lines and red triangles show the parametrisation with which a mock observation of a flat galaxy with 90° inclination has been generated. The parametrisation for the mock observation is twice as dense as for the fit of the mock observation performed with tirific. The smearing effect has not increased dramatically. The fitted parameters are represented by black dots and lines. b) Testing tilted-ring fitting with tirific. Red lines and triangles show the parametrisation with which a mock observation of a heavily warped galaxy has been generated. The fitted parameters are represented by black dots and lines.

first fitting run, the initial parameters were set to the known values of the input mock observations. During the fitting process, only the surface brightness, the rotation velocity, and the orientational parameters were left as free parameters. The number of used point sources was reduced to a fifth of the point sources used for the input model. Using models with $3.5 \cdot 10^6$ point sources, the fitting results are shown in Fig. 3.4 b). Save the innermost two data points, the input model is reproduced nearly perfectly. For the innermost two or three data points, tirific fits significantly wrong an inclination that deviates maximally 11.3° from the input model. This is explained as follows. First, as for the model generation a significantly lower number of point sources has been used, an increase in the quantisation noise results in a higher uncertainty of the fitted values. Second, in the range of the innermost data points, tirific fits to a very low number of independent data points. If the volume that tirific fits to inside a radius of $r = 36''$ is estimated by $V = 2\pi r \cdot 2v_{\text{rot}}^{\text{max}}$ with $v_{\text{rot}}^{\text{max}} = 90 \text{ km} \cdot \text{s}^{-1}$ being the rotation velocity at

that radius, then tirific maximally fits to a number of $\frac{V}{\Omega_B \cdot 2.34 v_{\text{disp}}}$ independent data points, Ω_B being the (two-dimensional) observational beam and v_{disp} being the velocity dispersion. This amounts to less than < 12 independent data points that about 3-4 independent parameters are fitted to. This means that for tirific, inside a radius of 3-4 observational beams a fit of the full account of free parameters has to be taken with great care.

The next and last test shows how this fault can be overcome. For this test, the input parameters to tirific were not chosen to be equal to the parameters chosen to construct the mock observation but they were chosen to randomly deviate from the input model parameters (see 3.5). The surface brightness was allowed to vary maximally by an amount of 40 percent, the rotation velocity by an amount of 40 percent, position angle and inclination by 30° . The scaleheight was increased by $0.5''$, the central position shifted by $-1.5''$ in RA and $0.1''$ in DEC, the systemic velocity by 9 km s^{-1} and finally the global velocity dispersion by an amount of -1.4 km s^{-1} . For the fit of the datacube, rotation velocity, surface brightness, inclination and position angle were fitted independently for every single ring, the other parameters were fitted varying together. Again, a reduced number of point-sources was chosen for the fitting process. The result of the fit process is shown in Fig. 3.5 a). Except for the first three radii, some of which are assigned highly deviating values, all other parameters are fitted with a reasonable accuracy. The reason has been discussed before. The number of independent data points in the input datacube is too low to reach a reliable fit for the innermost data points. The fitted surface brightness oscillates about the true value in the range from $192'' - 204''$ and the inclination is fitted wrongly at a radius of $204''$. Obviously, this data point is fitted wrongly because a second χ^2 minimum can be found by mirroring about 90° , a model with an inclination of a being equivalent to a model with an inclination of $180^\circ - a$. In order to overcome that problem, a second, consecutive fit was performed, as would be done examining a real observation. The orientational parameters of the four innermost rings were reset to their mean value. The inclination at $204''$ was mirrored about 90° . A linear regression of the surface brightness was performed in-between $12''$ and $60''$ and the values of the data points in-between $0''$ and $60''$ corrected accordingly. A linear regression of the surface brightness was performed in-between $192''$ and $240''$ and the values of the data points corrected in the same way. Then, with the new input-parameters the fitting process was started again. This time, all four inner rings were forced to keep the same inclination and position angle, hence reducing the number of 16 free parameters for the four inner rings to 10. As can be seen, this strategy works very well, as the result is a convincing, nearly perfect, fit.

While it can be seen that with tirific it is possible to produce reasonable fits to observations of well-behaved galaxies, this experiment also shows that tirific will not always produce a fit without being watched first go. Corrections of the fitting process are necessary. In the test-case shown, the deduction of a final

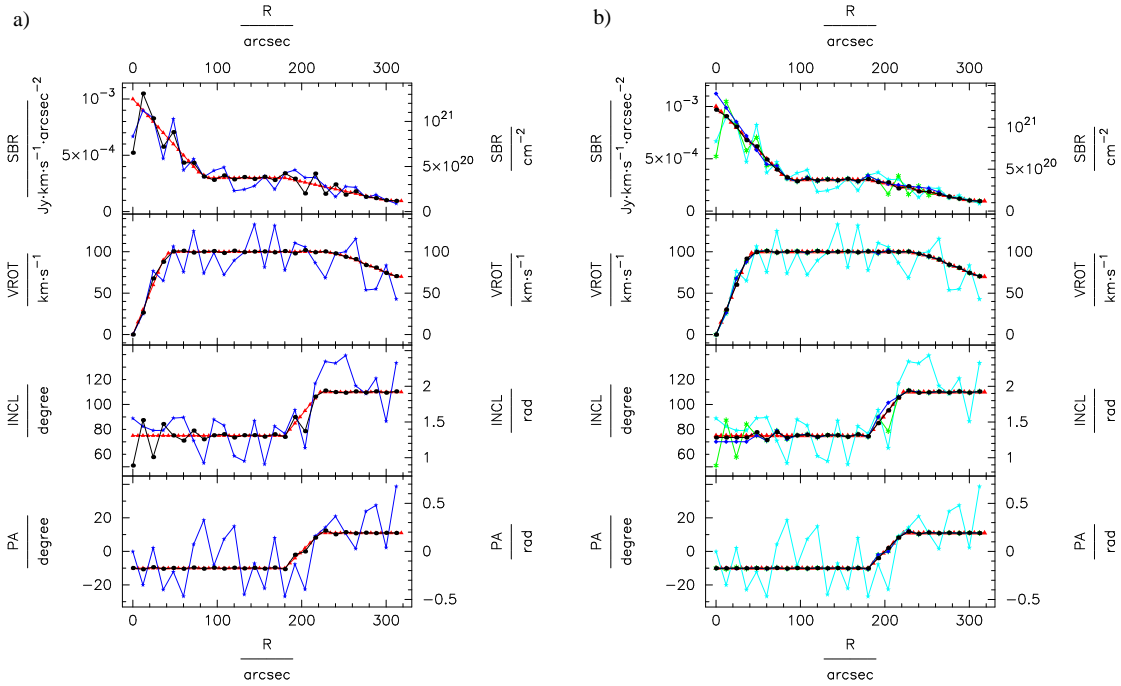


Fig. 3.5: Testing tilted-ring fitting with tirific. a) Red lines and red triangles show the parametrisation with which a mock observation of a heavily warped galaxy has been generated. Blue lines and stars show the input first guess to tirific. The fitted parameters are represented by black filled circles and black lines. Fit results after a first run. The model deviates heavily for some of the innermost three data points. b) Fit results after a second run, for which the results of a) have been corrected manually and the orientation of the innermost four data points was forced to be the same. Red triangles and lines show the parametrisation of the mock observation. Green asterisks and green lines represent the first guess from a), light blue stars and lines the first fitting result, blue diamonds represent the input parameters for the second run. Black dots show the results of the fit.

model was simple. Hence the virtual user did the very best to reduce the number of parameters by assuming that flat disk to be present for the first four data points in the mock galaxy. Reality might bear more difficult cases and a judgement of the fit-quality and decisions for or against some fitting strategy have to be made by a sensible being.

This is of course a major drawback that is but shared by all automated fit routines and future work might make it possible to remove a lot of responsibility from the user.

3.4.4 Tirific performance and the user interface

Tirific is slow, despite much effort to reduce the computing time to reach a single χ^2 value. The time needed to perform the last fit described in the previous section can serve as an orientation. A number of 20 parameters was fitted to the input cube. To reach a solution, in the “golden section” mode, a number of 845 models was generated. The computing time needed for that, working with an AMD Athlon XP 2400+ CPU, was 134 minutes, including initialisation, resulting in a mean of about 9.5 seconds per model examined. Depending on the input datacube on which tirific is supposed to work and the number of point sources used, tirific needs a minimum of 0.5 seconds per model to perform a point-source generation, one or two convolutions and a final χ^2 evaluation. An initialisation can take up to one hour. It is clear that with this performance, tirific cannot be used to crunch a large number of datacubes in a short time on a single computer. It can well be used for single case studies, the original intention of the program. Future development, however, will include a parallelisation of the code in order to make the use of computer clusters possible. Furthermore, the possibilities to use more sensible fitting procedures as introduced ad hoc will be exhausted.

A second major drawback a user will be confronted with is the scarceness of its current user interface. Tirific is currently embedded in the GIPSY environment. Although being one of the most used and most extended software packages for the analysis of datacubes, which cannot be avoided analysing HI datacubes, GIPSY regrettably comes with a user interface that is not up-to-date with current standards. Up to now, the development of tirific was focused on the computational performance, and not on the user-friendliness. Hence, monitoring functions to track a fitting process and input possibilities are restricted to a simple text-based mode. A more appropriate GUI is on the way. Furthermore, tirific will be offered independent of the GIPSY environment.

3.5 Graphics and analysis output

Tirific comes with a number of output possibilities to visualise and to further process the fit results. The most important are:

- An ASCII table output with the best-fit values. This can be obtained for the single parameters and will then contain a list with a row-number of the input radii. A second possibility is the output of a similar list for the (much higher number of) sub-rings that are used to generate the real model in tirific.
- An ASCII tirific default file alleviating a modification of a tirific result in order to restart a fitting process.



Fig. 3.6: Some output possibilities of tirific. a) An overlay of a representation of the warp structure of a galaxy with ellipses, an “inclinogram”. b) A three-dimensional spatial model datacube generated from the fit results, processed with the xray task of the Karma software package (Gooch, 1995). c) A “tiltogram” shows the mutual inclination of the planes of the fitted rings at different distances from the centre.

- An output synthetic datacube constructed with the best-fit values.
- An “inclinogram” FITS datacube that can be used to visualise the best-fit ring orientations (Fig. 3.6 a).
- A three-dimensional FITS datacube that shows the model galaxy as a three-dimensional structure. With an appropriate visualisation software (e.g. Karma’s xray, Gooch, 1995), the best-fit model galaxy can be visualised seen from different viewing angles (Fig. 3.6 b).
- A “tiltogram” FITS image, which shows the mutual inclination of the galaxy disk. This is a valuable tool to interpret fit results for warped galaxies (Fig. 3.6 c).
- Plots in different formats showing best-fit data points and some derived quantities in dependence of radius (Figs. 3.1-3.5) with the possibility to change the appearance and over-plotting of user-provided data points.

The high variety of output possibilities can be considered as a strength of tirific, especially if the user intends to use the program for an analysis of warped disks, or, being nearly equivalent, deeply integrated HI datacubes of disk galaxies.

3.6 Results and discussion

Tirific has been introduced as a program that fits a tilted-ring model directly to spectroscopic datacubes. It has been shown that the tirific tilted-ring model has a

high flexibility and allows a modelling even of galaxy disks that appear asymmetric in projection. It could be shown that *tirific* is not affected by major drawbacks of fitting routines that perform a tilted-ring fit on velocity-fields. Velocity-fields are severely affected by systematics that depend on a priori unknown factors, such as the surface density distribution of the examined disk. Using a direct fit to the datacube, *tirific* reduces these systematics significantly, delivering the unknown surface density profile as an extra. In fact, the systematics that affect a tilted-ring model fitted by *tirific* depend only on the validity of the model itself and not on the way the model is derived, as it does not need an intermediate step (a velocity-field) from an observed datacube to the model. Hence, the systematic errors introduced by using a kinematical tilted-ring model to fit a galaxy disk are reduced and straightforward. In terms of a derived rotation curve, *tirific* tends to favour naturally too strong a curvature, other than fitting routines that fit to the velocity-field. Thus, using a rotation curve derived with *tirific* has a higher weight in attempts to discriminate centrally steep mass density profiles of galaxies.

The biggest advantage of *tirific* lies in its applicability for edge-on- and warped galaxies as it does not need un-ambiguous velocities assigned to certain positions on the sky. Several tests showed that *tirific* is able to reach a best-fit model that comes very close to artificial input models with a large edge-over warp, provided the number of independent data points is high enough at a certain radius. A low amount of independent data points becomes a problem only inside a radius of 3-4 observational HPBWs and can be overcome by putting additional constraints on the model, such as the assumption of the flatness of the inner disk.

The major drawback of *tirific* is its slowness. Despite optimised strategies to keep *tirific* fast, performing a single fit when using a conventional PC takes a long time. Hence, *tirific* is not (yet) usable to perform many fits in a short time unless a certain amount of computational power can be employed.

It is of course the application on real observational data that will show how useful *tirific* will be in order to gain new insights in the kinematic structure of rotating disks, especially galaxy disks. It should but be noted that the few initial tests shown here are promising. Although one could in principle perform an infinite number of additional tests under varying conditions, the main goal – to show that the fitting process can lead to a satisfactory result – was reached.

Tirific can be deemed the most straightforward realisation of a tilted-ring fitting routine. Hence, its possible inapplicability is directly connected with the tilted-ring model not being applicable to reproduce an observed galaxy. As a closing remark, a number of reasons for the failure of a *tirific* tilted-ring modelling shall be given, which are major caveats for any realisation of a tilted-ring modelling. Once realised, they should be overcome in due time, work being in progress.

- *Tirific* models a galaxy as a disk consisting of rings whose surface bright-

ness does not vary azimuthally. It is not to be expected that an azimuthal variance of the disk surface brightness on small scales (compared to the circumference of a ring) will seriously affect a fitting of the disk with the tilted-ring model, as such small-scale corrugations can be expected to average out on the whole. If, however, a galaxy shows density asymmetries on large scales, e.g. if one side of the galaxy contains significantly more tracer material than the other side, *tirific* may run into difficulties. Any such large-scale asymmetry would leave a characteristic imprint on a difference map of the modelled and the original datacube, such that this possibility can be checked for. An investigation of the behaviour of *tirific* in the presence of large-scale asymmetries of the tracer material will be presented elsewhere in due course. Furthermore, the implementation of azimuthally varying surface brightness is a future issue for *tirific*.

- *Tirific* models a disk in which the material orbits on circles. Systematic deviations of such an orbital structure are not taken into account by a pure tilted-ring modelling. It is well known that in the presence of bars or spiral arms this is not true. Also, if on large scales the overall potential is not spherically symmetric, this leads to “oval” (Bosma, 1978) distortions of the velocity structure on large scales. If the disk material is not on circular orbits, this may lead to a “wrong” fit of the orientational parameters as a real ellipticity of orbits is confused with an ellipticity that is due to a (wrong) geometrical inclination of the disk. Such a confusion has its limits, though, and the imprints of deviations from circularity of orbits can well be spotted using a simple analysis of the residual velocity-field (see e.g. Franx et al., 1994; Schoenmakers et al., 1997), the difference of a velocity-field produced using the results of a *tirific* fit, and a velocity-field derived from the original datacube. *Tirific* does not yet provide the possibility to perform a fit of harmonics of the rotation velocity along a ring, but it is of course planned to implement this feature.
- In the test cases shown in Sect. 3.3 and 3.4, artificial instrumental noise was not simulated. Additional Gaussian noise will raise the statistical errors of the fits, especially in regions where the surface brightness of the tracer material is low. One can expect that a fit will be somewhat worse up to unreliable at large radii, while it is not expected that the results shown above would change significantly in regions where the signal-to-noise ratio is high. Non-Gaussian noise that is usually inherent to datacubes stemming from synthesis observations (HI or CO) might have a larger influence. A method to remove the influence of the CLEANing that is usually used to produce datacubes from interferometric observations, can in principle be realised in an extension of *tirific*. Instead of using a Gaussian beam for a convolution, it is a possibility to use the Dirty beam of the observation in

order to compare a tirific model directly to the Dirty Map from a synthesis observation, hence performing a model-based CLEANing. The largest contributor of non-Gaussian noise in synthesis observations, though, is the incorrect subtraction of the underlying continuum emission, which it is hard to account for straightforwardly.

- A tilted-ring model is intended to be a purely kinematic tool to get an idea of a galaxy's structure and its internal motions. An obvious shortcoming is that one inevitably uses a whole lot of (hopefully) redundant parameters to describe the motions in a galaxy disk and the distribution of the tracer material, still accepting negative side effects, that arise from the non-physicality of the model, in the case of tirific a slightly wrong estimation of the rotation velocity. It is desirable to do both, to improve the complexity of the model, and at the same time using physics in order to reduce the number of parameters needed. A simple example is to use a modification of tirific in order to directly fit a rotation curve stemming from the stellar and gaseous mass-distribution and an hypothetical mass-profile of a Dark Matter halo while retaining the possibility to bend the disk.

4 New rules for the behaviour of warps

HI observations of three disk galaxies showing regular large scale warps are presented. The kinematics and geometry of the galaxies are modelled by fitting a tilted-ring model directly to the datacube. Using this method one is neither hampered by orbit crowding nor by beam smearing. In addition to the well-known rules for the behaviour of warps the warps of the examined galaxies show the following features: i) At large radii the HI disk settles again into a coplanar disk that is inclined with respect to the inner disk ii) The rotation velocity changes at the commencement of the warp. iii) At the same radius, where the stellar disk has faded, the surface density of the warp drops to a low, very slowly decreasing value. A careful literature search shows that these properties are shared by a number of other galaxies. The change in the rotation velocity indicates that the radius at which the warp starts to evolve marks at the same time the transition between two dynamical regimes, one governed by the stellar disk and one governed by the Dark Matter halo. This kind of warp is likely a general intrinsic and long-lived feature of disk galaxies and might be manifesting a common bending mode of disk and halo.

4.1 Introduction

Warps in the disks of spiral galaxies are ubiquitous. If traced sufficiently well beyond the optical radius, independently of the environment, galaxy disks bend away from the plane defined by the inner portion of the disk (García-Ruiz et al., 2002b). While the literature does not provide a uniform picture, the most recent studies (García-Ruiz et al., 2002b; Sánchez-Saavedra et al., 2003) indicate that most warps are of the form of an S-shaped grand-design warp, the projection of the galaxy resembling an S or an integral sign.

Usually, warping becomes evident at large radii, where the stellar disk has faded substantially and is seen best in the HI component. Hence, people became aware of the phenomenon as being inherent to galaxy disks in the middle of the 70's (Rogstad et al., 1974; Sancisi, 1976; Bosma, 1978), when observations of the neutral hydrogen component with high spatial resolution were made possible employing synthesis techniques, the gaseous disk of an undisturbed galaxy being usually 2-3 times larger than the stellar one. Later it became evident that also stellar disks are warped at their edges with such a high frequency of occurrence that today it is usually assumed that all galaxies are warped to some degree and that the identification of a flat disk is mainly a question of a certain threshold set to identify vertical disturbances as warps (Sánchez-Saavedra et al., 1990a,b; Reshetnikov & Combes, 1998; Schwarzkopf & Dettmar, 2001; Sánchez-Saavedra

et al., 2003). This means that any theory of galaxy evolution must contain an explanation for the existence and the structure of warps.

It is possible to spot by eye that warps roughly follow a common behaviour, but at the same time hard to quantify regularities. The reason for this is that warps usually occur at the edges of galaxies. As the mass density of the luminous matter in these regions is usually low, they are both, hard to observe, and easily subject to external disturbances. Quite a few of the mechanisms proposed to generate warps rely on the fact that the galaxy interacts with its surroundings. It is but a challenge to show that observed features are inherent to the warping phenomenon and not local and/or temporal appearances. Timescales are large at large radii and local disturbances can retain their structure for quite some time.

Nevertheless, a few rules (in the sense that they are not followed strictly by all galaxies) for the behaviour of warps exist, the most important ones are: i) Galactic (HI-)disks are planar within R_{25} . Inside a transition radius $R_{tr} \approx R_{Ho}$ the kinematical minor axis is straight. (Rule 1 in Briggs 1990. This implies that, if the galactic disk is precessing, the disk keeps the same precession frequency inside R_{tr} , while a warp is already occurring.) ii) Warps change character at R_{tr} (Rule 2 in Briggs 1990). iii) For radii larger than R_{Ho} ($\approx R_{tr}$) the kinematical minor axis progresses in the direction of the galactic rotation. (Rule 3 in Briggs 1990, implying that a co-precession with the inner disk stops at radii $\gtrsim R_{tr}$.) iv) A unique reference frame exists in which the kinematical minor axis exhibits two straight regimes, one inside R_{tr} and one beyond R_{tr} . (Rule 4 in Briggs 1990. One thus finds an outer regime, in which co-precession is also present, cf. Revaz & Pfenniger 2001.)

v) Warps are common and occur in all environments (Rogstad et al., 1974; Bosma, 1978). There is an indication that the amplitude of warps is higher in dense environments (Reshetnikov & Combes, 1998; Schwarzkopf & Dettmar, 2001; Sánchez-Saavedra et al., 2003) and that warps are more asymmetric in dense environments (García-Ruiz et al., 2002b). vi) No warp exists that shows clear differences of amplitude in the stellar and the gaseous component (Cox et al. 1996, but see also Florido et al. 1991). vii) Galaxies with a large concentration of their Dark Matter halos (as derived from their kinematics) are less likely to be warped (Bosma, 1978). While the rules i),ii),iii),v),vi) are commonly accepted, iv) is a controversial point that has been put down to projection effects (Briggs & Hamphuis, 1991), and vii) has been put into question by Castro-Rodríguez et al. (2002). All rules concerning the shape of warps have counterexamples. This points towards the fact that at least two distinguishable mechanisms to excite warps exist, and that one of both defines a global shape of galaxy disks, while the other one may have a greater importance for individual cases in a dense environment.

A few concurring explanations and theories for warps exist. They have to cope with the fact that a warp in a galactic disk, once excited, will generally tend to

wind up due to differential precession. The strictest constraints on warp formation scenarios are given by the ubiquity of warps and the rules i) and iii). Warps have to be long-lived or, if they are not, they have to be excited frequently by interaction with some invisible external agent (but see also Revaz & Pfenniger, 2004). While possibilities may exist to maintain a galaxy disk at the same precession frequency throughout, it is not simple to find a solution for which at a certain radius the disk starts to precess differentially.

Recent studies of Sánchez-Salcedo (2004); Sánchez-Salcedo (2005) indicate that the intergalactic medium in form of magnetic fields (Battaner et al., 1990b,a; Battaner & Jimenez-Vicente, 1998) or intergalactic gas (Kahn & Woltjer, 1959; López-Corredoira et al., 2002) may be ruled out as an interaction partner that enables warp formation in a group environment or in the field. Current estimations of the intergalactic magnetic field strength are well below what would be required to ignite warps in galaxies, moreover the result of the interaction of the gas disk of a galaxy would rather be a thickening of the disk, as a magnetically induced warp would rapidly wind up. A ballistic accretion flow of intergalactic gas directly onto the disk would be a possible origin of warps. Again, the measured densities of this medium are well below of what would be required, except inside a cluster environment. Furthermore, beneath other constraints, the warp shape would always show a certain amount of asymmetry as an accretion flow would not only result in a torque imposed on the disk but also in an axisymmetric forcing of the disk with the result of the mixture of a bowl-shaped and an integral shaped warping. While the Milky Way warp is asymmetric, its shape is incompatible with an accretion flow as a possible origin.

A possibility of warp excitation without the need for an interaction is discussed by Revaz & Pfenniger (2004). A galaxy with a lightweight spherical halo (weighing of at most a bit more than half the total mass of the galaxy) and hence a reduced stabilising pressure gradient on the disk could bear relatively long-lived bending instabilities. Such warps have the drawback that their amplitude is too small to explain the numerous isolated galaxies with large symmetric warps. Furthermore, while they resemble a realistic warp shape at a first glance, cases exist that violate rule vi) in the sense that a kinematical minor axis winds up at large radii, but in the wrong direction. Self-inflicted bending instabilities might play a role in the range of the stellar disk, but on larger scales they do not explain observations well.

Tidal interactions with small companion galaxies as a possible origin of warps are an attractive proposal. In the concordance picture every galaxy is expected to host a system of Dark Matter lumps (the “satellite catastrophe”, Moore et al., 1999a), the biggest of which are large enough to bind a stellar system. If the impact of the tidal interaction with small companions suffices in order to produce warps that have the right shape, an explanation for the ubiquity of warps is found

while at the same time the correlation of the warp amplitude and asymmetry with the environmental density is explained. Small systems are not detected easily, and the suspicion is stirred with every companion or sign of tidal debris detected in the near of strongly warped galaxies (e.g. Shang et al., 1998), while in denser environments possible interaction partners grow in density and mass.

After initial work by Burke (1957), Kerr (1957), Elwert & Hablick (1965) and Avner & King (1967) with differing results, Hunter & Toomre (1969) showed, in a first self-consistent calculation, that the interaction with companions of double the size of the Large Magellanic Cloud would be a possible scenario for the origination of warps, if their perigalactica would lie much closer to the centre of the galaxy than it is the case for the LMC. Weinberg (1998) proposed a resonant deformation of the Dark Matter halo halfway between the satellite and the galactic centre, a wake, as possible agent to enable the angular momentum to be transferred efficiently from far satellite galaxies to the galactic disk. García-Ruiz et al. (2002a), however, simulated the LMC-Milky Way system with a live halo and found that still the amplitude of the Milky Way warp could not be reached. So, if tidal interaction shall cause warps, the companion should have a perigalacticon at much smaller radii, like the Sgr dwarf system in the case of the Milky Way (Bailin, 2003). Bailin & Steinmetz (2004a) showed that indeed a companion galaxy with the properties of Sgr could cause a transient warping of the disk that is ignited at every pericentric passage of the satellite and damps out during one orbital time with a large enough amplitude to account for the Galactic warp, provided the satellite orbit is orientated at an angle of 45° with respect to the disks spin axis. Whether such a transient warping in this specific case and generally obeys the observational rules for warps is not clear. Until the opposite is shown, it may be speculated that a warp that flattens out on the timescale of an orbital time of a close companion will show a periodically varying structure that does not fit to the rather static shape described by Briggs (1990) rules. As in any case the pericentric distance of objects that might cause warps is restricted to be small, it is to be suspected that while tidal interaction might be one cause of the enhancement of the warp amplitudes in galaxy groups and clusters or pairs of galaxies, a different possibility should be sought in order to explain the ubiquitous warping. This might be different when one allows for a non-standard cosmological picture. In a MONDian universe, the far-field enhancement results in the greater impact of satellite galaxies on the disk dynamics. Indeed, Brada & Milgrom (2000) show in a simulation that the LMC *would* be able to ignite a warp of an amplitude as seen in the Milky Way.

Could it thus be that grand-design warps are long-lived structures? One of the ideas to make a warp long-lived is to find a mode of precession which is self-preserving. The possibility and necessity of bending modes in the presence or without the presence of a Dark Matter halo in order to ensure a long-lived warping of the disk has been studied excessively (Lynden-Bell, 1965; Hunter & Toomre,

1969; Binney, 1978; Tubbs & Sanders, 1979; Dekel & Shlosman, 1983; Toomre, 1983; Sparke, 1984, 1985; Sparke & Casertano, 1988; Kuijken, 1991). Unfortunately the proposed bending mode theories fail for two reasons. Firstly, the existence of such modes would imply that the galaxy precesses as a whole entity. Thus, Briggs (1990) findings that this is not the case at large radii (see iii) was observational evidence against these bending modes. Proposals that warps could be temporary features that reflect the settling into a bending mode or a modified-tilt mode (Hofner & Sparke 1994, see also Christodoulou & Tohline 1986) could be excluded when the halo was not longer regarded as a stiff entity but as a live (reactive) system. Halo and disk exchange angular momentum via dynamical friction which leads to a rapid mutual alignment and a damping or wind-up of any warp in the shape of a bending mode in which the halo would be stiff (Nelson & Tremaine, 1995; Dubinski & Kuijken, 1995; Binney et al., 1998). It is nevertheless an issue of discussion whether for a realistic setup bending modes of a coupled disk-halo system might exist, a point stressed by Binney et al. (1998). They observe that while in their simulations the warp winds up rapidly, the “warping energy” is still preserved and does not damp away. For the right setup of an initial model, a simulation could maybe converge to a steady-state “mode”, involving disk and (flattened) halo. Aware of the problems, bending modes invoking a stiff halo might run into, Ostriker & Binney (1989) and Binney (1992) demonstrated that secondary cosmic infall on the halo, reorientating it steadily might be responsible for warp formation. Various simplifying computer simulations in which cosmic infall is taken into account, have been studied. Debattista & Sellwood (1999) found a surprisingly realistic warp resembling the rules for the behaviour of warps, simulating the evolution of a initially flat disk in a Dark Matter halo with inclined spin axis. Jiang & Binney (2000) simulated the evolution of a disk-halo system into which halo material was injected into an inclined torus, simulating infall. They produced a warp, which unrealistically starts already at the centre of the disk. Finally, Bailin & Steinmetz (2003), found that a realistic warp would show up and vanish on an intermediate time-scale in an N-body disk in a static spherical halo potential, subject to a typical net torque found in CDM simulations. Crucially, in these simulations, the impact of dynamical friction is unattended.

Binneys (1998) picture got recent support. In a series of high-resolution simulations in a concordance framework, Bailin et al. (2005) examined the settlement of a system containing a galactic disk and a Dark Matter halo. They observe that the (still) slightly flattened triaxial halo tilts at a radius of $0.1r_{\text{vir}}$ and is thus in a state of misalignment with itself. While in the inner part being well aligned with the disk, it settles to a random orientation beyond $0.1r_{\text{vir}}$. This misalignment is maintained over a large period of time (2.2Gyr), indicating that the coupling between the inner and the outer portion of the halo is weak enough to prevent a mixing of angular momentum. If a very thin gaseous disk would exist at large

radii it would settle towards the preferential plane defined by the outer portion of the halo. Bailin et al. (2005) are pessimistic about the existence of such an extended disk. If existent, however, eventually the whole system might settle into a common bending mode that looks similar to the shape found for the Dark Matter halo.

In this chapter the examination of the kinematical warp structure of three galaxies, selected to show prototype symmetric grand-design warps of intermediate up to large amplitudes, is presented.

The goal of this study is to review the rules found by Briggs (1990), to check upon their validity and furthermore to possibly constrain furtherly the general structure of grand-design warps, making use of the higher sensitivity provided by today's telescopes and improved analysis methods. While it is known that all warps show asymmetries to some degree (e.g. García-Ruiz et al., 2002b), grand-design warps are by definition (anti-)symmetric. In order to separate the symmetric structures from asymmetric structures in a realistic warp, it is thus necessary to know first which features are inherent to the symmetric grand design warp. Two approaches are possible. One can either select a large sample of galaxies and try to find common features among the warps in a rough, easy-going manner, or one can try to chose a few exemplary cases that then are examined thoroughly. The second approach was chosen here.

The most suitable objects are galaxies with a distinctly warped HI disk that show both regular kinematics and morphology. Both should be symmetric with respect to the centre. This way, a bias is introduced, when the results are interpreted as being exemplary for the bulk of warps, as the galaxies examined are prototypes of a special kind of warp, namely the integral signed one. If, however, most warps are dominated by the integral-sign shape or an $m=1$ vertical disturbance in the disk, then the results may with some care be extrapolated to the global warp population and serve as a basis for further studies of a more statistical character. The most recent statistical studies indicate that most warps are dominated by the symmetric $m=1$ bending structure (García-Ruiz et al., 2002b; Sánchez-Saavedra et al., 2003).

The chapter is laid out as follows: In Sect. 4.2 the selection and global properties of the observed galaxies are described. Sect. 4.3 presents details of the HI synthesis observations conducted with the Westerbork Synthesis Radio Telescope and the data reduction performed. In Sect. 4.4 the data analysis by means of a new technique to perform a tilted-ring modelling is described, the results of which are shown in Sect. 4.5. In Sect. 4.6 the fitting results are critically reviewed and the influence of violating systematic effects is taken into account. Sect. 4.7 contains a discussion of the final results in view of possible mechanisms that drive warping. Supplementary figures and tables not essential for a first reading of the chapter are placed in the last section.

4.2 The examined galaxies

The selection of suitable candidates was dominated by the desire to choose prototype grand-design warps that do not show direct signs of tidal interaction or other peculiarities in their HI structure. No effort was made to select certain types of galaxies. The galaxies were selected to contain no large-scale bars. The assumption inherent to the applied method to parametrise the disk geometry is that the orbits of the galaxy material in the disk are circular. Hence, a bar, in the vicinity of which this assumption is violated, imposes a problem for the interpretation of the results. In order to avoid large problems of this kind, only galaxies classified as non-barred in the RC3 (de Vaucouleurs et al., 1991) were considered in the selection process. The galaxies were chosen not to be a member of a galaxy cluster. Individual warps in such an environment are possibly not good representatives of the classical integral-signed warp, as the environmental properties in clusters are not representative for a common disk galaxy. Most galaxies and certainly most spiral galaxies, which is the population addressed studying warps, do not reside in galaxy clusters.

In order to be able to get an impression whether a galaxy would serve for the intended purpose, the WHISP (van der Hulst et al., 2001) database, which provides HI total intensity maps and, equally important, velocity maps of a large sample of galaxies, was consulted in order to select the spiral galaxies NGC 2541, UGC 3580, and NGC 5204 as suitable objects.

NGC 2541 is a well known smaller late-type spiral galaxy in the NGC 2841 galaxy group that contains 7 larger spiral galaxies in total plus possibly a number of dwarf galaxies. While listed in the RC3 as a non-barred galaxy, it is categorised as showing a bar in the PGC (Paturel, 1989). Chapelon et al. (1999) and Cabrera-Lavers & Garzón (2004) showed in photometric analyses that this galaxy shows a central isophotal twist that they interpreted as a bar with a diameter of $\approx 38''$. Analysing photometric observations, Coccato et al. (2004) in a spectrophotometric study did not confirm the presence of a bar, but found a severe velocity gradient along the minor axis of the galaxy with the aid of long-slit spectroscopic measurements. Using Fabry-Pérot spectroscopy, Garrido et al. (2004) found a characteristic kinematical feature at the end of the assumed bar, which they estimated to exist up to a radius of $30''$. Two possible interpretations for this irregularity in the centre of the galaxy exist. Either, NGC 2541 possesses a small bar or an inclined inner disk. It is a convenient coincidence that NGC 2541 is part of the HST key project to measure the Hubble constant and has been used as a Tully-Fisher calibrator. Its distance has been measured with great accuracy using the Cepheid period-luminosity relation (Ferrarese et al., 1998; Freedman et al., 2001).

UGC 3580 is an early type spiral of similar size as NGC 2541. This galaxy is poorly studied and has no obvious companions. While the RC3 (de Vaucouleurs

et al., 1991) categorises this galaxy as being unbarred, in the PGC (Paturel, 1989) it is classified as containing a central bar.

NGC 5204 is a rather small galaxy of Magellanic type. It entered this study because of its extraordinary beautiful warp, which is very symmetric and has at the same time a rather large amplitude. The stellar- and HI disk are rather featureless, the galaxy is supposed to lie at the border of the M101 group (Karachentsev et al., 1994, 2003) but has no obvious companions or interaction partners. The distance of 4.6 Mpc (see also below), determined by Karachentsev et al. (2003), is rather low for a membership in the M101 group. Because of its symmetry, it entered several kinematical and dynamical studies Sicotte et al. (e.g. 1996); Sicotte & Carignan (e.g. 1997); Swaters et al. (e.g. 2000); Swaters (e.g. 2001); Swaters et al. (e.g. 2003), being studied most thoroughly by Sicotte & Carignan (1997), using a complex method in order to derive the disk geometry and the kinematics.

Basic properties of the galaxies, derived in this work or taken from literature, are listed in Tab. 4.1.

4.3 HI observations and data reduction

The galaxies were observed in the HI emission line in-between December 2002 and May 2003 with the upgraded WSRT: NGC 2541 and UGC 3580 for 1×12 hours, NGC 5204 for 2×12 hours. Details of the observations are listed in Tab. 4.2.

The data underwent a standard data reduction with the Miriad (Sault et al., 1995) software package.

After the conversion of the raw data into Miriad format, the amplitudes of the visibilities were corrected for changes in the baseline system temperature, roughly proportional to the square root of the product of the single antenna temperatures tracked by the WSRT. A rather insensitive median filter was applied to the visibilities and the worst interferences were flagged automatically. The calibrator- and the source visibilities were then inspected and remaining obvious interferences were flagged. The visibilities were then calibrated using a single calibrator point source. In the case of NGC 5204, the visibility datasets of both observations were merged into one visibility file, which obviously was not necessary for the single observations of NGC 2541 and UGC 3580. After a first inversion and inspection of the data, the data were edited again in order to erase visibilities contaminated by interferences. For that purpose, both, the continuum visibilities and datacubes after trial inversions were inspected. If further interferences became evident in any of the furtherly discussed reduction steps, the following steps were repeated after flagging those data points.

Name	(1)	NGC 2541	UGC 3580	NGC 5204
Type	(2)	SA(s)cd	SA(s)a	SA(s)m
RA	(3)	08 ^h 14 ^m 40 ^s .07	06 ^h 55 ^m 30 ^s .86	13 ^h 29 ^m 36 ^s .51
DEC	(4)	+49°03'41".2	+69°33'47".0	+58°25'07".4
v_{sys}	(5)	559.5 ± 2.0	1200.1 ± 2.0	200.8 ± 4.0
D	(6)	11.2 ± 0.8	14.0 ± 2.9	2.9 ± 0.7
sc	(7)	54.396 ± 3.879	68.017 ± 13.849	14.270 ± 3.306
m_B	(8)	12.36 ± 0.34	13.87 ± 0.35	11.71 ± 0.12
m_I	(9)	10.86 ± 0.06	11.55 ± 0.08	9.79 ± 0.10
m_B^c	(10)	11.60 ± 0.34	13.34 ± 0.35	11.30 ± 0.12
m_I^c	(11)	10.57 ± 0.07	11.25 ± 0.09	9.71 ± 0.10
M_B	(12)	-18.6 ± 0.4	-17.4 ± 0.6	-16.0 ± 1.2
M_I	(13)	-19.7 ± 0.2	-19.5 ± 0.5	-17.6 ± 1.2
L_B	(14)	4.487 ± 1.544	1.413 ± 0.734	0.407 ± 0.437
L_I	(15)	3.195 ± 0.498	2.667 ± 1.109	0.485 ± 0.520
F_{HI}	(16)	142.2 ± 14.2	41.6 ± 4.2	134.4 ± 13.4
M_{HI}	(17)	4.226 ± 0.736	1.931 ± 0.810	0.275 ± 0.130
r_{25}	(18)	172.6 ± 60.2	97.1 ± 28.0	140.3 ± 10.0
r_{HI}	(19)	420.0 ± 30.0	240.0 ± 30.0	240.0 ± 30.0
r_t	(20)	590.0 ± 30.0	375.0 ± 30.0	420.0 ± 30.0
R_{25}	(21)	9.39 ± 0.67	6.60 ± 1.34	2.00 ± 0.46
R_{HI}	(22)	22.85 ± 1.63	16.32 ± 3.32	7.20 ± 0.79
R_t	(23)	32.09 ± 2.29	25.51 ± 5.19	5.99 ± 1.39
v_t	(24)	127.2 ± 25.0	121.3 ± 16.9	105.0 ± 25.0
M_{dyn}	(25)	> 120.76 ± 48.24	> 87.26 ± 30.09	> 15.36 ± 8.13
$\frac{M_{\text{HI}}}{L_B}$	(26)	0.9 ± 0.2	1.4 ± 0.3	0.7 ± 0.1
$\frac{M_{\text{HI}}}{L_I}$	(27)	1.3 ± 0.2	0.7 ± 0.1	0.6 ± 0.1
$\frac{M_{\text{dyn}}}{M_{\text{HI}}}$	(28)	> 29 ± 4	> 45 ± 11	> 56 ± 15
$\frac{M_{\text{dyn}}}{L_B}$	(29)	> 27 ± 12	> 62 ± 24	> 38 ± 21
$\frac{M_{\text{dyn}}}{L_I}$	(30)	> 38 ± 16	> 33 ± 12	> 32 ± 17

Tab. 4.1: Basic properties of the examined galaxies. (1) Name of galaxy. (2) Classification of galaxy (de Vaucouleurs et al. (1991)). (3) Right Ascension (J2000) (NED). (4) Declination (J2000) (NED). (5) Optical heliocentric systemic velocity (kms^{-1}). (6) Distance of object (Mpc, Freedman et al. 2001 and this work). (7) Scale between distance on sky and true distance ($''/\text{pc}$). (8) Apparent B-band magnitude (mag LEDA). (9) Apparent I-band magnitude (mag LEDA). (10) Apparent B-band magnitude corrected for dust extinction (mag, LEDA). (11) Apparent I-band magnitude corrected for dust extinction (mag). (12) Absolute B-band magnitude (mag). (13) Absolute I-band magnitude (mag). (14) B-band luminosity ($10^9 L_{\odot}$). (15) I-band luminosity ($10^9 L_{\odot}$). (16) Total HI flux (Jykm^{-1}). (17) HI mass ($10^9 M_{\odot}$). (18) Blue optical radius ($''$, LEDA). (19) HI radius ($''$). (20) Terminal radius ($''$). (21) Blue optical radius (kpc, LEDA). (22) HI radius (kpc). (23) Terminal radius (kpc). (24) Rotation velocity at terminal radius (kms^{-1}). (25) Dynamical mass ($10^9 M_{\odot}$). (26) Ratio of HI mass and B-band luminosity ($M_{\odot} L_{\odot}^{-1}$). (27) Ratio of HI mass and I-band luminosity ($M_{\odot} L_{\odot}^{-1}$). (28) Ratio of dynamical mass and HI mass. (29) Ratio of dynamical mass and B-band luminosity ($M_{\odot} L_{\odot}^{-1}$). (30) Ratio of dynamical mass and I-band luminosity ($M_{\odot} L_{\odot}^{-1}$).

Inspecting trial dirty maps, frequency ranges were determined in which neither line emission nor frequency dependent interferences were found. A continuum subtraction was performed on the uv-data by fitting first order polynomials to each visibility record in the frequency domain of these frequency ranges. Averaging the fitted polynomials over the bandpass, a continuum visibility dataset was generated that was used in order to calibrate the complex gains by means of a self-calibration. A dirty continuum map with a size a few times larger than the primary beam with a corresponding dirty beam was generated by inverting the continuum visibilities applying a uniform weighting. Then, this map was cleaned applying the Clark clean algorithm, the stopping condition being determined by a threshold of the peak intensity in the residual map (the clean cutoff level). Inspecting the resulting clean image, a clean mask was determined by selecting an intensity level above which no emission was contained in residual sidelobes after the previous cleaning. Then, the dirty image was cleaned again with a lower intensity threshold for the residual, but the clean region restricted to the clean mask determined before. This procedure was repeated until convergence was reached, i.e., the quality of the image did not improve anymore. The clean-table was then used in order to generate a point source map. In the clean-table, all emission below a suitable threshold was masked out. The point source map was then used in order to correct the calibration table of the continuum visibilities via self-calibration. This whole procedure was repeated choosing successively lower values for the clean cutoff level (well below the 1-sigma level of the clean image), the threshold to determine the clean mask, and the threshold to determine point-source maps, until the image quality did not improve anymore. The self-calibration was applied either on the gain phases exclusively or, if necessary, in later steps on both, phase and amplitude.

After the self-calibration, the improved continuum gain table was copied from the continuum visibility dataset to the original visibilities. Then, again, a continuum subtraction was performed, choosing the best variant in-between subtracting the inversions of the point source maps from the visibilities and/or subtracting first or second order polynomial fits. Two datasets of different velocity resolution were extracted by one time binning the visibilities and the other time leaving out a binning and subsequent hanning smoothing.

Dirty maps were generated applying varying weighting schemes for the inversion, also employing a robust weighting. For the further work it turned out that two kinds of datacubes were most suitable, a cube generated applying a uniform weighting with the full velocity resolution (furtherly referred to as high-resolution cube), and a more sensitive cube with a robust weighting of 0.4 and binned once in the velocity regime (furtherly referred to as low-resolution cube) taking into account only baselines with a length less than $6.4\text{k}\lambda_{\text{HI}}$ ($\lambda_{\text{HI}} \approx 21.1\text{cm}$). The resulting maps were cleaned as described above, with the difference that the clean regions were determined not on a full-resolution datacube but on a smoothed

cube, the size for the Gaussian convolution kernel approximately amounting to double the size of the clean beam. Representative samples of resulting channel maps are shown in Figs. 4.8 and 4.8. Total intensity maps and first moment maps were generated by first masking the cubes with the finally applied clean masks. The resulting maps are shown in Fig. 4.1 and 4.10.

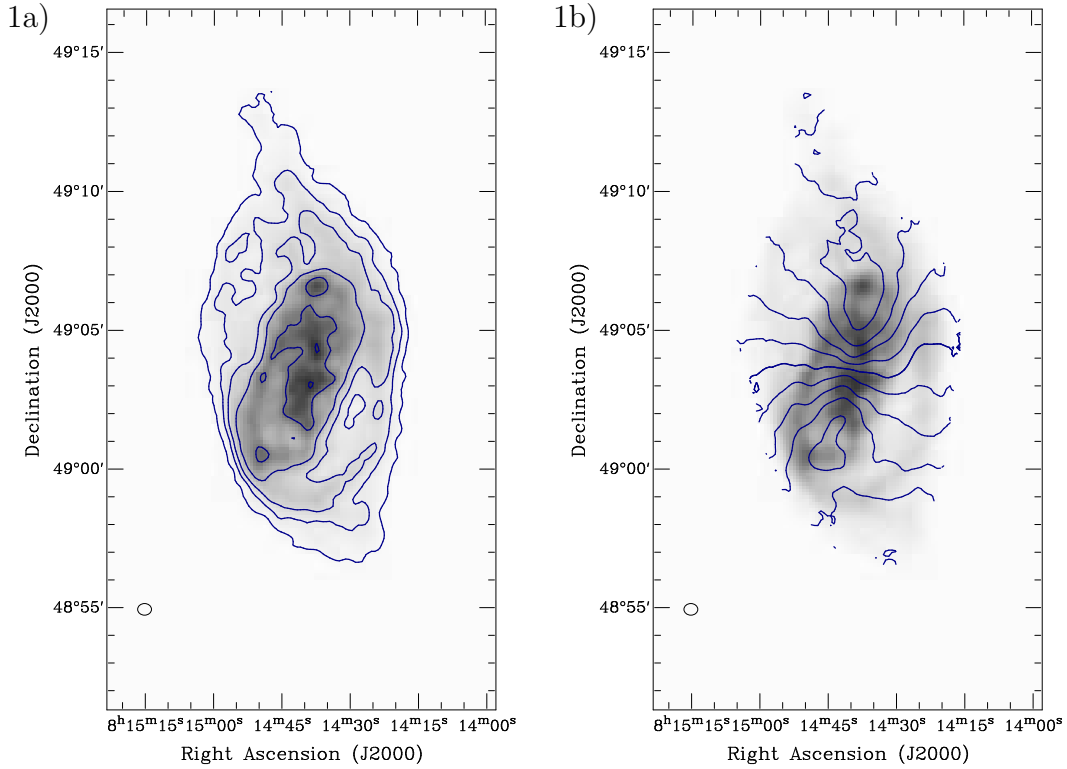


Fig. 4.1: Total intensity maps (a, left) and first moment velocity-fields (b, right) derived from the low-resolution datacubes overlaid on total intensity grey-scale maps. The ellipse in the lower left corner represents the clean beam. NGC 2541. The contours represent the $5, 20, 40, 80, 160, 240 \cdot 10^{19} \text{ atoms cm}^{-2}$ levels and the $v_{\text{sys}} \pm 0, 20, 40, 60, 80, 100 \text{ km s}^{-1}$ levels respectively (see Tab. 4.2). The approaching side is orientated towards NE.

For the calculation of the total HI flux as shown in Tab. 4.1, a primary beam correction was applied, while for the further work uncorrected maps were used in order to keep the noise distributed uniformly over the channel maps. The rms noise σ_{rms} for a cube was calculated by fitting half Gaussians to a histogram of the pixel values in the single channel maps and adopting a mean value of the widths of these Gaussians in the emission-free channels. For the total intensity maps a maximal noise $\sigma_{\text{rms,tot}}$ was calculated by multiplying σ_{rms} by $\sqrt{N} dv$, where N is an approximate number of channels in which galactic emission is detected and dv is the channel width. Because the total intensity maps are calculated in each pixel from a different number of channels, the noise per pixel is varying over the

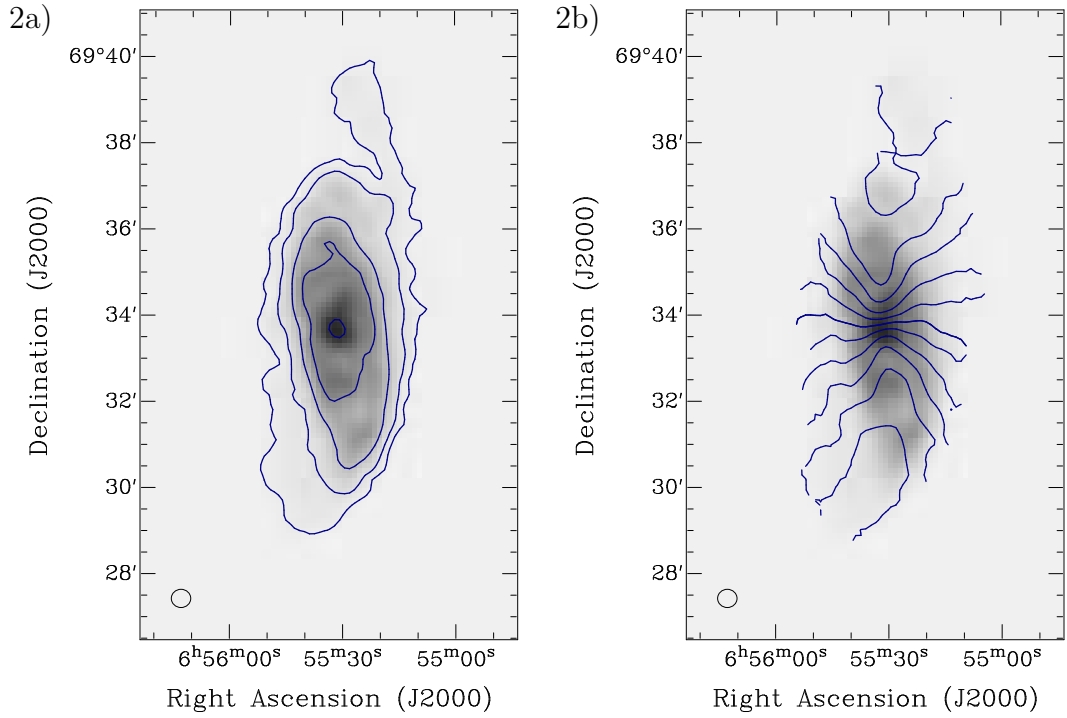


Fig. 4.1: (continued) UGC 3580. The contours represent the $6, 19, 57, 114, 228 \cdot 10^{19} \text{ atoms cm}^{-2}$ levels and the $v_{\text{sys}} \pm 0, 20, 40, 60, 80, 100 \text{ km s}^{-1}$ levels respectively (see Tab. 4.2). The approaching side is orientated towards SE.

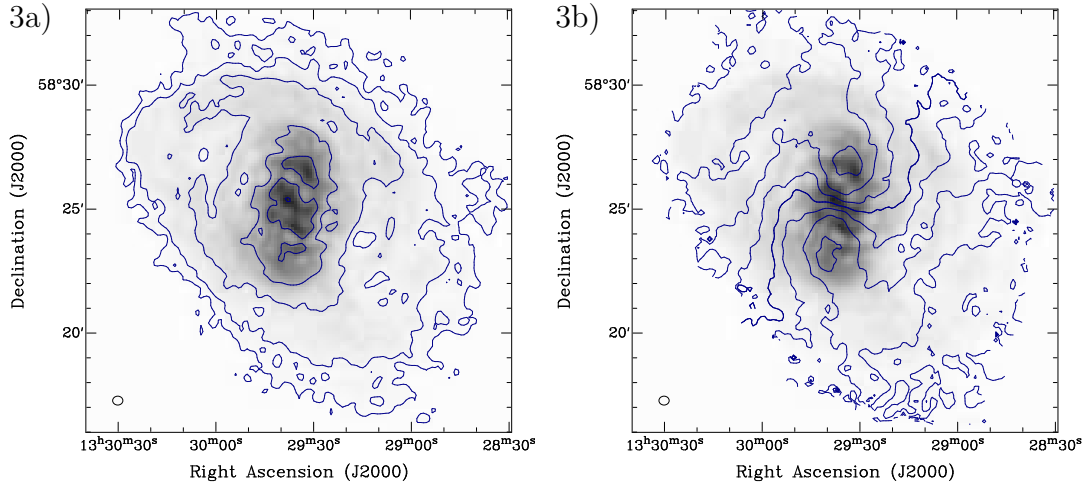


Fig. 4.1: (continued) NGC 5204. The contours represent the $2.5, 8, 25, 75, 145, 225 \cdot 10^{19} \text{ atoms cm}^{-2}$ levels and the $v_{\text{sys}} \pm 0, 15, 30, 45, 60 \text{ km s}^{-1}$ levels respectively (see Tab. 4.2). The approaching side is orientated towards NE.

maps but always lower than $\sigma_{\text{rms,tot}}$. Tab. 4.2 gives an overview.

Name (1)	NGC 2541		UGC 3580		NGC 5204	
Integration (2)	1 × 12		1 × 12		2 × 12	
Date (3)	4-5/01/03		1-2/01/03		24-27/04/03	
Resolution (4)	high	low	high	low	high	low
Weighting (5)	uniform	robust 0.4	uniform	robust 0.4	uniform	robust 0.4
dx (6)	4	7	4	7	4	7
dv (7)	2.06	4.12	2.06	4.12	2.06	4.12
HPBW _{maj} (8)	14.4	30.0	12.2	25.4	12.67	24.81
HPBW _{min} (9)	12.0	25.2	11.4	27.1	11.4	21.51
PA _{beam} (10)	3.1	4.4	−9.2	−11.5	−1.4	−19.6
σ_{rms} (11)	0.81	0.45	0.84	0.49	0.59	0.39
σ_{rms}^N (12)	2.14	0.54	2.74	0.65	1.86	0.65
$\sigma_{\text{rms}}^\sigma$ (13)	0.172	0.043	0.219	0.052	0.149	0.053
$\sigma_{\text{rms,tot}}$ (14)	0.022	0.018	0.022	0.020	0.014	0.0135
$\sigma_{\text{rms,tot}}^N$ (15)	14.4	2.56	17.3	3.17	10.8	2.78
$\sigma_{\text{rms,tot}}^\sigma$ (16)	1.15	0.205	1.39	0.254	0.864	0.223

Tab. 4.2: Summary of observations and data reduction. (1) Name of galaxy. (2) Total on-source integration time (h). (3) Observation dates (4) Type of datacube, for the high-resolution cube no binning in velocity direction was applied and use of the full array information was made, for the low-resolution cube the data were binned 2 channels into one in the velocity regime and only visibilities inside a radius of $6.4\text{k}\lambda_{\text{HI}}$ were used. (5) Applied weighting scheme. (6) Pixel size ($''$). (7) Channel width (km s^{-1}). (8) Half-power-beam-width along the beam major axis ($''$). (9) Half-power-beam-width along the beam minor axis ($''$). (10) Beam position angle ($^\circ$). (11) rms noise (mJy/beam) in the cubes. (12) rms noise per velocity resolution element ($10^{19}\text{ atoms cm}^{-2}$). (13) rms noise per velocity resolution element ($\text{M}_\odot\text{ pc}^{-2}$). (14) Maximal rms noise in the total intensity map (Jy/beam km s^{-1}). (15) Maximal rms noise in the total intensity map ($10^{19}\text{ atoms cm}^{-2}$). (16) Maximal rms noise in the total intensity map ($\text{M}_\odot\text{ pc}^{-2}$).

4.4 Tilted-ring modelling

The HI kinematics of the observed galaxies were parametrised by means of the tilted-ring model (Rogstad et al. 1974). A galactic disk is represented by a number of concentric and mutually inclined rotating rings, which are described by a set of parameters that (partially) are allowed to vary from ring to ring. These are usually the (common) central position and the systemic velocity, the rotation velocity, and two orientational parameters for each ring.

The publicly available programs to fit a tilted-ring model to observational data are somewhat restricted. The fastest method is to fit a model to the velocity-field (e.g. Begemann, 1987). It needs an intermediate step, the calculation of a velocity-field, in which each data point is representing the projected velocity of a

tracer material in an ideally flat disk. As discussed in detail in Teuben (2002) or in Chap. 3, this method introduces incalculable systematic errors via the so-called beam smearing or smoothing effect, which are severest for galaxies close to edge-on. Moreover, in cases where the line-of sight crosses the disk twice or more, methods that employ velocity-fields are bound to fail. An alternative is given by fitting synthetic observations to datacubes. For this purpose, however, until recently, only programs were available that perform this task in an automated way under the assumption of a flat disk (e.g. Irwin & Seaquist, 1991).

In order to study warped galaxies via a tilted-ring model it is advisable to employ a ring-fitting algorithm that calculates a model-datacube from the given set of parameters and optimises the model to fit to the original observation.

An automated routine “tirific” was developed that is able to perform this business. It was applied in order to analyse the three galaxies that are the subject of this chapter. A short repetition of the functionality of tirific shall be given here. The detailed description can be found in Chap. 3 or on the tirific home page (www.astro.uni-bonn.de/~gjozsa/tirific.html).

For a set of parameters, a model data cube is computed by Monte-Carlo integration and subsequent convolution with an artificial observing beam. The quality of such a model is determined by the comparison with the original data cube evaluating the quadratic sum of the difference between the original and modelled data cube χ^2 . In the fitting process the χ^2 is minimised by a cyclic optimisation of each single parameter in the model (a “golden-section” algorithm, see Chap. 3). While the method is expensive in terms of computing-time and thus does not (yet) allow the calculation of statistical errors, a few tests showed that the program reaches the regime of a well-defined minimum in parameter-space and can obtain very reliable models (see Chap. 3). Larger errors are expected to turn up in the very central regions, where the number of independent data points to fit to is small. The strongest source for disagreements between model and the measurement, however, is expected to be the (unavoidable) deviations of the galaxy morphology from the assumed symmetry inherent to the tilted-ring model.

The model parameters that describe a tirific tilted-ring model are

i) For each ring:

- The radius.
- The circular velocity.
- The scaleheight (for the specification of the vertical density distribution see below).
- The surface brightness.

- The inclination.
- The position angle defined as the angle between the N-axis and the minor axis of each ring from N over E.
- The Right Ascension of the central position.
- The Declination of the central positions.
- The systemic velocity.

ii) For all rings:

- A global isotropic velocity dispersion.
- The layer type for the vertical density distribution.
- The constant total flux of one point source, the cloud flux.

Initial guesses for the parametrisation of the examined galaxies were taken from literature (Sicotte & Carignan, 1997) or estimated from velocity fields. It turned out that, while tirific in the golden-section mode successfully reached local minima in the parameter space, in order to find reliable global minima, a few iterations with tirific were necessary under personal revision of the intermediate results.

For each galaxy, the low-resolution cube was analysed first, initially choosing a spacing of the ring radii of $30''$. For the analysis of the low-resolution cubes, the number of point sources varied between $1.7 \cdot 10^6$ and $4.0 \cdot 10^6$. The centre of the galaxy, the global velocity dispersion, and the scaleheight were kept as free parameters but were not allowed to vary independently from ring to ring (in case of the velocity dispersion, the user has no other chance). The symmetry of the examined galaxies allowed for this restriction in order to lower the number of free parameters. For each ring, the surface brightness, the orientational parameters, and the rotation velocity was varied independently. Typical stopping conditions were chosen such that after a reasonable number of iterations, in the range of 5000-10000 model calculations, tirific found local minima. With that, a possible change in the best-fit parameters can be supposed to be about a factor 10-100 lower than the errors that were finally assigned to the data points. E.g., the stopping condition in order to find the minimum in the rotation velocity of a single ring was chosen such that if a change of $0.1 - 0.2 \text{ km s}^{-1}$ was necessary in order to optimise the χ^2 , a further iteration process of all parameters was enforced. Finally, a minimum error of $4 - 8 \text{ km s}^{-1}$ was assigned to the rotation velocities as a sensible estimate, thus a possible change of the best-fit results lies well in-between these error bars. Throughout, the numerical noise was taken into account in the χ^2 evaluation (a noise weighting of 1, see Chap. 3).

Typically for the first iterations, a few parameter groups showed outliers from a global trend of variation with radius, meaning that *tirific* found a local minimum that probably was not a representation of a global minimum in the χ^2 landscape. Therefore, the whole fitting process was frequently started again with adjusting the outlying parameters and changing the spacing of the ring radii in order to reach a robust fit. After five to ten such iterations of parameter adjustment and fitting, a stable solution was found to be present. Any outlier from a global trend became an outlier again after adjusting that parameter and fitting again. Such persistent outlying data points, best visible in the rotation curve of NGC 2541 in the intermediate range of radii were finally accepted as a real feature in the parametrisation. Large jumps in a parameter describing a smooth disk that don't fit into a global trend, cannot be due to a sudden change of the potential. In such cases, it has to be concluded that the tilted-ring model is not a good representation of the galaxy kinematics in the regions where such toggles show up. The reasons for such deviations to turn up may be sought in the presence of spiral arms or other features causing a deviation from the assumed orbital symmetry. Fortunately, while obviously not a good representation for singular data points at single regions in the galaxies, it turns out that globally, the tilted-ring model works extremely well in order to parametrise the kinematics and the surface brightness profile of the galaxies. As however suspected, the dominant contribution to the errors is given by the local deviations of the galaxy morphology and kinematics from the assumed symmetry. The tilted-ring model is a good but not a perfect description, a reason why some trials to achieve results and error bars with the Metropolis fitting method implemented in *tirific* were not successful. A χ^2 calculated by *tirific* is strongly influenced by the local deviations of the surface brightness from azimuthal symmetry. Hence, while the model delivers a very good estimation for the azimuthal mean of the surface brightness and reliable orientational parameters as shown below, a probability for a model is not easily estimated taking the standard χ^2 as the standard measure

$$dP = \exp\left(-\frac{\chi^2}{2}\right) \quad . \quad (4.1)$$

This would assume that a perfect parameter combination representing the true state of the galaxy existed. Lacking the possibility of a robust error estimation, error bars are frequently assigned by bootstrapping, a method not applicable with *tirific* in the current form. A suitable amount of fit results useful for a statistics would cost a too large amount of computing time, given the fact that on a normal Personal Computer one optimisation process within which about 10000 models are calculated takes (only) one day and one night. For the estimation of errors, which are more due to the deviation of the galaxies kinematics and morphology from the ideal symmetry, than to the statistical noise in the datacubes, a traditional, crude method was applied by comparing fits to different sides of the galaxy. For each galaxy, a model was calculated from the best-fitting

parameters derived in the previously described analysis. For this model, only point-sources were calculated that belong to the receding or approaching part of the galaxy, i.e., that have an azimuth in-between $-\frac{\pi}{2}$ and $\frac{\pi}{2}$ or $\frac{\pi}{2}$ and $\frac{3\pi}{2}$ respectively. The model was subtracted from the original datacube and a fitting process was started again, keeping the central position and the systemic velocity fixed, producing only point-sources of the opposite side. This way, two best-fit models were produced, one for the receding side of the galaxy, one for the approaching side. Preliminary error bars were calculated as the maximal deviation of the data points from the fits to the approaching and the receding side from the previous fit results achieved taking into account the full extent of the galaxy. The errors of the central position and the systemic velocity of the galaxy had to be estimated without a cross-check but these global values proved to be very robust from fit to fit and changes were well inside the observational beam and the velocity resolution respectively, less than $4''$ or 1 km s^{-1} . The errors that may be adopted here, can be estimated to be less than $12''$ for the position of the kinematical centre and less than 2 km s^{-1} for the systemic velocity. The “error bars” derived in this way have a weak statistical meaning but they give a halfway objective measure for the reliability of the data points. In a few cases, where error bars calculated this way were obviously too large or too small, the data were visually inspected and errors were estimated by varying the parameter in question and comparing resulting artificial datacubes with the original datacube until a significantly worse model than the best-fit model was produced. Fig. 4.4 shows the fit results and illustrates the error bar estimation for the low-resolution datacubes.

Interestingly, in all cases, the models show a central tilt of the disk in the innermost few tens of arcseconds. It is hard to decide whether this is due to the fact that *tirific* fails a good performance for these (few) data points (see also Chap. 3), if it reflects a real tilt, or if the model is misguidedly confusing non-circular motion with a change in the orientational parameters. Therefore, for each galaxy, another type of model was fitted to the datacubes assuming a flat disk in the the inner part of the galaxy. The disk was forced to retain equal but variable orientational parameters inside a radius outside of which the outer warp starts, i.e. well inside the radius where the orientational parameters start to change substantially. Then, comparing the original datacubes with the artificial datacubes from the models with an inner flat disk and with a radius-dependent orientation of the inner disk, it was decided whether to accept a model with an inclined inner disk. Where in doubt whether a tilt of the inner disk was necessary in order to reproduce the original spectra, a model with an inner flat disk was preferred. 4.11 shows comparisons of models calculated with an inner flat disk and without an inner flat disk by means of position-velocity diagrams along the kinematical major axes.

Except for the case of NGC 2541, the data were found to be consistent with an inner flat disk, while for NGC 2541 the spectra were slightly better represented

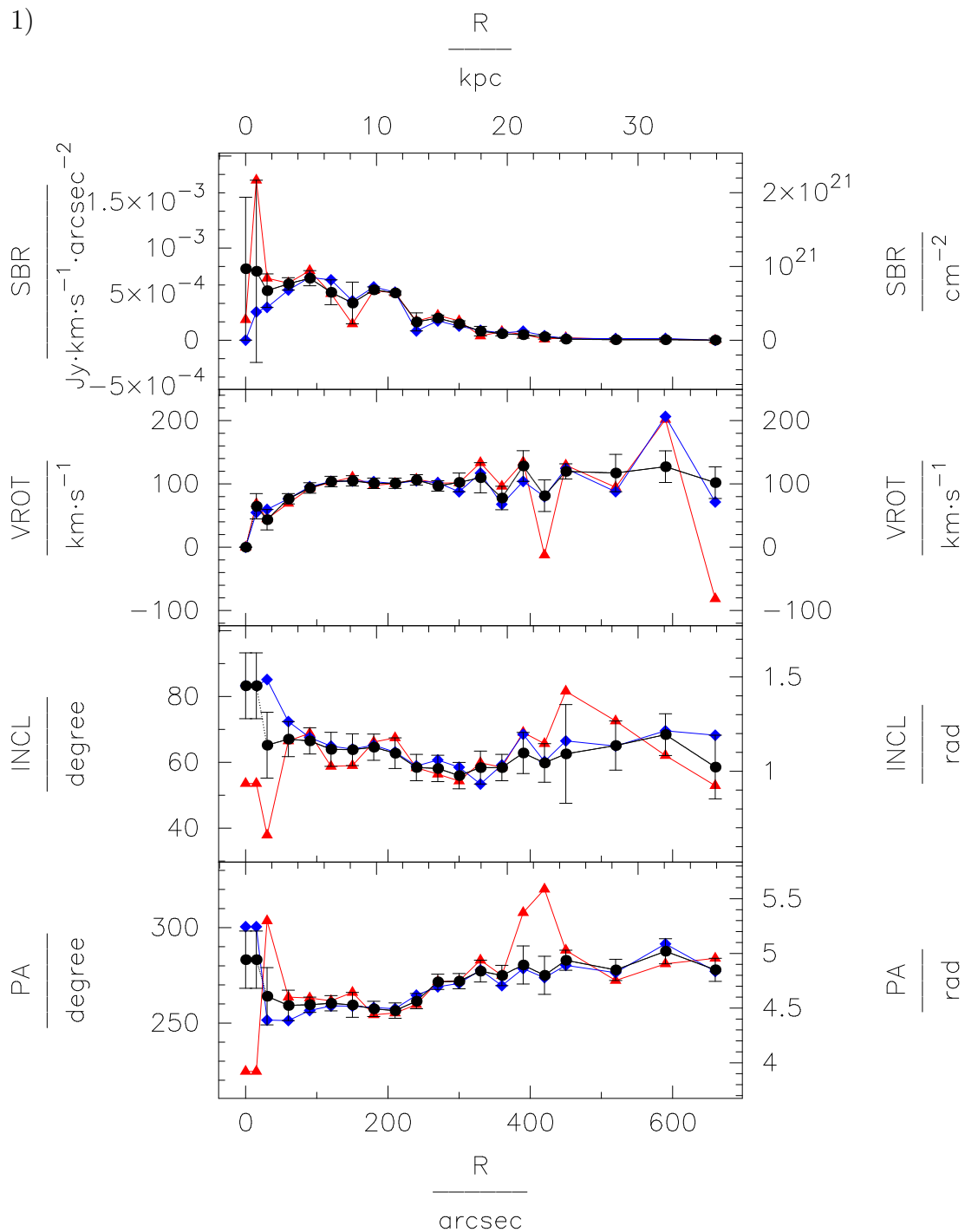


Fig. 4.2: Determination of the orientational parameters, the surface brightness for the outer disk, the rotation velocity for the outer disk, and error bars. SBR: surface brightness. VROT: rotation velocity. INCL: inclination. PA: position angle. R: radius. The black curves (dots) show the best-fit taking into account both sides of the galaxies. The red curves (triangles) show the results when fitting only the receding side, the blue curves (diamonds) show the results for the approaching side. Preliminary error bars were estimated as the maximum deviation of the both-sides fit from the single-sided fits. For extraordinarily high or low values the error bars were re-determined by visual inspection of the datacubes and comparison with a series of model datacubes. NGC 2541.

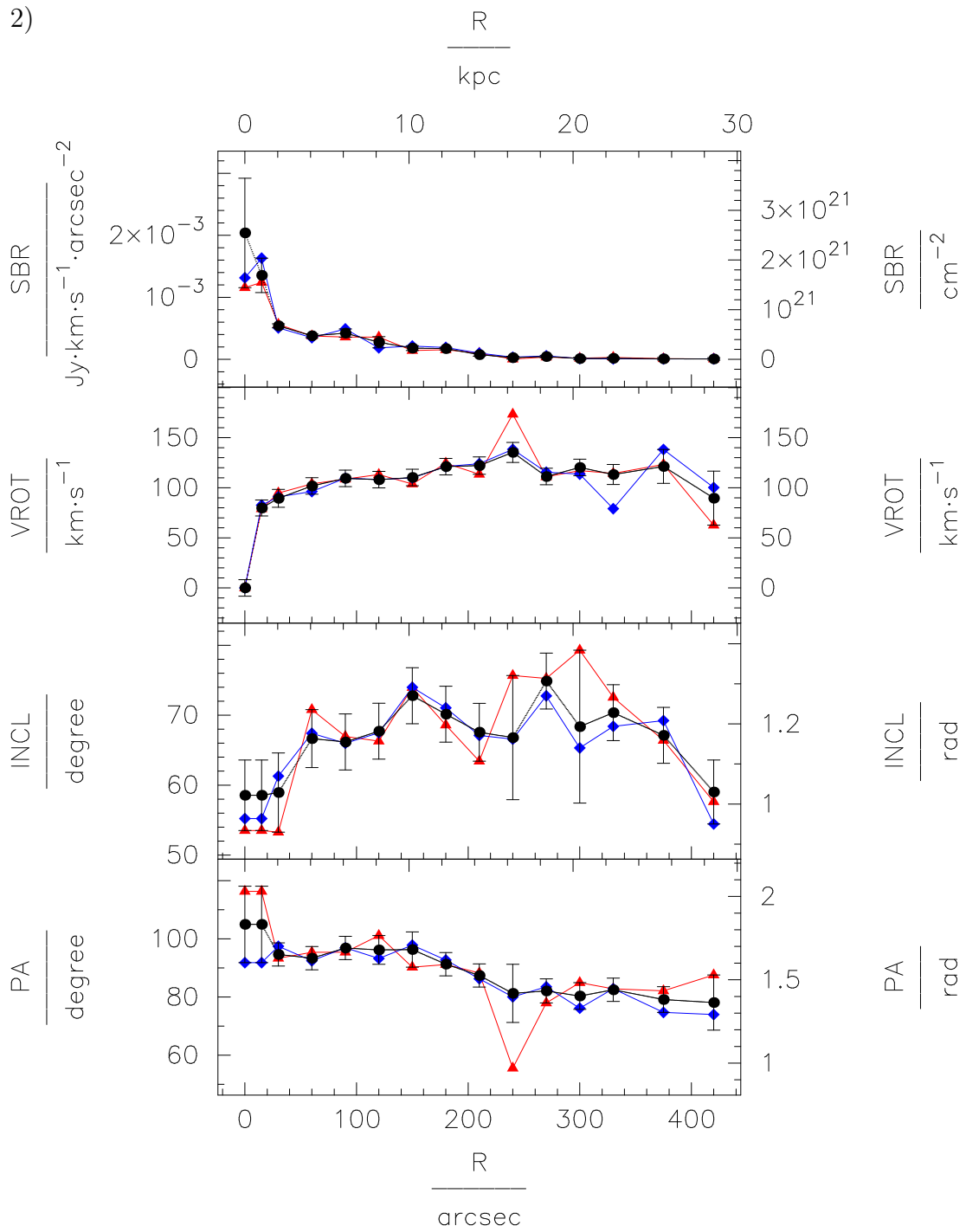


Fig. 4.2: (continued) UGC 3580.

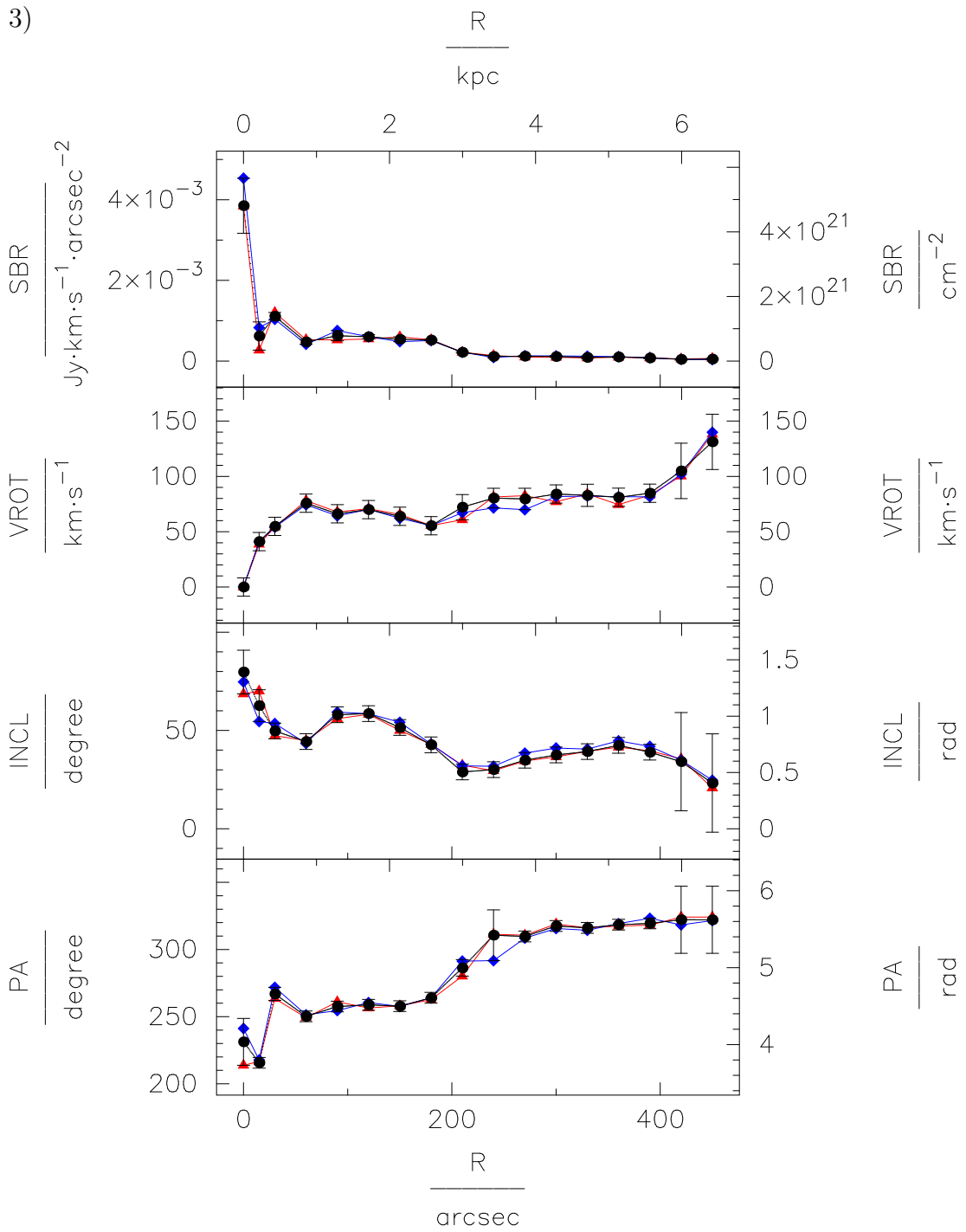


Fig. 4.2: (continued) NGC 5204.

allowing for an inner change of the disk orientation. For this galaxy, which is supposed to contain a bar (but see Coccato et al., 2004), the innermost four data points have to be treated with care, as is more or less the case for all galaxies. *Tirific* simply does not fit to enough independent data points in order to be able to figure out the orientational parameters plus surface brightness and rotation velocity. This is reflected in the larger error bars manually assigned to the parameters. The finally adopted error bars of the orientational parameters for UGC 3580 and NGC 5204 in the region of the flat inner disk are the difference between the original fit results without enforcing a flat inner disk and the best-fit results with enforcement of a flat inner disk, while for NGC 2541 the previously determined error bars were adopted.

In order to refine the spatial resolution of the rotation curve and the surface brightness profile, the high-resolution datacubes were used. Up to an optimally chosen maximal radius, the spacing of the ring radii was refined to a value of $12''$ interpolating the fit results from the previous run and the HI datacube was fitted again following the same procedure as described above, keeping but the orientational parameters fixed. The number of point sources was raised to a value in-between $5.0 \cdot 10^6$ and $1.4 \cdot 10^7$. The final results for the parametrisations are shown in Fig. 4.4. Fig. 4.8 illustrates the way, in which the high resolution data were taken into account: Error bars in the orientational parameters were adopted by interpolation from the low-resolution data, while the error bars in the surface brightness profile and the rotation velocity were again derived by fitting to the receding and approaching halves of the galaxy. Fig. 4.8 shows the good agreement of the derived surface brightnesses and the rotation velocities fitting to the low-resolution- and the high-resolution data respectively. This implies a good agreement of the high-resolution datacube and the low-resolution datacube with respect to the detection of smooth components in the HI distribution. In the central disk the bulk of the detected gas is clumpy enough or shows a large enough gradient in the surface brightness to be detected for both datacubes.

Several ways to check the quality of the finally resulting fits are possible and have been exhausted. Fig. 4.8 shows contour-plots overlaying the low-resolution datacubes with the synthetic datacubes. Fig. 4.4 shows overlays of corresponding moment maps of the original data and the synthetic ones, Fig. 4.5 shows position-velocity diagrams along the kinematical major and minor axes. Remarkably, with *tirific* it is possible to trace the HI disks further than they are seen in the moment maps. Those are usually based on a masked cube on which a certain threshold in the intensity levels (of smoothed channel maps) determines whether the emission belongs to a galaxy or whether one sees only noise. Without difficulty *tirific* is run on an unmasked datacube and emission is detected where the human eye is not able to distinguish it from noise. The reason for that lies in the azimuthal averaging *tirific* uses to produce a model datacube and to finally fit it to the observation. In principle, under the assumption that the HI is distributed

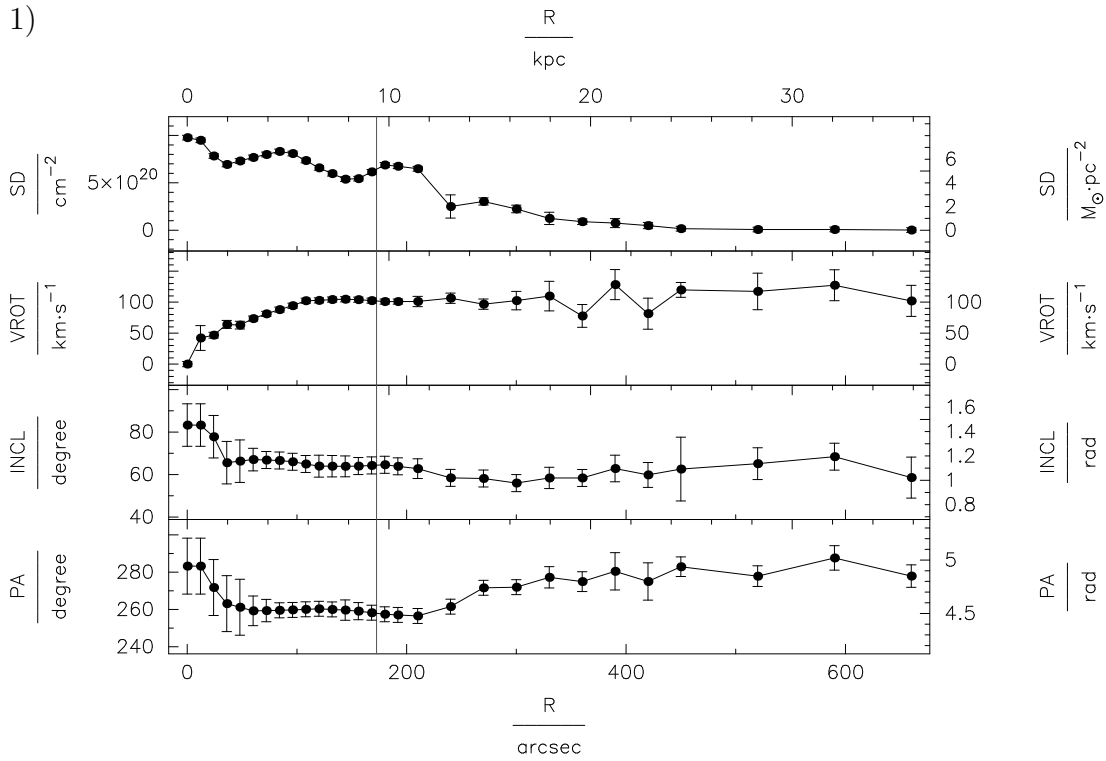


Fig. 4.3: Final parametrisations of the galaxies. *SBR*: surface brightness. *VROT*: rotation velocity. *INCL*: inclination. *PA*: position angle. *R*: radius. The vertical line denotes the optical radius r_{25} . NGC 2541.

smoothly in the outer regions, this drastically enhances the sensitivity of the fit. Data points at large radii, however, are more uncertain as the tracer material becomes less and less abundant.

All comparisons show an extremely good agreement of measurement and model up to largest radii until the HI distribution in the galaxies becomes (at last) distinctly asymmetric. Hence, one can conclude that the tilted-ring model is able to reproduce both, the kinematics and the azimuthally averaged surface brightness profile of the HI components of the galaxies. Tab. 4.4 shows the finally adopted global parameters of the models. In all fitting processes, the scaleheight with an assumed $sech^2$ -law and the dispersion were kept as free parameters. The uncertainties of these quantities may be estimated from the differences in the low-resolution fits and the high-resolution fits. The resulting values for both parameters lie in an acceptable range. As both values were fitted as global parameters, their values are not very meaningful in terms of a physical interpretation. It is however remarkable that systematically the velocity dispersion found for the high-resolution data is higher than that found for the low-resolution data and

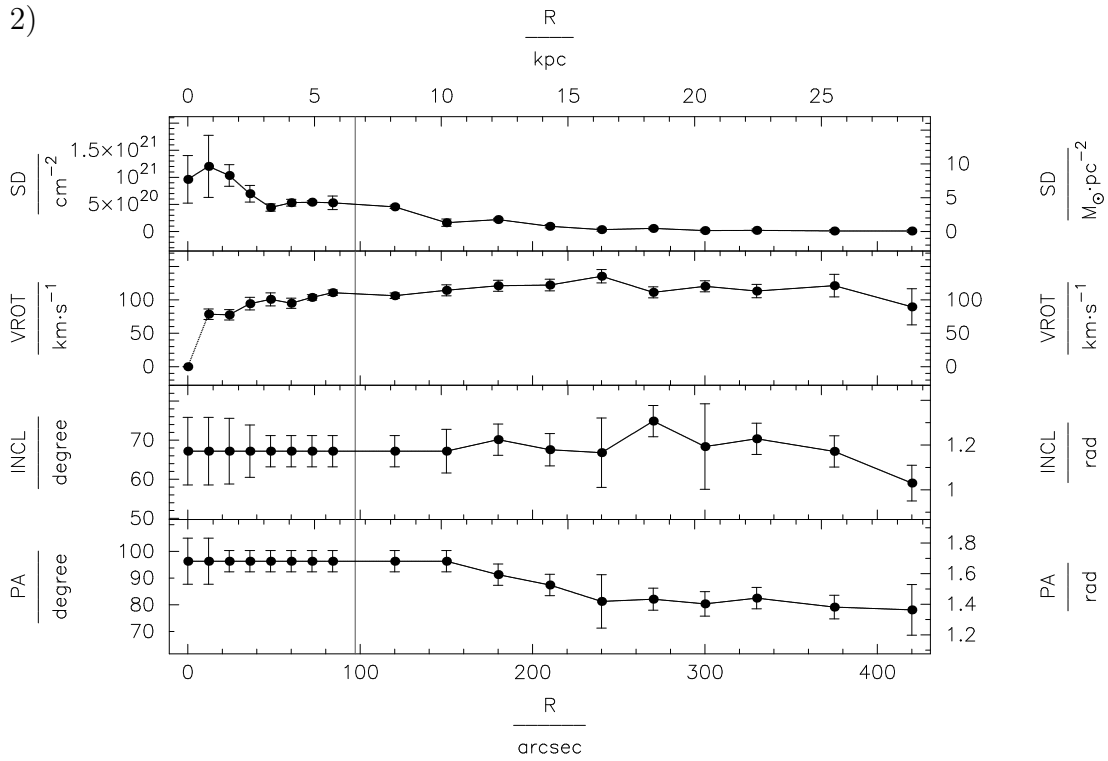


Fig. 4.3: (continued) UGC 3580.

that the scaleheight is systematically lower when fitting to the high-resolution data than that found when fitting to the low-resolution data. A straightforward simple explanation lies in the weighting applied to achieve both datacubes. For the high-resolution data, the detected HI is more confined to the disk as the fitted scaleheight is lower. This points to the fact that in the low-resolution datacubes, a smoother component is detectable that is not as confined to the disk. Remarkably, a close look at the Figs. 4.5 shows that at the lowest contour levels all sample galaxies possess an excess in the width of the velocity profiles in the central regions, mostly evident for NGC 5204. While these excesses, known as “beards” are symmetric and hence their presence does not alter the statement with respect to the quality of the fits, it is evident that a single-disk model is not able to completely describe the gas-distribution at the lowest level. Seemingly, a gas component is present in the sample galaxies that belongs to a thickened disk or a halo of neutral gas that rotates at a lower rotation speed than the central disk. Such features have been detected and analysed in other galaxies (e.g. Fraternali et al., 2004). Hence, it is not surprising that the scaleheight in the low-resolution fits is higher, as partly the halo gas, detected with a higher sensitivity in the low-resolution cubes, alters the results of the fits with respect to the scaleheight.

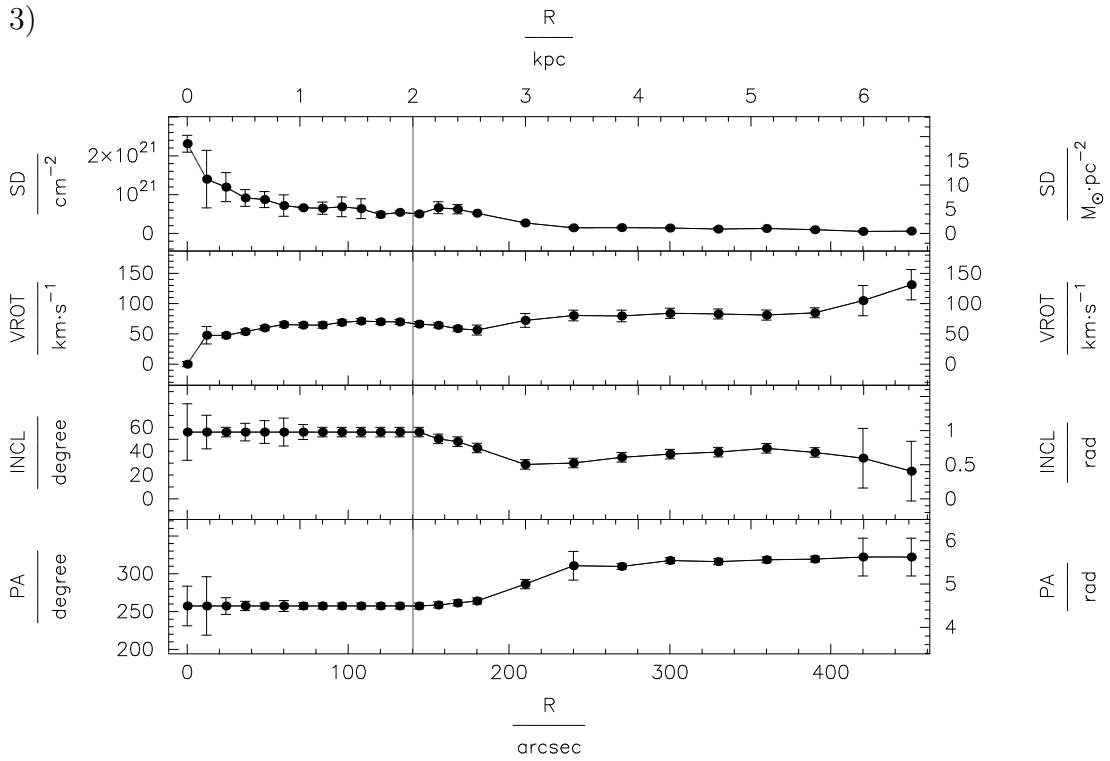


Fig. 4.3: (continued) NGC 5204.

The issue of the “beards” that are present in all of the three sample galaxies will be followed up elsewhere. At the same time the fitted velocity dispersion is higher for the high-resolution datacube. This can be explained by the fact that the fitted velocity dispersion is determined mostly by local deviations in the disk from the assumed symmetry. It fits into this picture that NGC 2541, which is the galaxy with the most pronounced spiral arms in the small sample shows the most obvious deviations in the velocity dispersion comparing high-resolution- and low-resolution fits, and at the same time the highest uncertainties in the parametrisation of the radially dependent parameters.

Tab. 4.8 shows the radially dependent best-fit parameters and additionally, for a simplified further use, the normal vectors of the rings as derived quantities.

In order to estimate some of the global parameters shown in Tab. 4.1, an estimation of the distance of the galaxies was necessary. In the case of NGC 2541, the cepheid distance given in Freedman et al. (2001) was adopted. For the two remaining galaxies, having HI data at hand together with I-band magnitudes from the literature, the Tully-Fisher relation as described in Sakai et al. (2000) was

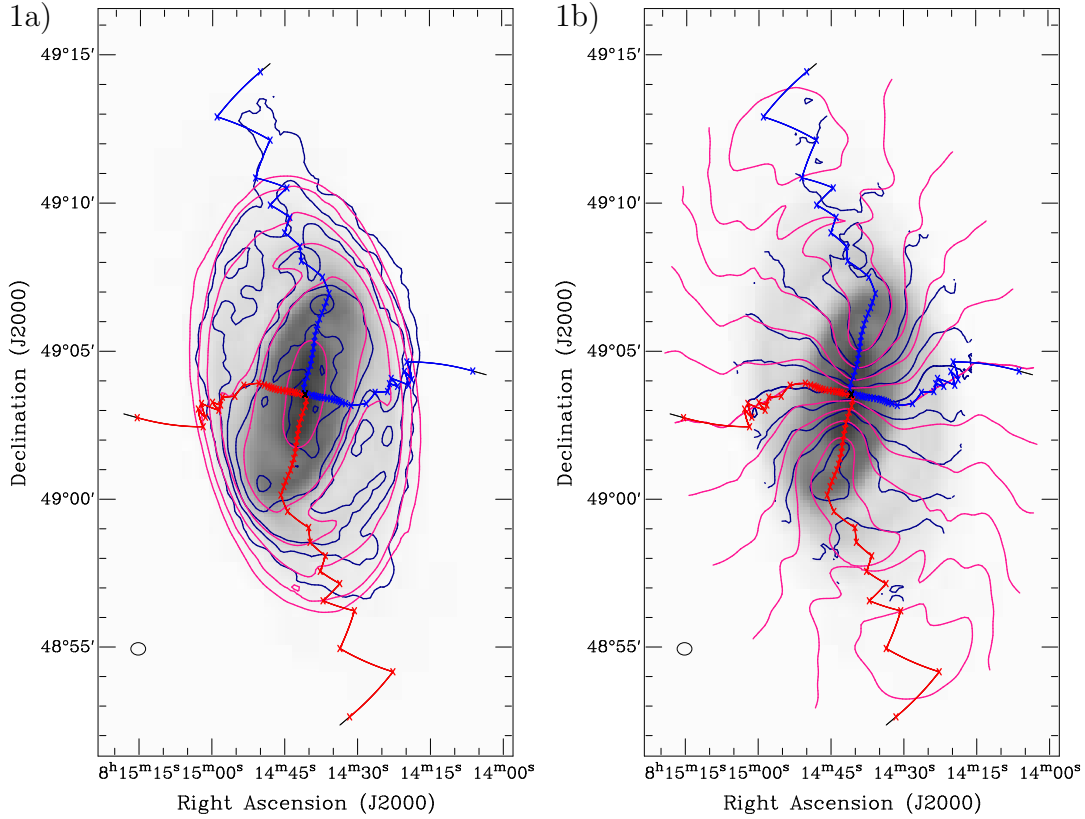


Fig. 4.4: Total intensity contour plots (a, left) and first moment velocity-fields (b, right) derived from the low-resolution datacubes, blue original, pink model, overlaid on total intensity grey-scale maps derived from the model datacubes. The over-plotted lines represent the kinematical major and minor axes. The red kinematical major axis lies in the receding part of the galaxy, the blue kinematical major axis in the approaching part. NGC 2541. The contours represent the $5, 20, 40, 80, 160, 240 \cdot 10^{19} \text{ atoms cm}^{-2}$ levels and the $v_{\text{sys}} \pm 0, 20, 40, 60, 80, 100 \text{ km s}^{-1}$ levels respectively (see Tab. 4.2).

applied. In order to estimate the line-width of the integrated spectrum at the 50- and 20 percent peak level used in this relation, the spectra were not taken from the original data but from model datacubes generated with the best-fit values for the surface brightness profile and the rotation curve, in which the galaxies were but artificially flattened by changing the inclination to a value of 90° and the position angle to 0° . This way, an observation of an ideally flat galaxy is faked, making a further correction for the inclination unnecessary and at the same time taking away the uncertainties inherent to a systematic change of the inclination within the galaxy. The apparent I-band magnitudes of the galaxies were taken from the LEDA database, corrected for internal extinction following Sakai et al. (2000) and Galactic extinction. A (marginal) k-correction was applied in order to finally derive the corrected apparent I-band magnitudes of the galaxies. With

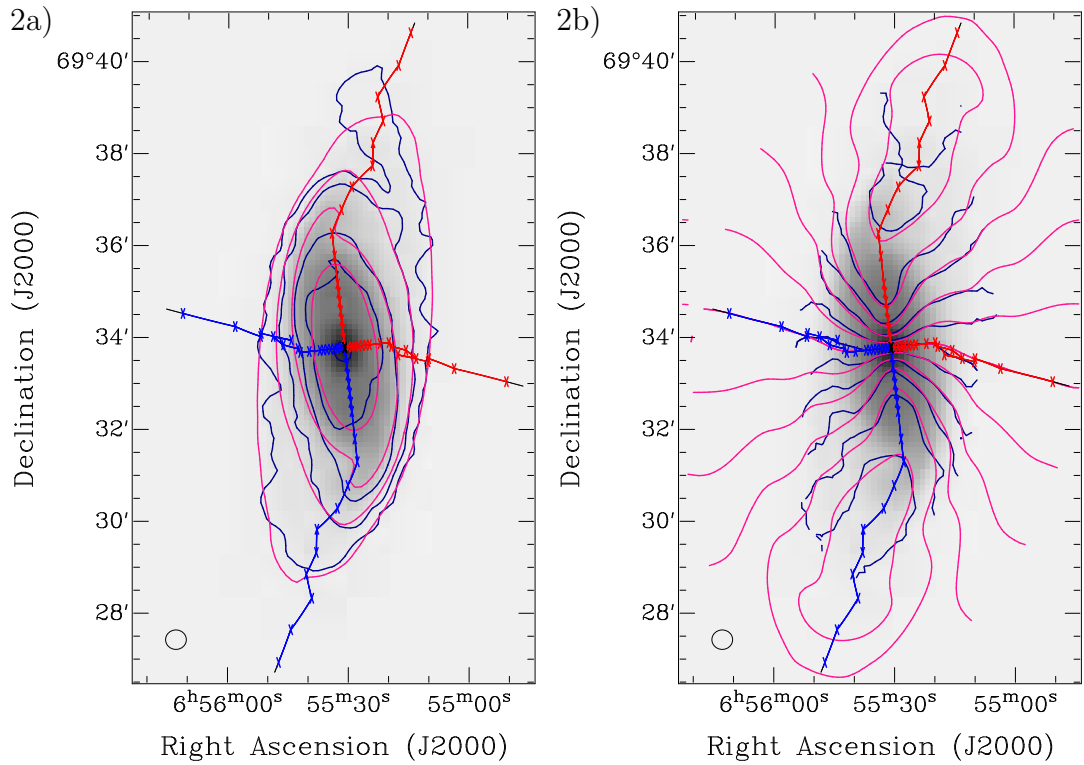


Fig. 4.4: (continued) UGC 3580. The contours represent the 6, 19, 57, 114, 228 $\cdot 10^{19} \text{ atoms cm}^{-2}$ levels and the $v_{\text{sys}} \pm 0, 20, 40, 60, 80, 100 \text{ km s}^{-1}$ levels respectively (see Tab. 4.2).

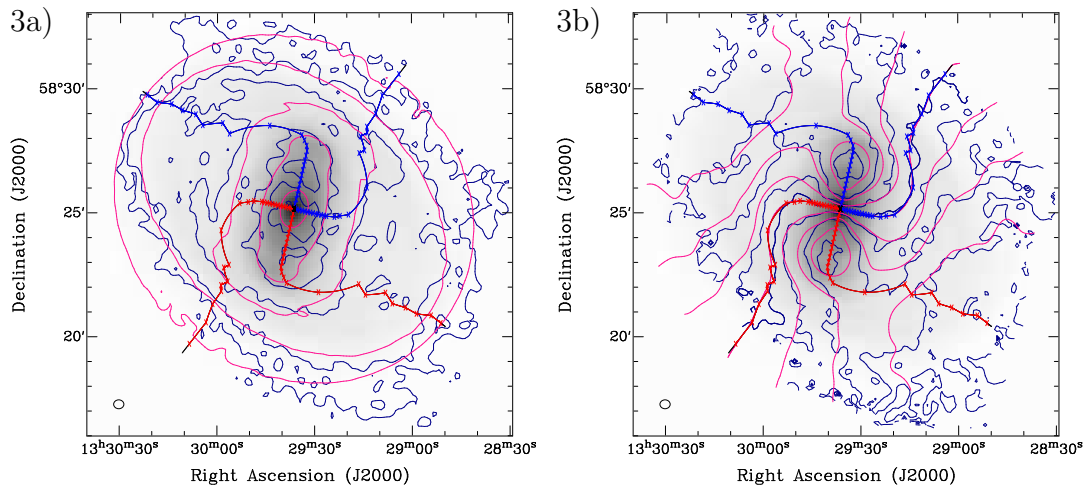


Fig. 4.4: (continued) NGC 5204. The contours represent the 2.5, 8, 25, 75, 145, 225 $\cdot 10^{19} \text{ atoms cm}^{-2}$ levels and the $v_{\text{sys}} \pm 0, 15, 30, 45, 60 \text{ km s}^{-1}$ levels respectively (see Tab. 4.2).

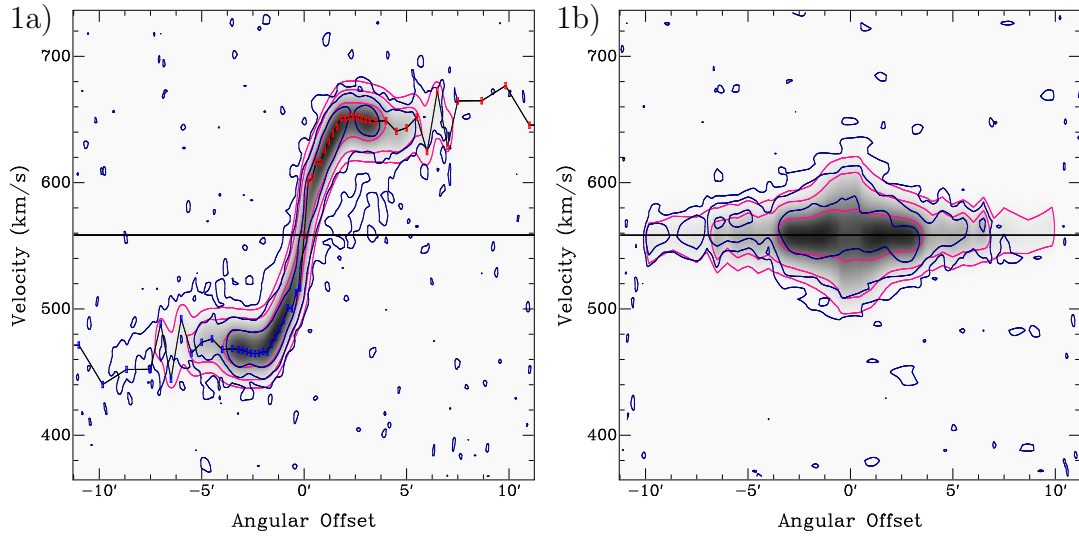


Fig. 4.5: a) *PV*-diagrams along the kinematical major axis comparing the final best-fit models (pink contours) with the original low-resolution data (blue contours). The vertical line marks the systemic velocity, the boxes connected with the lines denote the rotation curve corrected for the inclination. b) *PV*-diagrams along the kinematical minor axis comparing the final models (pink contours) with the original low-resolution data (blue contours). Contour levels are 1, 4, 16 mJy/beam. NGC 2541.

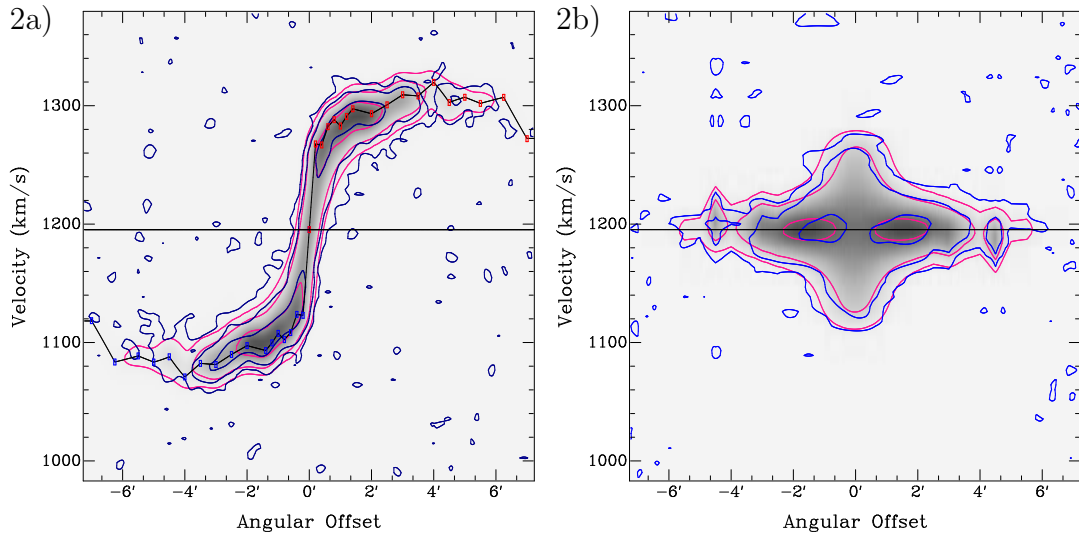


Fig. 4.5: (continued) UGC 3580. Contour levels are 1, 4, 16 mJy/beam

the absolute magnitudes derived from the integrated spectra of the galaxies using the Tully-Fisher relation by Sakai et al. (2000), the distance moduli μ and with

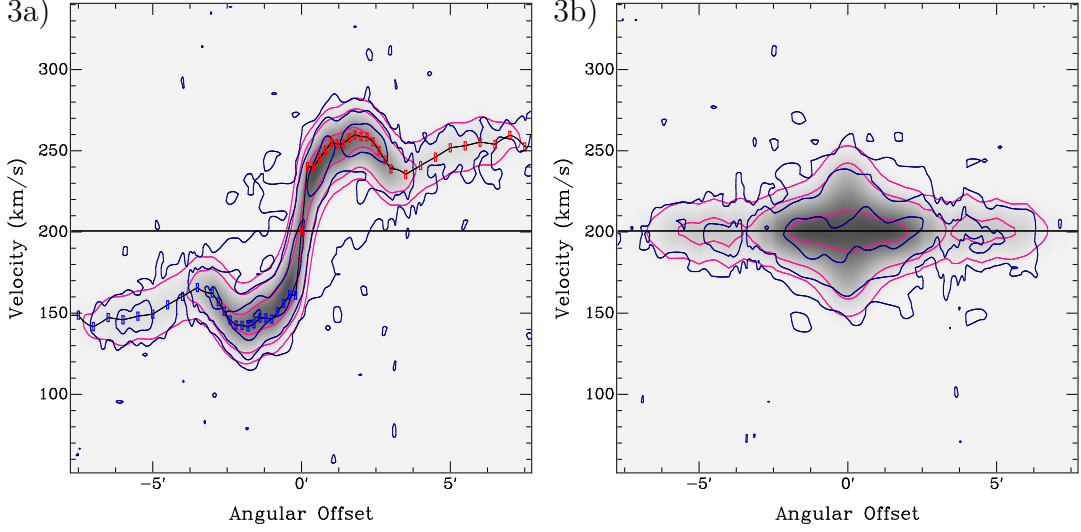


Fig. 4.5: (continued) NGC 5204. Contour levels are 1, 4, 16, 32 mJy/beam

Name (1)	NGC 2541		UGC 3580		NGC 5204	
RA (2)	08 ^h 14 ^m 40 ^s .83		06 ^h 55 ^m 30 ^s .89		13 ^h 29 ^m 36 ^s .30	
DEC (3)	+49°03'33".6		+69°33'47".4		+58°25'10".8	
RA* (4)	08 ^h 14 ^m 40 ^s .07		06 ^h 55 ^m 30 ^s .86		13 ^h 29 ^m 36 ^s .51	
DEC* (5)	+49°03'41".2		+69°33'47".0		+58°25'07".4	
v_{sys} (6)	559.5		1200.1		200.8	
Resolution (7)	high	low	high	low	high	low
$v_{\text{disp,tot}}$ (8)	13.4	11.4	9.6	9.4	9.4	9.7
$v_{\text{disp,int}}$ (9)	13.3	10.8	9.4	8.7	9.2	9.0
z_0 (10)	11.5	12.1	7.4	9.7	15.5	20.6
z_0^{pc} (11)	628	656	506	658	222	294

Tab. 4.3: Global best-fit tilted-ring parameters for the examined galaxies. (1) Name of galaxy. (2) Right Ascension (J2000), fitting results. (3) Declination (J2000), fitting results. (4) Right Ascension (J2000) from NED. (5) Right Ascension (J2000) from NED. (6) Heliocentric optical systemic velocity (kms^{-1}). (7) Type of datacube used for analysis, high-resolution or low-resolution. (8) Dispersion (kms^{-1}). (9) Internal dispersion, instrumental dispersion subtracted (kms^{-1}). (10) Global scaleheight ($''$) (11) Global scaleheight (pc)

these the distances were derived. A comparison for NGC 2541 of the Tully-Fisher distance of $(10.2 \pm 1.7) \text{Mpc}$ with the cepheid distance of $(11.22 \pm 0.8) \text{Mpc}$ as derived by (Freedman et al., 2001) shows that this method works well. The adopted distances made a determination of the physical scales of the galaxies possible and with that an estimation of the dynamical masses, the HI masses, and the luminosities of the galaxies. In order to determine a lower limit to the dynamical masses of the galaxies, a terminal radius R_t (in physical units) was determined as

the second-last radius of the best-fit models and the dynamical mass

$$M_{\text{dyn}} = \frac{R_{\text{t}} v_{\text{t}}^2}{G} \quad . \quad (4.2)$$

inside that radius was calculated with the best-fit rotation velocity v_{t} at that radius and the gravitational constant G . The absolute (corrected) magnitudes and the luminosities

$$L_{\text{I,B}} = 10^{0.4(M_{\odot\text{I,B}} - M_{\text{galI,B}})} \quad , \quad (4.3)$$

where $M_{\text{galI,B}}$ denotes the absolute extinction- and k-corrected magnitudes in the I- and the B-band were calculated. For this the adopted distance moduli and the corrected I-band magnitudes also used for the distance estimation were used, while the corrected B-band magnitudes from LEDA were adopted. The adopted absolute magnitudes of the sun which determine the scale for the luminosities were $M_{\odot}^{\text{B}} = 5^{\text{m}48}$ in the B-band and $M_{\odot}^{\text{I}} = 4^{\text{m}08}$ in the I-band respectively (cf. Binney & Merrifield, 1998). The HI-mass M_{HI} was calculated with

$$\frac{M_{\text{HI}}}{M_{\odot}} = 2.36 \cdot 10^5 \left(\frac{D}{\text{Mpc}} \right)^2 \frac{F_{\text{HI}}}{\text{Jy km s}^{-1}} \quad , \quad (4.4)$$

where D is the adopted distance and F_{HI} the total HI flux of the galaxies, under the assumption that the galaxies are optically thin in the HI component.

4.5 Global features in the tilted-ring models

The tilted-ring models shown in a pure but prosaic form in Fig. 4.4 can be visualised in different ways, shown in the Figs. 4.6. These shall be used in order to present the major results of this study. Basically, all rules for the behaviour of warps formulated by Briggs (1990) are followed by the three galaxies within the given error bars. The disks stay flat out to approximately r_{25} , and starts to show the warp at somewhat larger radii. The Figs. 4.6 a)-c) show the tip-LON plots introduced by Briggs (1990) in order to develop his rules. They show the projection of the normal vector of each ring onto a plane. In order to be somewhat complete, in the Figs. 4.6a) this plane is chosen to be the celestial plane. These plots are a bijective visualisation of the orientational parameters shown Fig. 4.4. Briggs first, second, and third rule can be checked upon inspecting tip-LON plots in which the reference plane is chosen to be the central (flat) plane of the galaxies as shown in the Figs. 4.6 b). According to the first rule, the so-called line of the nodes should stay straight for a few data points in the region of the commencement of the warps, in other words the tips of the normal vectors should lie on one straight line that goes through the origin of the plots. While this is barely visible in the case of UGC 3580, which but has the warp with the smallest amplitude in the sample, this feature is apparent for the two galaxies

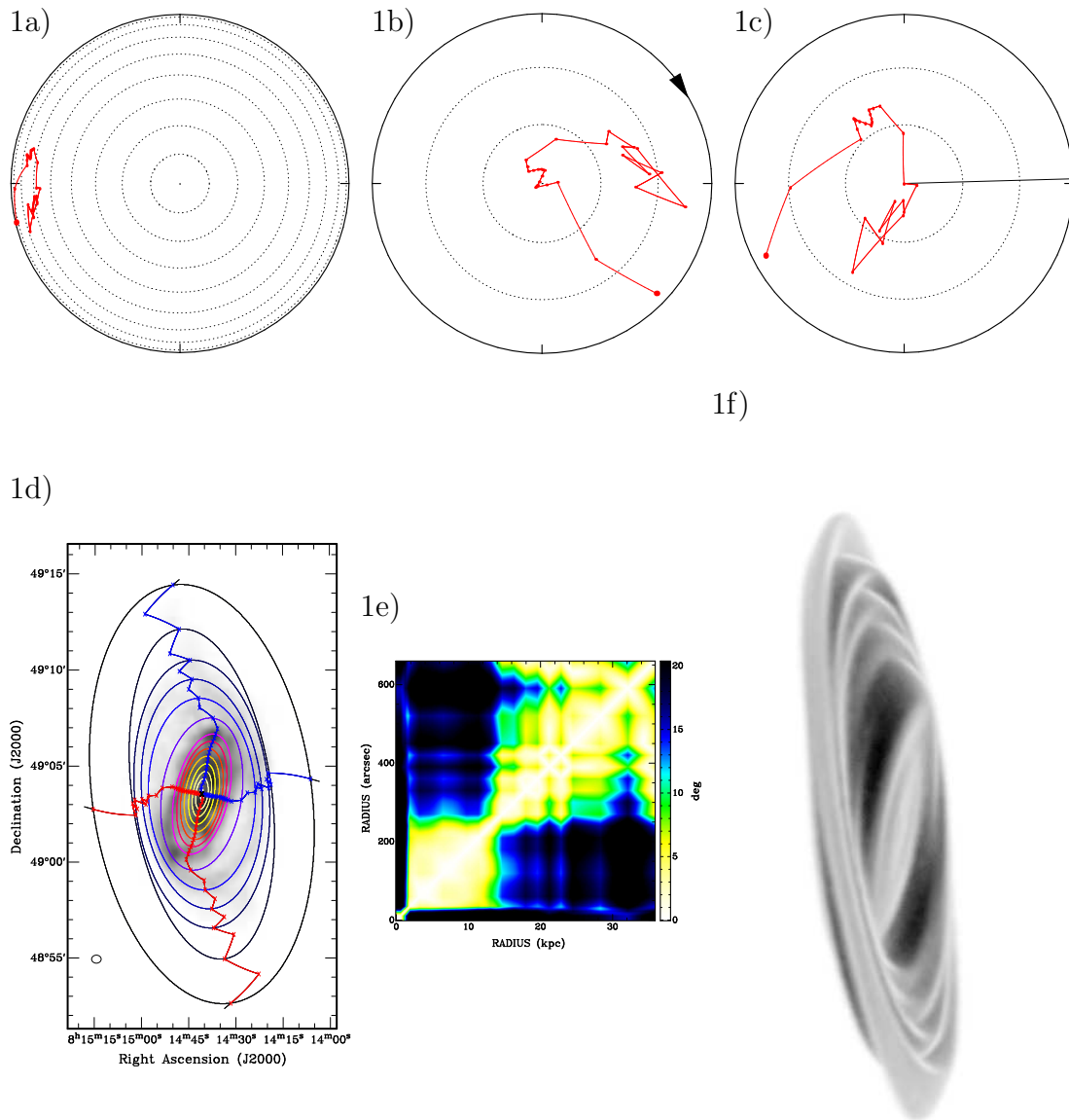


Fig. 4.6: Various visualisations of the adopted tilted-ring models for the galaxies. a)-c) tip-LON plots, the filled circles are the projection of the tip of the normal vectors of the rings at different radii onto a reference plane the innermost radius (0) denoted by a larger circle. The circles in the Figs. a)-c) are drawn at intervals of 10° . a) The reference plane is the celestial plane. b) The reference plane is the inner flat disk. c) The reference plane is chosen such that two straight LONs are visible, resembling the fourth rule of Briggs (1990). At larger radii the dots are clustered around the same position, indicating an outer planar disk. d) Inclination map of the galaxies overlaid on the original total intensity maps. The ellipses mark the projection of a ring on the celestial plane, lines and crosses mark the kinematical major and minor axes. In red the kinematical major axis in the receding part of the galaxies is plotted, in blue the kinematical major axis of the approaching part. e) Tiltogram of the galaxies. This is a pixel map showing the mutual inclination of rings at different radii. Most clearly, this diagram shows the existence of two planar disks, an inner one and an outer one. f) Three-dimensional model of the HI disk of the galaxies according to the derived tilted-ring model. The model is rotated and artificially made opaque in order to show again the presence of an outer planar disk. NGC 2541.

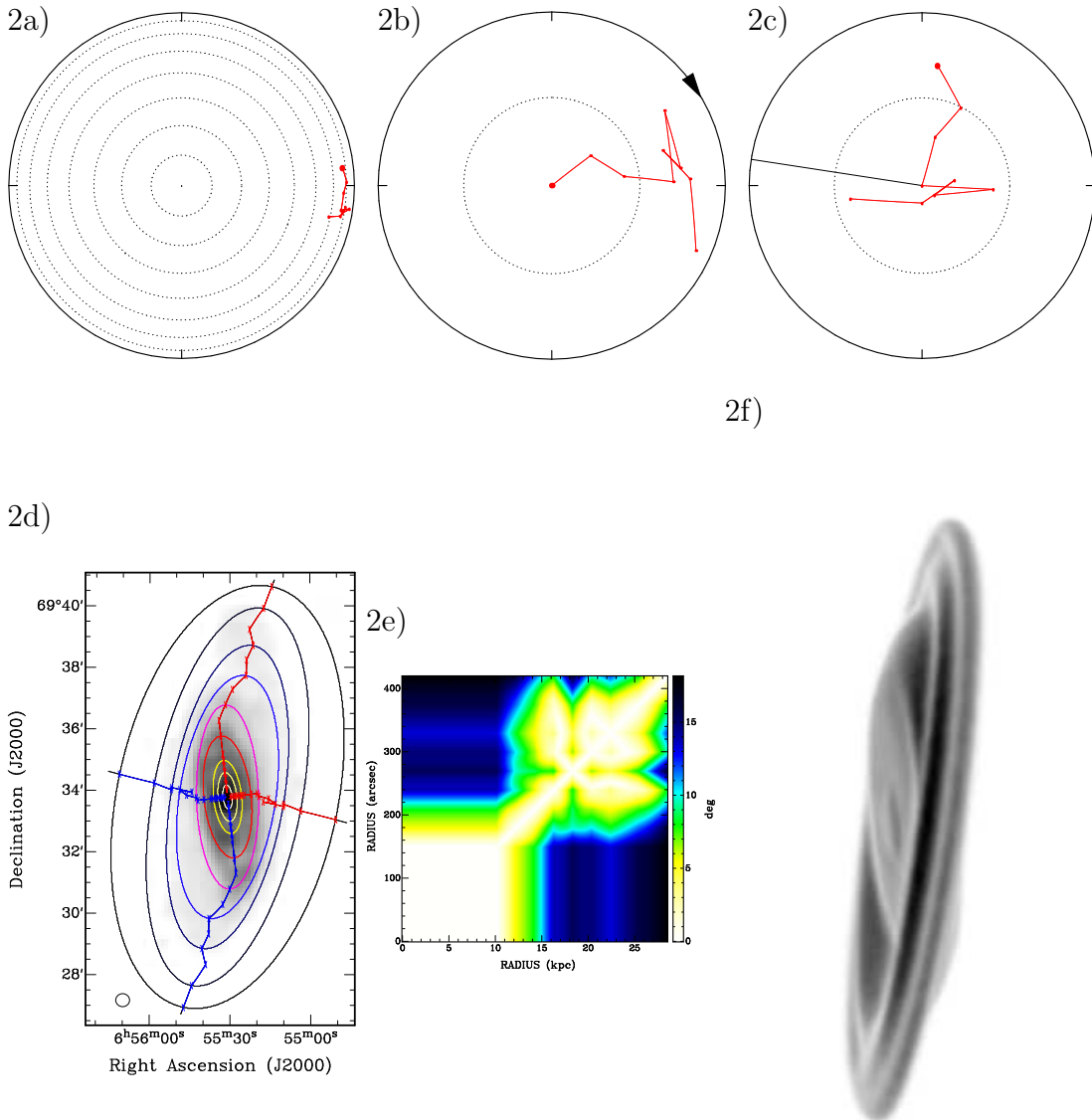


Fig. 4.6: (continued) UGC 3580.

NGC 2541 and NGC 5204. Beyond a certain radius r_{tr} , the lines-of-the nodes are supposed to form a leading spiral. In order to check this, optical images of the galaxies have been inspected and the sense of rotation has been determined from dust-lane features if a bulge was present and from the orientation of spiral arms, supposed to be trailing. In the Figs. 4.6b) the sense of rotation is indicated by an arrow. The plots show that within the errors of the measurement this rule is followed by the examined galaxies. Again, the feature is visible clearest in the case of NGC 5204, the galaxy with the largest warp in the sample, but also for

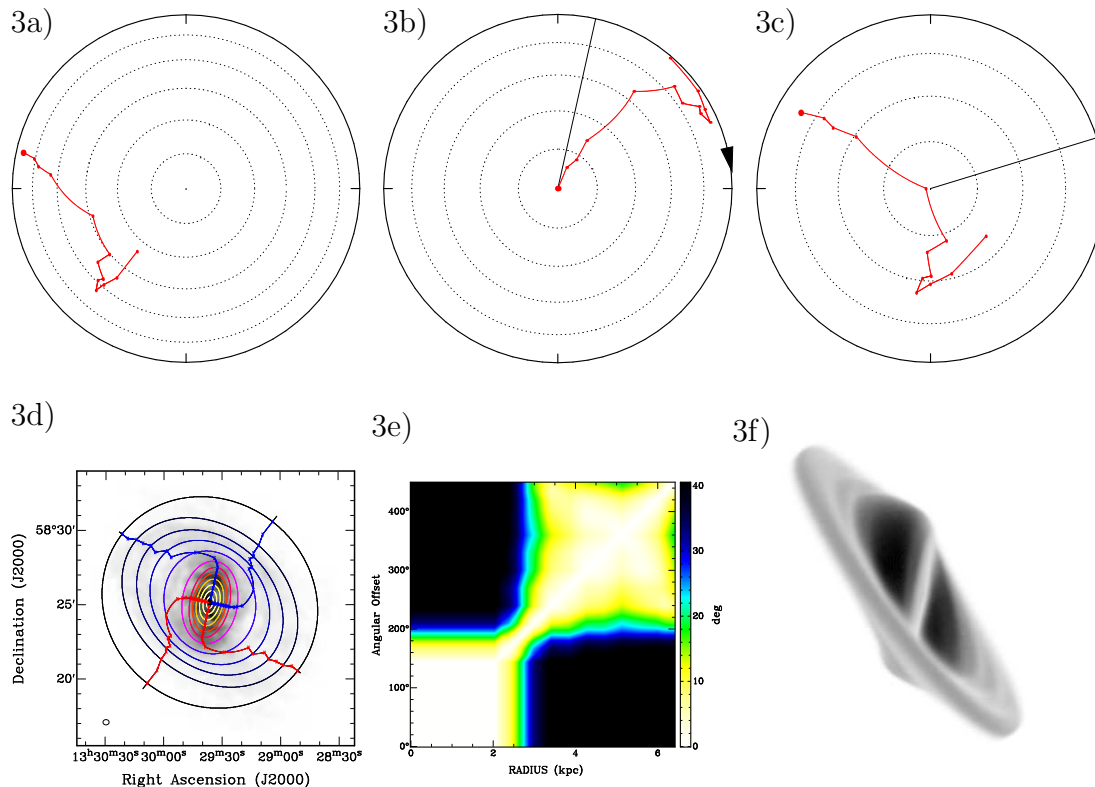


Fig. 4.6: (continued) NGC 5204

NGC 2541 and UGC 3580 the feature is present. A rather thrilling question is whether the “forgotten” fourth rule of Briggs is obeyed by the sample galaxies. His observation that a reference frame can be found in which two straight lines of the nodes exist, one for inner part of the galaxy and one for the outer part, has been a matter of discussion and it has been declared as being meaningless by Briggs himself (Briggs & Humphuis, 1991). Indeed, this rule is reproducible with the parametrisations derived here. The Figs. 4.6c) show the attempts to find the reference plane in which this feature is best visible. As will be shown below, this was not a hard task. The question remains whether this rule has a physical meaning.

With the high sensitivity of the HI observations used and the new applied technique to derive reliable tilted-ring models it was possible to trace the disk up to large radii. The question to answer here is therefore how a warp evolves at large radii and whether new insights about the large-scale structure of galactic disks can be found. Indeed, it is amazingly simple to show a poorly reported feature of grand design warps to be present in all three observed galaxies. The Figs. 4.6e) show a tiltogram. This is basically a table, in which each entry represents the inclination of a (sub-)ring with another ring at a different radius. This

is comparable with a table showing distances between cities frequently found attached to road maps. The diagonal always has a value of 0° and the diagram is symmetric with respect to a mirroring about the diagonal (it hence contains a lot of redundancies). While not fixing the orientation of the whole galactic disk in an external reference frame, the diagram determines the internal structure of the galaxy in the scope of the tilted-ring model. It is therefore an orientation independent representation of the orientational parameters of the tilted-ring model. Looking at the three diagrams for the examined galaxies it is directly evident that the galactic disks are divided into two regions, within which the mutual inclination of rings does not change much. Hence, all three HI disks show two separate regions within which the orientational parameters do not change significantly that but are misaligned with each other. In other words, *the galaxies show an outer and an inner planar disk that are connected by a region in which the disk orientation changes more or less rapidly.* The Figs. 4.6f) are the most figurative visualisation of the best-fit models in form of a three-dimensional smoothed point-source model, rotated about an axis and made opaque in order to show the two-disk structure in the parametrisations. For the generation of these plots, the last two data points with their large errors were not taken into account. Having demonstrated the presence of the two distinguishable flat disks in the galaxies, their presence can be made out in all visualisations showed: At large radii, the orientational parameters stay at the same value within the error bars in the Figs. 4.4 and in the tip-LON plots the data points that belong to large radii cluster about the same position. Knowing this, it is a simple task to find a realisation of a tip-LON plot in which the two “straight” lines of the nodes are visible. The fundamental plane of the plot has to be chosen to be the plane in which a ring lies that is in the intermediate region between the two disks. This position can be determined by looking at the tiltogram as the radius at which the two regions contact. It is then not astonishing that rule 4 is seemingly obeyed by the sample galaxies, as a few rings lie in the intermediate region that must connect two clusters of points in the tip-LON diagram. If the transitional region where the disk changes from one orientation to the other is small, two “straight” lines of the nodes are seen looking at a tip-LON plot. While the statement is true that the presence of two *straight* lines of the nodes is possibly only an impression one gets looking at the plot, it is not true that the fourth rule has no physical meaning, as claimed by Briggs & Hamphuis (1991) himself. In the case of the examined galaxies, it is a consequence of the fact that the galaxies contain two mutually inclined but internally planar HI disks connected by a rather small intermediate region in which the disk surface tilts rapidly.

The question arises whether the changes in the disk orientation are accompanied by other signs for a change in the physical conditions for the disk at the transition radius. An answer can be found looking at the Figs. 4.4. At the transition radius both, the rotation curve, and the surface brightness profiles change character

relatively suddenly for all examined galaxies. The surface density shows a drop and reaches a regime in the region of the outer disk where the gradient of the profile becomes very shallow, a feature that has already been connected with the warping phenomenon by García-Ruiz et al. (2002b). In Tab. 4.1 the HI radius r_{HI} is included as the radius at which this transition occurs. The value is obvious and can be read out from the best-fit parametrisation.

But also the rotation velocity shows a distinct feature in the tilted-ring models derived for the galaxies. For all sample galaxies the rotation curves show a sudden rise at the transition radius and then become flat again in the region of the outer disk. In order to have a robust estimate of the amplitude of this jump and to check, if a rotation curve without a sudden rise could still be compatible with the original data, another series of fits to the low-resolution data was performed. For each galaxy, two regions were selected for which the rotation curve was flat, one inner region, and one outer region. Then, for these regions, as a first guess, an average rotation velocity was assigned. Two fits were performed for each galaxy, leaving all parameters variable as in the initial fitting process (also the orientational parameters) but one time enforcing both regions to have the same rotation velocity, the other time keeping the rotation curve flat in each separate region, but allowing the rotation velocity of both regions to vary. Then, the resulting artificial datacubes were compared with the original datacubes. The results are shown in Fig. 4.14.

As can be seen in the plotted position-velocity diagrams, to decide by a visual inspection whether the 2-velocity model fits better to the original datacubes is not a simple task at least in the case of NGC 5204 and NGC 2541. A thorough inspection of the data, which cannot be presented in detail here, but showed that the original datacubes were slightly better represented by the model datacubes resulting from the fits allowing for two separate rotation velocities. The change in the rotation velocity derived from the model allowing for two separate regimes with a flat rotation curve was 14.6kms^{-1} for NGC 5204, 9.7kms^{-1} for UGC 3580, and 6.6kms^{-1} for NGC 2541. Representing the galaxies with the tilted-ring model, the rotation curve shows a sudden increase of the rotation velocity at the commencement of the warp.

4.6 Non-circular motions and their possible influence on the results

Given the fact that the best-fit model datacubes as well as the total intensity maps match their observed counterparts very well, two of the results given above are un-doubtable, the presence of the outer planar disk and the drop in the surface brightness profile at the transition radius.

The third observation is that the rotation velocity shows a change at the transition radius. This in any case means that the dynamical conditions change at this radius, indicated by the change of the rotation velocity when employing the tilted-ring model in order to parametrise the kinematics. This approach, however, contains a weak point. In the presence of non-circular motion as may be caused by a large bar or a triaxial Dark Matter halo, the tilted-ring model is possibly not a good description of the kinematics and has therefore to be confined. Franx et al. (1994) and Schoenmakers et al. (1997) proposed a simple approach to enable a parametrisation of non-circular motion if present in galaxies, a harmonic decomposition of the velocity-field in azimuthal direction. While a similar method implemented in an algorithm that fits models directly to a datacube (instead of using a velocity-field) would be the best approach in order to estimate the contribution of systematic non-circular motions in the sample galaxies, the possibility is not yet included in *tirific* (but can be expected soon). Hence, as also the estimation of deviations of the underlying potential from sphericity is not a major topic of this chapter, a simple approach has been used in order to get an impression of the influence of deviations in the kinematics of the galaxies from the symmetry inherent to the tilted-ring model. For each galaxy, the first moment map of the best-fit model datacubes was subtracted from the first moment map derived from the original observation. These velocity difference maps are especially suitable to spot possible errors in the fits. Such errors either arise because the model parameters are not chosen optimally or because the model is not able to represent the galaxy kinematics. Given the fact that one can be quite confident that the best-fit parameters found are in fact the parameters that fit a tilted-ring model to the datacubes best, the deviations that show up are real kinematic features that cannot be represented by the assumption of circular orbits. The Figs. 4.7 show the velocity difference maps derived from the low-resolution original and model datacubes for the sample galaxies and a histogram of the pixel values in the maps overlaid with a Gaussian with the weighted mean, the standard deviation and the area of the histogram.

Just by looking at the difference maps it is obvious that for UGC 3580 and NGC 5204 and for the inner disk of NGC 2541 the largest systematic contribution to the deviations are of antisymmetric nature. If a minimum is located at a position on a ring, a maximum is present at the opposite position on the ring with respect to the galactic centre. For the inner disks of UGC 3580 and NGC 5204 the extrema are very well aligned with the kinematical major axis, as is partly the case for NGC 2541. This galaxy has a distinct antisymmetric feature in the very central region, that belongs to the bar or inner inclined ring. In the outer regions, UGC 3580 and NGC 5204 basically maintain the orientation of the antisymmetric orientation of the residual velocity along the kinematical major axis, although less clear. In the region of the outer disk, NGC 2541 shows a

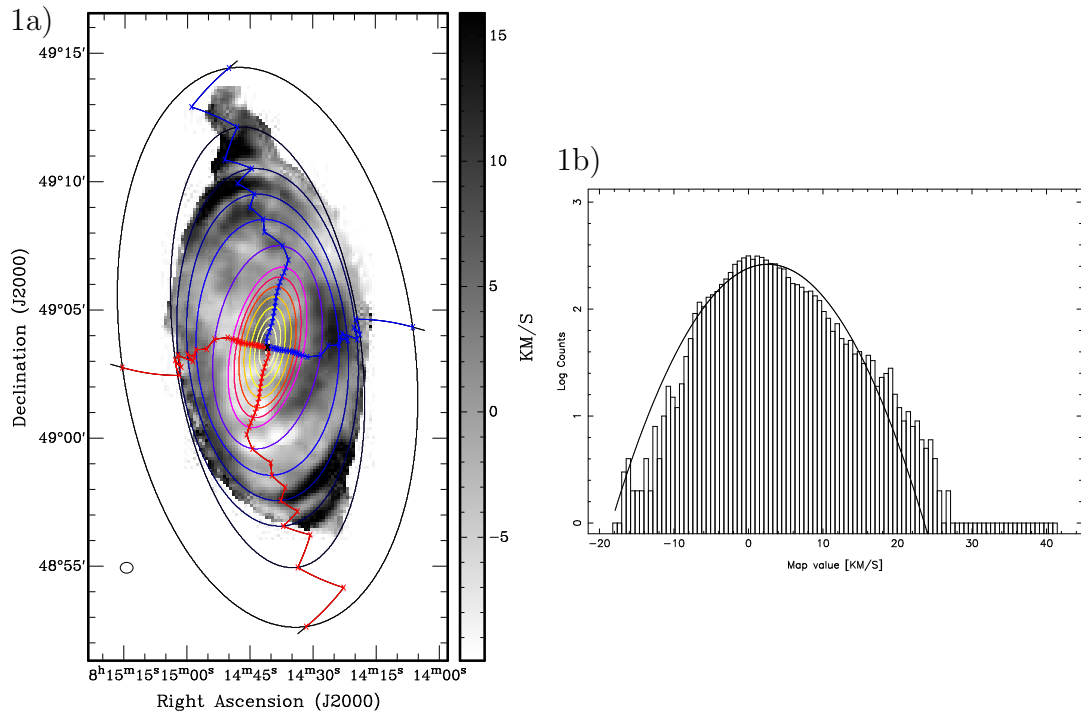


Fig. 4.7: a) Difference velocity maps derived by subtracting the model first moment map from the original first moment map. b) Histogram of the pixel values of a). The solid line shows a Gaussian with a peak position identical with the mean, a width equal to the rms, and an area equal to the area of the histogram. NGC 2541.

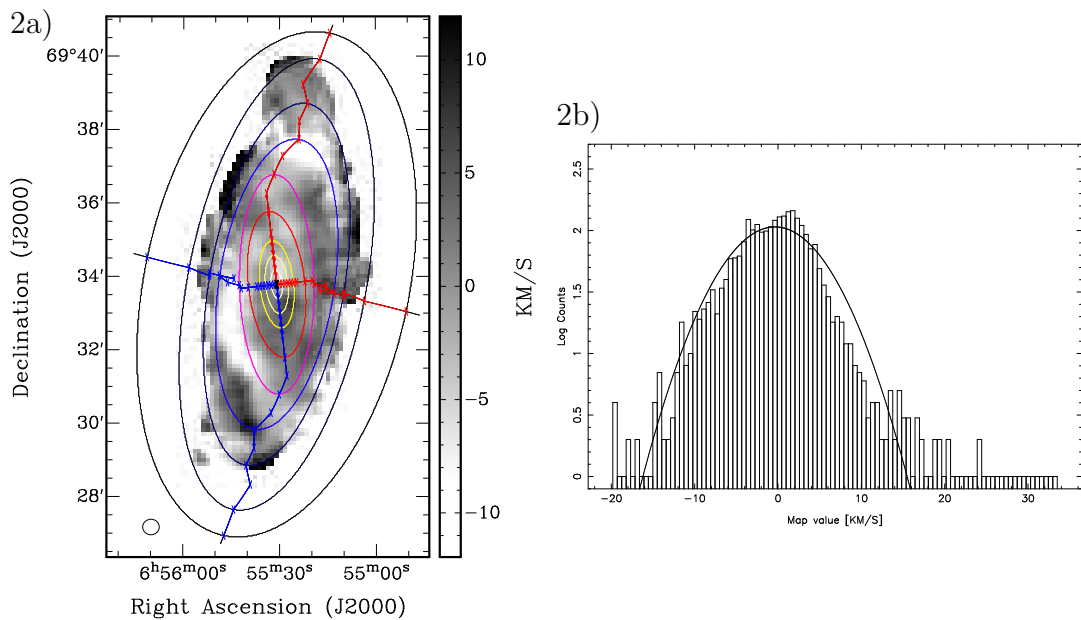


Fig. 4.7: (continued) UGC 3580.

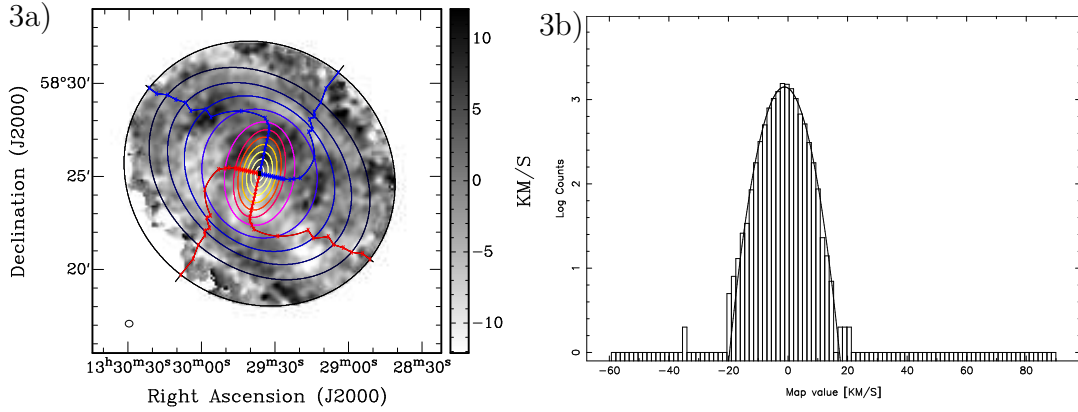


Fig. 4.7: (continued) NGC 5204.

systematic enhancement of the velocity difference. Also the obviously erroneous wiggles visible in the parametrisation leave their imprint in the velocity difference map. As simple estimation of the possible influence on the rotation curve can be made by taking into account the rms present in the residual velocity maps. The mean and the rms of the pixel values in the maps was calculated and, to get an upper limit, corrected for the lowest measured inclination present in the galaxies. The results are shown in Tab. 4.4.

Name (1)	\bar{v}_d (2)	σ_{v_d} (3)	i_{\min} (4)	$\frac{\sigma_{v_d}}{\sin i}$ (5)
NGC 2541	2.6	6.3	56.0	7.6
UGC 3580	-0.4	5.2	66.8	5.6
NGC 5204	-1.2	4.8	28.9	10.0

Tab. 4.4: Basic statistics of the velocity difference maps. (1) Galaxy name. (2) Mean of the deviation velocities (kms^{-1}). (3) Standard deviation of the deviation velocities (kms^{-1}). (4) Minimal measured inclination in the galaxy. (5) σ_{v_d} corrected for i_{\min} .

For all difference maps, the standard deviation of the pixel values are well below the best-fit velocity dispersions. This is also true for the values corrected for the minimal inclination except in the case of NGC 5204, where the corrected values lie nevertheless near to the best-fit velocity dispersion. This indicates that – while visibly present as systematic features in the velocity difference maps – non-circular motions do not violate largely the results given in the previous section. Testing various regions in the maps with extrema, one finds that in these regions the overall mean values do not differ much from σ_{v_d} . Hence, the errors in the rotation velocity introduced by not accounting for non-circular motions should be less

than the inclination-corrected standard deviations in the maps. For NGC 5204 and UGC 3580, this means that the rise in the rotation velocity is possibly a real feature reflecting a radial feature in the potential, while for NGC 2541 this conclusion cannot be drawn. To be emphasised again, the change in the rotation velocity when fitting a tilted-ring model with the inherent assumptions about the galaxy symmetries is a feature that points towards a distinct change in the dynamical conditions in the galaxy when the disk orientation switches, whether the origin of this feature is a wrong fit under the assumption of the circularity of orbits or it is reflecting a real feature in the underlying profile of the potential.

Concerning the origin of the systematics in the velocity deviation maps, one can only speculate for the time being. The possibility that the antisymmetric features along the kinematical major axis might be due to a erroneous fit of the rotation velocities should be discarded, taking into account the accuracy with which *tirific* is able to find best-fit solutions (see Chap. 3). Franx et al. (1994), using epicyclic theory, showed that an antisymmetric feature in the residua of velocity maps could be due to the presence of a coherent bar-like feature in the underlying mass distribution. In the presence of a triaxial halo, such a feature should thus turn up. Another possibility to produce an antisymmetric contribution to the recession velocity is to invoke a coherent precession, expected to be present in a warped structure in a few warp theories. Both possibilities will be followed up and reported on in the near future.

Directly visible in the case of NGC 2541, a constant plateau in the difference velocities is added in the outer disk. This is reflected in the histogram, where a systematic shift of the difference velocity can be seen. The mean value in the velocity difference map is large. A simple explanation can be sought in the fact that the tilted-ring models fitted assume one centre and one systemic velocity for all radii. This assumption could be wrong. Battaglia et al. (2005) showed that in the case of NGC 5055 the residuals in the recession velocities could be minimised, allowing the systemic velocity and the centre of the galaxy to vary with radius. Interestingly, a transition of these quantities occurred at the commencement of the warp of NGC 5055. The same feature might be present in NGC 2541, explaining at the same time why *tirific* had difficulties in finding a reliable rotation velocity at some radii for this galaxy. Hints for the same phenomenon to be present for can be found considering the deviation-velocity histogram and the mean values of the deviation velocities for the two remaining galaxies of the sample. As the deviation is not tremendously large, it can finally be concluded, that the errors introduced by fitting a tilted-ring model with a common centre and a common systemic velocity are bearable and the results presumably robust.

4.7 Discussion and summary of the results

The warp structure of the three galaxies NGC 2541, UGC 3580, and NGC 5204 has been examined and in all cases remarkably similar and distinct features have been found to be present in the warped disks. While the change of the rotation curve at the commencement of the warp needs a high-quality analysis to be found, it would be somewhat astonishing that the two-disk structure of warps should never have been reported in previous studies – if the examined galaxies are representative for disk galaxies with grand-design warps –. And indeed, searching the literature, one can find several reports of the same warp structure in other disk galaxies as well as hints. The rule 4 found by Briggs (1990) is a direct consequence of a two-disk structure of warps as shown above, hence a close inspection of the tilted-ring models found for a number of galaxies in the same paper should reveal whether this important feature is possibly present in the examined galaxies. While the sensitivity of the observations used for the study of Briggs was far worse than for the observations employed here, a look at the viewgraphs shown in this publication shows that a two-disk structure can be deduced from the orientational parametrisations of NGC 628, NGC 1058, NGC 2841, NGC 3344, NGC 3718, NGC 5055, and M 83, although the outer disk in this study would have been considerably smaller than the ones detected in the present study. It is remarkable, that NGC 628, which has been used by Briggs & Hamphuis (1991) in order to show that galaxies exist that clearly violate his rule 4, shows nevertheless a flat outer disk. The reason is that the transitional region is quite large. Hence, the impression of two straight lines is hampered, as many data points lie in-between the two flat disks. If one takes into account that the data points at the largest radii might have much larger errors as given by Briggs, the sample of galaxies with a two-planar-disk structure as found by Briggs can be enlarged by NGC 2903, possibly NGC 3198, and NGC 5033, leaving in total two parametrisations of Briggs galaxy sample that are not showing a flat outer disk, M 33 and DDO 13, for both of which the disk is not traced out to large radii. Kuijken (1991) was the first to state that the flatness of the outer disk in NGC 2841 is somewhat remarkable. The fact that a flat outer disk is present in most of the galaxies examined by Briggs (1990) was noted also by Corbelli & Schneider (1997), who found the same feature to be distinctly present in our neighbouring galaxy M 33, leaving DDO 13 as the only galaxy in Briggs sample a flat outer disk cannot be assigned to (possibly because its kinematics are not traced towards larger radii). The parametrisations used by Briggs were not homogeneous. They were partly the results of automated fits to velocity-fields and partly by-eye fits of models to datacubes and have to be treated with the necessary care. Corbelli & Schneider (1997) used the same method as was used in the present study, an automated fit of artificial datacubes. In the case of NGC 5055, an analysis of the velocity-field of Battaglia et al. (2005) tracing the disk out to much larger radii, resulted in orientational parameters that seem to be inconsistent with an

outer flat disk for this galaxy, showing that the conclusion that all galaxies with a grand-design warp show a flat outer disk is debatable in singular cases. The results of Battaglia et al. (2005) will be checked upon in due course.

Remarkably, the study of Corbelli & Schneider (1997) also shows the same rise in the rotation curve at the commencement of the warp for M 33. Also Battaglia et al. (2005) found a sharp drop of the rotation velocity at the commencement of the warp for NGC 5055, as well as Bottema (1996) for NGC 4013. Hence, it can be suspected that a change of the rotation velocity at the radius where a warp starts is a feature inherent to warped galaxies.

Also the third feature reported in Sect. 4.5, the sharp drop in the HI surface density at the same transition radius is known, as already mentioned in the introductory part, and has been reported by García-Ruiz et al. (2002b) examining a large sample of edge-on galaxies, but also in detailed case-studies (Corbelli & Schneider, 1997; Battaglia et al., 2005).

It is clear that not all symmetric warps show the three features reported on in this work (e.g. UGC 7321, see Uson & Matthews, 2003), but it may be concluded, as tentative as the small number of suitably well examined galaxies allows for, that a large class of symmetric warps exists, “grand design” integral-shaped warps, in which they are present. It follows that seen edge-on, grand design warps of the observed class do not resemble an integral sign but rather an integral sign with serifs, the serifs belonging to the extended, planar, and dim outer disk.

As Briggs’ 1990 rules, these findings rely on observations of a rather small number of galaxies that do show a suitable symmetric warp and should be treated with the appropriate care. Nevertheless, a few independent studies of galaxies with grand-design warps seem to agree to a high degree. Hence, Briggs fourth rule shall be re-formulated here, and two rules shall be added:

- Rule 4: (Grand-design-) warped disk galaxies show an outer planar disk. Hence they have an inner flat disk in which most of the visible stars reside and an outer flat disk. Both regions are connected at the transition radius, at which the disk orientation changes rapidly.
- Rule 5: At the transition radius the HI surface density profile shows a drop. Beyond the transition radius the HI surface density is falling only slowly with radius or even remains constant.
- Rule 6: Under the assumption of circularity of orbits, the rotation curve shows a sudden change at the transition radius.

Based on a rather small sample of galaxies, examined with differing accuracy and different techniques, these results certainly need further confirmation from examinations of larger samples of galaxies.

The question remains whether these rules – assuming that they are by large and large obeyed by galaxies with integral-sign warps – can give a clue on the underlying mechanism that drives warping in disk galaxies. As shown in Sect. 4.1 and Chap. 2, without changing the standard dynamics, three proposed mechanisms to explain warps can be deemed as good candidates to explain the ubiquity of warps and their structure. The presence of a Dark Matter halo *in connection with the infall of intergalactic material* reorientating the angular momentum vector of the halo is one of the proposed mechanisms for warping. Debattista & Sellwood (1999) showed that a Dark matter halo with misaligned angular momentum that aligns with the disk by dynamical friction produces a temporal warp that follows the rules found by Briggs (1990). An outer planar disk seems not to be consistent with the simulation. While the lines of the nodes presented in this paper show the right twist in the direction of the galactic rotation, the final clustering about one position is not observed. “The leading spiral, reminiscent of Briggs’ 1990 third rule, develops through clockwise differential precession in the outer parts [...], a consequence of gravitational coupling between the inner and the outer disk”. All disk material precessing in retrograde sense, the leading spiral develops because the precession is becoming slower and slower in the outer disk. A flat outer disk, however, would only be consistent with a possibly completely absent precession towards larger radii or a co-precession also present in the outer disk. As Debattista & Sellwood (1999) state, in the outer disk precession is nearly absent in their simulation, one might argue that still the scenario of misaligned angular momentum is a valid hypothesis, but requiring more extended disks. It is a question how feasible the maintenance of such large disks is. A second possibility for warp formation that invokes the same mechanism, cosmic infall, as a prime agent for warping, was examined by Bailin & Steinmetz (2003). They calculated the net gravitational torque that a disk is typically subject to at differing radii in a cosmological environment and simulated the behaviour of a galactic disk under the influence of this (radially dependent) torque. Indeed, the outcome of this simulation was a realistic warp that forms as a consequence of a bending wave proceeding outwards in the disk. Unfortunately, although the authors claim to resemble a realistic warp, they do not check in detail whether the found warp structures are compatible with observations. The sense of spirality of the line of the nodes is not reported on. It seems, though, that they are able to reproduce a flat outer disk: The outermost parts of their simulated disk galaxy remain at their original position over quite some time. A major caveat comes from the method they used in order to represent the Dark Matter halo. It was represented by a static potential. Hence, dynamical friction, which is an essential agent to transfer angular momentum from disk to halo and vice versa and is therefore of great importance in any warping scenario (Toomre, 1983; Nelson & Tremaine, 1995; Dubinski & Kuijken, 1995; Binney et al., 1998), was ignored in their simulation, also when calculating the net torquing. While it may be understood, how a gravitational torque can be maintained via cosmic infall, it is not clear if a disk

would evolve in the same way if it would be able to effectively exchange angular momentum with the Dark Matter halo. Indeed, the simplified simulations of Jiang & Binney (1999), in which cosmic infall was simulated by actively injecting particles on an orbit inclined with respect to the disk, showed that a realistic warp could not be achieved. Their simulated disk lacked a flat inner part. It is thus at least questionable whether cosmic infall is the prime agent to drive the ubiquitous warping of disk galaxies.

This, however leaves some room for speculation. There are some direct consequence of the extension of the rules for the behaviour of warps. The two-disk structure of warps together with the third rule of Briggs, that the line of the nodes advances in the (prograde) direction of rotation, allows a few conclusions. The galactic disk consists of two distinguishable but connected regions each of which is in a state of co- or zero precession. A precession in the central disk provided, which is a possible option regarding the results of Sect. 4.6, the precession velocity of the outer disk must be either slower in the case of a retrograde precession, which naively is the preferred option, or faster in the case of a retrograde precession, which is an implausible option. The rules 5 and 6 hint to the same fact, that the warp starts where the physical conditions in the potential change for the galaxy. Rule 5, along with the fact that usually a warp starts where the optical disk fades away, shows that a warp starts where there the mass-surface density drops below a certain value, where hence the potential is then probably dominated by the Dark Matter halo, a fact that also the change of the rotation curve points towards. Possibly, the warp marks a transition from a disk-dominated region to a halo-dominated region. Mass decompositions of M33 by Corbelli & Salucci (2000) and NGC 5055 by Battaglia et al. (2005) support such a picture. It is visible that the transition radius for those galaxies lies at a somewhat larger radius, but near to the radius, where the halo becomes dynamically dominant over the disk.

Given the observational evidence and the lack of working scenarios for warp formation, the proposal of Binney et al. (1998, see Sect 4.1) should be taken seriously. If a long-lived internal misalignment of the flattened Dark Matter halo is common among disk galaxies, then an extended HI disk with low surface mass density is expected to align with the outer halo. It is furtherly to be expected that the inner halo precesses together with the inner disk under the influence of the torque imposed from the more flattened outer halo, as well as the outer halo under the influence of the inner disk-halo system, which could fit to the observation that the precession frequency of inner and outer disk must differ. The simulations of Bailin et al. (2005, see Sect 4.1) showed that such a misalignment is maintained and the mutual inclination of disk and outer halo is nearly unchanged over large timescales, meaning that the exchange of angular momentum between inner disk-halo system and outer halo is small. Hence, this scenario is possibly a way to explain the ubiquity of warps that should be followed up in theory, whether a

large HI disk is consistent with the current concordance picture or not. If such a theory is successful, warps trace the orientation of the Dark Matter halo. Bailin et al. (2005) found that the mutual inclination of the inner and the outer disk was randomly distributed in the simulated galaxies. This should be reflected in the fact that warps of large and small amplitude should nevertheless show the same specific features in their warps. Reminding this, it is very remarkable that the two galaxies with an intermediate warp indeed seem to show a rather similar warp structure as the one examined galaxy with an extremely large warp amplitude, the difference being the warp amplitude only. Moreover, the examined galaxies were of completely different type, a late-type spiral galaxy, an early type spiral galaxy, and a dwarf galaxy. The warp features described here seem to be independent of type and mass, again consistent with the hypothesis that warps reflect an internal misalignment of the halo.

This chapter shall be closed with a request to theory. The findings in this analysis suggest that a (disk-)halo-halo misalignment is a plausible scenario to explain the ubiquitous grand-design warps in disk galaxies. If this is so, and such a misalignment – including an extended lightweight outer disk – is a possible scenario an elaborate theoretical description of the properties of such warps possibly allows in turn to gain better insight in the internal structure and the dynamical properties of disk and halo by measuring warp properties.

4.8 Supplementary figures and tables

Here, supplementary figures and tables are put. All figures that are not immediately needed when reading the chapter for the first time, are put here.

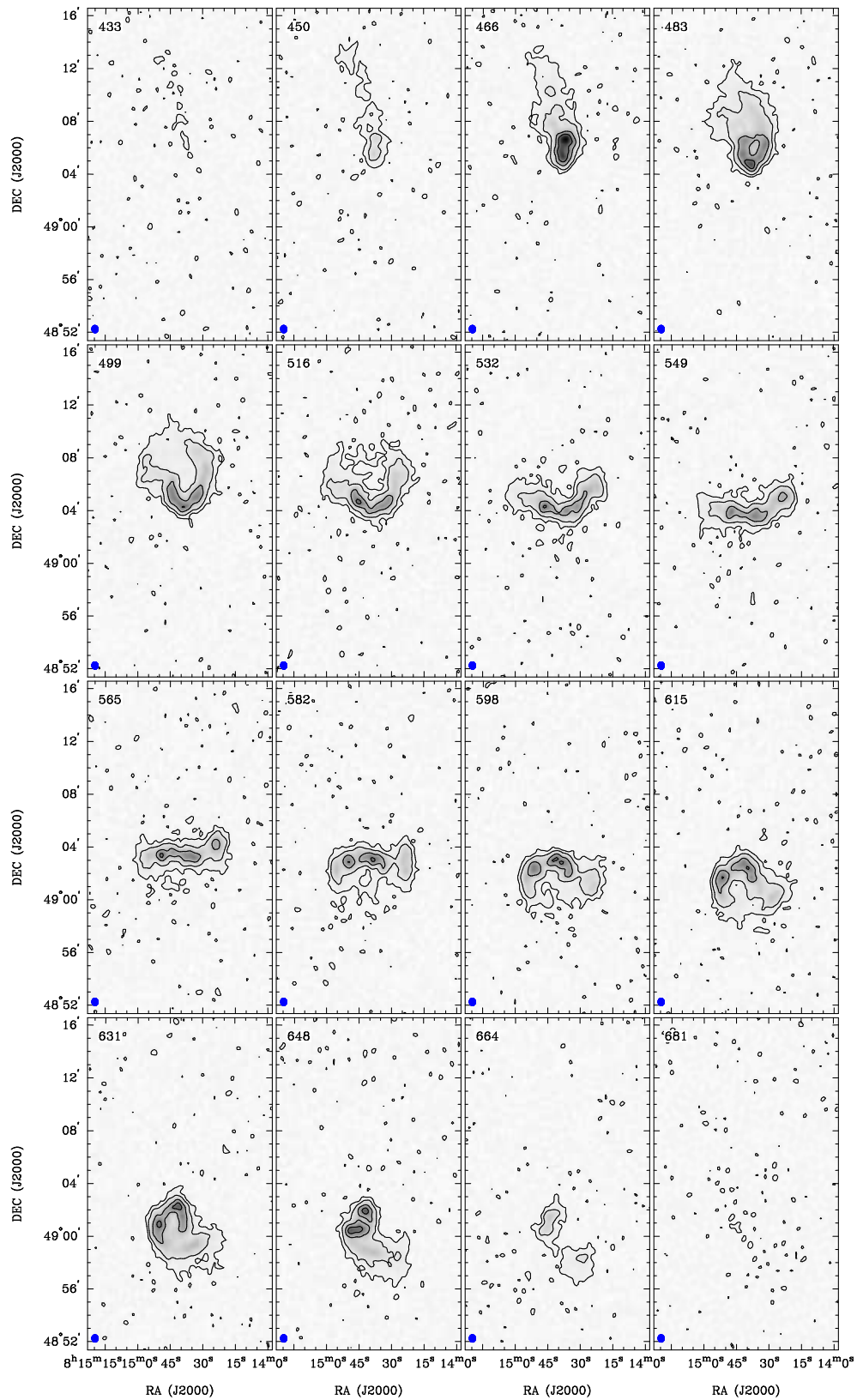


Fig. 4.8: Selected images from the low-resolution datacubes (channel resolution of 4.12km s^{-1} , robust weighting of 0.4, only visibilities with a baseline length $< 6.4\text{k}\lambda_{\text{HI}}$ used). The numbers on the upper left give the heliocentric radio velocity in km s^{-1} . The blue dot represents the clean beam. NGC 2541. The contours represent the 1, 4, 16, 32 mJy/beam levels.

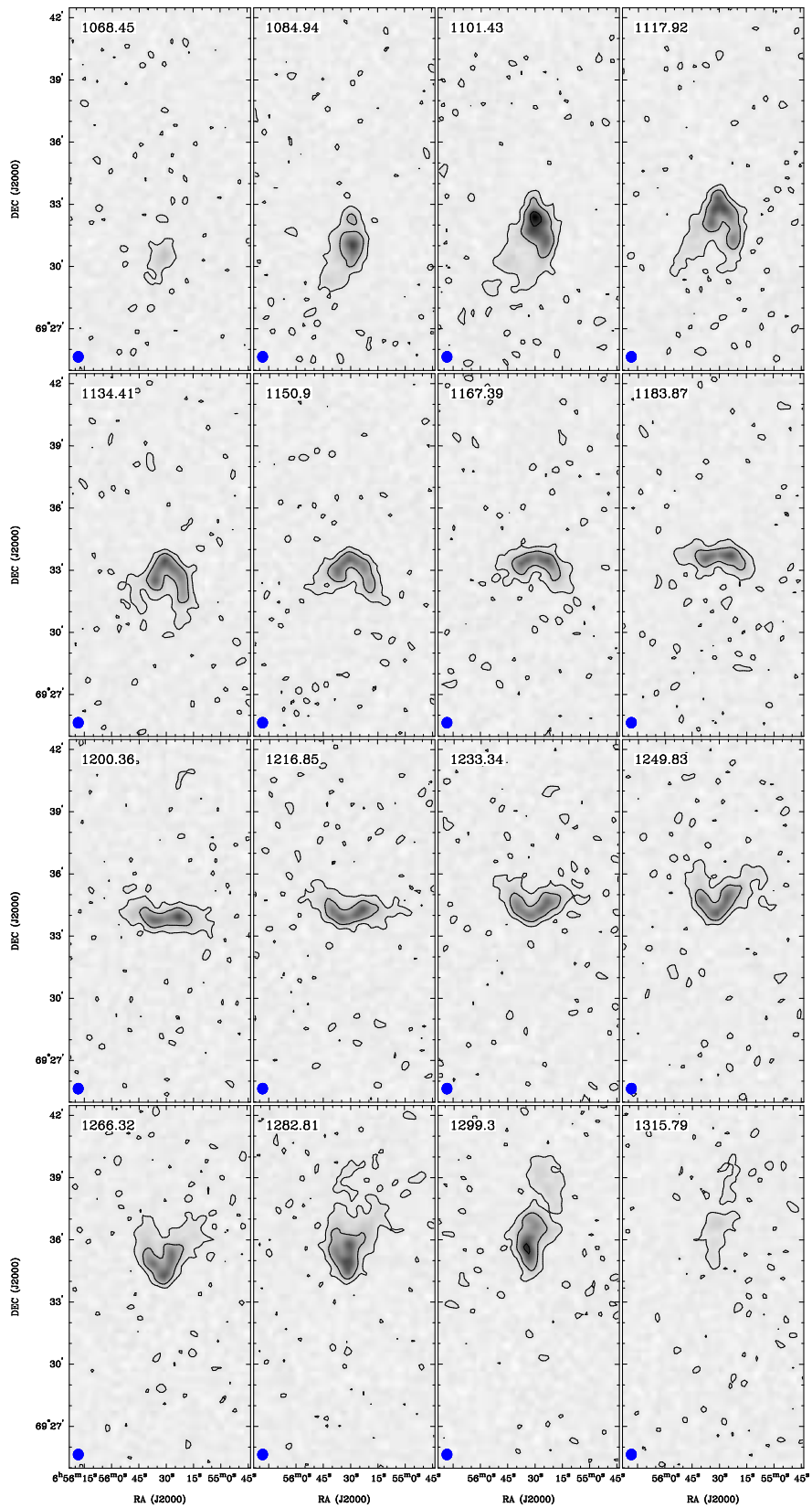


Fig. 4.8: (continued) UGC 3580. The contours represent the 1,6,24 mJy/beam levels.

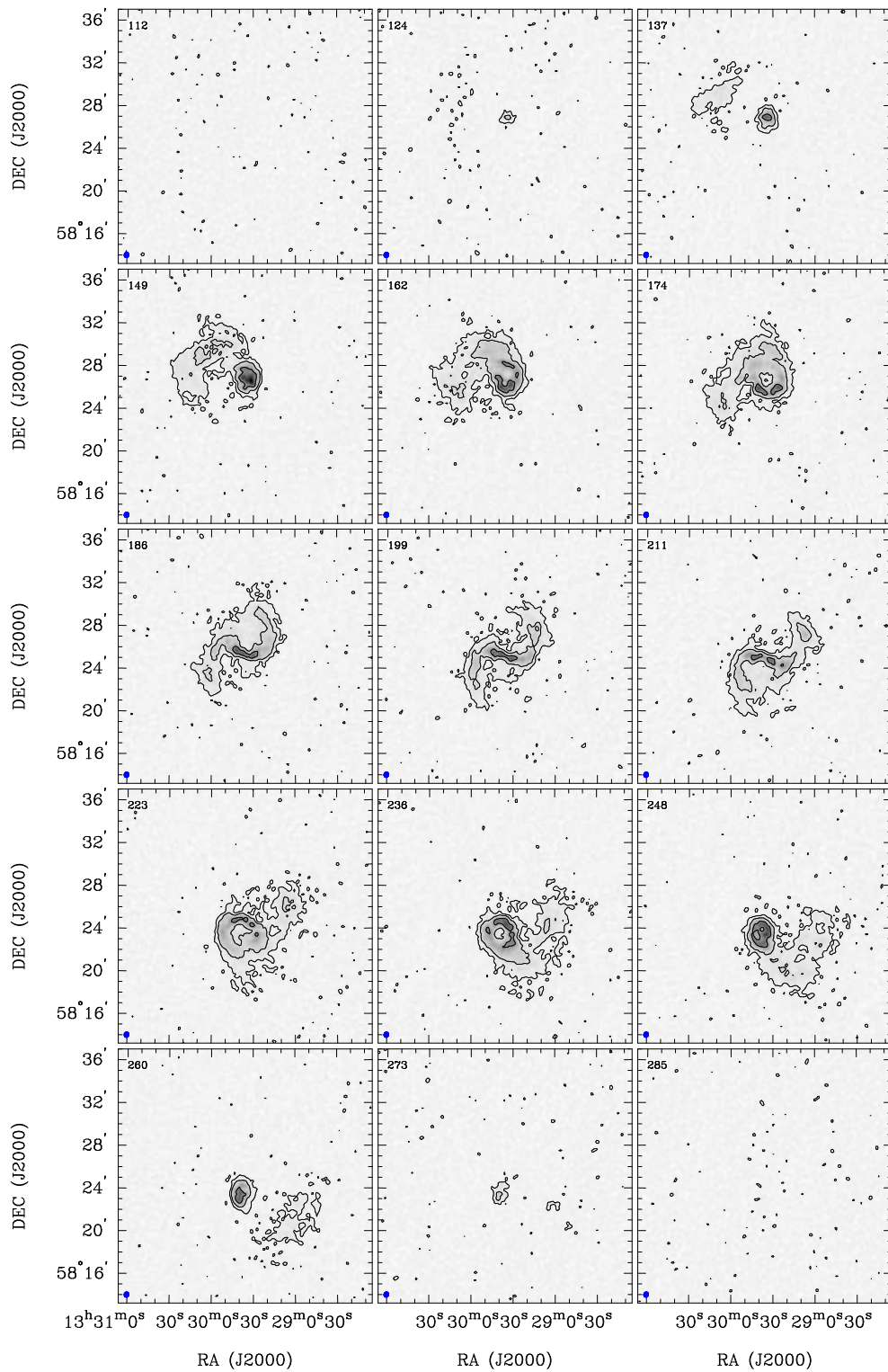


Fig. 4.8: (continued) NGC 5204. The contours represent the 1,4,16mJy/beam levels.

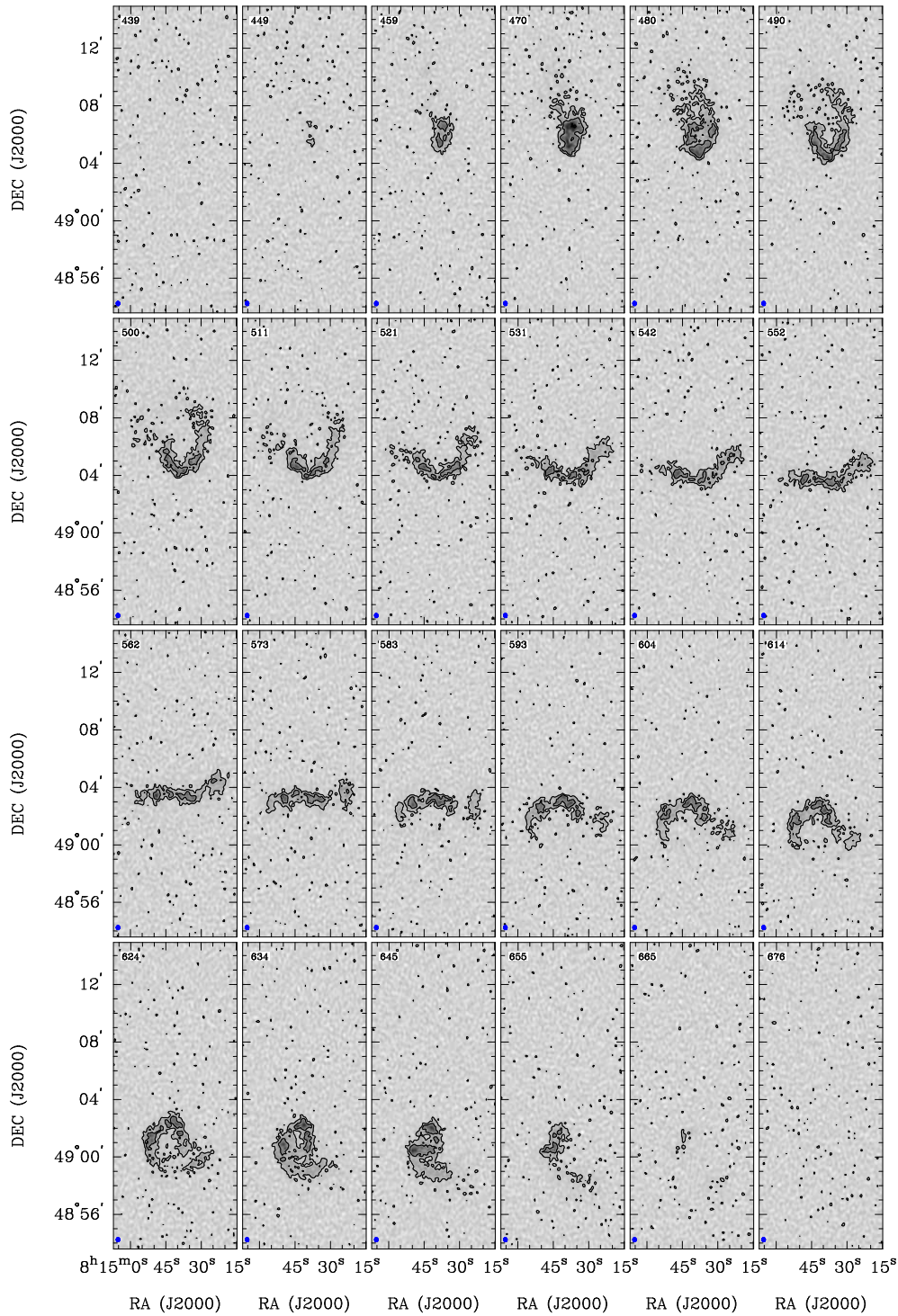


Fig. 4.9: Selected images from the high-resolution datacubes (channel resolution of 2.06km s^{-1} , uniform weighting, all visibilities used). The numbers on the upper left give the heliocentric radio velocity in km s^{-1} . The blue dot represents the clean beam. NGC 2541. The contours represent the 2, 6, 18 mJy/beam levels.

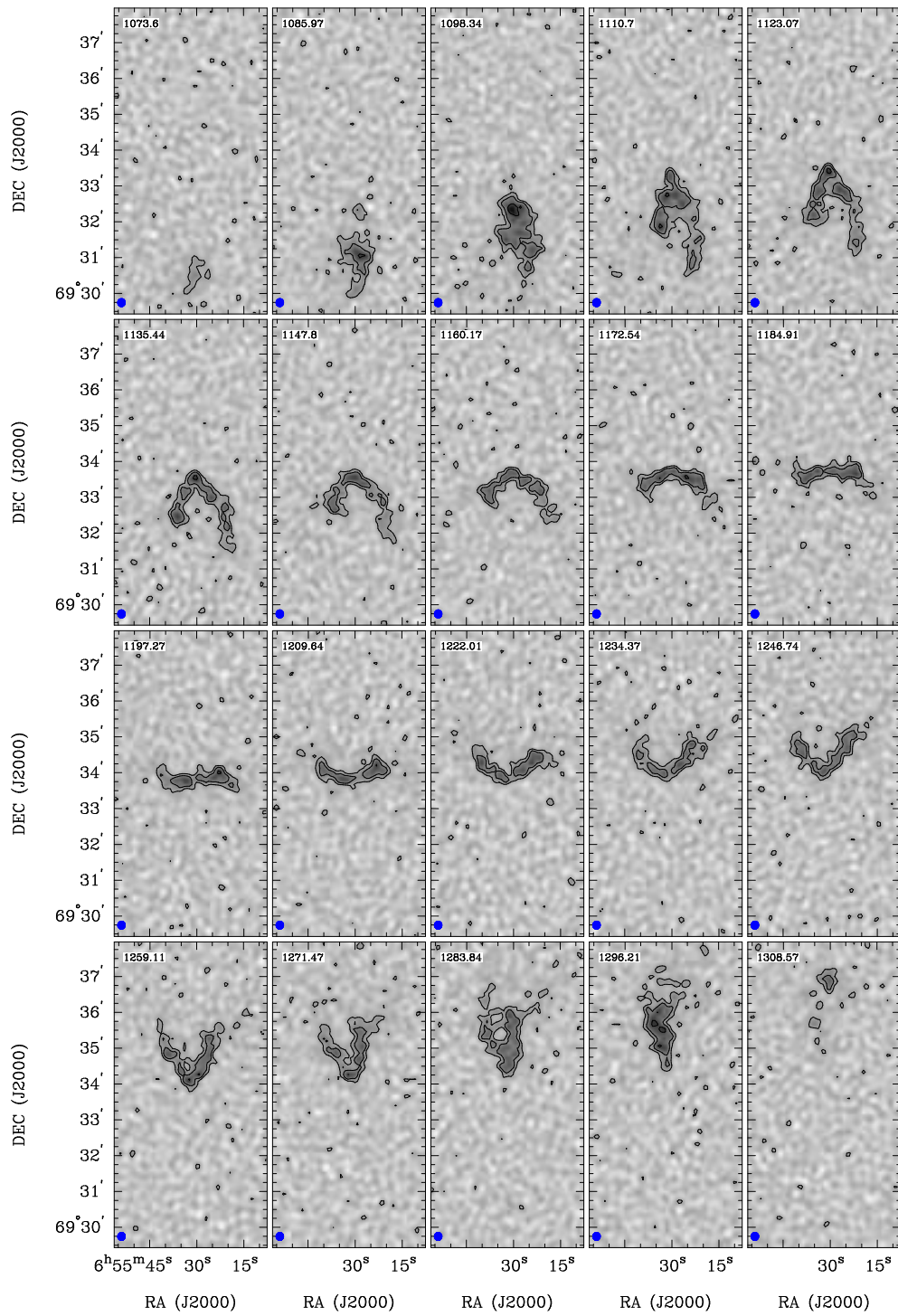


Fig. 4.9: (continued) UGC 3580. The contours represent the 2, 8, 16 mJy/beam levels.

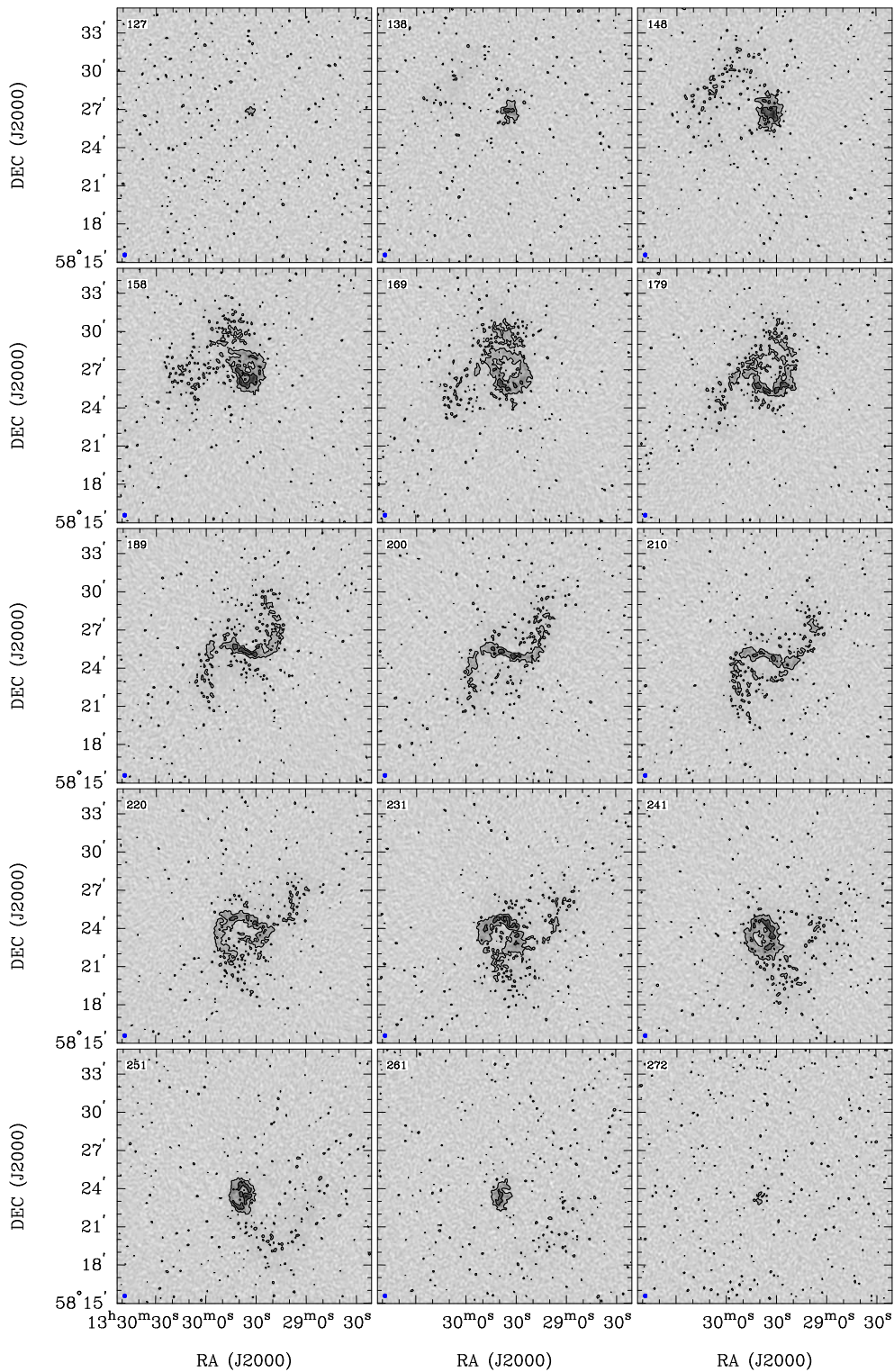


Fig. 4.9: (continued) NGC 5204. The contours represent the 1.5, 6 mJy/beam levels.

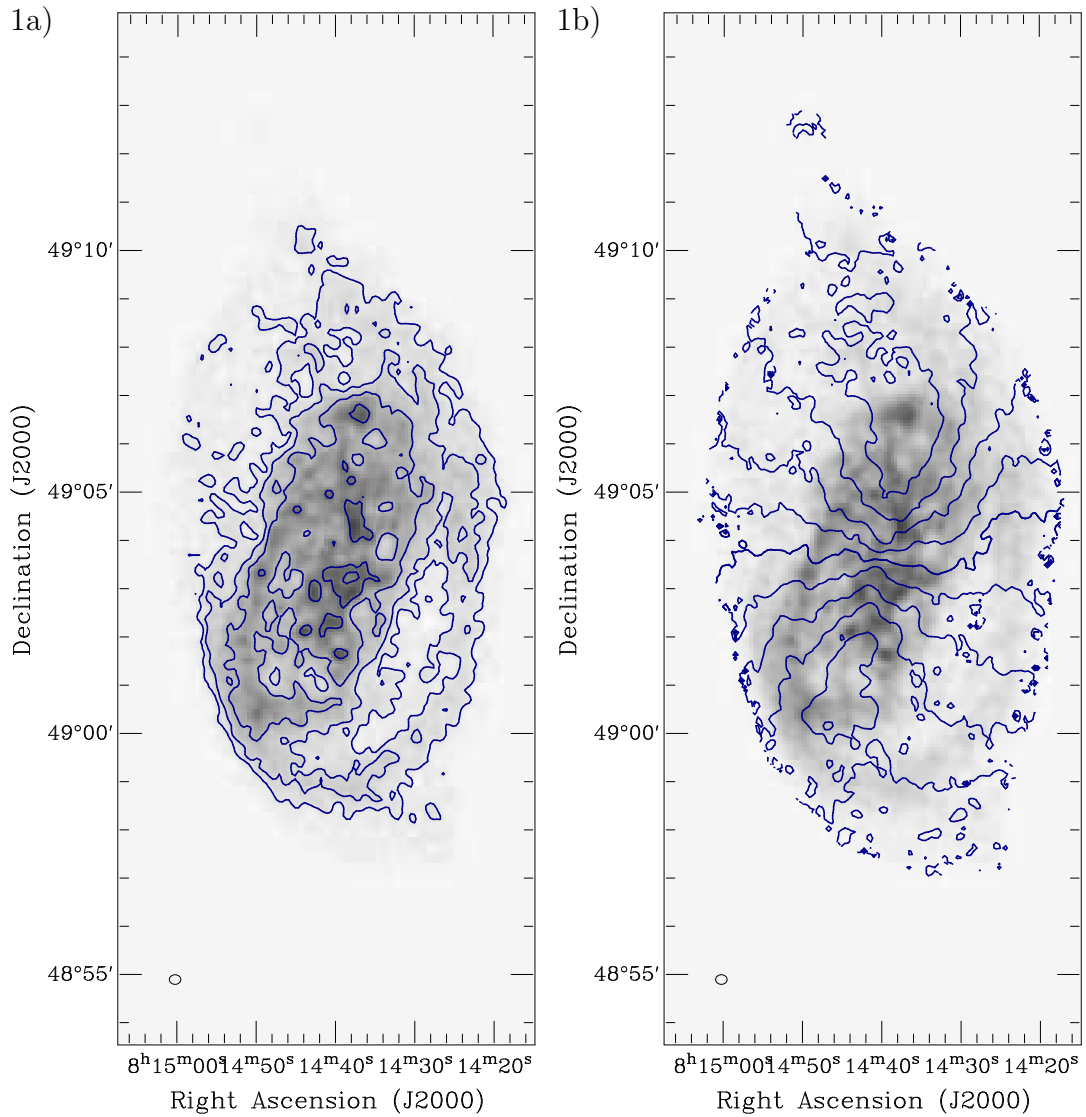


Fig. 4.10: Total intensity maps (a, left) and first moment velocity-fields (b, right) derived from the high-resolution datacubes overlaid on total intensity grey-scale maps. The ellipse in the lower left corner represents the clean beam. NGC 2541. The contours represent the $29, 58, 115, 230, 345 \cdot 10^{19} \text{ atoms cm}^{-2}$ levels and the $v_{\text{sys}} \pm 0, 20, 40, 60, 80, 100 \text{ km s}^{-1}$ levels respectively (see Tab. 4.2). The approaching side is orientated towards NE.

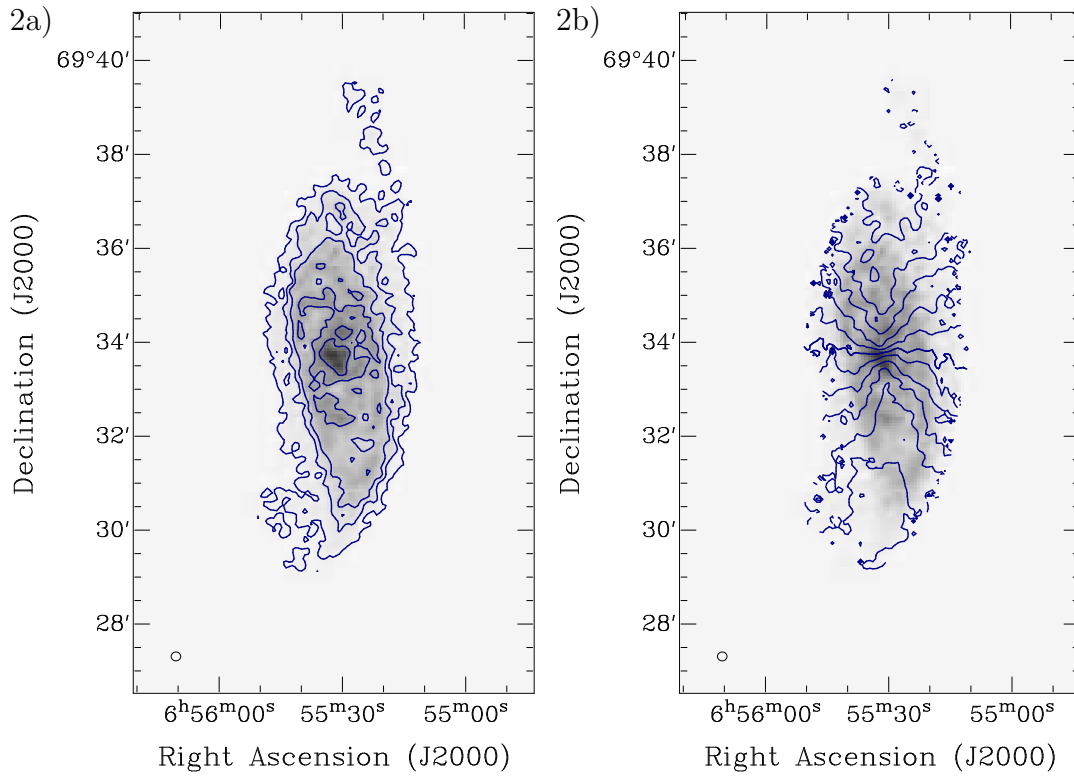


Fig. 4.10: (continued) UGC 3580. The contours represent the $8, 35, 69, 139, 208 \cdot 10^{19} \text{ atoms cm}^{-2}$ levels and the $v_{\text{sys}} \pm 0, 20, 40, 60, 80, 100 \text{ km s}^{-1}$ levels respectively (see Tab. 4.2). The approaching side is orientated towards SE.

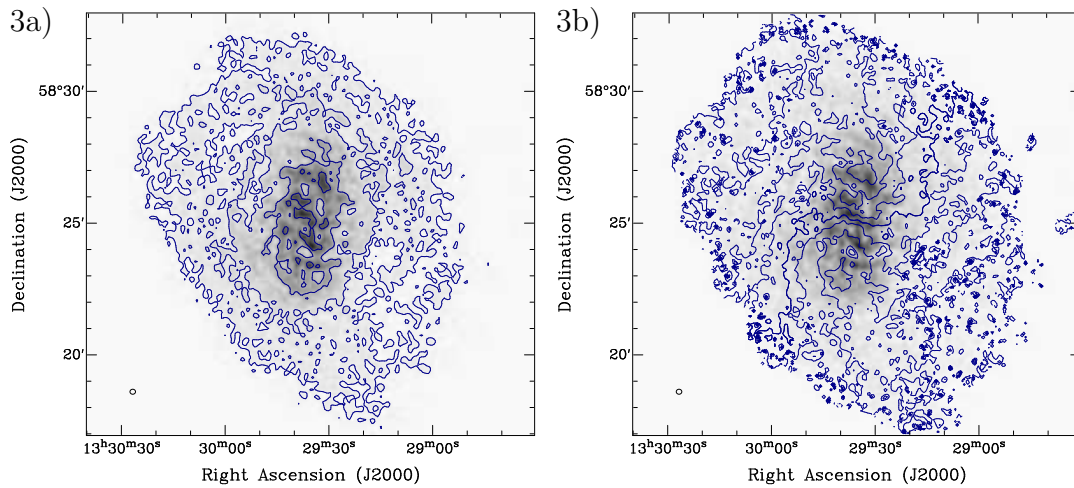


Fig. 4.10: (continued) NGC 5204. The contours represent the $11, 32, 97, 194 \cdot 10^{19} \text{ atoms cm}^{-2}$ levels and the $v_{\text{sys}} \pm 0, 15, 30, 45, 60 \text{ km s}^{-1}$ levels respectively (see Tab. 4.2). The approaching side is orientated towards NE.

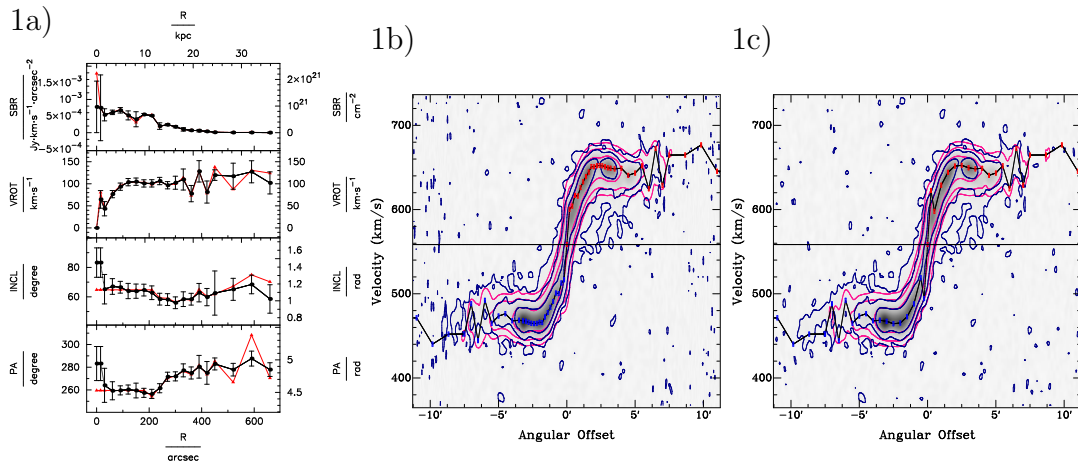


Fig. 4.11: Comparison of best-fit models of low-resolution datacubes with and without enforcing an inner flat disk. a) In black (dots): Best-fit parameters without enforcing an inner flat disk. In red (triangles): Best-fit parametrisation enforcing a flat inner disk. SBR: surface brightness. VROT: rotation velocity. INCL: inclination. PA: position angle. R: radius. b) PV-diagrams along the kinematical major axis comparing best-fit models with an inner flat disk (pink contours) with the original low-resolution data (blue contours). The vertical line marks the systemic velocity, the boxes connected with the lines denote the rotation curve corrected for the inclination. c) PV-diagrams along the kinematical major axis comparing best-fit models without enforcing an inner flat disk (pink contours) with the original low-resolution data (blue contours). Contour levels are at 1,4,16 mJy/beam. The data are consistent with an inner flat disk, while for NGC 2541 a close inspection showed that allowing for a central tilt resulted in slightly better results. NGC 2541.

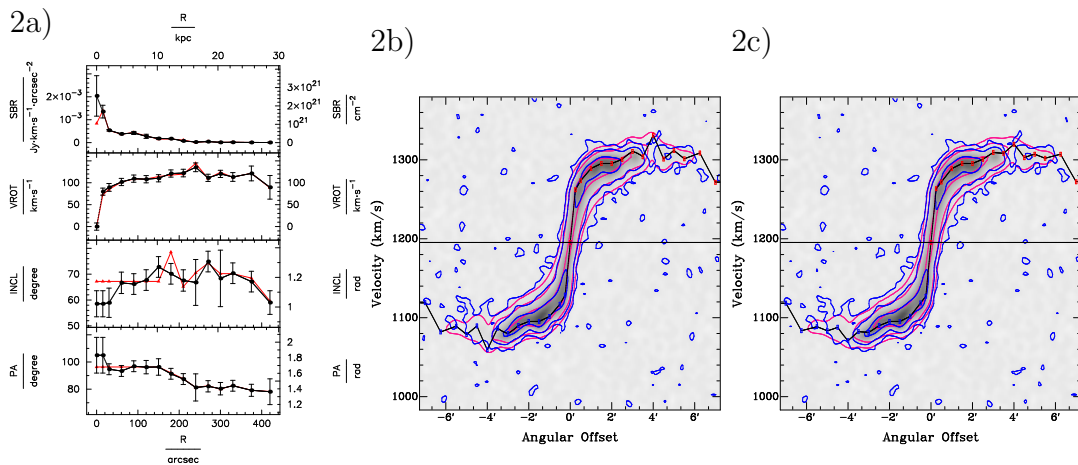
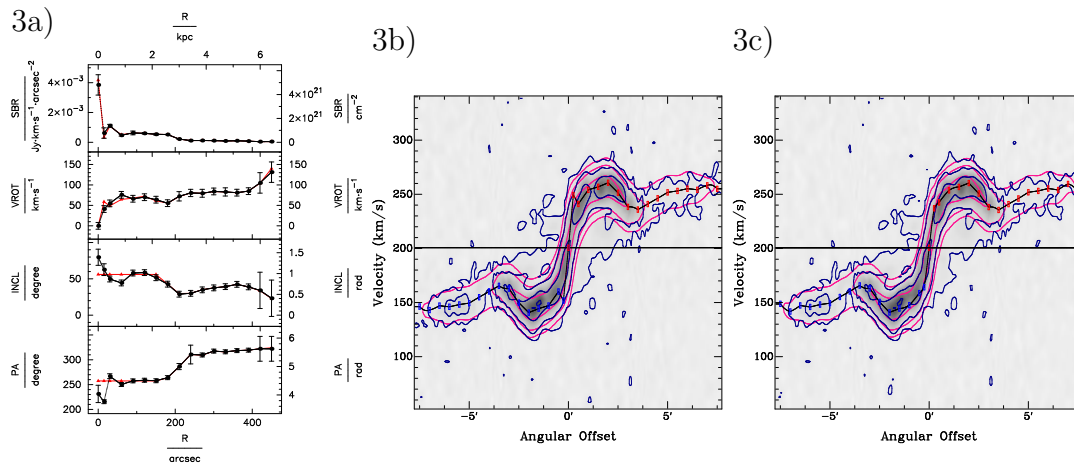


Fig. 4.11: (continued) UGC 3580. Contour levels are at 1,4,16 mJy/beam.



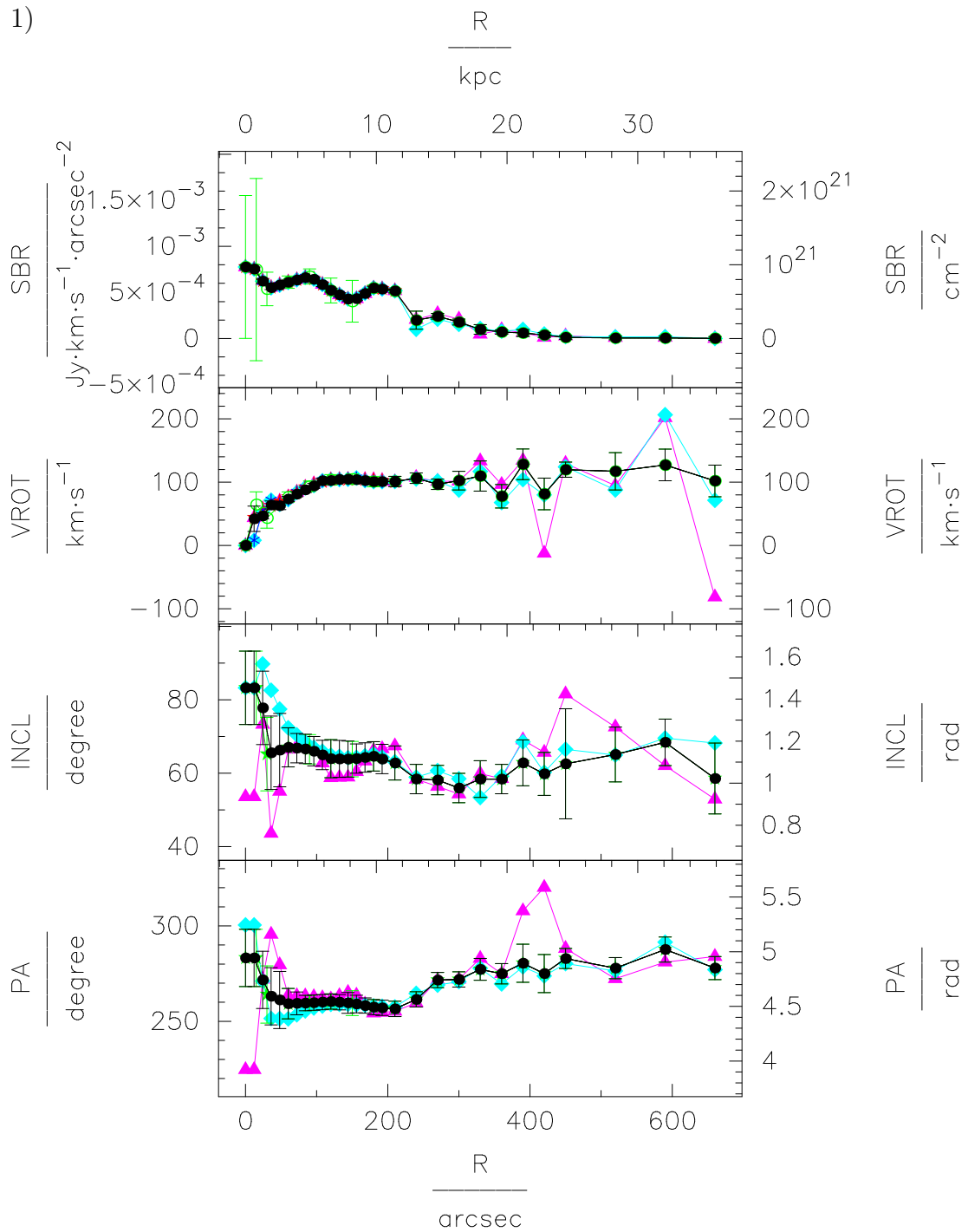


Fig. 4.12: Determination of the final parametrisations of the galaxies. Viewgraphs showing the models and error bar estimation. SBR: surface brightness. VROT: rotation velocity. INCL: inclination. PA: position angle. R: radius. Black curves (dots): finally adopted model and error bars. Red curves (stars): receding side fitting results from high resolution fitting. Blue curves (asterisks): approaching side fitting results from high resolution fitting. Pink (triangles): interpolated receding side fitting results from low resolution fitting. Light blue (diamonds): interpolated approaching side fitting results from low resolution fitting. Green (open circles): Results and preliminary error bars from low resolution fitting. NGC 2541.

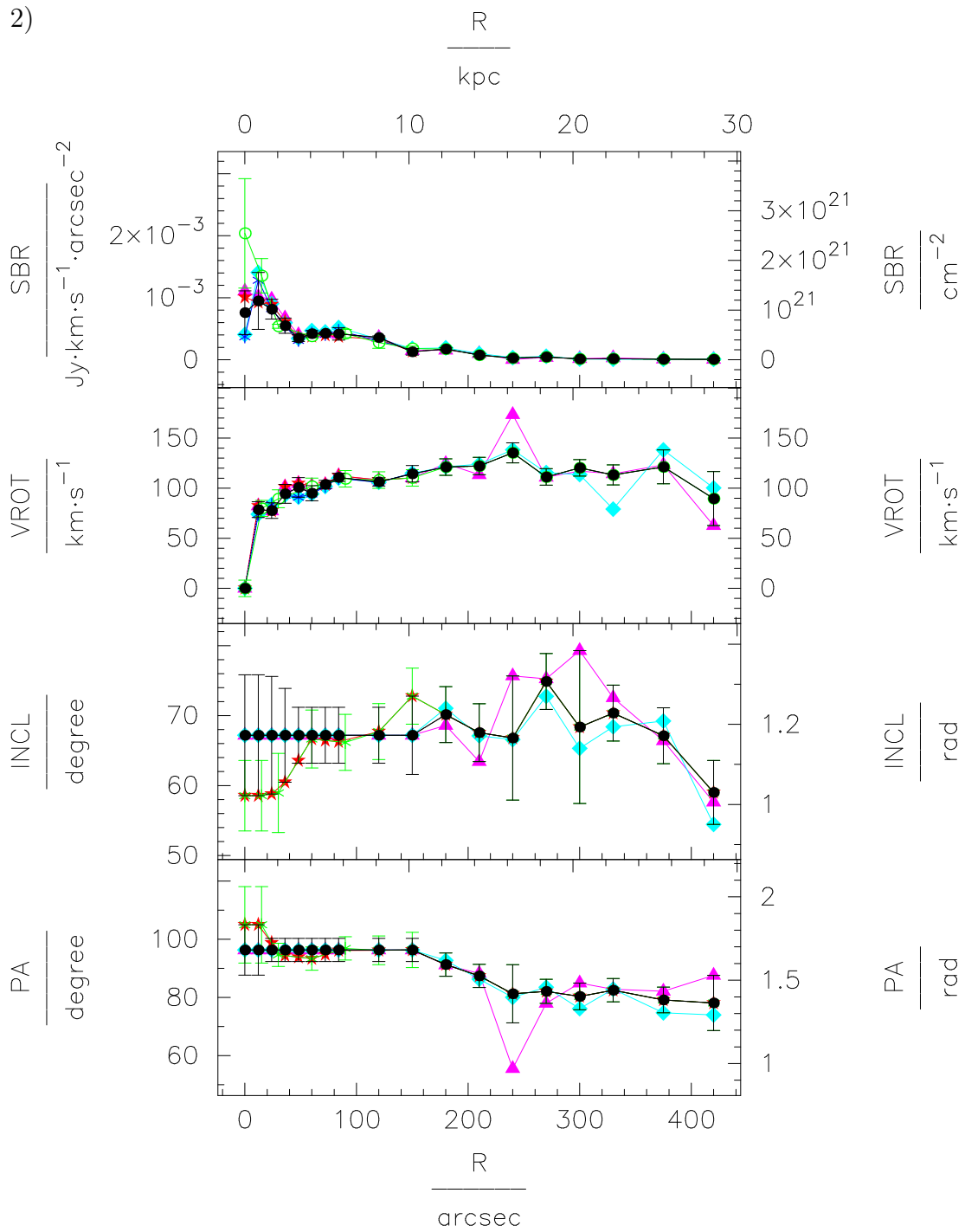


Fig. 4.12: (continued) UGC 3580. Red data points (stars) in the position angle and the inclination viewgraphs mark the adopted data points from the low resolution fits used for error bar estimation.

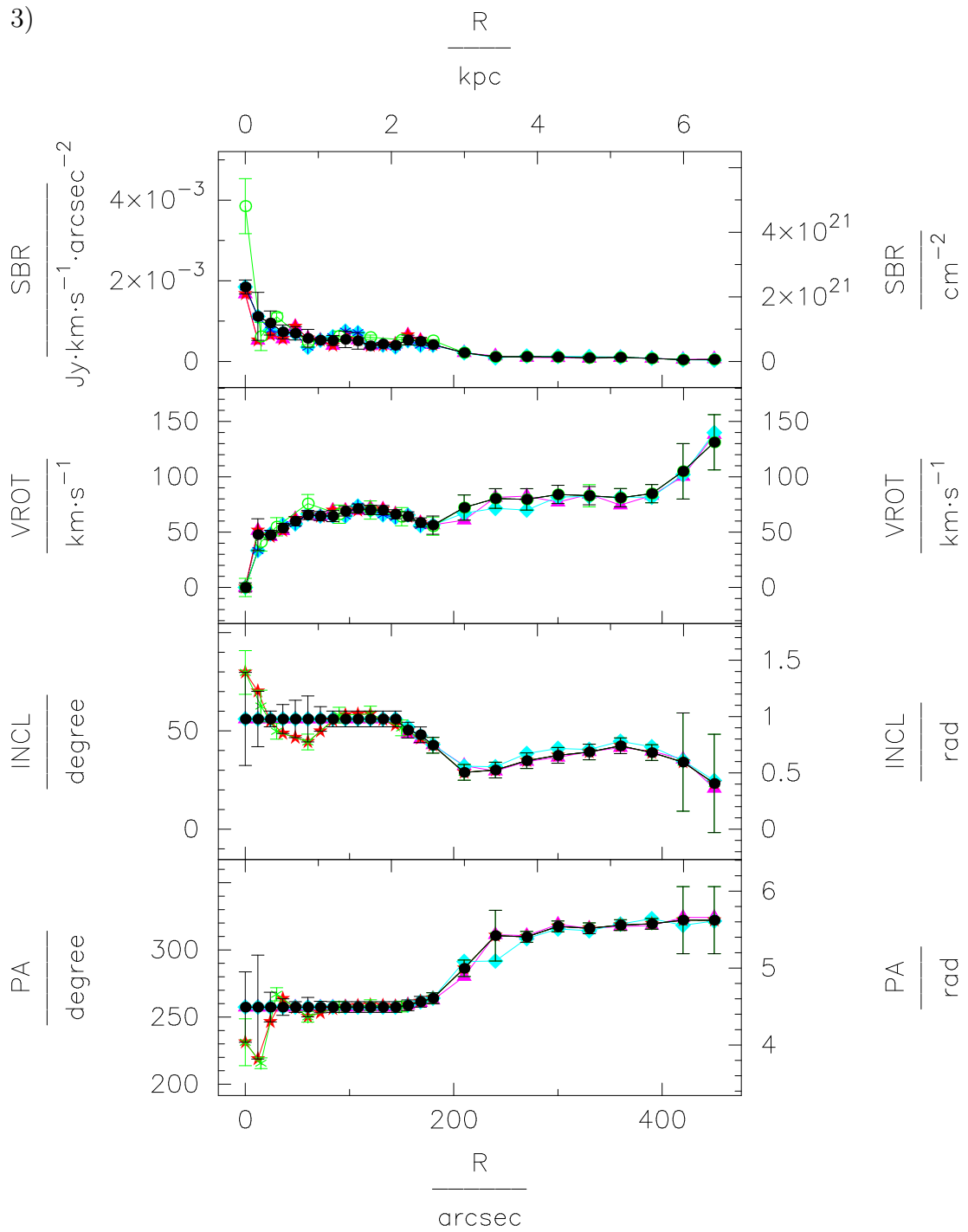


Fig. 4.12: (continued) NGC 5204. Red data points (stars) in the position angle and the inclination viewgraphs mark the adopted data points from the low resolution fits used for error bar estimation.

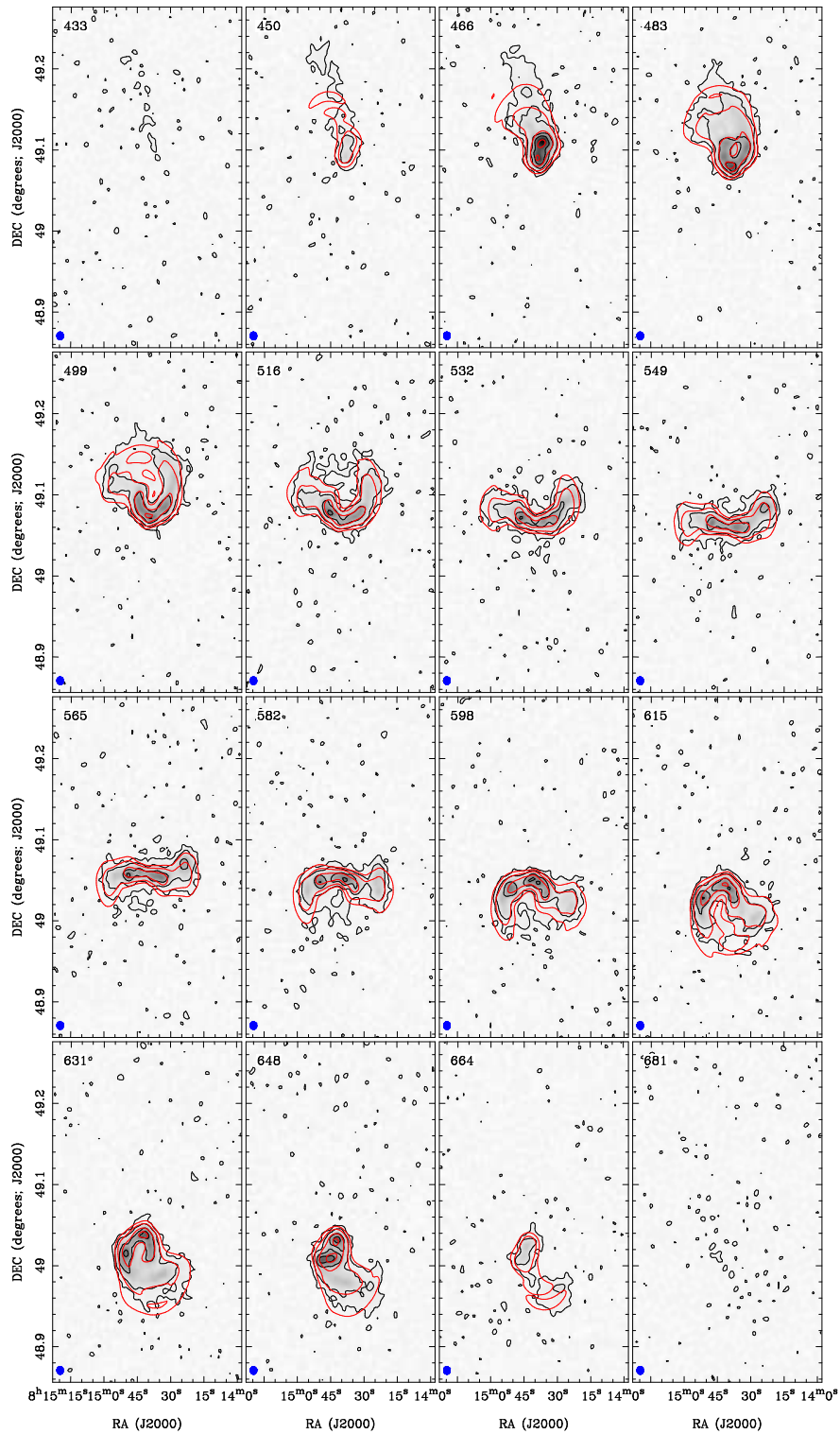


Fig. 4.13: Selected images from the low-resolution datacubes overlaid with contours of the original dataset (blue) and the final model datacube (pink). The numbers on the upper left give the heliocentric radio velocity in km s^{-1} . The blue dot represents the clean beam. NGC 2541. The contours represent the 1, 4, 16, 32 mJy/beam levels.

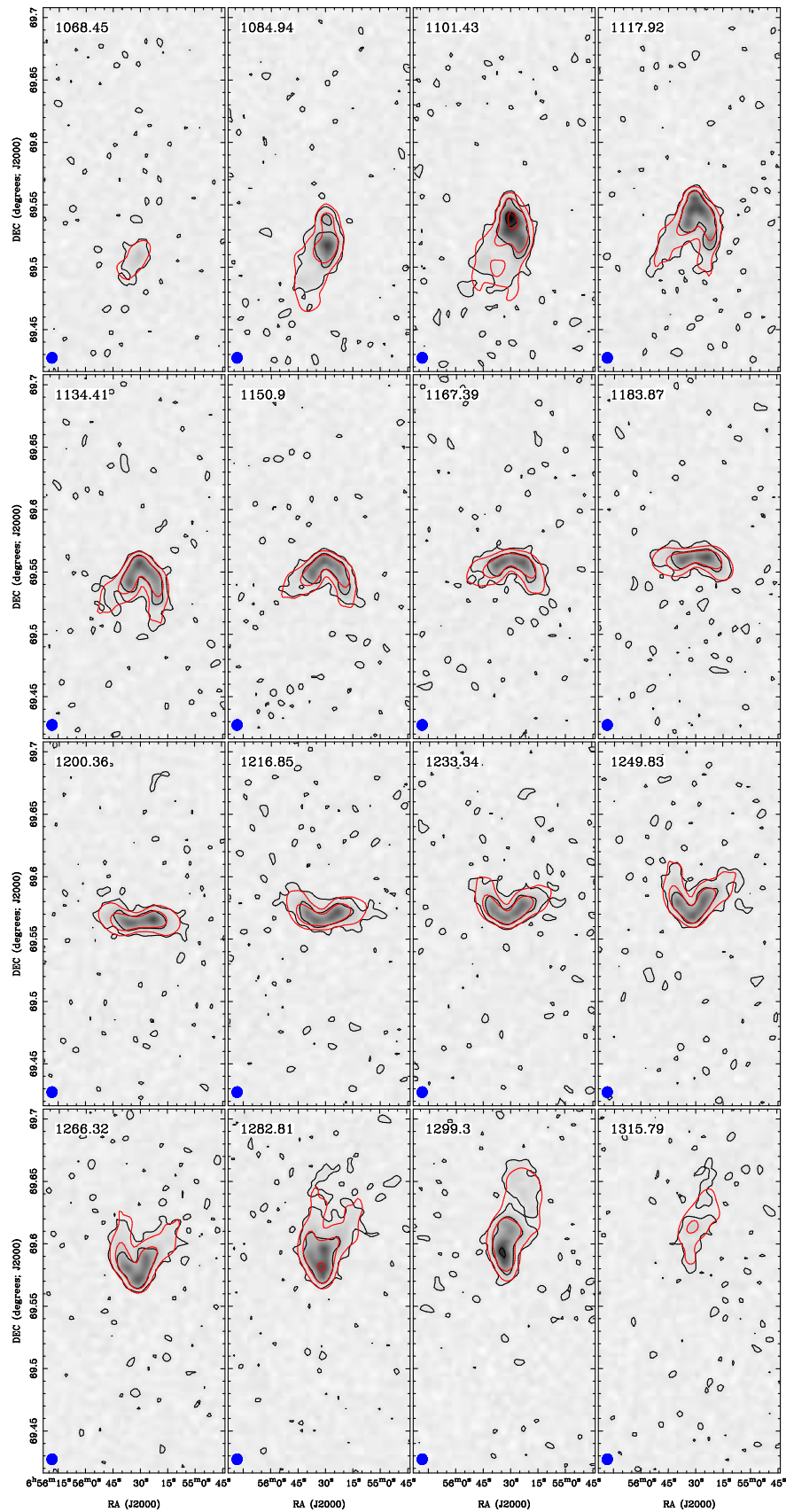


Fig. 4.13: (continued) UGC 3580. The contours represent the 1, 6, 24 mJy/beam levels.

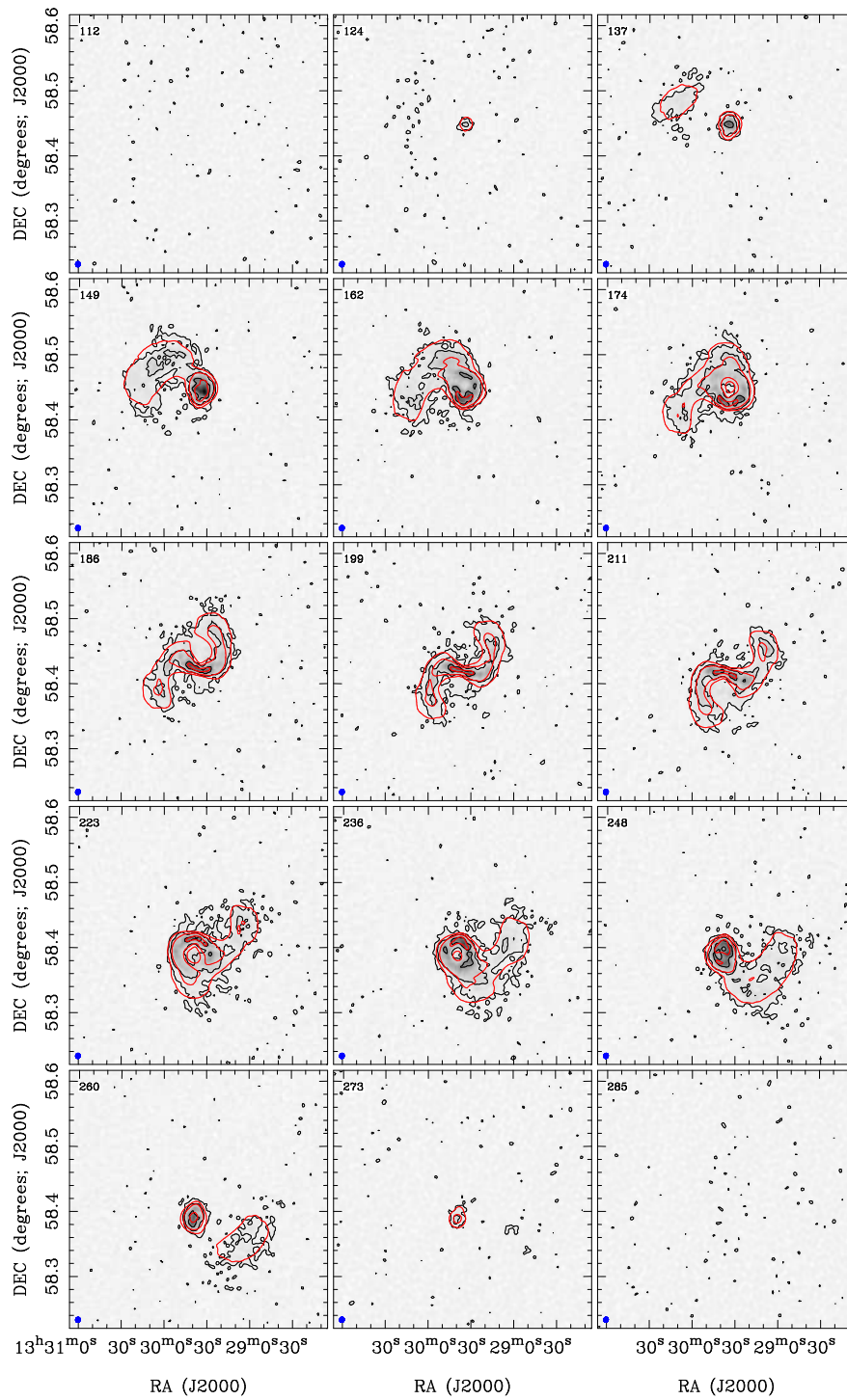


Fig. 4.13: (continued) NGC 5204. The contours represent the 1, 4, 16 mJy/beam levels.

r_p (1)	r_t (2)	Δr_t (3)	$I_{\text{tot.f}}$ (4)	$\Delta I_{\text{tot.f}}$ (5)	N_{HI} (6)	ΔN_{HI} (7)	σ (8)	$\Delta \sigma$ (9)	v_{rot} (10)	Δv_{rot} (11)
0	0.00	0.00	77.6	2.0	96.9	2.5	7.8	0.2	0.0	4.1
12	0.65	0.05	75.4	2.0	94.2	2.5	7.5	0.2	42.1	20.0
24	1.31	0.09	62.3	2.0	77.8	2.5	6.2	0.2	46.7	4.7
36	1.96	0.14	55.1	2.0	68.9	2.5	5.5	0.2	64.0	6.4
48	2.61	0.19	58.1	2.0	72.5	2.5	5.8	0.2	62.9	6.3
60	3.26	0.23	61.0	2.0	76.2	2.5	6.1	0.2	73.4	4.1
72	3.92	0.28	63.5	2.0	79.3	2.5	6.4	0.2	81.0	4.1
84	4.57	0.33	66.1	2.0	82.5	2.5	6.6	0.2	87.9	4.1
96	5.22	0.37	64.3	2.0	80.3	2.5	6.4	0.2	94.2	4.1
108	5.87	0.42	58.4	2.0	73.0	2.5	5.8	0.2	102.3	4.1
120	6.53	0.47	52.3	2.0	65.3	2.5	5.2	0.2	102.7	4.1
132	7.18	0.51	47.5	2.0	59.3	2.5	4.8	0.2	104.2	4.1
144	7.83	0.56	42.8	2.0	53.5	2.5	4.3	0.2	104.6	4.1
156	8.49	0.61	43.3	2.0	54.0	2.5	4.3	0.2	104.0	4.1
168	9.14	0.65	48.9	2.0	61.1	2.5	4.9	0.2	102.5	4.1
180	9.79	0.70	54.7	2.0	68.3	2.5	5.5	0.2	100.9	4.1
192	10.44	0.74	53.6	2.0	67.0	2.5	5.4	0.2	100.9	4.1
210	11.42	0.81	51.6	2.0	64.4	2.5	5.2	0.2	101.0	8.2
240	13.06	0.93	19.9	9.8	24.8	12.2	2.0	1.0	106.3	8.2
270	14.69	1.05	24.1	3.1	30.1	3.8	2.4	0.3	96.7	8.2
300	16.32	1.16	17.9	3.2	22.3	4.0	1.8	0.3	102.4	14.8
330	17.95	1.28	9.9	5.2	12.4	6.5	1.0	0.5	109.7	23.8
360	19.58	1.40	7.1	2.4	8.9	3.0	0.7	0.2	77.7	18.4
390	21.21	1.51	6.0	3.8	7.5	4.7	0.6	0.4	128.3	24.2
420	22.85	1.63	3.9	2.6	4.9	3.3	0.4	0.3	81.3	25.0
450	24.48	1.75	1.3	2.0	1.6	2.5	0.1	0.2	119.7	12.0
520	28.29	2.02	0.6	2.0	0.7	2.5	0.1	0.2	117.2	29.5
590	32.09	2.29	0.6	2.0	0.8	2.5	0.1	0.2	127.2	25.0
660	35.90	2.56	0.1	2.0	0.2	2.5	0.0	0.2	102.0	25.0

Tab. 4.5: Radially dependent best-fit parameters for the examined galaxies. (1) Radius ($''$). (2) Radius (kpc, according to Tab. 4.1). (3) Error of r_t (kpc) (4) Face-on surface brightness (Jy km s^{-1}). (5) Error of $I_{\text{tot.f}}$ (Jy km s^{-1}). (6) Face-on HI column density ($10^{19} \text{ atoms cm}^{-2}$). (7) Error of N_{HI} ($10^{19} \text{ atoms cm}^{-2}$). (8) Face-on surface density ($\text{M}_{\odot} \text{ pc}^{-2}$). (9) Error of σ ($\text{M}_{\odot} \text{ pc}^{-2}$). (10) Rotation velocity (kms^{-1}). (11) Error of v_{rot} (kms^{-1}).

r_p (1)	i (12)	Δi (13)	pa (14)	Δpa (15)	n_W (16)	Δn_W (17)	n_N (18)	Δn_N (19)	n_{LOS} (20)	Δn_{LOS} (21)
0	83.3	10.0	283.2	15.0	-0.967	0.063	-0.227	0.253	0.117	0.173
12	83.3	10.0	283.2	15.0	-0.967	0.063	-0.227	0.253	0.117	0.173
24	77.8	10.0	271.7	15.0	-0.977	0.038	-0.029	0.256	0.211	0.171
36	65.6	10.0	263.1	15.0	-0.904	0.077	0.109	0.237	0.414	0.159
48	66.3	10.0	261.2	15.0	-0.905	0.078	0.141	0.237	0.402	0.160
60	67.0	5.3	259.2	7.9	-0.905	0.043	0.172	0.126	0.390	0.086
72	66.8	4.0	259.4	6.0	-0.904	0.032	0.169	0.095	0.393	0.064
84	66.6	4.0	259.5	4.0	-0.903	0.030	0.167	0.064	0.397	0.064
96	66.0	4.0	259.8	4.0	-0.899	0.030	0.163	0.063	0.407	0.064
108	65.0	4.0	260.1	4.0	-0.893	0.031	0.156	0.063	0.423	0.063
120	64.0	5.2	260.4	4.0	-0.886	0.041	0.150	0.062	0.439	0.081
132	63.9	5.0	260.0	4.0	-0.884	0.040	0.156	0.062	0.440	0.079
144	63.9	4.9	259.7	5.5	-0.883	0.040	0.161	0.084	0.440	0.077
156	64.0	4.0	259.1	4.6	-0.882	0.033	0.170	0.071	0.438	0.063
168	64.3	4.0	258.2	4.0	-0.882	0.032	0.184	0.062	0.434	0.063
180	64.6	4.0	257.4	4.0	-0.882	0.032	0.197	0.062	0.429	0.063
192	63.9	4.0	257.1	4.0	-0.875	0.033	0.201	0.061	0.440	0.063
210	62.8	4.6	256.5	4.0	-0.865	0.039	0.207	0.061	0.457	0.072
240	58.4	4.0	261.5	4.0	-0.843	0.037	0.126	0.059	0.524	0.059
270	58.1	4.0	271.6	4.0	-0.849	0.037	-0.024	0.059	0.528	0.059
300	56.0	4.0	271.9	4.0	-0.828	0.039	-0.028	0.058	0.560	0.058
330	58.4	5.0	277.2	5.7	-0.845	0.047	-0.107	0.085	0.524	0.074
360	58.4	4.0	274.9	5.3	-0.849	0.037	-0.073	0.079	0.524	0.059
390	62.8	6.3	280.4	10.0	-0.875	0.057	-0.161	0.153	0.456	0.097
420	59.8	5.9	275.0	10.0	-0.861	0.053	-0.075	0.150	0.503	0.088
450	62.6	15.0	282.9	5.3	-0.865	0.119	-0.198	0.084	0.461	0.232
520	65.1	7.5	277.8	5.5	-0.899	0.056	-0.124	0.087	0.421	0.118
590	68.4	6.3	287.6	6.6	-0.886	0.050	-0.281	0.102	0.368	0.103
660	58.6	9.7	277.9	6.0	-0.845	0.088	-0.117	0.090	0.521	0.144

Tab. 4.5: (continued) NGC 2541. **(12)** Inclination ($^\circ$). **(13)** Error of i ($^\circ$). **(14)** Position angle ($^\circ$). **(15)** Error of pa ($^\circ$). **(16)** Inclination ($^\circ$). **(17)-(23)** are Cartesian components of the spin normal vector \mathbf{n} of the ring and their errors. **(17)** Spin normal vector component towards W (natural units). **(18)** Error of n_W (natural units). **(19)** Spin normal vector component towards N (natural units). **(20)** Error of n_N (natural units). **(21)** Spin normal vector component towards observer (natural units). **(22)** Error of n_{LOS} (natural units).

r_p (1)	r_t (2)	Δr_t (3)	$I_{\text{tot},f}$ (4)	$\Delta I_{\text{tot},f}$ (5)	N_{HI} (6)	ΔN_{HI} (7)	σ (8)	$\Delta \sigma$ (9)	v_{rot} (10)	Δv_{rot} (11)
0	0.00	0.00	75.9	35.2	94.8	44.0	7.6	3.5	0.0	0.0
12	0.82	0.17	94.8	45.9	118.4	57.3	9.5	4.6	78.5	7.9
24	1.63	0.33	81.6	15.9	101.9	19.9	8.2	1.6	77.6	7.8
36	2.45	0.50	55.0	12.3	68.6	15.3	5.5	1.2	94.3	9.4
48	3.26	0.66	34.9	5.4	43.6	6.7	3.5	0.5	100.8	9.8
60	4.08	0.83	42.0	5.0	52.4	6.3	4.2	0.5	95.0	7.6
72	4.90	1.00	42.7	2.1	53.3	2.7	4.3	0.2	103.7	4.1
84	5.71	1.16	41.8	10.1	52.2	12.6	4.2	1.0	110.7	4.1
120	8.16	1.66	35.9	2.5	44.8	3.1	3.6	0.3	106.2	4.1
150	10.20	2.08	12.9	5.4	16.1	6.7	1.3	0.5	114.4	8.2
180	12.24	2.49	17.4	2.0	21.7	2.5	1.7	0.2	121.1	8.2
210	14.28	2.91	7.6	2.4	9.5	3.0	0.8	0.2	122.2	8.7
240	16.32	3.32	2.8	2.2	3.5	2.7	0.3	0.2	135.3	10.0
270	18.36	3.74	4.5	2.0	5.7	2.5	0.5	0.2	111.2	8.2
300	20.41	4.15	1.4	2.0	1.7	2.5	0.1	0.2	120.3	8.2
330	22.45	4.57	1.7	2.0	2.1	2.5	0.2	0.2	113.2	10.0
375	25.51	5.19	0.8	2.0	1.0	2.5	0.1	0.2	121.3	16.9
420	28.57	5.82	0.7	2.0	0.9	2.5	0.1	0.2	89.6	27.0

Tab. 4.5: (continued) UGC 3580.

r_p (1)	i (12)	Δi (13)	pa (14)	Δpa (15)	n_W (16)	Δn_W (17)	n_N (18)	Δn_N (19)	n_{LOS} (20)	Δn_{LOS} (21)
0	67.2	8.6	96.3	8.6	0.916	0.060	0.102	0.138	0.388	0.139
12	67.2	8.6	96.3	8.6	0.916	0.060	0.102	0.138	0.388	0.139
24	67.2	8.4	96.3	4.0	0.916	0.057	0.102	0.064	0.388	0.135
36	67.2	6.7	96.3	4.0	0.916	0.046	0.102	0.064	0.388	0.108
48	67.2	4.0	96.3	4.0	0.916	0.028	0.102	0.064	0.388	0.064
60	67.2	4.0	96.3	4.0	0.916	0.028	0.102	0.064	0.388	0.064
72	67.2	4.0	96.3	4.0	0.916	0.028	0.102	0.064	0.388	0.064
84	67.2	4.0	96.3	4.0	0.916	0.028	0.102	0.064	0.388	0.064
120	67.2	4.0	96.3	4.0	0.916	0.028	0.102	0.064	0.388	0.064
150	67.2	5.6	96.3	4.0	0.916	0.038	0.102	0.064	0.388	0.090
180	70.1	4.0	91.3	4.0	0.940	0.024	0.021	0.066	0.340	0.066
210	67.6	4.1	87.4	4.0	0.923	0.028	-0.042	0.064	0.382	0.067
240	66.8	8.9	81.3	10.0	0.909	0.065	-0.139	0.159	0.394	0.142
270	74.9	4.0	82.1	4.1	0.956	0.020	-0.133	0.069	0.261	0.067
300	68.4	10.9	80.4	4.6	0.916	0.070	-0.156	0.074	0.369	0.177
330	70.4	4.0	82.5	4.0	0.934	0.025	-0.123	0.065	0.336	0.066
375	67.1	4.0	79.2	4.4	0.905	0.030	-0.173	0.070	0.389	0.064
420	59.0	4.6	78.1	9.5	0.839	0.050	-0.177	0.139	0.515	0.068

Tab. 4.5: (continued) UGC 3580.

r_p (1)	r_t (2)	Δr_t (3)	$I_{\text{tot},f}$ (4)	$\Delta I_{\text{tot},f}$ (5)	N_{HI} (6)	ΔN_{HI} (7)	σ (8)	$\Delta \sigma$ (9)	v_{rot} (10)	Δv_{rot} (11)
0	0.00	0.00	184.7	17.4	230.6	21.7	18.5	1.7	0.0	4.1
12	0.17	0.04	111.8	59.4	139.6	74.2	11.2	5.9	47.7	14.4
24	0.34	0.08	95.3	29.9	119.0	37.3	9.5	3.0	47.5	4.1
36	0.51	0.12	73.2	17.3	91.4	21.6	7.3	1.7	53.8	4.1
48	0.68	0.16	69.8	16.5	87.1	20.6	7.0	1.7	59.9	4.1
60	0.86	0.20	57.4	22.1	71.7	27.5	5.7	2.2	65.4	4.1
72	1.03	0.24	52.7	2.0	65.9	2.5	5.3	0.2	64.6	4.1
84	1.20	0.28	52.0	12.6	65.0	15.7	5.2	1.3	64.5	5.1
96	1.37	0.32	54.8	20.4	68.4	25.5	5.5	2.0	68.9	4.4
108	1.54	0.36	51.0	20.4	63.6	25.4	5.1	2.0	71.2	4.1
120	1.71	0.40	38.8	5.4	48.5	6.7	3.9	0.5	70.1	4.1
132	1.88	0.44	43.4	3.1	54.2	3.9	4.3	0.3	69.8	4.1
144	2.05	0.48	40.1	3.9	50.1	4.8	4.0	0.4	66.2	4.1
156	2.23	0.52	53.0	12.2	66.2	15.2	5.3	1.2	64.2	4.1
168	2.40	0.56	49.9	9.5	62.3	11.9	5.0	1.0	58.7	4.1
180	2.57	0.60	41.7	2.0	52.1	2.5	4.2	0.2	56.3	8.2
210	3.00	0.69	21.7	2.0	27.0	2.5	2.2	0.2	72.2	11.4
240	3.42	0.79	11.5	2.6	14.4	3.2	1.2	0.3	80.4	8.9
270	3.85	0.89	11.9	2.0	14.9	2.5	1.2	0.2	79.6	9.7
300	4.28	0.99	11.2	2.1	14.0	2.6	1.1	0.2	84.0	8.2
330	4.71	1.09	9.1	3.0	11.3	3.7	0.9	0.3	82.9	8.2
360	5.14	1.19	10.2	2.0	12.8	2.5	1.0	0.2	81.1	8.2
390	5.57	1.29	7.8	2.0	9.7	2.5	0.8	0.2	84.8	8.2
420	5.99	1.39	4.2	2.0	5.2	2.5	0.4	0.2	105.0	25.0
450	6.42	1.49	4.7	2.0	5.9	2.5	0.5	0.2	131.2	25.0

Tab. 4.5: (continued) NGC 5204.

r_p (1)	i (12)	Δi (13)	pa (14)	Δpa (15)	n_W (16)	Δn_W (17)	n_N (18)	Δn_N (19)	n_{LOS} (20)	Δn_{LOS} (21)
0	56.1	23.7	257.4	26.2	-0.810	0.240	0.181	0.374	0.558	0.343
12	56.1	14.1	257.4	38.7	-0.810	0.181	0.181	0.547	0.558	0.204
24	56.1	4.0	257.4	11.0	-0.810	0.051	0.181	0.156	0.558	0.058
36	56.1	7.4	257.4	6.2	-0.810	0.073	0.181	0.089	0.558	0.107
48	56.1	9.5	257.4	4.0	-0.810	0.092	0.181	0.060	0.558	0.138
60	56.1	11.7	257.4	7.2	-0.810	0.113	0.181	0.105	0.558	0.169
72	56.1	6.2	257.4	4.3	-0.810	0.061	0.181	0.062	0.558	0.090
84	56.1	4.0	257.4	4.0	-0.810	0.040	0.181	0.057	0.558	0.058
96	56.1	4.0	257.4	4.0	-0.810	0.040	0.181	0.057	0.558	0.058
108	56.1	4.0	257.4	4.0	-0.810	0.040	0.181	0.057	0.558	0.058
120	56.1	4.0	257.4	4.0	-0.810	0.040	0.181	0.057	0.558	0.058
132	56.1	4.0	257.4	4.0	-0.810	0.040	0.181	0.057	0.558	0.058
144	56.1	4.0	257.4	4.0	-0.810	0.040	0.181	0.057	0.558	0.058
156	50.4	4.0	258.8	4.0	-0.756	0.045	0.150	0.053	0.638	0.054
168	48.0	4.0	261.4	4.0	-0.735	0.047	0.111	0.052	0.669	0.052
180	42.7	4.0	264.0	4.0	-0.674	0.051	0.070	0.047	0.735	0.047
210	28.9	4.0	286.3	6.1	-0.464	0.060	-0.136	0.053	0.876	0.034
240	30.1	4.0	310.6	18.9	-0.381	0.117	-0.327	0.132	0.865	0.035
270	34.8	4.0	309.7	4.0	-0.439	0.051	-0.365	0.048	0.821	0.040
300	37.6	4.0	317.5	4.0	-0.412	0.049	-0.449	0.050	0.793	0.043
330	39.3	4.0	316.1	4.0	-0.439	0.049	-0.456	0.050	0.774	0.044
360	42.4	4.0	318.5	4.0	-0.447	0.049	-0.505	0.050	0.738	0.047
390	39.0	4.0	319.4	4.0	-0.409	0.049	-0.478	0.050	0.778	0.044
420	34.1	25.0	322.2	25.0	-0.344	0.294	-0.443	0.322	0.828	0.245
450	23.3	25.0	322.1	25.0	-0.242	0.281	-0.312	0.334	0.919	0.172

Tab. 4.5: (continued) NGC 5204.

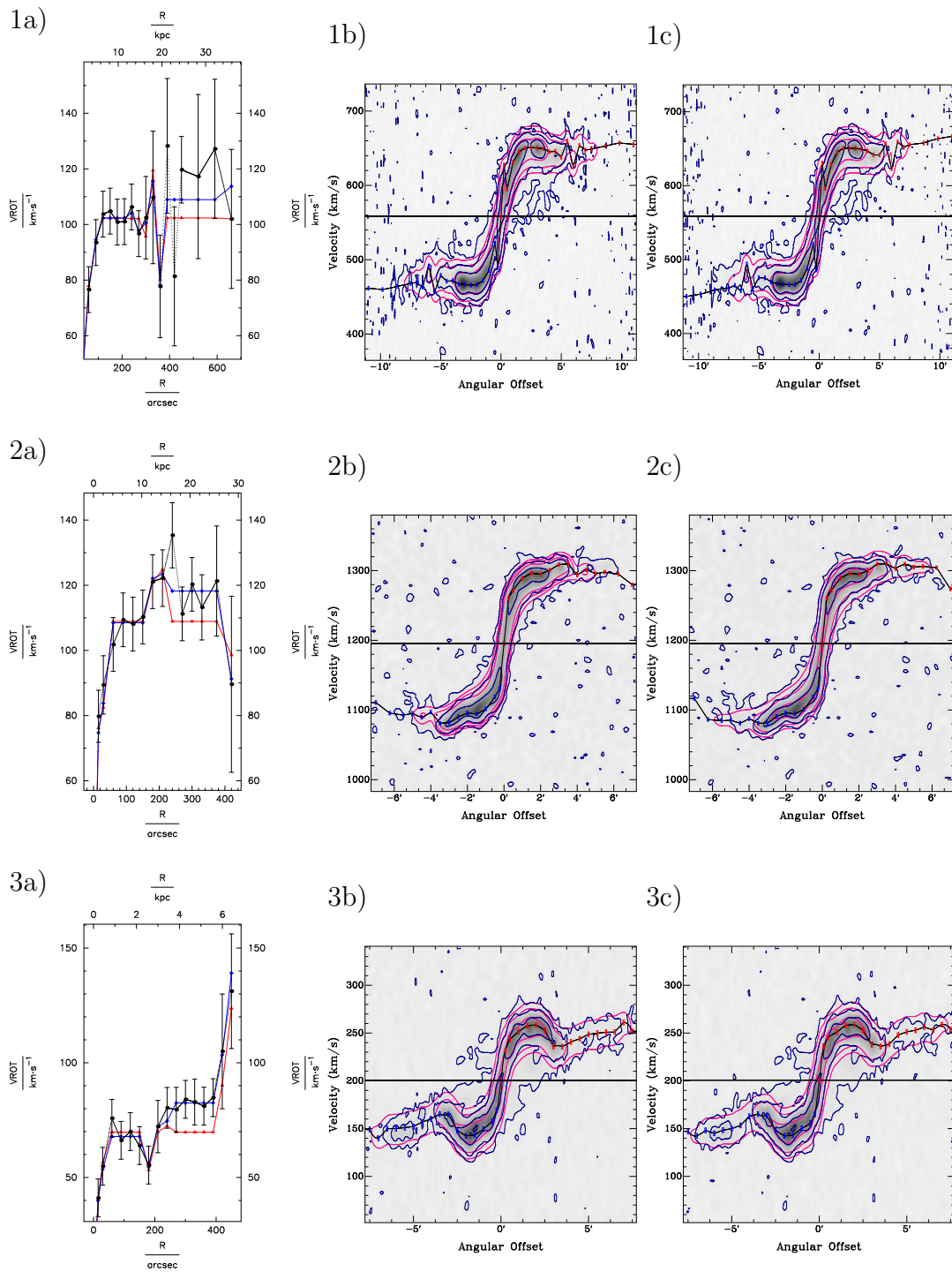


Fig. 4.14: Comparison of fits to the low-resolution datacube selecting two regions with flat rotation curves. Two fits to the datacube were performed. a) shows the fitting results for the rotation curve. b) and c) are comparisons of PV-diagrams of original datacube and model datacube along the kinematical major axis. b) and the blue curve in plot a): Enforcing the two selected regions to have the same rotation velocity. c) and the red curve in plot a): Enforcing the rotation curve to be flat inside the selected regions but allowing the rotation velocity to vary from region to region. Black curve in a): Low-resolution best-fit rotation curve 1) NGC 2541. Contours at 1,4,16 mJy/beam. 2) UGC 3580. Contours at 1,4,16 mJy/beam. 3) NGC 5204. Contours at 1,4,16,32 mJy/beam.

5 The warped Spindle NGC 2685

Deep HI and optical (i' -band) observations of the Spindle Galaxy NGC 2685 are presented, which until now is referred to as a prototype two-ringed polar ring galaxy. The HI observations show that the gaseous disk of NGC 2685 does not consist of two separate mutually inclined regions but builds a coherent structure that changes its orientation smoothly with radius, the appearance of both rings being due to projection effects. A comparison of the HI total-intensity maps with the optical image shows that at large radii the stellar disk, formerly known as the outer ring is well aligned with the HI disk. The form of the dust-lane structures obscuring the NW part of the inner stellar body indicates that also at smaller radii NGC 2685 possesses a disk containing gas, dust, and stars in which the single constituents are well aligned. NGC 2685 is not a polar-ring galaxy but a galaxy with an extremely warped disk, similar to the well known NGC 3718, the central bright stellar object possibly being a fast-rotating or tumbling bulge with a spin-axis misaligned with the inner disk but aligned with the outer disk. The HI disk is parametrised in terms of a tilted-ring model. Residual velocity maps show that in the reach of the elliptical central body the motion of the disk material is possibly deviating from circularity while beyond that radius it is well described by circular orbits.

5.1 Introduction

NGC 2685 obtained the name “Spindle Galaxy” by Sandage (1961) who referred to this peculiar object as “perhaps the most unusual galaxy in the Shapely-Ames catalogue”. In projection it contains a central bright object elongated from the NE to the SW. The whole of the NE side of the central object is obscured by dust-lanes with attached star-forming regions. Dust-lanes and H II regions are missing on the SW side. In projection the dust-lanes resemble a helical structure, hence NGC 2685 is frequently also called the “Helix”. At larger radii an outer stellar ring is visible on optical photographs that seemingly has the same orientation as the central object. The existence of such an object has stirred the phantasy and the curiosity of researchers since its existence is known and a search in the early literature on NGC 2685 is recommendable only because it is a splendid demonstration of human creativity.

Today, NGC 2685 is treated as a prototype two-ringed polar ring galaxy. A polar ring galaxy is defined by Whitmore et al. (1990) as a galaxy containing two systems of comparable size with the same systemic velocity and centre and nearly orthogonal angular momentum vectors. An inner gaseous component that was rotating rapidly about the projected minor axis of the central object was detected by Ulrich (1975) by means of a long-slit observation. She showed that inside

radii of $4''$ to $10''$ this component shows differential rotation with a projected amplitude of about 125 km s^{-1} . This was confirmed by Schechter & Gunn (1978), who analysed stellar absorption spectra and emission spectra employing long-slit observations along the projected major and minor axis of the central body. For the stellar component they found a velocity gradient along the major axis. They observed that the central galaxy shows a non-solid body rotation with a projected amplitude of 115 km s^{-1} and concluded that it was a lenticular galaxy seen edge-on, coining the third name of NGC 2685, ‘‘Pancake’’. They substantiated their conclusions by the fact that the velocity dispersion along the major axis was equal to or smaller than the rotation velocity. Their observations were later confirmed by Whitmore et al. (1990). Hence, NGC 2685 was claimed to be a polar-ring galaxy with a gaseous component that rotates at rather small radii on a polar orbit about a central lenticular galaxy. The today’s picture of NGC 2685 as containing two independent, clearly separated kinematic systems in the neutral gas was drawn by Shane (1977; 1980) and sustained in independent studies by and Mahon (1992) and Schinnerer & Scoville (2002). Examining WSRT observations of the galaxy, he concluded that the neutral gas resides in two rings, one connected with the dust-lane structure seen in the galaxy and one perpendicular gas ring at large radii, orientationally aligned with the central stellar body, rotating at a speed of about 150 km s^{-1} . He also remarked that the outer projected HI-ring resembles particular structures in the stellar outer ring of NGC 2685, indicating that the the outer gas and the outer stellar ring belong to the same structure. Whitmore et al. (1990) showed that the inner ring structure showed excess luminosity with respect to the central body, indicating the existence of a stellar component in the inner ring and the helical structure. In the same study they strengthened the picture of the central stellar body of NGC 2685 as being a lenticular galaxy by analysing the light profile along the major axis. They found it being compatible with a bulge-exponential disk system. Peletier & Christodoulou (1993), however, revised this finding. Examining deep optical observations, they found the light profile of the central body rather to be consistent with an E6/E7 elliptical than with a lenticular galaxy. They showed that the ‘‘inner ring’’ is only slightly bluer ($B - V = 0.71$) than the central body ($B - V = 0.87$) and thus contains an old stellar population. Assuming a rather low metallicity, they estimated the age of the stellar component in the helical structure to be about 5 Gy, while a solar abundance would give an age of at least 2 Gy. Eskridge & Pogge (1997) showed in a spectroscopic study of the H II regions in the helical structure that the metallicity in this component is about solar ($0.8 - 1.1 Z_{\odot}$). The helical structure of NGC 2685 has a gas phase abundance typical of an Sbc or Sc spiral galaxy (Eskridge & Pogge, 1997), while a colour (Peletier & Christodoulou, 1993) of an earlier type disk galaxy. Peletier & Christodoulou (1993), however, remarked that their measurement could be biased towards redder colours because of dust-reddening, possibly making the two observations consistent with each other. Interestingly, NGC 2685 resembles quite some qualities of low-mass spiral galaxies. The content of molecular gas with

$< 6 \cdot 10^6 M_{\odot}$ at an assumed distance of 13.5 Mpc is comparably low compared to the HI mass of NGC 2685 and also the ratio of blue luminosity and the mass of the molecular gas is low (Richter et al., 1994; Schinnerer & Scoville, 2002). A low FIR luminosity (Schinnerer & Scoville, 2002) indicates no starburst activity in this galaxy. The HI mass of the galaxy is fairly low compared to the blue luminosity ($\approx 0.3 M_{\odot} L_{\odot, B}$, Richter et al., 1994). As but the light coming from NGC 2685 is dominated by the bright lenticular object or central bulge, the helical structure itself together with the outer ring contains the gas in that galaxy. Except for its large metallicity NGC 2685 has the global properties of a low-surface-brightness galaxy with a bright central object.

Several formation mechanisms have been proposed in order to explain the structure of NGC 2685, most of which are based on the assumption that this galaxy contains two orthogonal rings. The age estimates for the helical structure (Peletier & Christodoulou, 1993) point towards the fact that this feature is long-lived, but not an extremely old component. Any theory explaining the structure of the galaxy has to take into account that fact. Usually, polar rings are assumed to be the result of secondary accretion or merger events around an existing galaxy (see Bournaud & Combes 2003 for a review), either a slow head-on collision and merger of two spiral galaxies, the result of which is the destruction of one galaxy leaving but a polar-ring structure (Bekki, 1997, 1998), or an accretion event where material is accreted from a gas-rich object (e.g. Schweizer et al., 1983; Reshetnikov & Sotnikova, 1997). While NGC 2685 is the dominating member of a small group of galaxies (Richter et al., 1994, see also below) and hence possible gas donators are in the reach, the structure of NGC 2685 imposes a problem for those scenarios. Firstly, the the high metallicity in the helical structure is typical for big spiral galaxies, which cannot be found in the reach of NGC 2685. Secondly, the Helix seemingly contains two orthogonal rings. If they are the result of one accretion event, a mechanism has to be sought to deposit the material into two preferred planes, while two accretion events as proposed by Shane (1980) are a somewhat unlikely scenario (see also Taniguchi et al., 1990). In order to stabilise a polar structure, which is necessary to make it consistent with the age-estimations for polar rings in general, it has been proposed to infer a generally triaxial shape of the underlying potential in which the polar orientation is then a preferred plane (see e.g. Whitmore et al., 1990; Reshetnikov et al., 1994) that the gas can partly settle into after an accretion event. If the ring material is massive, Sparke (1986) showed that a triaxial potential is not necessary to maintain a polar-ring structure against the destructing force of differential precession. The self-gravity then results in a slightly up to substantially warped structure in a state of co-precession. While her model includes the possibility of two separate structures originating from a single accretion event, it is not applicable in the case of NGC 2685. Supposing the central object to be oblate and to trace the orientation of the overall potential of NGC 2685, it would be expected that the

polar ring is positioned at the largest radii, while in NGC 2685 the situation is reversed (see also Varnas, 1990; Peletier & Christodoulou, 1993), making again two accretion events necessary in order to explain the double-ring structure of NGC 2685. Peletier & Christodoulou (1993) simulated the time-evolution of an extended gas ring deposited at large radii under the influence of a potential consistent with the appearance of the central body. Including the possibility that the net potential might not only be oblate or oblate-like triaxial but also assuming a prolate or prolate-like triaxial shape of the potential they found that a stable configuration resembling the two-ringed structure evolves only if the underlying potential would be prolate-like triaxial, the Pancake becoming a Spindle again. Their result, however, stands in contrast to the fact that the central body shows a rapid rotation. Peletier & Christodoulou (1993) also considered the case of a prolate axisymmetric potential with figure rotation, a bar-like structure that could produce a velocity gradient (but not a flat rotation curve) if the central body would precess with the potential. In this case, they find that a warp-preferred surface is created in which the gaseous material is deposited. Since they took it as given that the structure of NGC 2685 is two-ringed with separate rings, this model was excluded. The existence of a warp in the helical structure was but one of the first suggestions brought in connection with the formation of the Spindles peculiar structure. The helical structure in the Spindle covers the whole NE central body. Such an appearance is in principle inconsistent with the presence of a single polar ring (Taniguchi et al., 1990, see also) if the dust-lanes trace the gas and the stars of the helix structure. Instead, they are consistent with a warped central structure. It was pointed out by Simonson & Tohline (1983) that NGC 2685 could be an extremely warped galaxy, motivated by the findings of Tohline & Durisen (1982) and van Albada et al. (1982). They found that under the influence of a prolate tumbling potential the gas would settle into a stable extremely warped plane. This would require that indeed the central body of NGC 2685 is of a prolate shape and tumbling, which would partly be consistent with the velocity gradient present in the central stellar object. Moreover, this hypothesis would require that NGC 2685 would show a warp rather than two rings.

The main purpose of this chapter is to show by means of an analysis of newly acquired optical and radio data that the structure responsible for the appearance of NGC 2685 with its two rings and the helix belongs to an extremely warped disk. Both, the inner and the outer ring of NGC 2685 are the result of projection effects. Furthermore, the precise structure of the warped gaseous disk is determined employing a tilted-ring model. Except possibly at the edges of the projected central body, a tilted-ring model with the inherent circular motion of the disk material is found to be fully sufficient to describe the kinematics of the galaxy.

The chapter is laid out as follows: In Sect. 5.2 observations conducted with

the WSRT and the INT and the data reduction is described. In Sect. 5.3 the resulting datacubes and the optical image are presented and it is shown that NGC 2685 possesses one coherent disk, and not two separate disks. In Sect. 5.7 the data analysis by means of a new technique to perform a tilted-ring modelling is described, the results of which are shown and discussed in Sect. 5.8. In Sect. 5.9 the fitting results are critically reviewed and the possible presence and location of non-circular motions is discussed. Sect. 5.10 contains a discussion of the final results. Supplementary figures and tables not essential for a first reading of the chapter are placed in the last section.

5.2 Observations and data reduction

NGC 2685 was observed 4x12h with the WSRT in the HI emission line and deep i' -band observations with the 2.5m INT Wide Field Camera (La Palma) were conducted.

5.2.1 Optical observations and data reduction

The optical observations were performed in 2004 from February 26th until March 4th under varying weather conditions during grey/bright time. NGC 2685 was observed along with a number of other objects, and was at useful elevations at the beginning of each night. The last four of seven granted nights proved to bear useful data over large periods of time, meaning but that NGC 2685 was observed nearly completely in the presence of the moon. In each night, sky flats and bias frames were obtained. Photometric standards were observed regularly, although highly varying weather conditions make a photometric calibration difficult.

In a subsequent series of short exposures with a maximum of 400s single exposure time using a wide dithering scheme in order to guarantee large enough an overlap of the single chips, The total on-source observing time of useful science frames for NGC 2685 amounts to a total of 13350s.

To obtain a co-added image from the data we made use of the GaBoDS Wide Field Imager reduction pipeline (Schirmer et al., 2003). After the overscan- and bias correction, the images of each chip were flatfielded, superflatfielded and defringed on a per-night basis. Non-Gaussian noise-features (cosmic rays, hot and cold pixels) were detected and masked and the single frames visually inspected in order to apply a manual masking or, in some cases, to reject single frames. The images were then photometrically (relatively) calibrated, background-subtracted and co-added, taking into account the sky background variation in the single chips and solving for astrometric distortion and for the relative sensitivity of the chips making use of the USNO-A2 standard catalog. Using known average zero-points

for the WFC the resulting un-binned co-added map can roughly be estimated to contain a noise level of $25.8 \text{ mag arcsec}^{-2}$.

NGC 2685 was observed with the WSRT in December 2002 and January 2004 (see Tab. 5.1). The data underwent a standard data reduction with the Miriad (Sault et al., 1995) software package as described in Chap. 4. As for NGC 5204 in Chap. 4 with two visibility datasets, the four visibility datasets were merged into one after the initial reduction steps (reading, flagging and primarily calibrating the data). Again, two datacubes were finally used for further analysis the properties of which are described in Tab. 5.1. The reduction of the data for this galaxy was different in one respect, namely the occurrence of an short-time interference in a very narrow frequency range in the cube. It is a speciality of Miriad that enforces a special treatment of such narrow-line interferences. Miriad uses a single map for the dirty beam that is used for CLEANing the data in order to safe computing time and memory. As frequency changes, for maps of equal size this would introduce an error, as the resolution and hence the dirty beam scales with the wavelength that changes slightly over the observing bandpass. In that case one would have to have a scaled dirty beam for every channel map. In order to circumvent this, Miriad scales the spatial size of channel maps instead of the dirty beam. A dirty beam changes naturally with differing uv-coverages and Miriad determines the dirty beam of a spectral observation as a result from an average uv-coverage. If one wants to have a single correct dirty beam one has to care for the uv-coverage not to differ from channel to channel. If a frequency-dependent interference turns up, either one decides to flag the whole bandpass for the affected records, or the data are reduced independently for each bandpass range with differing uv-coverages after flagging. This method was applied for the HI data reduction. After separating the visibilities into three datasets, two out of the frequency range in which the interference occurred, one matching this frequency range, the affected visibilities in the separated dataset were flagged. Each dataset was then binned, hanning smoothed, and cleaned independently. The clean table from the affected dataset was finally convolved with the clean beam of the unaffected datasets and merged with those. This ensured that the resulting cube has the same intensity scale over the whole frequency range. While the observation of NGC 2685 itself was not affected by the interference, they lay in the frequency range of a pair of unknown companion galaxies, described in the following chapter.

Representative samples of resulting channel maps are shown in the Figs. 5.11 and 5.11. Total intensity maps and first moment maps were generated by first masking the cubes with the finally applied clean masks. The resulting maps are shown in Fig. 5.1 and 5.15. As in Chap. 4, for the calculation of the total HI flux as shown in the Tabs. 5.2 and 5.3, a primary beam correction was applied, while for the further work uncorrected maps were used in order to keep the noise distributed uniformly over the channel maps. For the noise estimation in the

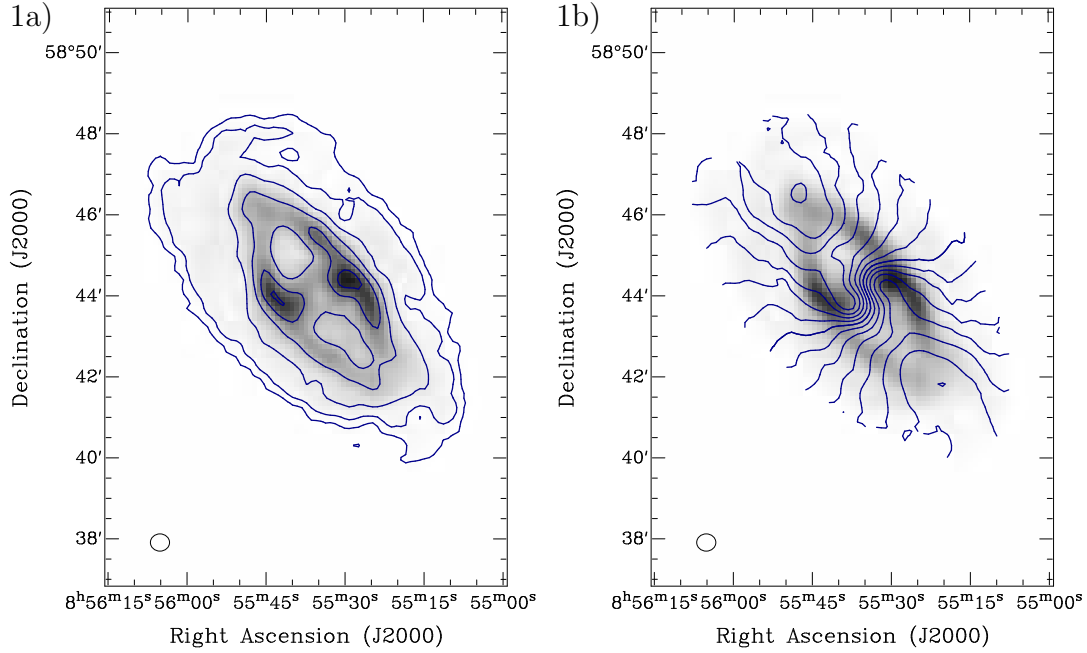


Fig. 5.1: *HI* total intensity maps (a, left) and first moment velocity fields (b, right) derived from the low-resolution datacubes overlaid on total intensity grey-scale maps. The ellipse in the lower left corner represents the clean beam. The contours represent the $1.5, 5, 16, 48, 96, 144 \cdot 10^{19} \text{ atoms cm}^{-2}$ levels and the $v_{\text{sys}} \pm 0, 20, 40, 60, 80, 100, 120, 140 \text{ km s}^{-1}$ levels respectively (see Tab. 5.1). The approaching side is orientated towards NE.

cubes the same approach as described in Chap. 4 was made. Tab. 5.1 gives an overview of the observations and the qualities of the finally obtained data.

5.3 Observations and the warped structure of NGC 2685

Basic properties of NGC 2685, derived in this work or taken from the literature, are listed in Tab. 5.2. Single estimates for the luminosities and other distance-dependent quantities differ from the literature as the distance of NGC 2685 was revised employing the Tully-Fisher relation (see Sect. 4.4). The derived total flux for NGC 2685 is in good agreement with single-dish measurements (Richter et al., 1994), showing that the *HI* measurements do not miss a substantial fraction of the flux.

Name	(1)	WSRT	
Integration	(2)	4 × 12	
Dates	(3)	19-20/12/02 21-22/12/02 7-8/01/03 8-9/01/03	
Resolution	(4)	high	low
Weighting	(5)	uniform	robust 0.4
dx	(6)	4	7
dv	(7)	2.06	4.12
HPBW _{maj}	(8)	13.7	28.4
HPBW _{min}	(9)	12.0	25.6
PA _{beam}	(10)	−0.6	10.6
σ_{rms}	(11)	0.42	0.24
σ_{rms}^N	(12)	1.16	0.30
$\sigma_{\text{rms}}^\sigma$	(13)	0.092	0.024
$\sigma_{\text{rms,tot}}$	(14)	0.012	0.012
$\sigma_{\text{rms,tot}}^N$	(15)	8.04	1.78
$\sigma_{\text{rms,tot}}^\sigma$	(16)	0.64	0.143
Name	(1)	INT WFC	
Integration	(2)	13350s	
Dates	(3)	26/02-04/03/04	
$\sigma_{i'}$	(17)	25.8	
$\sigma_{i',2''}$	(18)	21.3	

Tab. 5.1: Observations and data reduction, summary. **(1)** Name of telescope. **(2)** Total on-source integration time (h). **(3)** Observation dates **(4)** Type of datacube, for the high-resolution cube no binning in velocity direction was applied and use of the full array information was made, for the low-resolution cube the data were binned 2 channels into one in the velocity regime and only visibilities inside a radius of $6.4k\lambda_{\text{HI}}$ ($\lambda_{\text{HI}} \approx 21.1\text{cm}$) were used. **(5)** Applied weighting scheme. **(6)** Pixel size ("). **(7)** Channel width (km s^{-1}). **(8)** Half-power-beam-width along the beam major axis ("). **(9)** Half-power-beam-width along the beam minor axis ("). **(10)** Beam position angle ($^\circ$). **(11)** rms noise (mJy/beam) in the cubes. **(12)** rms noise per velocity resolution element ($10^{19}\text{atoms cm}^{-2}$). **(13)** rms noise per velocity resolution element ($M_\odot\text{pc}^{-2}$). **(14)** Maximal rms noise in the total intensity map (Jy/beam km s^{-1}). **(15)** Maximal rms noise in the total intensity map ($10^{19}\text{atoms cm}^{-2}$). **(16)** Maximal rms noise in the total intensity map ($M_\odot\text{pc}^{-2}$). **(17)** rms noise in the optical image (mag arcsec^{-2}). **(18)** rms noise in the optical image, 5 σ_{rms} -level for a 2" aperture (mag).

Type	(1)	(R)SB0+pec	F_{HI}	(15)	31.4 ± 3.1
RA	(2)	08 ^h 55 ^m 34 ^s .75	M_{HI}	(16)	0.816 ± 0.554
DEC	(3)	+58°44'03".9	r_{25}	(17)	146.9 ± 29.7
v_{sys}	(4)	875.2 ± 2.0	r_{HI}	(18)	200.0 ± 40.0
D	(5)	10.5 ± 3.5	r_{t}	(19)	420.0 ± 30.0
sc	(6)	50.907 ± 17.090	R_{25}	(20)	7.48 ± 2.51
m_{B}	(7)	12.05 ± 0.15	R_{HI}	(21)	10.18 ± 3.42
m_{I}	(8)	9.90 ± 0.10	R_{t}	(22)	21.38 ± 7.18
m_{B}^{c}	(9)	11.77 ± 0.15	v_{t}	(23)	146.7 ± 15.0
m_{I}^{c}	(10)	9.50 ± 0.13	M_{dyn}	(24)	$> 107.00 \pm 42.06$
M_{B}	(11)	-18.3 ± 0.7	$\frac{M_{\text{HI}}}{L_{\text{B}}}$	(25)	0.2 ± 0.03
M_{I}	(12)	-20.6 ± 0.7	$\frac{M_{\text{HI}}}{L_{\text{I}}}$	(26)	0.1 ± 0.01
L_{B}	(13)	3.361 ± 2.304	$\frac{M_{\text{dyn}}}{M_{\text{HI}}}$	(27)	$> 131.1 \pm 46.9$
L_{I}	(14)	7.485 ± 5.111	$\frac{M_{\text{dyn}}}{L_{\text{B}}}$	(28)	$> 31.8 \pm 12.9$
			$\frac{M_{\text{dyn}}}{L_{\text{I}}}$	(29)	$> 14.3 \pm 5.8$

Tab. 5.2: Basic properties of NGC 2685. **(1)** Classification of galaxy (de Vaucouleurs et al. (1991)). **(2)** Right Ascension (J2000) (NED). **(3)** Declination (J2000) (NED). **(4)** Optical heliocentric systemic velocity (kms^{-1}). **(5)** Distance of object (Mpc, Freedman et al. 2001 and this work). **(6)** Scale between distance on sky and true distance ($''/\text{pc}$). **(7)** Apparent B-band magnitude (mag, LEDA). **(8)** Apparent I-band magnitude (mag, LEDA). **(9)** Apparent B-band magnitude corrected for dust extinction (mag, LEDA). **(10)** Apparent I-band magnitude corrected for dust extinction (mag). **(11)** Absolute B-band magnitude (mag). **(12)** Absolute I-band magnitude (mag). **(13)** B-band luminosity ($10^9 L_{\odot}$). **(14)** I-band luminosity ($10^9 L_{\odot}$). **(15)** Total HI flux (Jykm s^{-1}). **(16)** HI mass ($10^9 M_{\odot}$). **(17)** Blue optical radius ($''$, LEDA). **(18)** HI radius ($''$). **(19)** Terminal radius ($''$). **(20)** Blue optical radius (kpc, LEDA). **(21)** HI radius (kpc). **(22)** Terminal radius (kpc). **(23)** Rotation velocity at terminal radius (kms^{-1}). **(24)** Dynamical mass ($10^9 M_{\odot}$). **(25)** Ratio of HI mass and B-band luminosity ($M_{\odot} L_{\odot}^{-1}$). **(26)** Ratio of HI mass and I-band luminosity ($M_{\odot} L_{\odot}^{-1}$). **(27)** Ratio of dynamical mass and HI mass. **(28)** Ratio of dynamical mass and B-band luminosity ($M_{\odot} L_{\odot}^{-1}$). **(29)** Ratio of dynamical mass and I-band luminosity ($M_{\odot} L_{\odot}^{-1}$).

5.4 The environment of the Spindle

During the reduction of the HI data it became clear that a number of rather small objects is present in the vicinity of NGC 2685. In the HI datacube, four objects were detected. This means that the already rather small NGC 2685 is probably the dominating member of a small loose group of galaxies. Two objects detected in HI are known dwarf galaxies, UGC 4683 and PGC 25002 while two very small objects were detected that are barely visible in the DSS maps. They lie very close to each other and are not separable in the HI maps. Apparently,

they are two objects of very low surface brightness but clearly visible in the gas component. Fig. 5.2 shows an overlay of the total HI map on a DSS image containing all detected objects. Tab. 5.3 shows characterising quantities derived

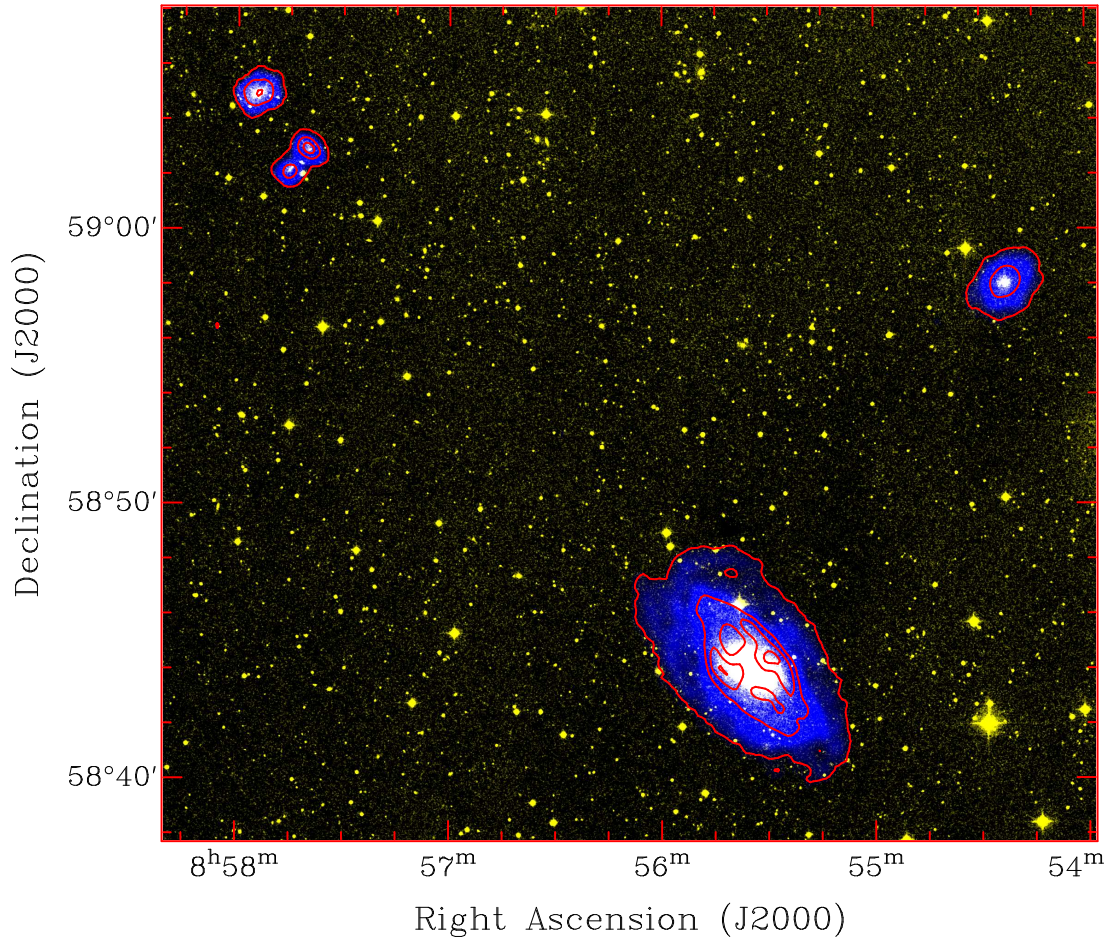


Fig. 5.2: HI total intensity maps of the observed field overlaid on a DSS (red) image. From top to bottom: UGC 4683, two unknown possibly merging objects, PGC 25002, NGC 2685. The contours represent the $1.5, 40, 85, 145 \cdot 10^{19}$ atoms cm^{-2} levels. Note that the map is primary-beam corrected.

from the measurements or taken from the literature. The total HI flux was derived from the (primary-beam corrected) total intensity maps and the corresponding HI mass was calculated under the assumption that the galaxy is at the same distance as NGC 2685. For the physical distance from NGC 2685, again the same distance from the observer as NGC 2685 was assumed. The diameters needed in order to calculate the dynamical masses of the objects have been roughly estimated by calculating the projected distance of the two points at extremal velocities in the moment 1 velocity maps. The HI spectra of the galaxies were used in order to

estimate the 20 percent peak line width and the systemic velocities of the objects. Then, the dynamical mass was calculated from these linewidths. In the case of the two unknown objects the estimation was difficult. They are approximately of the same size and have probably the same amplitude of rotation. The HI flux, systemic velocity and the linewidth is calculated taking both objects into account, while the dynamical mass was calculated estimating the extension of only one of both objects. For the scope of this study, this is accurate enough.

Name	(1)	PGC 25002	UGC 4683	unknown
Type	(2)	IB(rs)m	dI	unknown
RA	(3)	8 ^h 54 ^m 22 ^s .50.0	8 ^h 57 ^m 54 ^s .37.0	8 ^h 57 ^m 42 ^s .51.0
DEC	(4)	58°58'4"0.00	59°4'57"7.00	59°2'28"85.00
v_{sys}	(5)	1017.2 ± 8.2	927.0 ± 8.2	1187.0 ± 8.2
m_{B}	(6)	16.4	14.8	unknown, but very low
F_{HI}	(7)	3.3 ± 0.3	2.2 ± 0.2	2.1 ± 0.2
M_{HI}	(8)	8.5 ± 0.8	5.8 ± 0.6	5.4 ± 0.5
d_{2685}	(9)	1016 ± 28	1651 ± 28	1484 ± 28
D_{2685}	(10)	52 ± 17	84 ± 28	76 ± 25
w_{20}	(11)	95.0 ± 9.5	64.0 ± 6.4	72.5 ± 7.2
i	(12)	29.2	31.6	90.0
M_{dyn}	(13)	94.5 ± 49.0	22.1 ± 16.5	6.0 ± 5.6

Tab. 5.3: *Basic properties of the detected dwarf galaxies in the vicinity of NGC 2685. The data show that these galaxies probably cannot account for the ring in NGC 2685 and are dynamically unimportant. (1) Name of galaxy. (2) Classification of galaxy (de Vaucouleurs et al. (1991)). (3) Right Ascension (J2000) (NED). (4) Declination (J2000) (NED). (5) Optical heliocentric systemic velocity (kms^{-1}). (6) Apparent B-band magnitude (mag, Paturel 1989). (7) Total HI flux (Jykms^{-1}). (8) HI mass ($10^7 M_{\odot}$) at the same distance as NGC 2685. (9) Projected distance of object from NGC 2685 (") at the same distance as NGC 2685. (10) Projected distance of object from NGC 2685 (kpc) at the same distance as NGC 2685. (11) Profile width at 20 percent of the peak flux density (kms^{-1}). (12) Inclination ($^{\circ}$). (13) Dynamical mass ($10^8 M_{\odot}$) at the same distance as NGC 2685.*

Tab. 5.3 shows that none of the possible companion galaxies is large enough to be currently important for the dynamics of NGC 2685, taken together their mass makes up only about one fifth of the total dynamical mass in the observed galaxies. The most massive companion is PGC 25002 with about one tenth of the mass of NGC 2685. Its projected distance to NGC 2685 amounts to 95 kpc. The mass-ratio of PGC 25002 and NGC 2685 is roughly the same of the Milky Way and the Large Magellanic Cloud, which is currently at its pericentric passage and depositing quite some gas on a polar orbit about the Milky Way. Its position lies roughly in the direction of the projected minor axis of the central stellar body of

NGC 2685, such that it might be mused that this object deposited some amount of gas into a polar orbit about NGC 2685. This galaxy, however is an irregular galaxy, which are known to have a metallicity of typically 1/3 solar. Hence, a connection between the polar-ring structure of NGC 2685 and this galaxy is at least doubtful. The optical observations showed that a very faint elliptical stellar system is visible at the SW side of the galaxy (see Figs. 5.3). It is however unclear at which distance this object is with respect to NGC 2685. There is no evidence for an interaction as no HI feature seems to be connected with the object.

5.5 The stellar and gaseous components of NGC 2685

Fig. 5.3a) shows the optical image of the Spindle obtained with the INT WFC. To enable a comparison, Fig. 5.3b) shows the same image overlaid with a contour plot of the HI low-resolution total intensity map, while Fig. 5.3c) shows a grey-scale plot of the HI high-resolution total intensity map. A comparison by eye

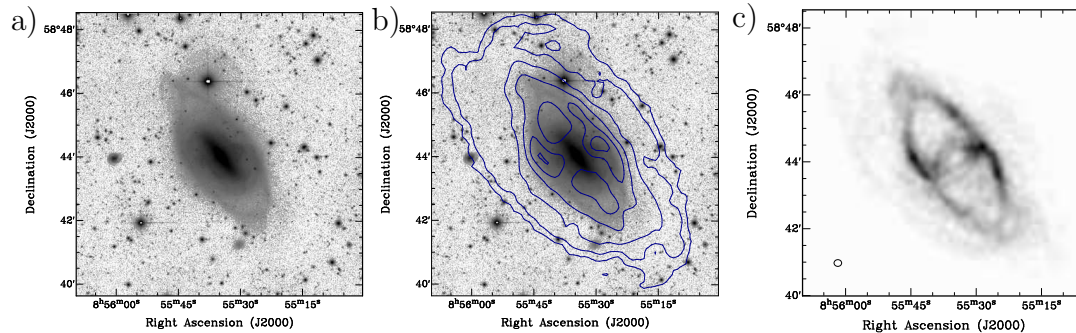


Fig. 5.3: Comparison of HI total intensity maps and the obtained i' -band image. a) Logarithmic grey-scale plot of the i' -band image. b) The same plot overlaid with a contour plot of the low-resolution total intensity HI map. Contours represent the $1.5, 5, 16, 48, 96, 144 \cdot 10^{19}$ atoms cm^{-2} levels. c) Grey-scale plot of the high-resolution HI total intensity map.

is completely sufficient in order to identify several structures in all maps. Firstly, the faint outer ring in the optical image resembles all the substructures of the outer HI ring to such a great detail that it is un-doubtable that both belong to the same structure and are physically aligned. Especially the small deviations from axisymmetry, a hook-like structure to the NE-side of the galaxy and a more diffuse structure towards the SW side are visible in all images, furthermore the form of the outer ring, distinctly deviating from ellipticity, is the same in the stellar and gaseous components. Secondly, there is no region inside the outer ring without stars or gas. This means that either a diffuse stellar and gaseous halo is present in this galaxy, or the galaxy possesses an extended disk. Below it will be shown that the latter is the case. Thirdly, looking at the high-resolution HI map, it seems that the helical structure is present in the HI component also.

This is most evident at the far side of the galaxy, where the high-resolution HI map shows two arms winding around the back-side of the central object. Seemingly, the HI follows the dust-lane structure like HI follows spiral arms in spiral galaxies. Fourthly, the projected brightness of both outer rings is largest about the minor axis. It can be concluded that the HI component in the galaxy belongs to a structure also containing stars the distribution of which follows the HI distribution. This fact is long known Shane (1980), but the data presented leave no place for doubt anymore. Remarkably, the HI maps, show a disk-like extension towards larger radii that cannot be seen in the stellar component. This feature could not be seen in the observations of Shane (1980) but is evident in the work of Schinnerer & Scoville (2002).

5.6 The warped structure of the gas disk of NGC 2685

It is believed that the HI component of NGC 2685 consists of two rings (Shane, 1977, 1980; Mahon, 1992; Schinnerer & Scoville, 2002). Here, a number of arguments shall be listed, why this is wrong.

The dust lanes As mentioned above, the appearance of the dust-lanes obscuring the NE part of the central body is inconsistent with a single central ring. In order to explain the structure seen, some warp in the component belonging to the dust-lanes has to be assumed. This was already realised by other authors. Nevertheless, a warp in the helical structure has in principle not to be present in the HI component.

The outer disk and the filled inner ring Beyond the outer ring NGC 2685 possesses a diffuse extended structure, most compatible with being a disk. The outer disk was already detected by Mahon (1992). It however caused some confusion when first seen in a pilot study to this project analysing service HI data of NGC 2685 obtained with the WSRT. One had to repeat the data reduction in order to be convinced of its reality. As mentioned above, another feature directly evident when looking at the HI maps is that inside the outer ring no position in the galaxy exists in which stars or gas are not detected. This is especially true for the optical image and the high-resolution HI total intensity map (Fig. 5.3), which have a high enough resolution in order to detect such holes that would be necessary in order to be able to argue against a halo or a disk-like structure to be present in the galaxy.

The spectral and integrated appearance of the HI component It is obvious that the outer ring of NGC 2685 has a strange projected shape, distinctly deviating from ellipticity. This already suggests a warped structure at least in the ring

as furthermore the surface brightness is not distributed evenly along the ring. A simple experiment demonstrates that the HI observations are inconsistent with even a sudden change of the orientation of two disk-like structures, which are the minimal requirement to speak of a two-ringed structure in the HI component of the Spindle galaxy. Usually, a tilted-ring model is employed in order to parametrise the geometry of warped objects or objects with two inclined rings. A galactic disk is represented by a number of concentric and mutually inclined rotating rings, which are described by a set of parameters that (partially) are allowed to vary from ring to ring. These are usually the (common) central position and the systemic velocity, the rotation velocity, and two orientational parameters for each ring (see Chaps. 3 and 4). Usually the velocity-field of a galaxy is analysed in order to derive such orientational parameters. This approach is delicate in the case of NGC 2685. The line-of-sight crosses the disk twice or more at several positions. Hence, one has to try to separate two kinematically distinct components and analyse them separately (e.g. Schinnerer & Scoville, 2002), or to perform a fit to the datacube itself. In this section, a very simple approach following the latter suggestion is chosen. Employing the *tirific* (see Chaps. 3 and 4) software that enables a least-squares optimisation fitting model datacubes to the observed datacube as shown in Sect. 5.8, two toy model datacubes were constructed “by hand” for demonstration reasons without aiming at a best-fit model. For the first one (“flip-model”) it was assumed that the HI disk of NGC 2685 flips at a certain radius without a smooth transition. This is the minimum assumption in order to have two separate rings or disks. The other model (“warp-model”), has a smooth transition from one disk orientation to the other. It was taken care to keep both models as simple as possible and to match at the same time the main features of the observations with a certain accuracy. In the warp model the projected appearance of two rings is a mixture of the crowding of orbits along the line-of sight and a change in surface density typical for a spiral galaxy, while for the flip-model sudden changes in the surface-brightness had to be assumed. In order to be compatible with the observations however, a model without a throughout filled disk could safely be excluded. For illustration reasons the same flat rotation curve in both models was assumed. Both models contain the same extended low-surface-density component. The parametrisations of both models and illustrative three-dimensional visualisations are shown in Fig. 5.4. The Figs. 5.6 show a comparison of the HI total intensity maps that would result from both models. Overlaid is a contour-plot of the measured total intensity map (low-resolution data). The appearance of both rings in the original total intensity map (Fig. 5.1) is far better represented by the warp model. Firstly, the diffuse appearance of the inner ring is reproduced in the warp model, while in the tilt model this ring is far more substantial. Secondly, and more important, the shape of the outer ring and the intensity distribution along the ring is clearly better represented by the warp model. While in the flip model an elliptic ring is produced, the shape of the outer ring is properly reproduced and deviating from

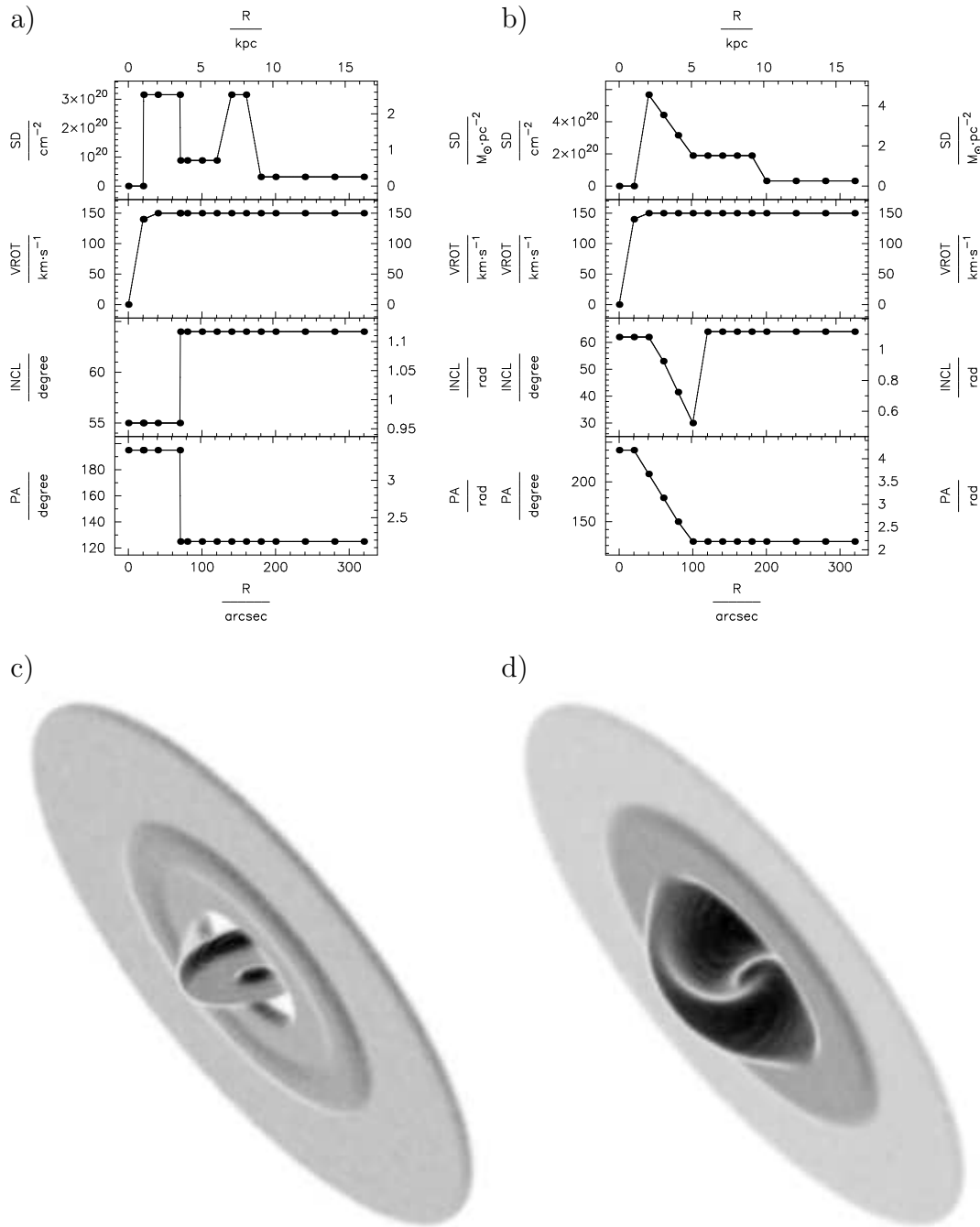


Fig. 5.4: Parametrisations of toy model datacubes. a) and b) Surface brightness profile, rotation curve and disk orientation. VROT: rotation velocity. INCL: inclination. PA: position angle. R: radius. c) and d) Three-dimensional visualisation of the disks a) and c) “Flip model”. The orientation of the disk flips at a certain radius, the minimum requirement in order to speak of a two-ring or two-disk system in NGC 2685. In order to match the ring structure in observed total intensity maps, sudden changes in the surface-brightness are necessary. b) and d) “Warp model”. In this model a coherent but heavily warped disk is assumed to reproduce the HI structure of NGC 2685. Sudden changes in the intensity are not required and the surface-brightness profile resembles that of a normal spiral galaxy.

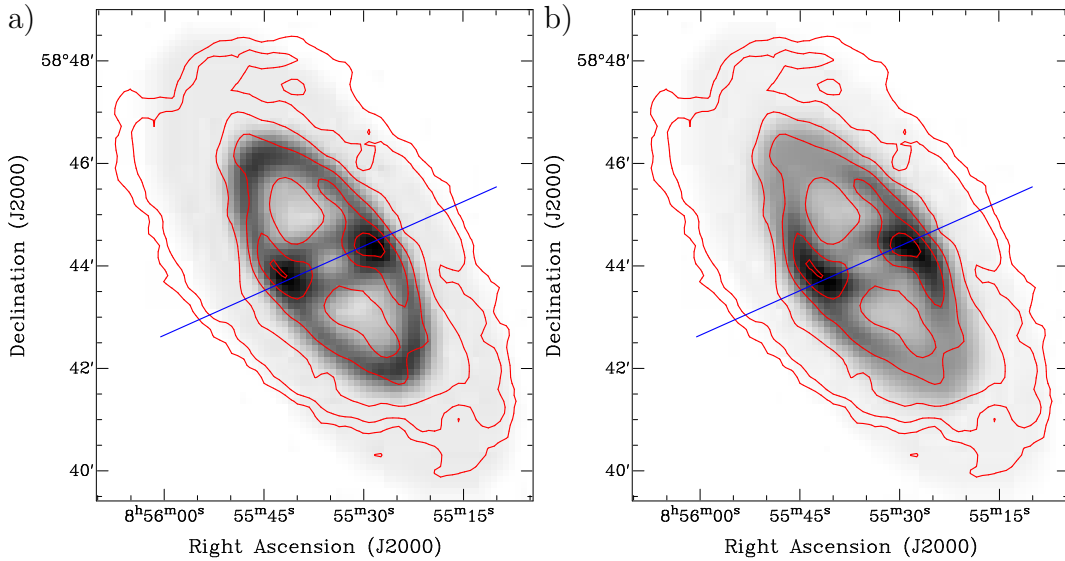


Fig. 5.5: *Toy model total intensity maps overlaid with a contour-plot of the measured total intensity map (low resolution). Contours represent the $1.5, 5, 16, 48, 96, 144 \cdot 10^{19} \text{ atoms cm}^{-2}$ levels. The lines indicate the line along which the spectra in the PV-diagrams shown in Fig. 5.6 are traced.*

ellipticity in the warp model. This is due to projection effects only. The maxima on the minor axis of the ring are highly concentrated on the position where the two disks adjoin in the tilt model, while in the warp model they are smoothed out along the outer ring as is the case in the observed total intensity map. The diffuse appearance of the projected surface brightness at the major axis positions is also seen in the warp model map, while not in the tilt model map.

The strongest argument comes but from position velocity diagrams along the major axis of the inner ring. The Figs. 5.6 show position velocity diagrams along the line shown in the Figs. 5.5 calculated from the original low-resolution datacube and the two toy model datacubes. These diagrams show – undoubtedly – why NGC 2685 clearly contains a coherent disk, regardless if non-circular motions play a role in the kinematics of the galaxy. Every discontinuity in the disk orientation would cause a gap between the spectral features that belong to the single constituents, as is the case for the flip-model. There is no connecting feature to be seen in-between the intensity maxima belonging to the “outer ring” (contours closer to the systemic velocity) and the intensity maxima belonging to the “inner ring”. The PV-diagram taken from the original datacube and from the warp model show this connection. This is the strongest evidence for the fact that the neutral gas component of NGC 2685 lies in an extremely warped but coherent disk. As has been showed above, this HI component is most probably part of the same structure as the stars and the dust that do not belong to the inner stellar body.

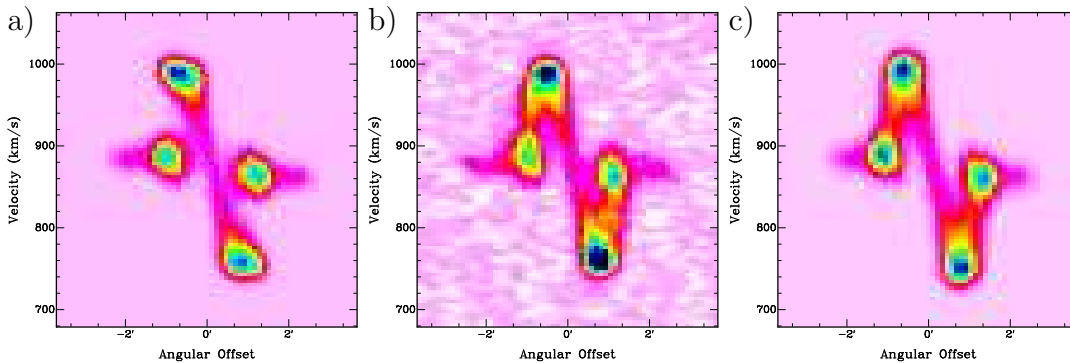


Fig. 5.6: *Position-velocity diagrams along the lines across the minor axis of the inner ring shown in Fig. 5.5. a) Taken from the flip-model datacube. b) Taken from the original datacube. c) Taken from the warp model datacube.*

NGC 2685 contains a stellar and gaseous disk that has the typical qualities of a (small) spiral galaxy. The disk is extremely warped and NGC 2685 owes its strange two-ringed appearance to projection effects. If the picture of NGC 2685 as a spiral galaxy is true, then the helical structure consists of dust-features contained in spiral arms that are wrapped around the central body in a warped structure. Similar cases are known. Schwarz (1985) quantified the structure of the warp in the huge spiral galaxy NGC 3718. It shows an extreme warp in its stellar and gaseous disk that changes its orientation by nearly 90° . In this galaxy, which has a different orientation on the sky and does not appear ring-like in projection the warp is already evident in optical photographs. Arnaboldi & Galletta (1993) showed in a similar approach as presented above that the galaxy NGC 660 shows probably a very simple disk structure with a large warp. NGC 660 was hitherto classified as polar-ring structure.

5.7 Tilted-ring modelling

The results of the previous chapter let hope that the kinematics of NGC 2685 can indeed be parametrised employing a tilted-ring model. In an extremely warped disk, however, deviations from the circularity of orbits might be too strong to allow for such an enterprise. Nevertheless, this enterprise has been undertaken employing the *tirific* software. If a tilted-ring model is an accurate enough description of the structure and the kinematics of the HI disk of highly warped systems, then the approach taken by using *tirific* is the only possible one, as naturally, every analysis that relies on velocity-field must fail. It was shown above that there is no way to separate two kinematically distinct regions in a datacube, as has been claimed to be possible by Schinnerer & Scoville (2002), as the galaxy is smoothly warped. Hence, as in this galaxy the line-of-sight surely crosses the disk twice and crowding of projected orbits of the disk material is present, the

only chance to parametrise the kinematics of NGC 2685 by means of a tilted-ring model lies in a direct fit to the datacube itself.

The analysis of the HI datacubes of NGC 2685 was identical with the one described in Chap. 4, with the difference that in this case it makes no sense to check for the existence of a flat region towards the centre of the galaxy. For details of the analysis not repeated here, Chap. 4 can be consulted.

As a flat disk is far from the true structure of the disk, the initial guess before starting the automated fitting routine had to be refined by “manually” adjusting the ring parameters until an accurate enough model was obtained to serve as an input to the fit. It was however not necessary to make a first guess as accurate as the toy warp model shown above.

Again, the low-resolution cube was analysed first using a spacing of ring radii of $20''$. This was necessary as in the region of the warp of the galaxy the parameters change rapidly with radius, making a sampling of the parameters at smaller distances in radius necessary. For the analysis of the low-resolution cubes a number of about $3.0 \cdot 10^6$ point-sources was used. As the gas disk of NGC 2685 is extremely symmetric, the centre of the galaxy, the global velocity dispersion, and the scaleheight were kept as free parameters but were not allowed to vary independently from ring to ring. For each ring, the surface-brightness, the orientational parameters, and the rotation velocity was varied independently. Throughout, the numerical noise was taken into account in the chi-square evaluation (a noise weighting of 1, see Chap. 3). The fitting process was repeated, adjusting the outlying parameters showing up in the first fit runs and changing the spacing of the ring radii in order to reach a robust fit. After a few of such iterations a stable solution was found. For the estimation of errors, fits solely to two different sides, the receding side and the approaching side of the galaxy, were performed as discussed in Chap. 4. Preliminary error bars were calculated as the maximal deviation of the data points from the fits to the approaching and the receding side from the previous fit results achieved taking into account the full extent of the galaxy. The errors of the central position and the systemic velocity of the galaxy were estimated without a cross-check to be less than $12''$ for the position of the kinematical centre and less than 2 km s^{-1} for the systemic velocity. In a few cases, where error bars calculated were obviously too large or too small, the data were visually inspected and errors

were estimated by varying the parameter in question and comparing resulting artificial datacubes with the original datacube until a significantly worse model than the best-fit model was produced. This was only necessary for some data points at the largest and the smallest radii (see Fig. 5.7). Fig. 5.7 shows the fit results and illustrates the error bar estimation for the low-resolution datacubes.

In order to refine the spatial resolution in the inner regions of the galaxy, the

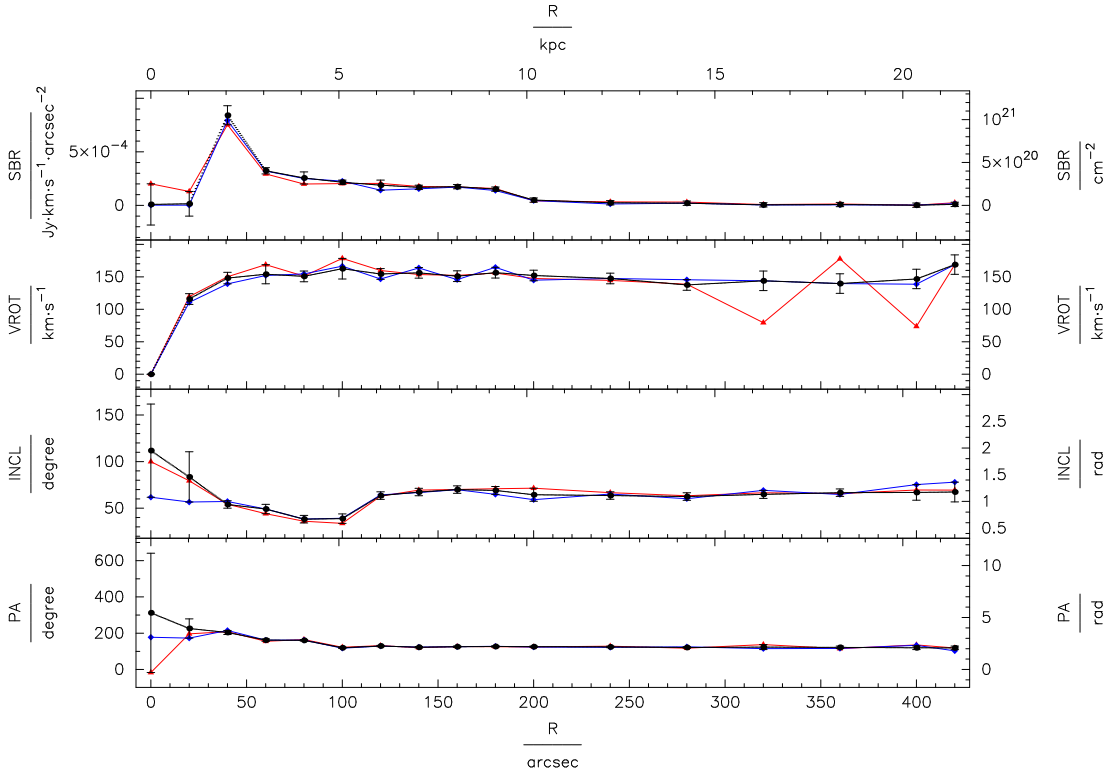


Fig. 5.7: Determination of the orientational parameters, the surface brightness for the outer disk, the rotation velocity from the first analysis using the low-resolution HI data and error bar estimation. SBR: surface brightness. VROT: rotation velocity. INCL: inclination. PA: position angle. R: radius. The black curve (dots) shows the best-fit rotation curve taking into account both sides of the galaxies. The red curve (triangles) shows the results when fitting only the receding side, the blue curve (diamonds) show the results for the approaching side. Preliminary error bars were estimated as the maximum deviation of the both-sides fit from the single-sided fits. For extraordinarily high or low values for the error bars, they were re-determined by visual inspection of the datacubes and comparison with a series of model datacubes.

high-resolution datacubes were used. Up to an optimally chosen maximal radius, the spacing of the ring radii was refined to a value of $12''$ interpolating the fit results from the previous run and the HI datacube was fitted again up to that radius following the same procedure as described above, including the orientational parameters. The number of point sources was increased to a value of

$8.6 \cdot 10^6$. The final results for the parametrisations are shown in Fig. 5.7. Fig. 5.11 illustrates the way, in which the high resolution data were taken into account. For the inner disk, the results from the fit to the high-resolution data and the corresponding error bars were taken, for the outer disk the results from the fits to the low-resolution datacubes. Fig. 5.11 shows the good agreement of the derived surface-brightnesses and the rotation velocities fitting to the low-resolution- and the high-resolution data respectively. This implies a good agreement of the high-resolution datacube and the low-resolution datacube with respect to the detection of smooth components in the HI distribution. A disagreement between the high-resolution fit and the low-resolution fit can be seen in the first two or three data points. Analysing the high-resolution datacube it was found that the HI surface brightness inside a radius of $10 - 15''$ was negligibly small, the gas becoming ionised in the stellar UV-field. Due to the lower resolution this could not be detected in the low-resolution datacube. It is clear that this makes the parametrisation of the first two or three data points very inaccurate or even impossible. At the origin, the orientational parameters are completely arbitrary, while starting with the second data point, the values presented here do have a physical meaning, although they have very large error bars. Several ways to

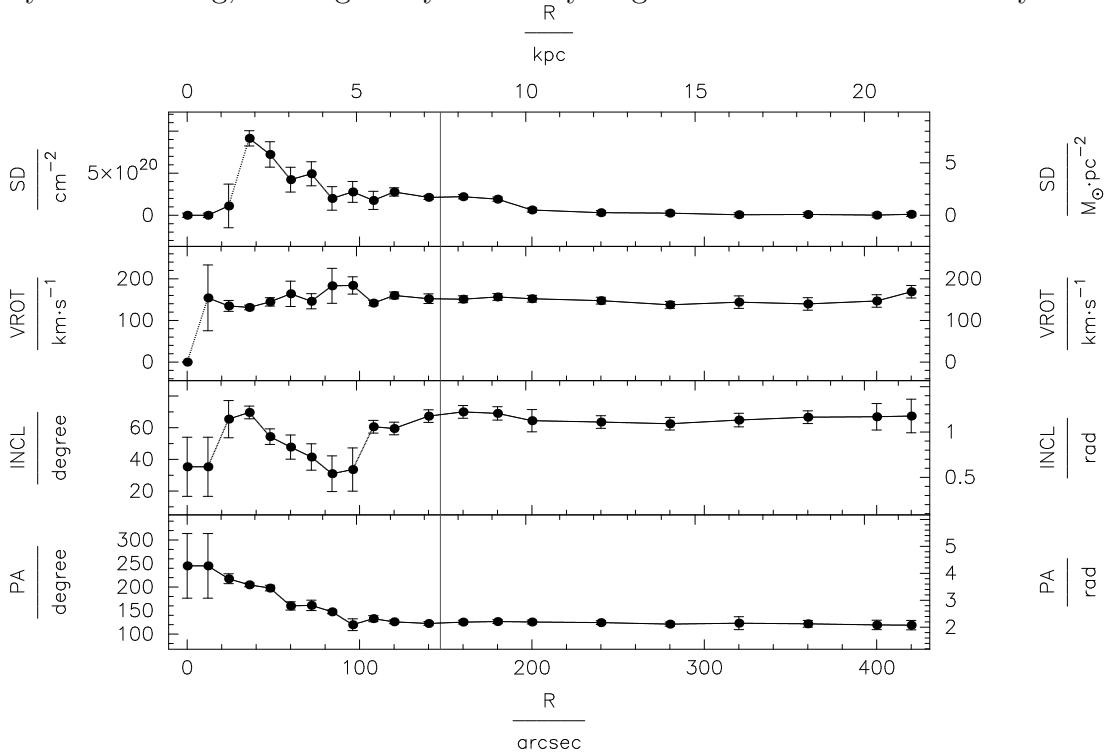


Fig. 5.8: Final parametrisations of the Spindle galaxy. *SBR*: surface brightness. *VROT*: rotation velocity. *INCL*: inclination. *PA*: position angle. *R*: radius. The vertical line denotes the optical radius r_{25} .

check the quality of the finally resulting fit are possible and have been exhausted.

Fig. 5.11 shows contour-plots overlaying the low-resolution datacube with the corresponding synthetic datacube. Fig. 5.9 shows overlays of corresponding moment maps of the original data and the synthetic ones, Fig. 5.10 shows position-velocity diagrams along the kinematical major and minor axes. All comparisons show

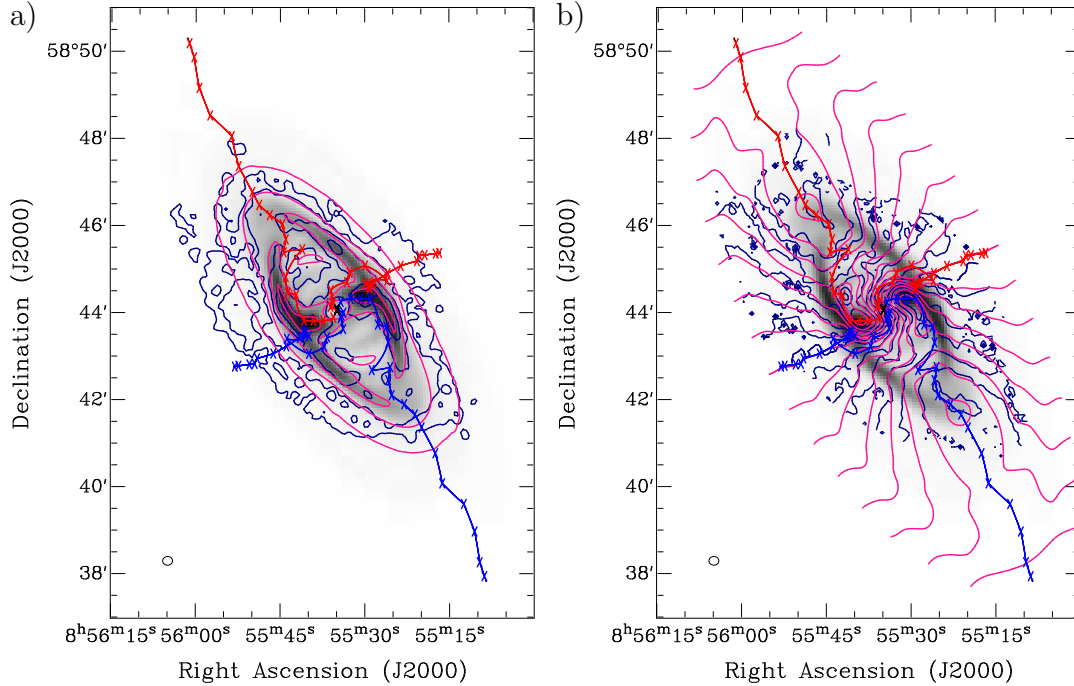


Fig. 5.9: Total intensity contour plots (a, left) and first moment velocity fields (b, right) derived from the low-resolution datacube, blue original, pink model, overlaid on total intensity grey-scale maps derived from the model datacube. The over-plotted lines represent the kinematical major- and minor axis respectively. The red kinematical major axis lies in the receding part of the galaxy, the blue kinematical major axis in the approaching part. The ellipse in the lower left corner represents the clean beam. The contours represent the $1.5, 5, 16, 48, 96, 144 \cdot 10^{19}$ atoms cm^{-2} levels and the $v_{\text{sys}} \pm 0, 20, 40, 60, 80, 100, 120, 140 \text{ km s}^{-1}$ levels respectively (see Tab. 5.1).

an extremely good agreement of measurement and model up to largest radii until the HI distribution in the galaxy becomes (at last) asymmetric. Hence, one can conclude that by large and large, the tilted-ring model is able to reproduce both, the kinematics and the azimuthally averaged surface-brightness profile of the HI component in NGC 2685. Tab. 5.7 shows the finally adopted global parameters of the models. In all fitting processes, the scaleheight with an assumed *sech*²-law and the dispersion were kept as free parameters. All parameters have reasonable values. While the internal velocity dispersion (the velocity dispersion in the galaxy itself) is in perfect agreement for both fits, the scaleheight differs from one fit to the other. One has to realise that but for both fits the scaleheight lies way below the spatial resolution of the datacubes. Therefore, the result is only meaningful in order to state that there is probably no thick component in the

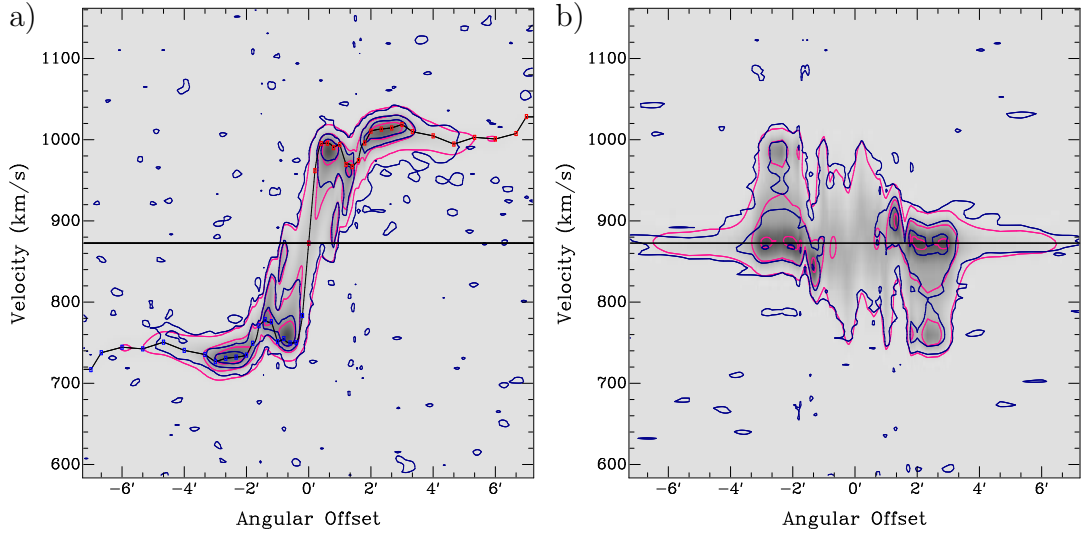


Fig. 5.10: a) PV-diagrams along the kinematical major axis comparing the final best-fit models (pink contours) with the original low-resolution data (blue contours). The vertical line marks the systemic velocity, the boxes connected with the lines denote the rotation curve corrected for the inclination. b) PV-diagrams along the kinematical minor axis comparing the final models (pink contours) with the original low-resolution data (blue contours). Contour levels are 0.5, 4, 10 mJy/beam.

disk of NGC 2685 and that the thickness of the disk is below what is measurable using HI observations.

Tab. 5.11 shows the radially dependent best-fit parameters and additionally, for a simplified further use, the normal vectors of the rings as derived quantities.

In order to estimate some of the global parameters shown in Tab. 5.2, as for the galaxies analysed in the previous chapter, the Tully-Fisher relation was applied again in order to estimate the distance of NGC 2685. This is done under the assumption that NGC 2685 is a disk galaxy that then follows the same brightness-mass-relation as spiral galaxies. Relative magnitudes in the I- and B-band were taken from LEDA. The calculated distance of $(10.5 \pm 3.5) \text{ Mpc}$ is in agreement with a distance estimation using a Hubble constant of $72 \text{ km s}^{-2} \text{ Mpc}^{-1}$ yielding a distance of 13.8 Mpc with the inherent uncertainty of the peculiar motion of the galaxy with respect to the reference frame of the 3K background emission. As both values reasonably agree, the Tully-Fisher distance estimate was assumed to be based on a correct assumption, choosing between two rather uncertain estimates. The calculated distance and distance-dependent quantities calculated and shown in Tab. 5.2 have to be treated with the necessary care. The adopted distance made a determination of the physical scales of the galaxies possible and with that an estimation of the dynamical masses, the HI masses, and the luminosities of the galaxies as discussed in Chap. 4.

RA	(1)	08 ^h 55 ^m 34 ^s .92	
DEC	(2)	+58°44'04".4	
RA*	(3)	08 ^h 55 ^m 34 ^s .75	
DEC*	(4)	+58°44'03".9	
v_{sys}	(5)	875.2	
(6) Resolution		high	low
$v_{\text{disp,tot}}$	(7)	9.8	10.2
$v_{\text{disp,int}}$	(8)	9.6	9.6
z_0	(9)	5.4	3.0
z_0^{pc}	(10)	275	155

Tab. 5.4: *Global best-fit tilted-ring parameters for the examined galaxies. (1) Right Ascension (J2000), fitting results. (2) Declination (J2000), fitting results. (3) Right Ascension (J2000) from NED. (4) Right Ascension (J2000) from NED. (5) Heliocentric optical systemic velocity (kms^{-1}). (6) Type of datacube used for analysis, high-resolution or low-resolution. (7) Velocity ispersion (kms^{-1}). (8) Internal dispersion, instrumental dispersion subtracted (kms^{-1}). (9) Global scaleheight (") (10) Global scaleheight (pc)*

5.8 Global features in the tilted-ring models

The tilted-ring model shown in Fig. 5.7 is visualised as in Sect. 4.5, shown in the Figs. 5.11. The best-fit parametrisation is rather similar to the warp toy model shown in Sect. 5.3 (Fig. 5.4). The gaseous disk of NGC 2685 is warped from the innermost radii on and then becomes remarkably flat towards large radii. For the innermost $12'' - 36''$, however, no reliable information can be derived from the data, as obviously the gas becomes ionised towards the centre of the galaxy. As this galaxy is warped, it is interesting how much the kinematic structure of NGC 2685 resembles the appearance of a normal warped galaxy. For this purpose, it shall be checked to what extent the extended rules for the behaviour of warps as laid down in Chap. 4 and by Briggs (1990) are obeyed by NGC 2685. Already the first rule of Briggs (1990) is violated. As it is the case for NGC 3718, there is no flat part in the inner disk of NGC 2685. While this is true, taking the plane of the first inner ring at a reasonable surface-brightness (ring 4) as a reference plane for a tip-LON plot shown in Fig. 5.11b), NGC 2685 seems to follow the third rule of Briggs (1990). The inner data points seem to share the same line-of the nodes, which then, at a radius of about $100''$, rapidly turns into a leading spiral with respect to the rotation direction of the galaxy (see arrow in Fig. 5.11b). The sense of rotation could be well determined by the position of the helical structure that must lie in front of the central body, closer to the observer. Remarkably, also the fourth rule of Briggs (1990) is followed also. In Chap. 4 it was shown that this feature is likely to turn up because of the fact that in normal warped galaxies two flat regions or two co-precessing regions exist. Indeed, towards larger radii,

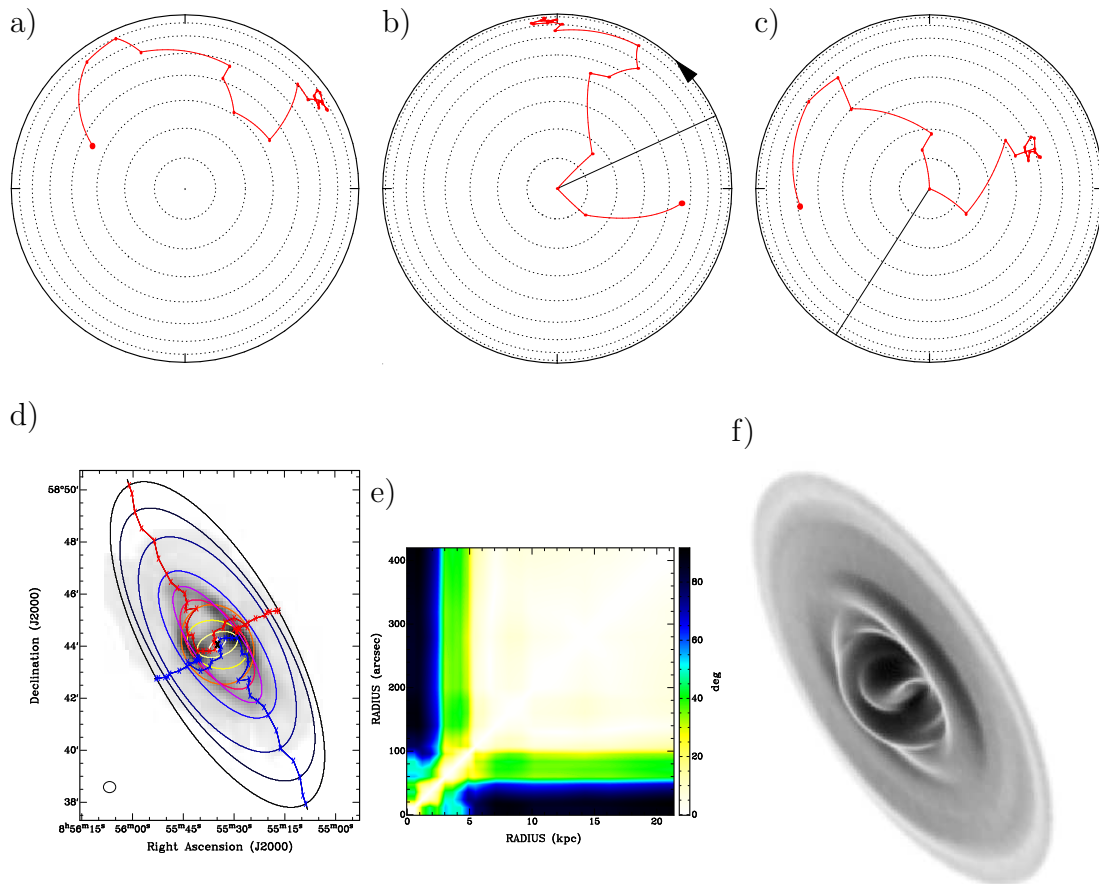


Fig. 5.11: Various visualisations of the adopted tilted-ring models for NGC 2685. a)-c) tip-LON plots, the filled circles are the projection of the tip of the normal vectors of the rings at different radii onto a reference plane the innermost radius (0) denoted by a larger circle. The circles in the Figs. a)-c) are drawn at intervals of 10° . a) The reference plane is the celestial plane. b) The reference plane is the ring at a radius of $36''$. As NGC 2685 does not contain an inner flat disk, this ring was chosen to be representative in order to check for the third rule of Briggs (1990). c) The reference plane is chosen such that two straight LONs are roughly visible, resembling the fourth rule of Briggs (1990). At larger radii the dots are clustered around the same position, indicating an outer planar disk. d) Inclinogram of the galaxies overlaid on the original total intensity maps. The ellipses mark the projection of a ring on the celestial plane, lines and crosses mark the kinematical major and minor axes. In red the kinematical major axis in the receding part of the galaxies is plotted, in blue the kinematical major axis of the approaching part. e) Tiltogram of the galaxies. This is a pixel map showing the mutual inclination of rings at different radii. f) Three-dimensional model of the HI disk of the galaxies according to the tilted-ring model. The model is rotated and artificially made opaque in order to show again the presence of an outer planar disk.

the HI disk of NGC 2685 is flat (see also Figs. 5.11e and f). Therefore, the warp of NGC 2685 also fulfils rule 4 laid down in the previous chapter as it possesses a flat disk at large radii. It is however not obvious whether the rotation curve and the surface-density profile can be brought into agreement with the rules 5 and 6 of the previous chapter. The HI surface-density profile shows the characteristic drop at a radius of approximately $200''$. The disk is but comparably flat from a radius of $100 - 120''$ on. Rule 6 may or may not be realised in the galaxy. In-between $60''$ and $100''$ the rotation curve has reached a high value that seems to drop at the transition radius of $100''$. It is not very clear if this feature is real, as in-between $60''$ and $100''$ the inclination has a rather low value, which imposes large uncertainties on the rotation curve.

Also for NGC 2685, in order to have a robust estimate of the amplitude of this change and to check, if a rotation curve without a sudden rise could still be compatible with the original data, another series of fits to the low-resolution data was performed. Two regions were selected, an inner one and an outer one, in which the best-fit rotation curve stays comparably flat. Two fits to the low-resolution datacube were performed, leaving all parameters variable as in the initial fitting process but one time enforcing both regions to have the same rotation velocity, the other time keeping the rotation curve flat in each separate region, but allowing the rotation velocity of both regions to vary. Then, the resulting artificial datacubes were compared with the original datacubes. The results are shown in Fig. 5.18. Carefully inspecting datacubes and position-velocity diagrams as shown in Fig. 5.18 a) and b) lead to the conclusion that a resulting change of 12.1 km s^{-1} in the rotation velocity is probably necessary in order to match the observations if one assumes circularity of orbits. Hence, one can conclude that while NGC 2685 does not follow all rules for the behaviour of warps, certain features that are observed for warps are present in the parametrisation of NGC 2685. Clear deviations are the presence of a warp in the inner region of the galaxy and the presence of the flat outer disk already at radii where the HI has still a high column-density. In this galaxy the drop of the HI surface-density-profile does not coincide with the start of the warp.

5.9 Non-circular motions

The previous sections showed that the kinematics of NGC 2685 can very well be represented by the tilted-ring model. The peculiar structure of NGC 2685 with the presence of its central stellar object – a stellar disk, an elongated bulge, or a large bar – should however show its imprints on the kinematics. Non-circular motions should be present. As already stated in Chap. 4, the best way to quantify the deviations from the circularity of orbits would be a harmonic decomposition of the velocity-field in azimuthal direction implemented in *tilirific*. In order to have

a first impression the same simple approach as in Chap. 4 was taken in order to get an impression of the influence of the non-sphericity in the potential of NGC 2685. The Figs. 5.12 show the velocity-difference maps or residual velocity maps derived from the low-resolution original and model datacubes for NGC 2685 and a histogram of the pixel values in the maps overlaid with a Gaussian with the weighted mean, the standard deviation and the area of the histogram. The

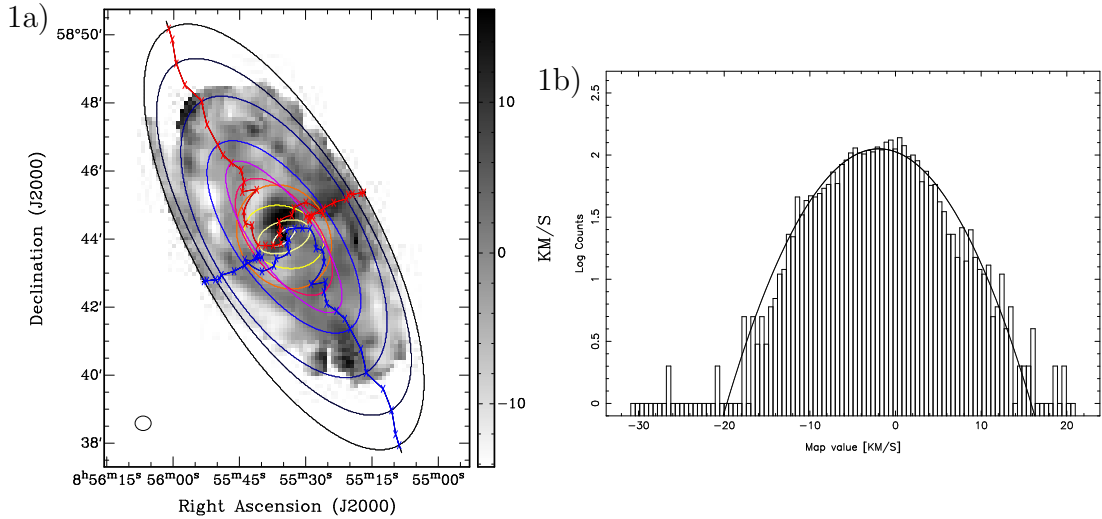


Fig. 5.12: a) Difference- or residual velocity maps derived by subtracting the model first moment map from the original first moment map. b) Histogram of the pixel values of a). The solid line shows a Gaussian with a peak position identical with the mean, a width equal to the rms, and an area equal to the area of the histogram.

most obvious, largest contribution in the residual velocity map is located at the tip of the inner stellar body. The major contribution is of axisymmetric nature, which suggests that the inner stellar body acts like a bar in the warped disk of NGC 2685 (see the previous chapter and Franx et al., 1994). Other features in the map cannot easily be quantified and are of more diffuse nature. The fact that the difference of the model velocity-field and the original velocity-field is in the mean offset by about 2 km s^{-1} (see Tab. 5.5) is maybe due to the fact that again an offset of the central position or the systemic velocity in different regions of the galaxy might be present that is unaccounted for in the fitting procedure. Except for the axisymmetric feature in the vicinity of the central stellar object, the residuals are low compared to the rotation velocity. The simple estimation of the possible influence on the rotation curve can be made by taking into account the rms present in the maps. The mean and the rms of the pixel values in the maps was calculated and, to get an upper limit, corrected for the lowest measured inclination present in the galaxies. The results are shown in Tab. 5.5.

The standard deviation of the pixel values is well below the best-fit velocity dispersions. Non-circular motions do not violate largely the results given in the

\bar{v}_d	σ_{v_d}	i_{\min}	$\frac{\sigma_{v_d}}{\sin i}$
(1)	(2)	(3)	(4)
-1.9	5.8	31.0	11.2

Tab. 5.5: *Basic statistics of the velocity difference maps. (1) Mean of the deviation velocities (km s^{-1}). (2) Standard deviation of the deviation velocities (km s^{-1}). (3) Minimal measured inclination in the galaxy. (4) σ_{v_d} corrected for i_{\min} .*

previous section, except possibly for the region at the tips of the central stellar object. Here, the maximum value in the residual map is 20.9 km s^{-1} , de-projecting this with the lowest inclination that is measured for the galaxy gives a local deviation of 41 km s^{-1} , which is about a quarter of the rotation velocity in the area of the feature. This makes the measurement of the change in rotation velocity questionable. As this is the case when parametrising normal warped galaxies with the tilted-ring-model this does not affect the statement that the measured change of rotation velocity is similar to that seen for normal warped galaxies.

5.10 Summary of the results and discussion

It was shown that the Spindle Galaxy NGC 2685 possesses a disk consisting of gas, stars and dust that has many properties of a spiral galaxy. In particular, the two-ringed appearance is due to projection effects and NGC 2685 possesses a coherent disk. This makes scenarios extremely improbable, in which the rings respectively the disk of NGC 2685 have been acquired in two separate accretion events. The disk of NGC 2685 cannot be young. This suggests that also the warp of NGC 2685 is a long-lived feature. As such, taking into account the proposed formation scenarios for NGC 2685, this observation is in favour of a figure-rotating prolate (-like) potential aligned with the central stellar as the underlying generator of the observed structure. Such a potential results in the creation of a warp-preferred plane in which the disk material resides (Tohline & Durisen, 1982; van Albada et al., 1982; Simonson & Tohline, 1983; Varnas, 1990; Peletier & Christodoulou, 1993; Bekki & Freeman, 2002). Peletier & Christodoulou (1993) showed that a figure rotating oblate potential is probably not able to bear the same result. Such figure rotation is not expected to occur in a standard cosmological environment (e.g. Bailin & Steinmetz, 2004b).

In order to quantify the geometry and the kinematics of NGC 2685, a tilted-ring model was fitted to the datacube. Interestingly, the gaseous disk of NGC 2685 shows many features of galactic disks with smaller warps. While the inner disk of NGC 2685 is warped throughout, it shows the same line-of the nodes over a large range of radii. This suggests that in the inner parts the galaxy disk is in a state of co-precession. This argument cannot be extended, though, to the

smallest radii, as no HI is detected there. The fit results suggest that NGC 2685 is not co-precessing at the smallest radii $< 30''$. NGC 2685 possesses a large, flat outer disk. Hence, it shows two regions that are separable and each of which is co-precessing or not precessing. The Spindle resembles the third rule of Briggs in that a tip-LON plot shows a line-of the nodes that is advancing in the direction of galaxy rotation. This implies that the inner and the outer disk precess in a way that, retrograde precession assumed, the outer disk precesses more slowly than the inner disk. The form of the rotation curve suggests that the two disks reside in different dynamical regions as is the case for normal warped galaxies (see Chap. 4). A major difference with respect to normal warped galaxies is that the typical drop of the HI surface-brightness profile, which is present also in the HI disk of the Spindle, does not coincide with the transition radius at which the galaxy disk changes its orientation.

NGC 2685 remains a dynamical puzzle and no conclusion about the origin of the warp in NGC 2685 can be drawn. The results of this work suggest the presence of a figure-rotating potential. The many similarities of NGC 2685 with a normal spiral galaxy especially in the kinematical structure of the warped disk suggest that NGC 2685 might indeed be a normal – but extremely warped – early type or barred late-type galaxy. The major differences of a warp without an inner flat region suggest that the disk of NGC 2685 too lightweight to keep the inner disk flat against the warping forces. Possibly, the lack of a heavy stellar disk is also the reason, why the drop of HI surface density in the outskirts is in this case not correlated with the start of the warp. NGC 2685 as a normal disk galaxy with a rather low surface brightness – The chapter shall be closed with this daring, but possibly not unfounded hypothesis.

5.11 Supplementary figures and tables

Here, supplementary figures and tables are put. All figures that are not immediately needed when reading the chapter for the first time, are put here.

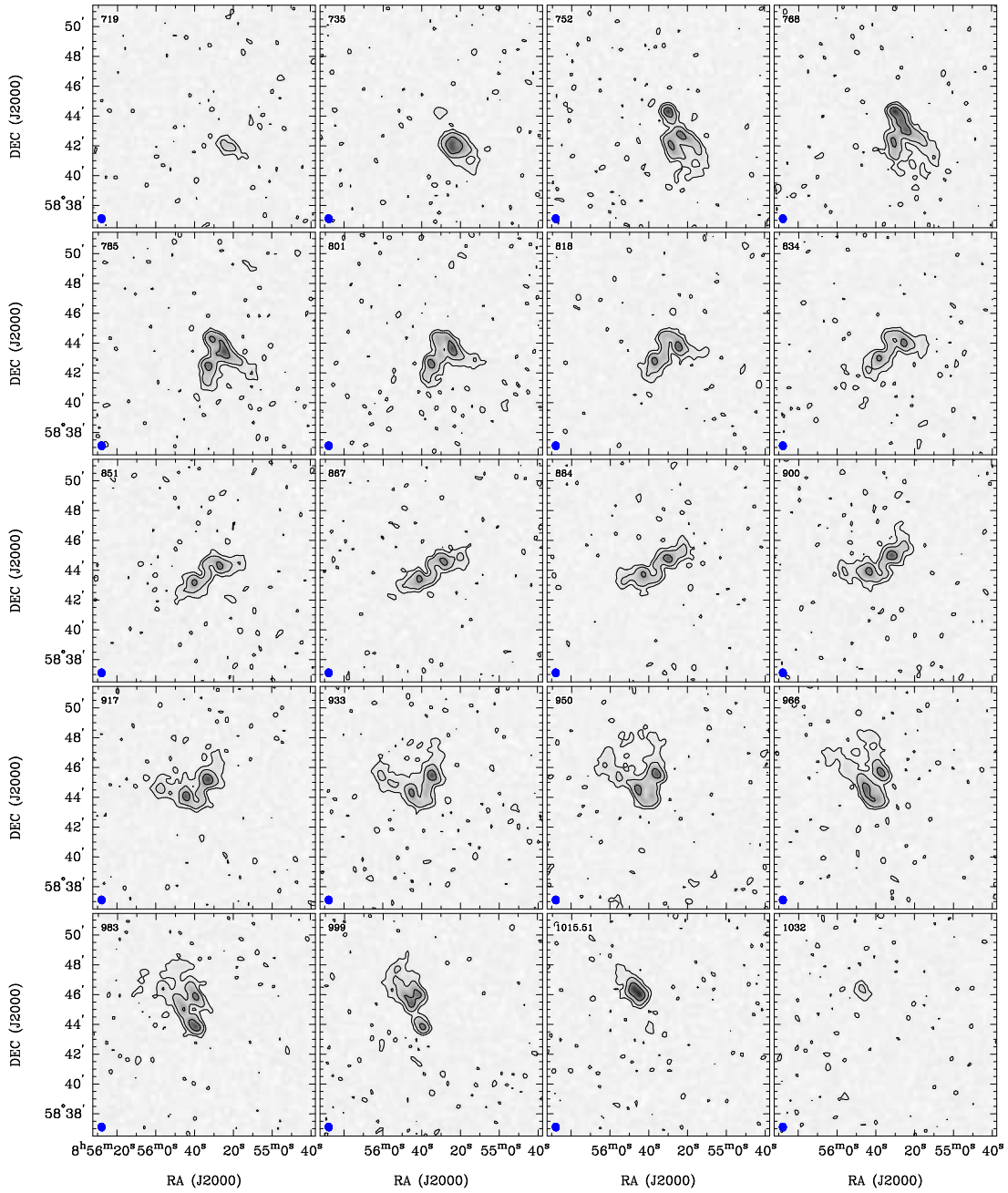


Fig. 5.13: Selected images from the low-resolution datacube (channel resolution of 4.12 km s^{-1} , robust weighting of 0.4, only visibilities with a baseline $< 6.4\text{ k}\lambda_{\text{HI}}$ regarded $\lambda_{\text{HI}} \approx 21.1\text{ cm}$). The numbers on the upper left give the heliocentric radio velocity in km s^{-1} . The blue dot represents the clean beam. The contours represent the 0.5, 2, 8 mJy/beam levels.

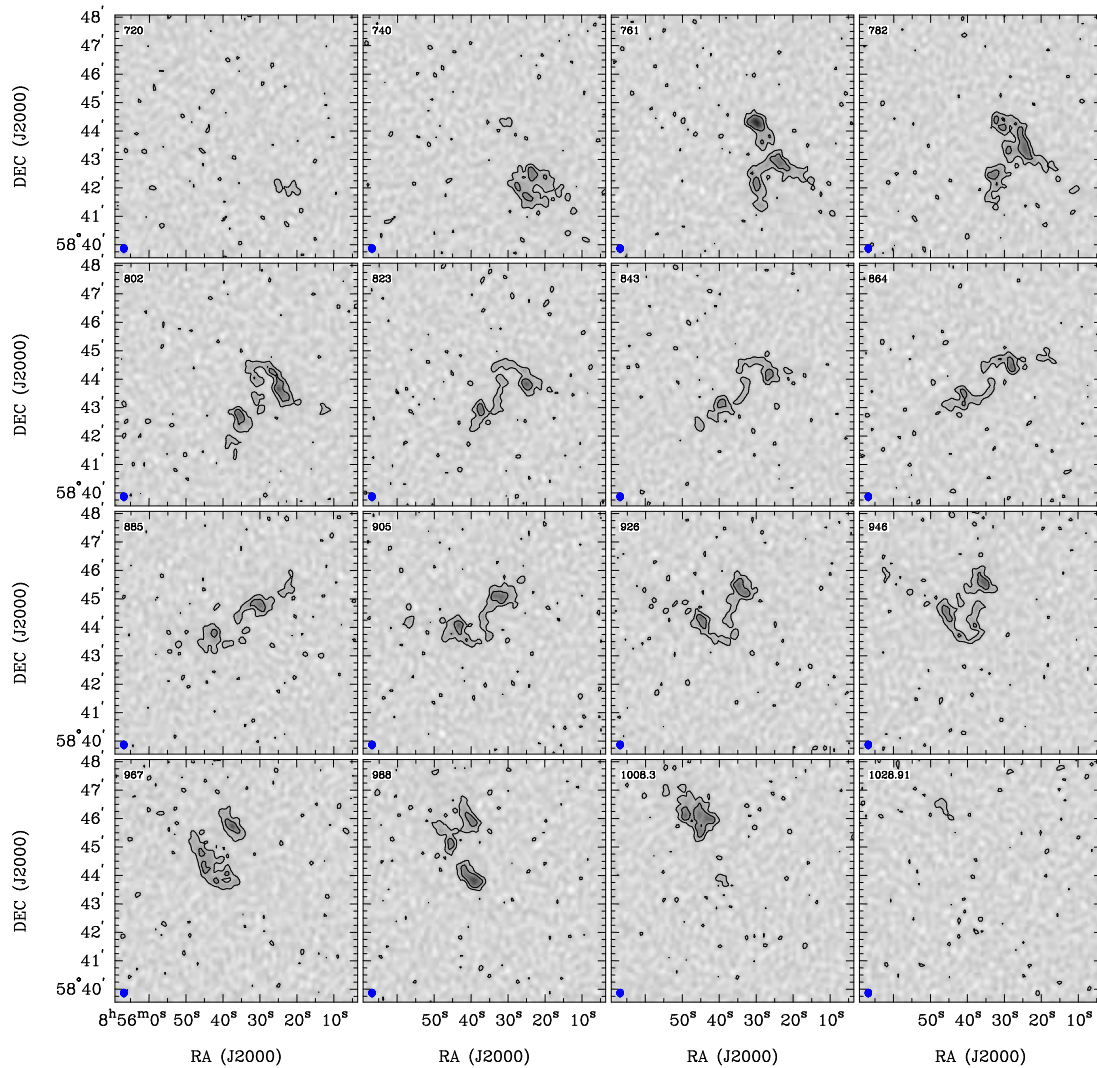


Fig. 5.14: Selected images from the high-resolution datacube (channel resolution of 2.06km s^{-1} , uniform weighting, all visibilities regarded). The numbers on the upper left give the heliocentric radio velocity in km s^{-1} . The blue dot represents the clean beam. The contours represent the 0.75, 3, 4.5 mJy/beam levels.

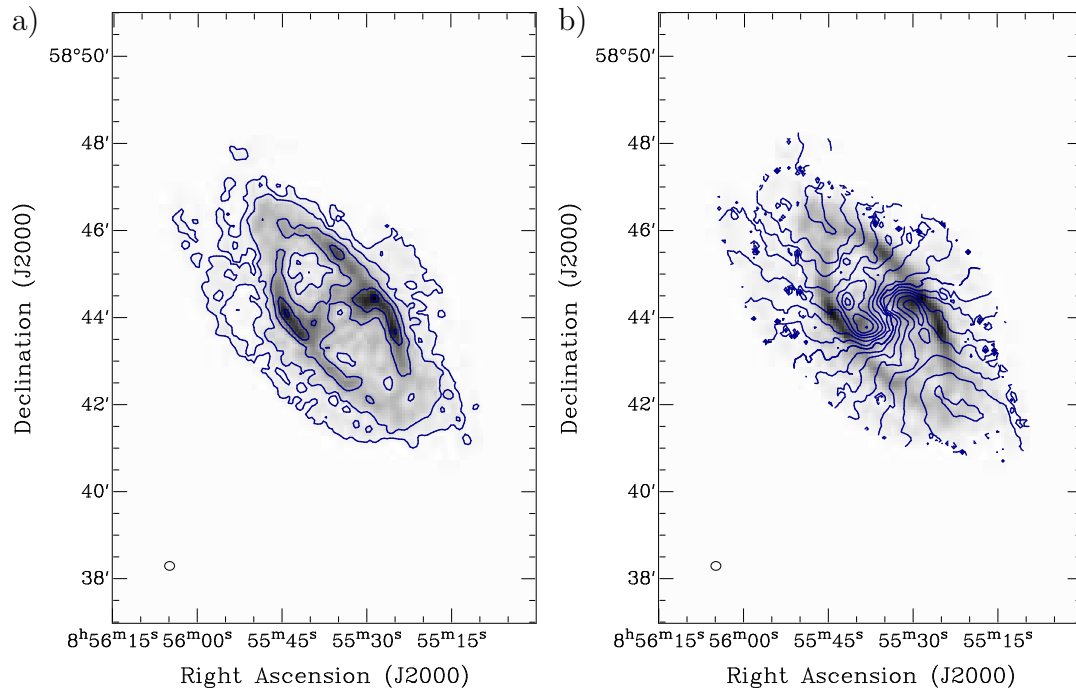


Fig. 5.15: Total intensity map (a, left) and first moment velocity field (b, right) derived from the high-resolution datacube overlaid on a total intensity grey-scale map. The ellipse in the lower left corner represents the clean beam. The contours represent the $8, 24, 72, 144, 217 \cdot 10^{19} \text{ atoms cm}^{-2}$ levels and the $v_{\text{sys}} \pm 0, 20, 40, 60, 80, 100, 120, 140 \text{ km s}^{-1}$ levels respectively (see Tab. 5.1).

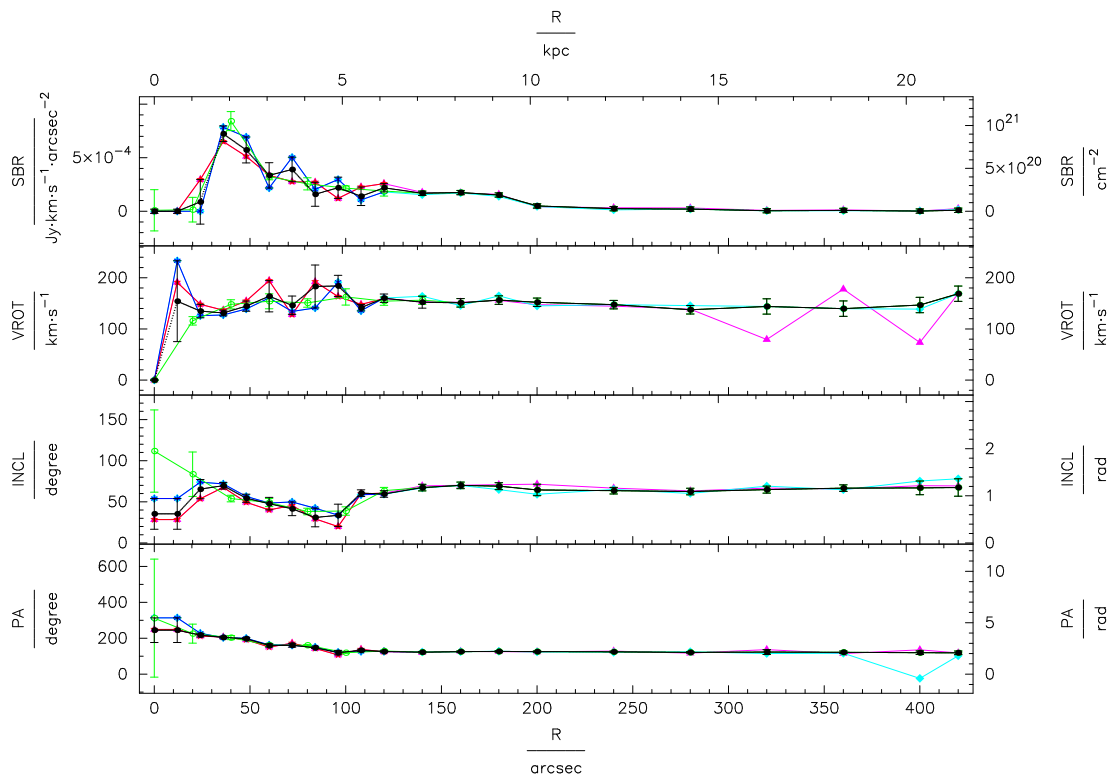


Fig. 5.16: Determination of the final parametrization of the HI disk of NGC 2685. Viewgraph showing the models and error-bar estimation. SBR: surface brightness. VROT: rotation velocity. INCL: inclination. PA: position angle. R: radius. Black curves (dots): finally adopted model and error-bars. Red curves (stars): receding side fitting results from high resolution fitting. Blue curves (asterisks): approaching side fitting results from high resolution fitting. Pink (triangles): receding side fitting results from low resolution fitting. Light blue (diamonds): approaching side fitting results from low resolution fitting. Green (open circles): Results and preliminary error-bars from low resolution fitting.

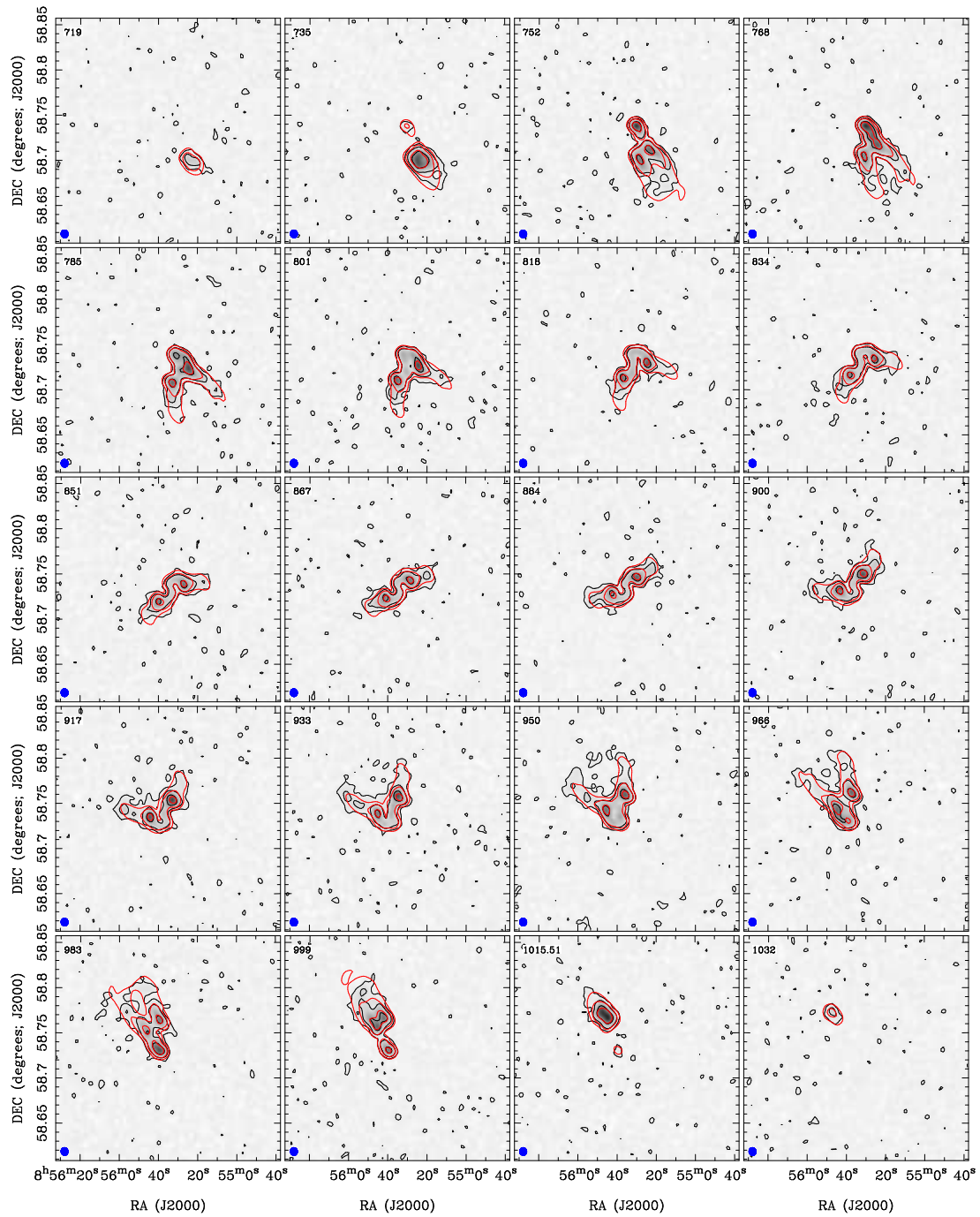


Fig. 5.17: Selected images from the low-resolution datacubes overlaid with contours of the original dataset (blue) and the final model datacube (pink). The numbers on the upper left give the heliocentric radio velocity in km s^{-1} . The blue dot represents the clean beam. NGC 2541. The contours represent the 0.5, 2, 8 mJy/beam levels.

r_p (1)	r_t (2)	Δr_t (3)	$I_{\text{tot.f}}$ (4)	$\Delta I_{\text{tot.f}}$ (5)	N_{HI} (6)	ΔN_{HI} (7)	σ (8)	$\Delta \sigma$ (9)	v_{rot} (10)	Δv_{rot} (11)
0	0.00	0.00	0.0	2.0	0.0	2.5	0.0	0.2	0.0	0.0
12	0.61	0.21	0.0	2.0	0.0	2.5	0.0	0.2	154.2	79.0
24	1.22	0.41	8.8	20.8	10.9	25.9	0.9	2.1	134.9	13.1
36	1.83	0.62	72.4	7.3	90.4	9.1	7.2	0.7	131.2	5.6
48	2.44	0.82	57.2	12.1	71.5	15.1	5.7	1.2	144.6	10.0
60	3.05	1.03	33.5	11.8	41.9	14.7	3.4	1.2	163.9	30.5
72	3.67	1.23	39.0	11.5	48.7	14.3	3.9	1.1	146.1	18.2
84	4.28	1.44	15.9	11.2	19.8	14.0	1.6	1.1	183.1	41.9
96	4.89	1.64	22.0	9.9	27.4	12.4	2.2	1.0	184.0	20.7
108	5.50	1.85	14.0	8.6	17.5	10.8	1.4	0.9	141.5	6.4
120	6.11	2.05	21.9	3.9	27.4	4.9	2.2	0.4	160.0	8.2
140	7.13	2.39	16.8	2.0	21.0	2.5	1.7	0.2	152.2	11.6
160	8.15	2.73	17.5	2.0	21.8	2.5	1.7	0.2	151.0	8.2
180	9.16	3.08	15.2	2.0	18.9	2.5	1.5	0.2	156.4	8.2
200	10.18	3.42	5.0	2.0	6.2	2.5	0.5	0.2	152.1	8.2
240	12.22	4.10	2.4	2.0	3.0	2.5	0.2	0.2	147.5	8.2
280	14.25	4.79	2.0	2.0	2.5	2.5	0.2	0.2	137.5	8.2
320	16.29	5.47	0.5	2.0	0.6	2.5	0.0	0.2	143.9	15.0
360	18.33	6.15	0.8	2.0	1.0	2.5	0.1	0.2	139.6	15.0
400	20.36	6.84	0.2	2.0	0.2	2.5	0.0	0.2	146.7	15.0
420	21.38	7.18	0.9	2.0	1.2	2.5	0.1	0.2	168.8	15.0

Tab. 5.6: Radially dependent best-fit parameters. (1) Radius ($''$). (2) Radius (kpc, according to Tab. 5.2). (3) Error of r_t (kpc) (4) Face-on surface brightness (Jy km s^{-1}). (5) Error of $I_{\text{tot.f}}$ (Jy km s^{-1}). (6) Face-on HI column-density ($10^{19} \text{ atoms cm}^{-2}$). (7) Error of N_{HI} ($10^{19} \text{ atoms cm}^{-2}$). (8) Face-on surface density ($\text{M}_{\odot} \text{ pc}^{-2}$). (9) Error of σ ($\text{M}_{\odot} \text{ pc}^{-2}$). (10) Rotation velocity (km s^{-1}). (11) Error of v_{rot} (km s^{-1}).

r_p (1)	i (12)	Δi (13)	pa (14)	Δpa (15)	n_W (16)	Δn_W (17)	n_N (18)	Δn_N (19)	n_{LOS} (20)	Δn_{LOS} (21)
0	35.3	18.7	245.0	68.7	-0.524	0.379	0.244	0.639	0.816	0.189
12	35.3	18.7	245.0	68.7	-0.524	0.379	0.244	0.639	0.816	0.189
24	65.4	11.7	217.7	10.5	-0.556	0.142	0.720	0.122	0.416	0.186
36	69.7	4.0	204.7	4.0	-0.392	0.060	0.852	0.035	0.348	0.065
48	54.4	4.9	197.9	5.9	-0.249	0.081	0.774	0.054	0.582	0.070
60	47.8	7.6	160.0	8.9	0.253	0.112	0.696	0.093	0.672	0.099
72	41.5	8.3	161.1	10.9	0.215	0.125	0.627	0.111	0.749	0.096
84	31.0	11.3	147.4	4.1	0.277	0.096	0.434	0.144	0.857	0.101
96	33.6	13.6	120.0	12.5	0.479	0.182	0.276	0.144	0.833	0.132
108	60.6	4.0	132.9	6.4	0.638	0.071	0.593	0.075	0.490	0.061
120	59.5	4.0	126.1	4.0	0.696	0.046	0.508	0.053	0.507	0.060
140	67.3	4.0	122.6	4.0	0.777	0.041	0.497	0.056	0.385	0.064
160	70.0	4.0	125.5	4.0	0.765	0.043	0.545	0.055	0.342	0.066
180	69.1	4.2	126.7	4.0	0.749	0.044	0.558	0.055	0.358	0.068
200	64.5	7.0	125.8	4.0	0.732	0.057	0.527	0.060	0.431	0.111
240	63.6	4.0	124.5	4.0	0.738	0.044	0.507	0.054	0.445	0.063
280	62.5	4.0	121.3	4.2	0.758	0.044	0.460	0.059	0.462	0.062
320	64.8	4.3	123.2	13.7	0.757	0.122	0.496	0.182	0.425	0.068
360	66.7	4.0	121.9	7.1	0.780	0.065	0.485	0.098	0.396	0.064
400	66.9	8.4	119.5	10.0	0.801	0.093	0.454	0.143	0.392	0.134
420	67.4	10.6	119.0	10.0	0.807	0.100	0.448	0.145	0.384	0.171

Tab. 5.6: (continued) **(12)** Inclination ($^\circ$). **(13)** Error of i ($^\circ$). **(14)** Position angle ($^\circ$). **(15)** Error of pa ($^\circ$). **(16)** Inclination ($^\circ$). **(17)-(23)** are Cartesian components of the spin normal vector \mathbf{n} of the ring and their errors. **(17)** Spin normal vector component towards W (natural units). **(18)** Error of n_W (natural units). **(19)** Spin normal vector component towards N (natural units). **(20)** Error of n_N (natural units). **(21)** Spin normal vector component towards observer (natural units). **(22)** Error of n_{LOS} (natural units).

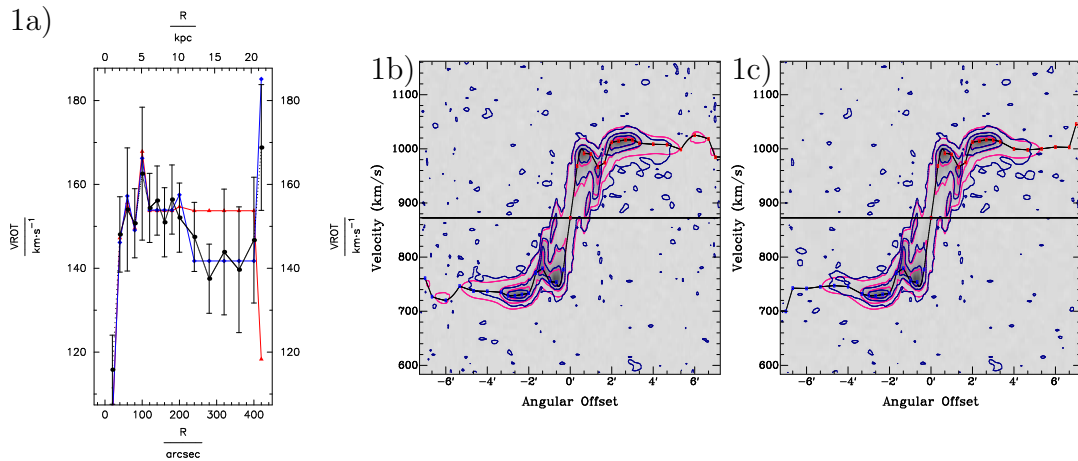


Fig. 5.18: Comparison of fits to the low-resolution datacube selecting two regions with flat rotation curves. Two fits to the datacube were performed. a) shows the fitting results for the rotation curve. b) and c) are comparisons of PV-diagrams of original datacube and model datacube along the kinematical major axis. b) and the blue curve (diamonds) in plot a): Enforcing the two selected regions to have the same rotation velocity. c) and the red curve (triangles) in plot a): Enforcing the rotation curve to be flat inside the selected regions but allowing the rotation velocity to vary from region to region. Black curve (dots) in a): Low-resolution best-fit rotation curve.

6 Final remarks

The thesis is summarised in this chapter. A final discussion that leads to the definition of future projects coming as a natural consequence of the work at hand is presented.

6.1 Summary

Warps in disk galaxies, a bending of the galactic disk away from a principal plane, are seen in nearly every disk galaxy. Therefore, they are of high interest in any global theory dealing with the structure and the formation of disk galaxies. Warps follow certain rules in the sense that similar features are shared to some degree by all warps of disk galaxies, while a warped galaxy frequently disobeys one or two rules. Two prototypes exist, the U-shaped- and the S-shaped warp. Usually a warp in a disk galaxy is a mixture of both, leading to an asymmetric appearance. The bulk of galaxies show predominantly an S-shaped warp, which is the reason why the structure and the formation of S-shaped warps is the most discussed issue in research dealing with galactic warps. As warps usually starts to evolve where the bright stellar disks fade, the domain of warp studies is the neutral gaseous disk of galaxies, which usually extends the optical disk by a factor of a few times.

This thesis deals with the structure of grand-design S-shaped warps (in the following referred to as warps) in disks of galaxies. They are attractive for two reasons. Firstly, they can be parametrised with the so-called tilted-ring model, modelling a galactic disk as a set of thick, concentric, and mutually inclined very thin rings with solid-body rotation. Secondly, they are particularly interesting as they are the predominant type of warp that is found in any environment even for isolated galaxies. A warp leads necessarily to a mutual torquing in the disk, causing the disk to precess at a certain rate at each radius. The differential precession rate, determining the possibly time-dependent structure of the warp is determined by the underlying mass structure of the galaxy. Hence, the exact knowledge about the structure of warps can in turn serve to constrain the distribution of mass in a galaxy, provided a satisfactory theory explaining this structure can be found.

The thesis discusses the current state-of-arts in observational astronomy dealing with the structure of warps. The most important observation is that warps are ubiquitous and their frequency of occurrence is independent of the environment. Hence, in order to explain warps by interaction with the environment, the external agent that drives the warping must be invisible enough in order not to be detectable for quite a number of seemingly isolated galaxies that show warps of high amplitude. It is shown that observed warps follow certain rules reported in

the literature. The most important “rules for the behaviour of warps” were set up by Briggs (1990) analysing tilted-ring models of warped galaxies. They could serve to eliminate a large number of warp theories as discussed in this thesis. In an extensive study of the literature on warp formation theories, it is concluded that two proposed scenarios can survive against the observations. The first scenario is that warps are frequently generated by the secondary infall of cosmic material reorientating the flattened Dark Matter halo. The second scenario is that warps are a steady-state structure in which the disk and the Dark Matter halo are aligned with each other in a way that the differential precession is substituted by a co-precession in two large ranges of radii, one belonging to the disk, one belonging to an outer flattened Dark Matter halo.

The second aspect of warps is that their structure has to be known accurately in order to enable the derivation of so-called rotation curves. A rotation curve, describing the circular velocity in the disk at every radius, is part of the parametrisation of a galactic disk in terms of the tilted-ring model. If the galactic disk is rotationally supported, that is, if the motion of the disk particles is sufficiently described by circular orbits on which the material responds to the net gravitational potential of the galaxy, a rotation curve can serve in order to derive the mass-distribution in a galaxy. Rotation curves have become a major tool in order to test cosmological predictions about the radial profile of Dark Matter halos, hence, for these studies, it is crucial to measure rotation curves, and coming with that the intrinsically changing orientation of the galactic disk, as accurate as possible.

The thesis reviews the standard cosmological picture of galaxy structure and discusses theoretical and practical concepts underlying a mass-decomposition in order to emphasise the importance of the derivation of accurate rotation curves and with that accurate methods to derive a tilted-ring model of disk galaxies. The cosmologically predicted shape of a Dark Matter halo is claimed by some authors to be inconsistent with measured rotation curves, while it is the insufficient accuracy of the rotation curves and the systematical errors that depend on the derivation method of the rotation curves that can well serve to weaken the arguments of these authors.

One of the major goals of the underlying work was to develop a computer program that is able to automatically fit a tilted-ring model to spectroscopic HI observations that does not have the deficiencies of the software available at that time. The usual method of fitting a tilted-ring model to a velocity-field, a map that assigns the recession velocity of the central disk to the data points, has two major disadvantages. It introduces incalculable systematics in the rotation curve that can well bias the results of mass-decompositions in favour of models of the mass-distribution in Dark Matter halos that fundamentally differ from the ones resulting in cosmological simulations. Furthermore, an analysis of a warped disk

or an edge-on disk galaxy is impossible, as no velocity-field exists that can unambiguously assign a single velocity to a point on the sky at which the observer looks through a disk twice. The structure of the developed computer program “tirific” is discussed and it is shown that the method to fit a tilted-ring model directly to datacubes works extremely well and does not have the deficiencies of the methods currently used.

HI synthesis observations of the galaxies NGC 2541, UGC 3580, and NGC 5204 were obtained in order to analyse the structure of their warps with the developed software. Indeed, with the improved sensitivity and the applied new method to derive tilted-ring models from the HI observations, it could be shown that the warps of the three galaxies show more important characteristic features in unison in their warps than reported by Briggs (1990). In this thesis these results are discussed. The three galaxies possess a large *flat* outer HI disk, the warp being the transition from the inner flat disk to the outer flat disk, invalidating at least in the studied cases every theory that reproduces a differential precession in the outer parts of the disk as proposed by Briggs (1990) on the basis of his tilted-ring models which by far did not trace the disk out to the large radii reached in the analysis presented. In particular models in which secondary cosmic infall is the major agent to produce warps become questionable if this feature is present commonly in warps. Two other shared features can be reported on. The HI disk shows a sudden drop in surface brightness at the commencement of the warp and the rotation velocity as determined with the tilted-ring model shows a sudden rise. A careful search in the literature shows that all three features are present to some extent also in other galaxies, in particular in our neighbouring galaxy M33. Hence, the observations could be laid down as an extension of Briggs rules. Computer simulations showed that a flattened Dark Matter halo is not able to maintain its orientation in the presence of a baryonic disk orientated differently with respect to the halos principal axes. In fact, Bailin et al. (2005) observed, analysing simulations in a standard-cosmological environment, that in the reach of the disk the halo almost instantaneously aligns with the disk, while maintaining its orientation at larger radii. They concluded that if a thin gaseous disk would exist in spiral galaxies that is sufficiently extended, this internal misalignment of the disk-halo system would result in a warp that has exactly the structure observed in the three examined galaxies. The two-disk structure found for the three galaxies matches exactly the structure of warps predicted by these authors. Furthermore, the kink in the rotation curve may be due to the fact that a warp occurs at the commencement of different dynamical regimes, a disk-dominated one and a halo-dominated one. The drop in the HI surface density at the commencement of the warp may serve the outer halo in order to maintain its orientation as no heavy disk component is visible anymore at the outer radii. It can be concluded that the concept of warps being a long-lived structure that reflects the disk-halo interplay as already proposed by Binney et al. (1998) is the

most attractive scenario for warp formation and maintenance. Unfortunately an elaborate theoretical treatment of such disk-halo normal modes does not exist yet.

One of the important virtues of *tirific* is the ability to analyse spectral datacubes of galaxies the disks of which cross the line-of-sight twice or more. This is demonstrated in the spectacular case of the so-called “Spindle Galaxy” NGC 2685, which is considered as a classical two-ringed polar ring galaxy. Deep HI synthesis observations and optical observations were obtained, on the basis of which it is shown that the appearance of two separate disks or rings in this galaxy is solely due to projection effects. NGC 2685 possesses instead a heavily warped gaseous and stellar disk, the structure of which could be analysed by means of a tilted-ring model employing *tirific*. It is shown that NGC 2685 resembles in many ways a spiral galaxy with a central elongated bulge or a central bar and its warp is by large and large a typical symmetric S-shaped warp. The similarities and differences of the warp of NGC 2685 with the warps of the three formerly examined galaxies are discussed. The disk of NGC 2685 is not flat in its inner part and the drop of the HI surface-density profile that is present also in the disk of NGC 2685 is detected at a radius where the disk of NGC 2685 has already become flat again. These differences may be connected with the fact that NGC 2685 has a rather dim disk. If the warp of NGC 2685 occurs at a radius where the galaxy potential switches from being disk-dominated to being Dark Matter-dominated, this means that the halo takes over the net gravitational potential at very small radii because the disk is rather lightweight. The halo does not need a drop in the HI surface-density profile in order to become gravitationally dominant. The proof of the warped structure of the disk of NGC 2685 invalidates a couple of theories that try to explain the appearance of NGC 2685. In particular, it seems to be necessary to invoke the action of a figure-rotating potential in order to explain the structure of NGC 2685. The resemblance of NGC 2685 to a disk galaxy and the fact that indeed its warp seems to follow to a great extent the rules for the behaviour of warps at least allows the speculation whether NGC 2685 is a prototype S-shaped warped galaxy with a comparably light-weight disk.

6.2 Outlook

Warps are an exciting field of research. “There seems little doubt that they are trying to tell us something about the halos which dominate their dynamics, and about the alter stages of galaxy formation” (Binney, 1992). Indeed, the results of this work point to the fact that with a parametrisation of warps, the underlying mass-distribution can be traced. If the picture of warps proposed in this thesis can be proven to be true, then a warp traces the preferential plane of the net potential in a galaxy, which in the inner region of galaxies is aligned with the

plane of the baryonic disk, and in the outer regions the preferential plane of a misaligned flattened Dark Matter halo. Once this dynamical challenge is solved, the structure of warps can then be used to constrain the structure of Dark Matter halos.

The first thing to go about is to make an effort to understand the structure of a common bending mode of disk and halo, which was proposed by Binney et al. (1998) and which is already evident in the numerical simulations presented by Bailin et al. (2005). Both issues have to be addressed. Firstly, an analytic description of such warps is needed and would enable the link between the warp structure and the underlying mass distribution in spiral galaxies that secondly needs to be confirmed in high-resolution numerical simulations. Seemingly, in such simulations the presence of a disk beyond radii allowed by the standard cosmological theory would be needed. This is mainly a plea towards the address of theoreticians.

On the observational side, a lot has to be done, and only a few things shall be mentioned here. The new rules for the behaviour of warps have been shown to be followed by three galaxies, while a literature search showed that indeed quite some galaxies seem to show the same features. It is of course of great interest to add a lot more galaxies the warp structure of which can be explored in order to put the new rules for the behaviour of warps on solid ground or to falsify them. While this would not need an observational effort – every galaxy is warped and plentiful of archive data await their analysis – the major difficulty lies in making *tirific* fast enough in order to be able to analyse a lot of galaxies in a reasonable time. Luckily, *tirific* offers unique opportunities to become faster. While the emphasis lay on the development of very fast routines that enable the calculation of single models and their goodness-of-fit estimation, the particular method to find a minimum in parameter space is very primitive. The implementation of efficient minimising algorithms in order to speed up the fitting process is hence a promising enterprise, maybe making *tirific* fast enough for an error-bar estimation using bootstrap methods or similar. Many possibilities exist to parallelise *tirific*, such as the parallel calculation of a number of trial models at the same time. *Tirific* will become substantially faster in order to enable the analysis of many galaxies in a short time.

Another issue to follow up is the analysis of U-shaped warps in order to put up similar rules as was done in this work for S-shaped warps. *Tirific* has already been used in order to successfully analyse the bowl-shaped warp of the spiral galaxy NGC 4414 (Meisner, 2005). This was possible, because *tirific* offers the opportunity to include a systematic shift of the galactic centre with radius. Hence, *tirific* offers the opportunity to parametrise also systems that could not be analysed before. In this field, work is already in progress.

Last but not least, one issue could not be solved with the tilted-ring model as it

is implemented in tirific. Tirific always uses circular orbits and does not allow for changes of the surface-brightness and the rotation speed along a ring. This means that in this work only a crude picture could be drawn of the deviations from circular orbits of the disk material. On the short timescale, two additional possibilities for a parametrisation will find their entry in the tirific software. Firstly, harmonical variations of the rotation velocity and intensity along the ring will be introduced in the tirific tilted-ring model. This can then serve in order to quantify planar deviations from the circularity of the orbits in disk galaxies and to trace the structure of spiral arms. The second extension refers to the antisymmetric feature that was shown to be present in the residual velocity fields of all observed galaxies. It is very improbable that this turns up because tirific works in the wrong way. Two other possibilities to produce such an antisymmetric feature in residual velocity fields are the presence of a bar, or, a most promising aspect, the precession of the disk. While the possibility of a bar-like variation of the potential can be examined by introducing harmonical velocity-variations along the rings, also secondly the possibility of a precession will be included in order to be able to measure the possible and expected precession of the galaxy disks.

There is a lot of exciting research work lying ahead to look forward to.

A Acknowledgments

I am deeply indebted to Tom “Il Magico” Oosterloo. The project was planned and conducted and fundamental ideas were developed under his supervision and with his help. He taught me the inner secrets of HI data reduction. He did not have to do that. I thank him for his corrections and suggestions concerning this thesis.

I am deeply indebted to Uli Klein for supervising this thesis project. Without his help, advice, and encouragement this thesis would not have been possible. He and Tom did a perfect job. I thank him for his aid correcting and improving this thesis.

I am indebted to Franz Kenn. While I was programming the C-code of tirific he developed a preliminary script version using the concepts of tirific, showing that the program would work indeed. He participated and participates in the development of tirific, a project that sometimes seemed too large for one person. I thank him for reading large parts of the thesis.

I thank Thomas Erben. He made the brilliant GaBoDS reduction pipeline available to me and spent a lot of time explaining the use of it in order to reduce the optical observations. He also did not have to do this.

I thank Ralf-Juergen Dettmar and the supervisors of the “Graduiertenkolleg 787”. He was a brilliant chairman of the gradschool. I cordially regret that the continuation of the gradschool was rejected by the Deutsche Forschungsgemeinschaft, as it was working extremely efficiently enabling students to become scientists.

I thank Eva Manthey for helping me to get started with conducting my first optical observations.

I thank Peter Kalberla for his help. He played a big role in starting this thesis project and was always very helpful, personally and scientifically.

I thank Karl-Heinz Mack, Daniela Vergani and Gianfranco Gentile for helping me at the start of the thesis project.

I thank Christina Stein-Schmitz for all her help in bureaucratic matters. Her willingness to help also “unimportant” persons is a great luck for all students of the AIfA.

I thank all members of the former RAIUB for a lot of discussion and advice, especially Michael Kappes, with whom I spent a lot of time talking about science, computers, music, and similar.

I thank the referees of this thesis, Uli Klein, Peter Schneider, Karl Maier, and Reinhard Klein for spending a lot of time on reading it.

I thank ASTRON for granting me a summer-studentship. During the weeks in Dwingeloo the basis of this thesis was founded.

The thesis project was partly financed by the Deutsche Forschungsgemeinschaft in the framework of the Graduiertenkolleg 787 “Galaxy Groups as Laboratories for Baryonic and Dark Matter”, the continuation of which has regrettably been rejected by the DFG.

The thesis project was partly financed by the University of Bonn in the framework of the “Research Group Bonn: Dark Matter and Dark Energy”.

I am deeply indebted to my wife and my daughter, who had to suffer from this thesis project and were always behind me when going on became harder. To have them at my side is pure luck.

I thank god for everything, especially but at this place for providing mankind with the virtue of patience.

References

- Abadi, M. G., Navarro, J. F., Steinmetz, M., & Eke, V. R. 2003a, *ApJ*, 591, 499
- Abadi, M. G., Navarro, J. F., Steinmetz, M., & Eke, V. R. 2003b, *ApJ*, 597, 21
- Arnaboldi, M. & Galletta, G. 1993, *A&A*, 268, 411
- Arp, H. 1966, *Atlas of Peculiar Galaxies* (California Institute of Technology, Pasaadena, CA)
- Avner, E. S. & King, I. R. 1967, *AJ*, 72, 650
- Baes, M., Davies, J. I., Dejonghe, H., et al. 2003, *MNRAS*, 343, 1081
- Bahcall, J. N., Schmidt, M., & Soneira, R. M. 1982, *ApJ*, 258, L23
- Bailin, J. 2003, *ApJ*, 583, L79
- Bailin, J., Kawata, D., Gibson, B. K., et al. 2005, *ApJ*, 627, L17
- Bailin, J. & Steinmetz, M. 2003, *Ap&SS*, 284, 701
- Bailin, J. & Steinmetz, M. 2004a, in *Satellites and Tidal Streams*, ASP Conf. Ser., 327, ed. F. Prada, D. Martinez Delgado, & T. J. Mahoney (San Francisco: ASP), 225
- Bailin, J. & Steinmetz, M. 2004b, *ApJ*, 616, 27
- Barteldrees, A. & Dettmar, R.-J. 1994, *A&AS*, 103, 475
- Battaglia, G., Fraternali, F., Oosterloo, T., & Sancisi, R. 2005, *A&A*, accepted
- Battaner, E., Florido, E., & Sánchez-Saavedra, M. L. 1990a, *A&A*, 236, 1
- Battaner, E., Florido, E., & Sánchez-Saavedra, M. L. 1990b, in *IAU Symp. 140: Galactic and Intergalactic Magnetic Fields*, ed. R. Beck, P. P. Kronberg, & R. Wielebinski (Dordrecht: Kluwer), 504
- Battaner, E., Garrido, J. L., Sánchez-Saavedra, M. L., & Florido, E. 1991, *A&A*, 251, 402
- Battaner, E. & Jimenez-Vicente, J. 1998, *A&A*, 332, 809
- Begemann, K. G. 1987, Ph.D. Thesis
- Bekki, K. 1997, *ApJ*, 490, L37
- Bekki, K. 1998, *ApJ*, 499, 635

- Bekki, K. & Freeman, K. C. 2002, *ApJ*, 574, L21
- Bell, E. F. & de Jong, R. S. 2001, *ApJ*, 550, 212
- Bell, E. F., McIntosh, D. H., Katz, N., & Weinberg, M. D. 2003, *ApJS*, 149, 289
- Bertin, G. & Casertano, S. 1982, *A&A*, 106, 274
- Bertin, G. & Mark, J. W.-K. 1980, *A&A*, 88, 289
- Binney, J. 1978, *MNRAS*, 183, 779
- Binney, J. 1991, in *Dynamics of Disc Galaxies*, ed. Sundelius, B. (Chalmers University), 297
- Binney, J. 1992, *ARA&A*, 30, 51
- Binney, J., Jiang, I., & Dutta, S. 1998, *MNRAS*, 297, 1237
- Binney, J. & Merrifield, M. 1998, *Galactic astronomy* (Princeton, NJ: Princeton University Press)
- Binney, J. & Tremaine, S. 1987, *Galactic dynamics* (Princeton, NJ: Princeton University Press)
- Blais-Ouellette, S., Amram, P., Carignan, C., & Swaters, R. 2004, *A&A*, 420, 147
- Blais-Ouellette, S., Carignan, C., Amram, P., & Côté, S. 1999, *AJ*, 118, 2123
- Böhm, A., Ziegler, B. L., Saglia, R. P., et al. 2004, *A&A*, 420, 97
- Boomsma, R., van der Hulst, J. M., Oosterloo, T. A., & Sancisi, R. 2002, *Bulletin of the American Astronomical Society*, 34, 708
- Borriello, A. & Salucci, P. 2001, *MNRAS*, 323, 285
- Bosma, A. 1978, PhD thesis
- Bosma, A. 1981a, *AJ*, 86, 1791
- Bosma, A. 1981b, *AJ*, 86, 1825
- Bosma, A. 1991, in *Warped Disks and Inclined Rings around Galaxies*, ed. S. Casertano, P. Sackett, & F. Briggs (Cambridge: CUP), 181
- Bottema, R. 1996, *A&A*, 306, 345
- Bottinelli, L. & Gougenheim, L. 1973, *A&A*, 29, 425
- Bournaud, F. & Combes, F. 2003, *A&A*, 401, 817

- Brada, R. & Milgrom, M. 2000, *ApJ*, 531, L21
- Briggs, F. & Hamphuis, J. 1991, in *Warped Disks and Inclined Rings around Galaxies*, ed. S. Casertano, P. Sackett, & F. Briggs (Cambridge: CUP), 190
- Briggs, F. H. 1990, *ApJ*, 352, 15
- Bryan, G. L. & Norman, M. L. 1998, *ApJ*, 495, 80
- Bureau, M. & Carignan, C. 2002, *AJ*, 123, 1316
- Burke, B. F. 1957, *AJ*, 62, 90
- Burkert, A. 1995, *ApJ*, 447, L25
- Cabrera-Lavers, A. & Garzón, F. 2004, *AJ*, 127, 1386
- Carignan, C. & Freeman, K. C. 1988, *ApJ*, 332, L33
- Casertano, S. 1983, *MNRAS*, 203, 735
- Castro-Rodríguez, N., López-Corredoira, M., Sánchez-Saavedra, M. L., & Batten, E. 2002, *A&A*, 391, 519
- Chapelon, S., Contini, T., & Davoust, E. 1999, *A&A*, 345, 81
- Christodoulou, D. M. & Tohline, J. E. 1986, *ApJ*, 307, 449
- Coccatto, L., Corsini, E. M., Pizzella, A., et al. 2004, *A&A*, 416, 507
- Corbelli, E. & Salucci, P. 2000, *MNRAS*, 311, 441
- Corbelli, E. & Schneider, S. E. 1997, *ApJ*, 479, 244
- Corsini, E. M., Pizzella, A., Coccatto, L., & Bertola, F. 2003, *A&A*, 408, 873
- Cox, A. L., Sparke, L. S., van Moorsel, G., & Shaw, M. 1996, *AJ*, 111, 1505
- de Blok, W. J. G. & Bosma, A. 2002, *A&A*, 385, 816
- de Blok, W. J. G., Bosma, A., & McGaugh, S. 2003, *MNRAS*, 340, 657
- de Blok, W. J. G. & McGaugh, S. S. 1997, *MNRAS*, 290, 533
- de Blok, W. J. G., McGaugh, S. S., & Rubin, V. C. 2001, *AJ*, 122, 2396
- de Jong, R. S. 1996, *A&A*, 313, 377
- de Vaucouleurs, G., de Vaucouleurs, A., Corwin, H. G., et al. 1991, *Third Reference Catalogue of Bright Galaxies* (Berlin Heidelberg New York: Springer)

- Debattista, V. P. & Sellwood, J. A. 1999, *ApJ*, 513, L107
- Dekel, A. & Shlosman, I. 1983, in *IAU Symp. 100: Internal Kinematics and Dynamics of Galaxies*, ed. E. Athanassoula (Dordrecht: Kluwer), 187
- Dubinski, J. & Kuijken, K. 1995, *ApJ*, 442, 492
- Eidelman, S., Hayes, K., Olive, K., et al. 2004, *Physics Letters B*, 592, 1
- Elwert, G. & Hablick, D. 1965, *Zeitschrift für Astrophysik*, 61, 273
- Eskridge, P. B. & Pogge, R. W. 1997, *ApJ*, 486, 259
- Ferrarese, L., Bresolin, F., Kennicutt, R. C., et al. 1998, *ApJ*, 507, 655
- Flores, R. A. & Primack, J. R. 1994, *ApJ*, 427, L1
- Florido, E., Battaner, E., Gros, A., Prieto, M., & Mediavilla, E. 1992, *Ap&SS*, 190, 293
- Florido, E., Prieto, M., Battaner, E., et al. 1991, *A&A*, 242, 301
- Fomalont, E. 1981, *NEWSLETTER. NRAO NO. 3*, P. 3, 3, 3
- Franx, M., van Gorkom, J. H., & de Zeeuw, T. 1994, *ApJ*, 436, 642
- Fraternali, F., Oosterloo, T., & Sancisi, R. 2004, *Ap&SS*, 289, 377
- Fraternali, F., Oosterloo, T., Sancisi, R., & van Moorsel, G. 2001, *ApJ*, 562, L47
- Freedman, W. L., Madore, B. F., Gibson, B. K., et al. 2001, *ApJ*, 553, 47
- Freeman, K. C. 1970, *ApJ*, 160, 811
- Freeman, K. C. 1978, in *IAU Symp. 77: Structure and Properties of Nearby Galaxies* (Dordrecht: Kluwer), 3–10
- Frigo, M. & Johnson, S. G. 2005, *Proceedings of the IEEE*, 93, 216, special issue on "Program Generation, Optimization, and Platform Adaptation"
- Frogel, J. A. & Stothers, R. 1977, *AJ*, 82, 890
- García-Ruiz, I. 2001, PhD thesis, Groningen
- García-Ruiz, I., Kuijken, K., & Dubinski, J. 2002a, *MNRAS*, 337, 459
- García-Ruiz, I., Sancisi, R., & Kuijken, K. 2002b, *A&A*, 394, 769
- Garrido, O., Marcelin, M., & Amram, P. 2004, *MNRAS*, 349, 225

- Gentile, G. 2003, Ph.D. Thesis, Bonn
- Gentile, G., Salucci, P., Klein, U., Vergani, D., & Kalberla, P. 2004, *MNRAS*, 351, 903
- Ghigna, S., Moore, B., Governato, F., et al. 2000, *ApJ*, 544, 616
- Gooch, R. 1995, in *Astronomical Data Analysis Software and Systems IV*, ASP Conf. Ser., 77, ed. R. Shaw, H. Payne, & J. Hayes (San Francisco: ASP), 144
- Gordon, K. J. 1971, *ApJ*, 169, 235
- Grebel, E. K., Gallagher, J. S., & Harbeck, D. 2003, *AJ*, 125, 1926
- Hayashi, E., Navarro, J. F., Power, C., et al. 2004, *MNRAS*, 355, 794
- Helfer, T. T., Thornley, M. D., Regan, M. W., et al. 2003, *ApJS*, 145, 259
- Hofner, P. & Sparke, L. S. 1994, *ApJ*, 428, 466
- Hunter, C. & Toomre, A. 1969, *ApJ*, 155, 747
- Ibata, R. A., Gilmore, G., & Irwin, M. J. 1994, *Nature*, 370, 194
- Ideta, M., Hozumi, S., Tsuchiya, T., & Takizawa, M. 2000, *MNRAS*, 311, 733
- Irwin, J. A. & Seaquist, E. R. 1991, *ApJ*, 371, 111
- James, R. A. & Sellwood, J. A. 1978, *MNRAS*, 182, 331
- Jiang, I. & Binney, J. 1999, *MNRAS*, 303, L7
- Jiang, I. & Binney, J. 2000, *MNRAS*, 314, 468
- Józsa, G. I. G. 2002, Diplomarbeit, Universität Bonn
- Kahn, F. D. & Woltjer, L. 1959, *ApJ*, 130, 705
- Karachentsev, I. D., Kopylov, A. I., & Kopylova, F. G. 1994, *Bull. Special Astrophys. Obs.*, 38, 5
- Karachentsev, I. D., Sharina, M. E., Dolphin, A. E., et al. 2003, *A&A*, 398, 467
- Kazantzidis, S., Kravtsov, A. V., Zentner, A. R., et al. 2004, *ApJ*, 611, L73
- Kenn, F. 2005, Diplomarbeit, Universität Bonn
- Kent, S. M. 1986, *AJ*, 91, 1301
- Kerr, F. J. 1957, *AJ*, 62, 93

- Kitayama, T. & Suto, Y. 1996, *ApJ*, 469, 480
- Koonin, S. E. & Meredith, D. C. 1990, *Computational Physics* (Redwood City, CA, USA: Addison-Wesley)
- Kravtsov, A. V., Klypin, A. A., Bullock, J. S., & Primack, J. R. 1998, *ApJ*, 502, 48
- Kronberg, P. P. 1995, *Nature*, 374, 404
- Kuijken, K. 1991, *ApJ*, 376, 467
- López-Corredoira, M., Betancort-Rijo, J., & Beckman, J. E. 2002, *A&A*, 386, 169
- Levenberg, K. 1944, *Quart. Appl. Math.*, 2, 164
- Lewis, B. M. 1968, *Proceedings of the Astronomical Society of Australia*, 1, 104
- Lin, D. N. C. & Lynden-Bell, D. 1982, *MNRAS*, 198, 707
- Liszt, H. S. & Burton, W. B. 1980, *ApJ*, 236, 779
- López-Corredoira, M., Beckman, J. E., & Casuso, E. 1999, *A&A*, 351, 920
- Lynden-Bell, D. 1965, *MNRAS*, 129, 299
- Mahon, M. E. 1992, *Bulletin of the American Astronomical Society*, 24, 1267
- Marquardt, D. 1963, *SIAM J. Appl. Math.*, 11, 431
- May, A. & James, R. A. 1984, *MNRAS*, 206, 691
- Meisner, T. 2005, *Diplomarbeit, Universität Bonn*
- Metropolis, N., Rosenbluth, A., Teller, A., & Teller, E. 1953, *J. Chem. Phys.*, 21, 1087
- Meza, A., Navarro, J. F., Steinmetz, M., & Eke, V. R. 2003, *ApJ*, 590, 619
- Milgrom, M. 1983, *ApJ*, 270, 365
- Moore, B. 1994, *Nature*, 370, 629
- Moore, B., Ghigna, S., Governato, F., et al. 1999a, *ApJ*, 524, L19
- Moore, B., Governato, F., Quinn, T., Stadel, J., & Lake, G. 1998, *ApJ*, 499, L5+
- Moore, B., Quinn, T., Governato, F., Stadel, J., & Lake, G. 1999b, *MNRAS*, 310, 1147

- Moore, B., Quinn, T., Governato, F., Stadel, J., & Lake, G. 1999c, MNRAS, 310, 1147
- Murai, T. & Fujimoto, M. 1980, PASJ, 32, 581
- Murali, C. 2000, ApJ, 529, L81
- Navarro, J. F., Frenk, C. S., & White, S. D. M. 1995, MNRAS, 275, 56
- Navarro, J. F., Frenk, C. S., & White, S. D. M. 1996, ApJ, 462, 563
- Navarro, J. F., Frenk, C. S., & White, S. D. M. 1997, ApJ, 490, 493
- Navarro, J. F., Hayashi, E., Power, C., et al. 2004, MNRAS, 349, 1039
- Navarro, J. F. & Steinmetz, M. 2000, ApJ, 528, 607
- Nelson, R. W. & Tremaine, S. 1995, MNRAS, 275, 897
- Oosterloo, T. A., Morganti, R., Sadler, E. M., Vergani, D., & Caldwell, N. 2002, AJ, 123, 729
- Ostriker, E. C. & Binney, J. J. 1989, MNRAS, 237, 785
- Paturel, G. 1989, Catalogue of principal galaxies (PGC) (Lyon: Base de Donnees Extragalactiques, Observatoire de Lyon)
- Pease, F. G. 1917, ApJ, 46, 24
- Peletier, R. F. & Christodoulou, D. M. 1993, AJ, 105, 1378
- Persic, M. & Salucci, P. 1995, ApJS, 99, 501
- Persic, M., Salucci, P., & Stel, F. 1996, MNRAS, 281, 27
- Petrou, M. 1980, MNRAS, 191, 767
- Pfenniger, D. & Combes, F. 1994, A&A, 285, 94
- Pfenniger, D., Combes, F., & Martinet, L. 1994, A&A, 285, 79
- Pickering, T. E., Impey, C. D., van Gorkom, J. H., & Bothun, G. D. 1997, AJ, 114, 1858
- Pisano, D. J., Barnes, D. G., Gibson, B. K., et al. 2004, ApJ, 610, L17
- Press, W. H., Flannery, B. P., & Teukolsky, S. A. 1986, Numerical recipes. The art of scientific computing (Cambridge: University Press)

- Prieto, M., Aguerri, J. A. L., Varela, A. M., & Muñoz-Tuñón, C. 2001, *A&A*, 367, 405
- Reed, D., Governato, F., Verde, L., et al. 2005, *MNRAS*, 357, 82
- Reshetnikov, V. & Combes, F. 1998, *A&A*, 337, 9
- Reshetnikov, V. & Combes, F. 1999, *A&AS*, 138, 101
- Reshetnikov, V. & Sotnikova, N. 1997, *A&A*, 325, 933
- Reshetnikov, V. P., Hagen-Thorn, V. A., & Yakovleva, V. A. 1994, *A&A*, 290, 693
- Revaz, Y. & Pfenniger, D. 2001, *A&A*, 372, 784
- Revaz, Y. & Pfenniger, D. 2004, *A&A*, 425, 67
- Richter, O.-G., Sackett, P. D., & Sparke, L. S. 1994, *AJ*, 107, 99
- Rogstad, D. H., Lockart, I. A., & Wright, M. C. H. 1974, *ApJ*, 193, 309
- Rogstad, D. H., Wright, M. C. H., & Lockhart, I. A. 1976, *ApJ*, 204, 703
- Rubin, V. C. & Ford, W. K. J. 1970, *ApJ*, 159, 379
- Rubin, V. C., Thonnard, N., & Ford, W. K. 1980, *ApJ*, 238, 471
- Sánchez-Saavedra, M. L., Battaner, E., & Florido, E. 1990a, *MNRAS*, 246, 458
- Sánchez-Saavedra, M. L., Battaner, E., & Florido, E. 1990b, *Ap&SS*, 171, 239
- Sánchez-Saavedra, M. L., Battaner, E., Guijarro, A., López-Corredoira, M., & Castro-Rodríguez, N. 2003, *A&A*, 399, 457
- Sánchez-Salcedo, F. J. 2004, *Journal of Korean Astronomical Society*, 37, 205
- Sakai, S., Mould, J. R., Hughes, S. M. G., et al. 2000, *ApJ*, 529, 698
- Salucci, P. & Burkert, A. 2000, *ApJ*, 537, L9
- Salucci, P., Walter, F., & Borriello, A. 2003, *A&A*, 409, 53
- Sánchez-Salcedo, F. J. 2005, accepted for publication in *MNRAS*
- Sancisi, R. 1976, *A&A*, 53, 159
- Sandage, A. 1961, *The Hubble atlas of galaxies* (Washington: Carnegie Institution)

- Sasaki, T. 1987, PASJ, 39, 849
- Sault, R. J., Teuben, P. J., & Wright, M. C. H. 1995, in *Astronomical Data Analysis Software and Systems IV*, ASP Conf. Ser., 77 (San Francisco: ASP), 433
- Schechter, P. L. & Gunn, J. E. 1978, AJ, 83, 1360
- Schinnerer, E. & Scoville, N. 2002, ApJ, 577, L103
- Schirmer, M., Erben, T., Schneider, P., et al. 2003, A&A, 407, 869
- Schmidt, M. 1956, Bull. Astron. Inst. Netherlands, 13, 15
- Schoenmakers, R. H. M., Franx, M., & de Zeeuw, P. T. 1997, MNRAS, 292, 349
- Schwarz, U. J. 1985, A&A, 142, 273
- Schwarzkopf, U. & Dettmar, R.-J. 2001, A&A, 373, 402
- Schweizer, F., Whitmore, B. C., & Rubin, V. C. 1983, AJ, 88, 909
- Sersic, J. L. 1968, *Atlas de galaxias australes* (Cordoba, Argentina: Observatorio Astronomico)
- Shane, W. W. 1977, BAAS, 9, 362
- Shane, W. W. 1980, A&A, 82, 314
- Shang, Z., Brinks, E., Zheng, Z., et al. 1998, ApJ, 504, L23
- Sharma, S. & Steinmetz, M. 2005, ApJ, 628, 21
- Shobbrook, R. R. & Robinson, B. J. 1967, Australian Journal of Physics, 20, 131
- Sicotte, V. & Carignan, C. 1997, AJ, 113, 609
- Sicotte, V., Carignan, C., & Durand, D. 1996, AJ, 112, 1423
- Simard, L. & Pritchett, C. J. 1999, PASP, 111, 453
- Simon, J. D., Bolatto, A. D., Leroy, A., & Blitz, L. 2003, ApJ, 596, 957
- Simon, J. D., Bolatto, A. D., Leroy, A., Blitz, L., & Gates, E. L. 2005, ApJ, 621, 757
- Simonneau, E. & Prada, F. 2004, *Revista Mexicana de Astronomia y Astrofisica*, 40, 69
- Simonson, G. F. & Tohline, J. E. 1983, ApJ, 268, 638

- Sparke, L. S. 1984, *ApJ*, 280, 117
- Sparke, L. S. 1985, in *The Milky Way Galaxy*, IAU Symp., 106, ed. H. van Woerden, R. J. Allen, & W. B. Burton (Dordrecht: Kluwer), 499
- Sparke, L. S. 1986, *MNRAS*, 219, 657
- Sparke, L. S. 1995, *ApJ*, 439, 42
- Sparke, L. S. & Casertano, S. 1988, *MNRAS*, 234, 873
- Spitzer, L. J. 1942, *ApJ*, 95, 329
- Swaters, R. A. 1999, PhD thesis
- Swaters, R. A. 2001, in *Galaxy Disks and Disk Galaxies*, ASP Conf. Ser., 230, ed. J. G. Funes & E. M. Corsini (San Francisco: ASP), 545
- Swaters, R. A., Madore, B. F., & Trewhella, M. 2000, *ApJ*, 531, L107
- Swaters, R. A., Madore, B. F., van den Bosch, F. C., & Balcells, M. 2003, *ApJ*, 583, 732
- Swaters, R. A., Sancisi, R., & van der Hulst, J. M. 1997, *ApJ*, 491, 140
- Takamiya, T. & Sofue, Y. 2002, *ApJ*, 576, L15
- Taniguchi, Y., Sofue, Y., Wakamatsu, K.-I., & Nakai, N. 1990, *AJ*, 100, 1086
- Teuben, P. 1995, in *Astronomical Data Analysis Software and Systems IV*, ASP Conf. Ser., 77, ed. R. Shaw, H. Payne, & J. Hayes (San Francisco: ASP), 398
- Teuben, P. J. 1991, in *Warped Disks and Inclined Rings around Galaxies*, ed. S. Casertano, P. Sackett, & F. Briggs (Cambridge: CUP), 40
- Teuben, P. J. 2002, in *Disks of Galaxies: Kinematics, Dynamics and Perturbations*, ASP Conf. Ser., 275, ed. E. Athanassoula, A. Bosma, & R. Mujica (San Francisco: ASP), 217
- Tohline, J. E. & Durisen, R. H. 1982, *ApJ*, 257, 94
- Toomre, A. 1983, in *IAU Symp. 100: Internal Kinematics and Dynamics of Galaxies*, ed. E. Athanassoula (Dordrecht: Kluwer), 177
- Tubbs, A. D. & Sanders, R. H. 1979, *ApJ*, 230, 736
- Ulrich, M.-H. 1975, *PASP*, 87, 965
- Uson, J. M. & Matthews, L. D. 2003, *AJ*, 125, 2455

- van Albada, T. S., Bahcall, J. N., Begeman, K., & Sancisi, R. 1985, *ApJ*, 295, 305
- van Albada, T. S., Kotanyi, C. G., & Schwarzschild, M. 1982, *MNRAS*, 198, 303
- van den Bosch, F. C., Robertson, B. E., Dalcanton, J. J., & de Blok, W. J. G. 2000, *AJ*, 119, 1579
- van den Bosch, F. C. & Swaters, R. A. 2001, *MNRAS*, 325, 1017
- van der Hulst, J. M., Terlouw, J. P., Begeman, K. G., Zwitter, W., & Roelfsema, P. R. 1992, in *Astronomical Data Analysis Software and Systems I*, ASP Conf. Ser., 25, ed. D. M. Worrall, C. Biemesderfer, & J. Barnes (San Francisco: ASP), 131
- van der Hulst, J. M., van Albada, T. S., & Sancisi, R. 2001, in *Gas and Galaxy Evolution*, ASP Conf. Ser., 240, ed. J. E. Hibbard, M. Rupen, & J. H. van Gorkom (San Francisco: ASP), 451
- van der Kruit, P. C. & Searle, L. 1981a, *A&A*, 95, 116
- van der Kruit, P. C. & Searle, L. 1981b, *A&A*, 95, 105
- van der Kruit, P. C. & Searle, L. 1982, *A&A*, 110, 79
- Varnas, S. R. 1990, *MNRAS*, 247, 674
- Verheijen, M. A. W. 1997, PhD thesis
- Wainscoat, R. J., Freeman, K. C., & Hyland, A. R. 1989, *ApJ*, 337, 163
- Warner, P. J., Wright, M. C. H., & Baldwin, J. E. 1973, *MNRAS*, 163, 163
- Weinberg, M. D. 1998, *MNRAS*, 299, 499
- Weldrake, D. T. F., de Blok, W. J. G., & Walter, F. 2003, *MNRAS*, 340, 12
- Westmeier, T., Brüns, C., & Kerp, J. 2005, in *Extra-Planar Gas*, ASP Conf. Ser., 331, ed. R. Braun (San Francisco: ASP), 105
- Whitmore, B. C., Lucas, R. A., McElroy, D. B., et al. 1990, *AJ*, 100, 1489
- Wright, M. C. H., Warner, P. J., & Baldwin, J. E. 1972, *MNRAS*, 155, 337

List of Figures

- 2.1 Various warp shapes, generated using a tilted-ring model. a) edge-on view opaque, b) edge-on view transparent (as seen in observations), c) inclined view opaque. 1) S- or integral-shaped warp, 2) U- or bowl-shaped warp, 3) Mixed, asymmetric or L-shaped warp. 24
- 2.2 Definition of warp angles α_e and α_w and beta angles β_e and β_w for a schematic edge-on warp. $r_{w,w/e}$ and $r_{t,w/e}$ are the warp starting radius and the projected distance along the major axis to the last measured point respectively. 30
- 3.1 Definition of the tirific orientational parameters inclination i and position angle pa . a) View of a circular orbit of the tracer material from an arbitrary position. A circular orbit appears as an ellipse to the observer as shown in b). The three-dimensional orientation of the orbit circle is parametrised by the position angle enclosed with the N-axis and the “descending” line-of-nodes LON,desc and the inclination. The descending line-of-nodes is the half-minor axis of the projected ellipse defined by the centre of the ellipse and the point where the galaxy material switches from having a higher recession velocity than the systemic velocity to having a lower recession velocity than the systemic velocity, moving anticlockwise along the ellipse. With the inclination being the angle between the celestial plane and the orbital plane, the orientation of the orbit is fixed. LOS is the line-of-sight, MA,app the approaching half-major axis, MA,rec the receding side half-major axis, LON,asc is the ascending line-of-nodes 50
- 3.2 Testing rotation curve extraction from velocity-fields. Black lines and dots show the parametrisation with which two mock observation have been generated. a) Top panel: rotation curve. Bottom panel: HI surface brightness and -density. The galaxy inclination is 60° . b) Same parametrisation as in a) but with an inclination of 75° . A velocity-field was generated as described in the text. Blue lines and blue triangles: Results from a ROTCUR fit with a free-angle of 0° and a uniform weighting. Red line and red stars: Results from a ROTCUR fit with a free-angle of 30° and a cosine weighting. Green line and green diamonds: Results from a cut along the galaxy major axis, corrected for the inclination. Black lines and black filled circles: Results from a tirific fit. 58

- 3.3 Testing rotation curve extraction with tirific. Red lines and red triangles show the parametrisation with which a mock observation of a flat galaxy with 60° inclination has been generated. The parametrisation for the mock observation is twice as dense as for the fit of the mock observation performed with tirific. At positions where the mock galaxy could not be fitted perfectly by this construction, tirific was forced to interpolate with the result of a model-inherent “beam smearing”. The fitted parameters are represented by black filled circles and black lines. a) Complete parametrisation. b) Zoom-in to show the effect. 61
- 3.4 a) Testing rotation curve extraction with tirific. Red lines and red triangles show the parametrisation with which a mock observation of a flat galaxy with 90° inclination has been generated. The parametrisation for the mock observation is twice as dense as for the fit of the mock observation performed with tirific. The smearing effect has not increased dramatically. The fitted parameters are represented by black dots and lines. b) Testing tilted-ring fitting with tirific. Red lines and triangles show the parametrisation with which a mock observation of a heavily warped galaxy has been generated. The fitted parameters are represented by black dots and lines. 63
- 3.5 Testing tilted-ring fitting with tirific. a) Red lines and red triangles show the parametrisation with which a mock observation of a heavily warped galaxy has been generated. Blue lines and stars show the input first guess to tirific. The fitted parameters are represented by black filled circles and black lines. Fit results after a first run. The model deviates heavily for some of the innermost three data points. b) Fit results after a second run, for which the results of a) have been corrected manually and the orientation of the innermost four data points was forced to be the same. Red triangles and lines show the parametrisation of the mock observation. Green asterisks and green lines represent the first guess from a), light blue stars and lines the first fitting result, blue diamonds represent the input parameters for the second run. Black dots show the results of the fit. 65

3.6	Some output possibilities of tirific. a) An overlay of a representation of the warp structure of a galaxy with ellipses, an “inclino-gram”. b) A three-dimensional spatial model datacube generated from the fit results, processed with the xray task of the Karma software package (Gooch, 1995). c) A “tiltogram” shows the mutual inclination of the planes of the fitted rings at different distances from the centre.	67
4.1	Total intensity maps (a, left) and first moment velocity-fields (b, right) derived from the low-resolution datacubes overlaid on total intensity grey-scale maps. The ellipse in the lower left corner represents the clean beam. NGC 2541. The contours represent the 5, 20, 40, 80, 160, 240 · 10 ¹⁹ atoms cm ⁻² levels and the $v_{\text{sys}} \pm 0, 20, 40, 60, 80, 100 \text{ km s}^{-1}$ levels respectively (see Tab. 4.2). The approaching side is orientated towards NE.	81
4.1	(continued) UGC 3580. The contours represent the 6, 19, 57, 114, 228 · 10 ¹⁹ atoms cm ⁻² levels and the $v_{\text{sys}} \pm 0, 20, 40, 60, 80, 100 \text{ km s}^{-1}$ levels respectively (see Tab. 4.2). The approaching side is orientated towards SE.	82
4.1	(continued) NGC 5204. The contours represent the 2.5, 8, 25, 75, 145, 225 · 10 ¹⁹ atoms cm ⁻² levels and the $v_{\text{sys}} \pm 0, 15, 30, 45, 60 \text{ km s}^{-1}$ levels respectively (see Tab. 4.2). The approaching side is orientated towards NE.	82
4.2	Determination of the orientational parameters, the surface brightness for the outer disk, the rotation velocity for the outer disk, and error bars. SBR: surface brightness. VROT: rotation velocity. INCL: inclination. PA: position angle. R: radius. The black curves (dots) show the best-fit taking into account both sides of the galaxies. The red curves (triangles) show the results when fitting only the receding side, the blue curves (diamonds) show the results for the approaching side. Preliminary error bars were estimated as the maximum deviation of the both-sides fit from the single-sided fits. For extraordinarily high or low values the error bars were re-determined by visual inspection of the datacubes and comparison with a series of model datacubes. NGC 2541.	88
4.2	(continued) UGC 3580.	89
4.2	(continued) NGC 5204.	90
4.3	Final parametrisations of the galaxies. SBR: surface brightness. VROT: rotation velocity. INCL: inclination. PA: position angle. R: radius. The vertical line denotes the optical radius r_{25} . NGC 2541.	92

4.3	(continued) UGC 3580.	93
4.3	(continued) NGC 5204.	94
4.4	Total intensity contour plots (a, left) and first moment velocity-fields (b, right) derived from the low-resolution datacubes, blue original, pink model, overlaid on total intensity grey-scale maps derived from the model datacubes. The over-plotted lines represent the kinematical major and minor axes. The red kinematical major axis lies in the receding part of the galaxy, the blue kinematical major axis in the approaching part. NGC 2541. The contours represent the $5, 20, 40, 80, 160, 240 \cdot 10^{19} \text{ atoms cm}^{-2}$ levels and the $v_{\text{sys}} \pm 0, 20, 40, 60, 80, 100 \text{ km s}^{-1}$ levels respectively (see Tab. 4.2). .	95
4.4	(continued) UGC 3580. The contours represent the $6, 19, 57, 114, 228 \cdot 10^{19} \text{ atoms cm}^{-2}$ levels and the $v_{\text{sys}} \pm 0, 20, 40, 60, 80, 100 \text{ km s}^{-1}$ levels respectively (see Tab. 4.2).	96
4.4	(continued) NGC 5204. The contours represent the $2.5, 8, 25, 75, 145, 225 \cdot 10^{19} \text{ atoms cm}^{-2}$ levels and the $v_{\text{sys}} \pm 0, 15, 30, 45, 60 \text{ km s}^{-1}$ levels respectively (see Tab. 4.2).	96
4.5	a) PV-diagrams along the kinematical major axis comparing the final best-fit models (pink contours) with the original low-resolution data (blue contours). The vertical line marks the systemic velocity, the boxes connected with the lines denote the rotation curve corrected for the inclination. b) PV-diagrams along the kinematical minor axis comparing the final models (pink contours) with the original low-resolution data (blue contours). Contour levels are $1, 4, 16 \text{ mJy/beam}$. NGC 2541.	97
4.5	(continued) UGC 3580. Contour levels are $1, 4, 16 \text{ mJy/beam}$. . .	97
4.5	(continued) NGC 5204. Contour levels are $1, 4, 16, 32 \text{ mJy/beam}$. .	98

4.6	Various visualisations of the adopted tilted-ring models for the galaxies. a)-c) tip-LON plots, the filled circles are the projection of the tip of the normal vectors of the rings at different radii onto a reference plane the innermost radius (0) denoted by a larger circle. The circles in the Figs. a)-c) are drawn at intervals of 10° . a) The reference plane is the celestial plane. b) The reference plane is the inner flat disk. c) The reference plane is chosen such that two straight LONs are visible, resembling the fourth rule of Briggs (1990). At larger radii the dots are clustered around the same position, indicating an outer planar disk. d) Inclinoqram of the galaxies overlaid on the original total intensity maps. The ellipses mark the projection of a ring on the celestial plane, lines and crosses mark the kinematical major and minor axes. In red the kinematical major axis in the receding part of the galaxies is plotted, in blue the kinematical major axis of the approaching part. e) Tiltogram of the galaxies. This is a pixel map showing the mutual inclination of rings at different radii. Most clearly, this diagram shows the existence of two planar disks, an inner one and an outer one. f) Three-dimensional model of the HI disk of the galaxies according to the derived tilted-ring model. The model is rotated and artificially made opaque in order to show again the presence of an outer planar disk. NGC 2541.	100
4.6	(continued) UGC 3580.	101
4.6	(continued) NGC 5204	102
4.7	a) Difference velocity maps derived by subtracting the model first moment map from the original first moment map. b) Histogram of the pixel values of a). The solid line shows a Gaussian with a peak position identical with the mean, a width equal to the rms, and an area equal to the area of the histogram. NGC 2541.	106
4.7	(continued) UGC 3580.	106
4.7	(continued) NGC 5204.	107
4.8	Selected images from the low-resolution datacubes (channel resolution of 4.12 km s^{-1} , robust weighting of 0.4, only visibilities with a baseline length $< 6.4\text{ k}\lambda_{\text{HI}}$ used). The numbers on the upper left give the heliocentric radio velocity in km s^{-1} . The blue dot represents the clean beam. NGC 2541. The contours represent the 1, 4, 16, 32 mJy/beam levels.	114
4.8	(continued) UGC 3580. The contours represent the 1, 6, 24 mJy/beam levels.	115

- 4.8 (continued) NGC 5204. The contours represent the 1, 4, 16 mJy/beam levels. 116
- 4.9 Selected images from the high-resolution datacubes (channel resolution of 2.06 km s^{-1} , uniform weighting, all visibilities used). The numbers on the upper left give the heliocentric radio velocity in km s^{-1} . The blue dot represents the clean beam. NGC 2541. The contours represent the 2, 6, 18 mJy/beam levels. 117
- 4.9 (continued) UGC 3580. The contours represent the 2, 8, 16 mJy/beam levels. 118
- 4.9 (continued) NGC 5204. The contours represent the 1.5, 6 mJy/beam levels. 119
- 4.10 Total intensity maps (a, left) and first moment velocity-fields (b, right) derived from the high-resolution datacubes overlaid on total intensity grey-scale maps. The ellipse in the lower left corner represents the clean beam. NGC 2541. The contours represent the $29, 58, 115, 230, 345 \cdot 10^{19} \text{ atoms cm}^{-2}$ levels and the $v_{\text{sys}} \pm 0, 20, 40, 60, 80, 100 \text{ km s}^{-1}$ levels respectively (see Tab. 4.2). The approaching side is orientated towards NE. 120
- 4.10 (continued) UGC 3580. The contours represent the $8, 35, 69, 139, 208 \cdot 10^{19} \text{ atoms cm}^{-2}$ levels and the $v_{\text{sys}} \pm 0, 20, 40, 60, 80, 100 \text{ km s}^{-1}$ levels respectively (see Tab. 4.2). The approaching side is orientated towards SE. 121
- 4.10 (continued) NGC 5204. The contours represent the $11, 32, 97, 194 \cdot 10^{19} \text{ atoms cm}^{-2}$ levels and the $v_{\text{sys}} \pm 0, 15, 30, 45, 60 \text{ km s}^{-1}$ levels respectively (see Tab. 4.2). The approaching side is orientated towards NE. 121

- 4.11 Comparison of best-fit models of low-resolution datacubes with and without enforcing an inner flat disk. a) In black (dots): Best-fit parameters without enforcing an inner flat disk. In red (triangles): Best-fit parametrisation enforcing a flat inner disk. SBR: surface brightness. VROT: rotation velocity. INCL: inclination. PA: position angle. R: radius. b) PV-diagrams along the kinematical major axis comparing best-fit models with an inner flat disk (pink contours) with the original low-resolution data (blue contours). The vertical line marks the systemic velocity, the boxes connected with the lines denote the rotation curve corrected for the inclination. c) PV-diagrams along the kinematical major axis comparing best-fit models without enforcing an inner flat disk (pink contours) with the original low-resolution data (blue contours). Contour levels are at 1,4,16 mJy/beam. The data are consistent with an inner flat disk, while for NGC 2541 a close inspection showed that allowing for a central tilt resulted in slightly better results. NGC 2541. 122
- 4.11 (continued) UGC 3580. Contour levels are at 1,4,16 mJy/beam. . . . 122
- 4.11 (continued) NGC 5204. Contour levels are at 1,4,16,32 mJy/beam. 123
- 4.12 Determination of the final parametrisations of the galaxies. Viewgraphs showing the models and error bar estimation. SBR: surface brightness. VROT: rotation velocity. INCL: inclination. PA: position angle. R: radius. Black curves (dots): finally adopted model and error bars. Red curves (stars): receding side fitting results from high resolution fitting. Blue curves (asterisks): approaching side fitting results from high resolution fitting. Pink (triangles): interpolated receding side fitting results from low resolution fitting. Light blue (diamonds): interpolated approaching side fitting results from low resolution fitting. Green (open circles): Results and preliminary error bars from low resolution fitting. NGC 2541. 124
- 4.12 (continued) UGC 3580. Red data points (stars) in the position angle and the inclination viewgraphs mark the adopted data points from the low resolution fits used for error bar estimation. 125
- 4.12 (continued) NGC 5204. Red data points (stars) in the position angle and the inclination viewgraphs mark the adopted data points from the low resolution fits used for error bar estimation. 126
- 4.13 Selected images from the low-resolution datacubes overlaid with contours of the original dataset (blue) and the final model datacube (pink). The numbers on the upper left give the heliocentric radio velocity in kms^{-1} . The blue dot represents the clean beam. NGC 2541. The contours represent the 1,4,16,32 mJy/beam levels. 127

4.13 (continued) UGC 3580. The contours represent the 1, 6, 24 mJy/beam levels.	128
4.13 (continued) NGC 5204. The contours represent the 1, 4, 16 mJy/beam levels.	129
4.14 Comparison of fits to the low-resolution datacube selecting two regions with flat rotation curves. Two fits to the datacube were performed. a) shows the fitting results for the rotation curve. b) and c) are comparisons of PV-diagrams of original datacube and model datacube along the kinematical major axis. b) and the blue curve in plot a): Enforcing the two selected regions to have the same rotation velocity. c) and the red curve in plot a): Enforcing the rotation curve to be flat inside the selected regions but allowing the rotation velocity to vary from region to region. Black curve in a): Low-resolution best-fit rotation curve 1) NGC 2541. Contours at 1, 4, 16 mJy/beam. 2) UGC 3580. Contours at 1, 4, 16 mJy/beam. 3) NGC 5204. Contours at 1, 4, 16, 32 mJy/beam.	136
5.1 HI total intensity maps (a, left) and first moment velocity fields (b, right) derived from the low-resolution datacubes overlaid on total intensity grey-scale maps. The ellipse in the lower left corner represents the clean beam. The contours represent the $1.5, 5, 16, 48, 96, 144 \cdot 10^{19} \text{ atoms cm}^{-2}$ levels and the $v_{\text{sys}} \pm 0, 20, 40, 60, 80, 100, 120, 140 \text{ km s}^{-1}$ levels respectively (see Tab. 5.1). The approaching side is orientated towards NE.	143
5.2 HI total intensity maps of the observed field overlaid on a DSS (red) image. From top to bottom: UGC 4683, two unknown possibly merging objects, PGC 25002, NGC 2685. The contours represent the $1.5, 40, 85, 145 \cdot 10^{19} \text{ atoms cm}^{-2}$ levels. Note that the map is primary-beam corrected.	146
5.3 Comparison of HI total intensity maps and the obtained i'-band image. a) Logarithmic grey-scale plot of the i'-band image. b) The same plot overlaid with a contour plot of the low-resolution total intensity HI map. Contours represent the $1.5, 5, 16, 48, 96, 144 \cdot 10^{19} \text{ atoms cm}^{-2}$ levels. c) Grey-scale plot of the high-resolution HI total intensity map.	148

5.4	<p>Parametrisations of toy model datacubes. a) and b) Surface brightness profile, rotation curve and disk orientation. VROT: rotation velocity. INCL: inclination. PA: position angle. R: radius. c) and d) Three-dimensional visualisation of the disks a) and c) “Flip model”. The orientation of the disk flips at a certain radius, the minimum requirement in order to speak of a two-ring or two-disk system in NGC 2685. In order to match the ring structure in observed total intensity maps, sudden changes in the surface-brightness are necessary. b) and d) “Warp model”. In this model a coherent but heavily warped disk is assumed to reproduce the HI structure of NGC 2685. Sudden changes in the intensity are not required and the surface-brightness profile resembles that of a normal spiral galaxy.</p>	151
5.5	<p>Toy model total intensity maps overlaid with a contour-plot of the measured total intensity map (low resolution). Contours represent the $1.5, 5, 16, 48, 96, 144 \cdot 10^{19}$ atoms cm^{-2} levels. The lines indicate the line along which the spectra in the PV-diagrams shown in Fig. 5.6 are traced.</p>	152
5.6	<p>Position-velocity diagrams along the lines across the minor axis of the inner ring shown in Fig. 5.5. a) Taken from the flip-model datacube. b) Taken from the original datacube. c) Taken from the warp model datacube.</p>	153
5.7	<p>Determination of the orientational parameters, the surface brightness for the outer disk, the rotation velocity from the first analysis using the low-resolution HI data and error bar estimation. SBR: surface brightness. VROT: rotation velocity. INCL: inclination. PA: position angle. R: radius. The black curve (dots) shows the best-fit rotation curve taking into account both sides of the galaxies. The red curve (triangles) shows the results when fitting only the receding side, the blue curve (diamonds) show the results for the approaching side. Preliminary error bars were estimated as the maximum deviation of the both-sides fit from the single-sided fits. For extraordinarily high or low values for the error bars, they were re-determined by visual inspection of the datacubes and comparison with a series of model datacubes.</p>	155
5.8	<p>Final parametrisations of the Spindle galaxy. SBR: surface brightness. VROT: rotation velocity. INCL: inclination. PA: position angle. R: radius. The vertical line denotes the optical radius r_{25}.</p>	156

- 5.9 Total intensity contour plots (a, left) and first moment velocity fields (b, right) derived from the low-resolution datacube, blue original, pink model, overlaid on total intensity grey-scale maps derived from the model datacube. The over-plotted lines represent the kinematical major- and minor axis respectively. The red kinematical major axis lies in the receding part of the galaxy, the blue kinematical major axis in the approaching part. The ellipse in the lower left corner represents the clean beam. The contours represent the $1.5, 5, 16, 48, 96, 144 \cdot 10^{19} \text{ atoms cm}^{-2}$ levels and the $v_{\text{sys}} \pm 0, 20, 40, 60, 80, 100, 120, 140 \text{ km s}^{-1}$ levels respectively (see Tab. 5.1). 157
- 5.10 a) PV-diagrams along the kinematical major axis comparing the final best-fit models (pink contours) with the original low-resolution data (blue contours). The vertical line marks the systemic velocity, the boxes connected with the lines denote the rotation curve corrected for the inclination. b) PV-diagrams along the kinematical minor axis comparing the final models (pink contours) with the original low-resolution data (blue contours). Contour levels are $0.5, 4, 10 \text{ mJy/beam}$ 158
- 5.11 Various visualisations of the adopted tilted-ring models for NGC 2685. a)-c) tip-LON plots, the filled circles are the projection of the tip of the normal vectors of the rings at different radii onto a reference plane the innermost radius (0) denoted by a larger circle. The circles in the Figs. a)-c) are drawn at intervals of 10° . a) The reference plane is the celestial plane. b) The reference plane is the ring at a radius of $36''$. As NGC 2685 does not contain an inner flat disk, this ring was chosen to be representative in order to check for the third rule of Briggs (1990). c) The reference plane is chosen such that two straight LONs are roughly visible, resembling the fourth rule of Briggs (1990). At larger radii the dots are clustered around the same position, indicating an outer planar disk. d) Inclinoqram of the galaxies overlaid on the original total intensity maps. The ellipses mark the projection of a ring on the celestial plane, lines and crosses mark the kinematical major and minor axes. In red the kinematical major axis in the receding part of the galaxies is plotted, in blue the kinematical major axis of the approaching part. e) Tiltogram of the galaxies. This is a pixel map showing the mutual inclination of rings at different radii. f) Three-dimensional model of the HI disk of the galaxies according to the tilted-ring model. The model is rotated and artificially made opaque in order to show again the presence of an outer planar disk. 160

- 5.12 a) Difference- or residual velocity maps derived by subtracting the model first moment map from the original first moment map. b) Histogram of the pixel values of a). The solid line shows a Gaussian with a peak position identical with the mean, a width equal to the rms, and an area equal to the area of the histogram. 162
- 5.13 Selected images from the low-resolution datacube (channel resolution of 4.12 km s^{-1} , robust weighting of 0.4, only visibilities with a baseline $< 6.4 \text{ k} \lambda_{\text{HI}}$ regarded $\lambda_{\text{HI}} \approx 21.1 \text{ cm}$). The numbers on the upper left give the heliocentric radio velocity in km s^{-1} . The blue dot represents the clean beam. The contours represent the 0.5, 2, 8 mJy/beam levels. 165
- 5.14 Selected images from the high-resolution datacube (channel resolution of 2.06 km s^{-1} , uniform weighting, all visibilities regarded). The numbers on the upper left give the heliocentric radio velocity in km s^{-1} . The blue dot represents the clean beam. The contours represent the 0.75, 3, 4.5 mJy/beam levels. 166
- 5.15 Total intensity map (a, left) and first moment velocity field (b, right) derived from the high-resolution datacube overlaid on a total intensity grey-scale map. The ellipse in the lower left corner represents the clean beam. The contours represent the 8, 24, 72, 144, $217 \cdot 10^{19} \text{ atoms cm}^{-2}$ levels and the $v_{\text{sys}} \pm 0, 20, 40, 60, 80, 100, 120, 140 \text{ km s}^{-1}$ levels respectively (see Tab. 5.1). 167
- 5.16 Determination of the final parametrisation of the HI disk of NGC 2685. Viewgraph showing the models and error-bar estimation. SBR: surface brightness. VROT: rotation velocity. INCL: inclination. PA: position angle. R: radius. Black curves (dots): finally adopted model and error-bars. Red curves (stars): receding side fitting results from high resolution fitting. Blue curves (asterisks): approaching side fitting results from high resolution fitting. Pink (triangles): receding side fitting results from low resolution fitting. Light blue (diamonds): approaching side fitting results from low resolution fitting. Green (open circles): Results and preliminary error-bars from low resolution fitting. 168
- 5.17 Selected images from the low-resolution datacubes overlaid with contours of the original dataset (blue) and the final model datacube (pink). The numbers on the upper left give the heliocentric radio velocity in km s^{-1} . The blue dot represents the clean beam. NGC 2541. The contours represent the 0.5, 2, 8 mJy/beam levels. 169

- 5.18 Comparison of fits to the low-resolution datacube selecting two regions with flat rotation curves. Two fits to the datacube were performed. a) shows the fitting results for the rotation curve. b) and c) are comparisons of PV-diagrams of original datacube and model datacube along the kinematical major axis. b) and the blue curve (diamonds) in plot a): Enforcing the two selected regions to have the same rotation velocity. c) and the red curve (triangles) in plot a): Enforcing the rotation curve to be flat inside the selected regions but allowing the rotation velocity to vary from region to region. Black curve (dots) in a): Low-resolution best-fit rotation curve. 172

List of Tables

- 2.1 Common spherical density profiles of Dark Matter halos. 1) Navarro et al. (1997), 2) Moore et al. (1998), 3) de Blok et al. (2001), 4) Navarro et al. (2004); Simon et al. (2005), r_{-2} and ρ_{-2} are the radius and the density where the logarithmic slope of the density profile equals -2 , Γ is the complete Gamma function, and γ the lower incomplete Gamma function, 5) Bahcall et al. (1982), 6) Burkert (1995), 7) “Universal Rotation Curve” (Persic & Salucci, 1995), cf. Gentile (2003), r_{opt} is the radius at which 83 percent of the optical light is encompassed, which defines the core radius r_0 . 20

- 4.1 Basic properties of the examined galaxies. (1) Name of galaxy. (2) Classification of galaxy (de Vaucouleurs et al. (1991)). (3) Right Ascension (J2000) (NED). (4) Declination (J2000) (NED). (5) Optical heliocentric systemic velocity (kms^{-1}). (6) Distance of object (Mpc, Freedman et al. 2001 and this work). (7) Scale between distance on sky and true distance ($''/\text{pc}$). (8) Apparent B-band magnitude (mag LEDA). (9) Apparent I-band magnitude (mag LEDA). (10) Apparent B-band magnitude corrected for dust extinction (mag, LEDA). (11) Apparent I-band magnitude corrected for dust extinction (mag). (12) Absolute B-band magnitude (mag). (13) Absolute I-band magnitude (mag). (14) B-band luminosity ($10^9 L_{\odot}$). (15) I-band luminosity ($10^9 L_{\odot}$). (16) Total HI flux (Jy km s^{-1}). (17) HI mass ($10^9 M_{\odot}$). (18) Blue optical radius ($''$, LEDA). (19) HI radius ($''$). (20) Terminal radius ($''$). (21) Blue optical radius (kpc, LEDA). (22) HI radius (kpc). (23) Terminal radius (kpc). (24) Rotation velocity at terminal radius (kms^{-1}). (25) Dynamical mass ($10^9 M_{\odot}$). (26) Ratio of HI mass and B-band luminosity ($M_{\odot} L_{\odot}^{-1}$). (27) Ratio of HI mass and I-band luminosity ($M_{\odot} L_{\odot}^{-1}$). (28) Ratio of dynamical mass and HI mass. (29) Ratio of dynamical mass and B-band luminosity ($M_{\odot} L_{\odot}^{-1}$). (30) Ratio of dynamical mass and I-band luminosity ($M_{\odot} L_{\odot}^{-1}$). 79

- 4.2 Summary of observations and data reduction. (1) Name of galaxy. (2) Total on-source integration time (h). (3) Observation dates (4) Type of datacube, for the high-resolution cube no binning in velocity direction was applied and use of the full array information was made, for the low-resolution cube the data were binned 2 channels into one in the velocity regime and only visibilities inside a radius of $6.4k\lambda_{\text{HI}}$ were used. (5) Applied weighting scheme. (6) Pixel size ($''$). (7) Channel width (kms^{-1}). (8) Half-power-beam-width along the beam major axis ($''$). (9) Half-power-beam-width along the beam minor axis ($''$). (10) Beam position angle ($^{\circ}$). (11) rms noise (mJy/beam) in the cubes. (12) rms noise per velocity resolution element ($10^{19} \text{ atoms cm}^{-2}$). (13) rms noise per velocity resolution element ($\text{M}_{\odot} \text{ pc}^{-2}$). (14) Maximal rms noise in the total intensity map (Jy/beam kms^{-1}). (15) Maximal rms noise in the total intensity map ($10^{19} \text{ atoms cm}^{-2}$). (16) Maximal rms noise in the total intensity map ($\text{M}_{\odot} \text{ pc}^{-2}$). 83
- 4.3 Global best-fit tilted-ring parameters for the examined galaxies. (1) Name of galaxy. (2) Right Ascension (J2000), fitting results. (3) Declination (J2000), fitting results. (4) Right Ascension (J2000) from NED. (5) Right Ascension (J2000) from NED. (6) Heliocentric optical systemic velocity (kms^{-1}). (7) Type of datacube used for analysis, high-resolution or low-resolution. (8) Dispersion (kms^{-1}). (9) Internal dispersion, instrumental dispersion subtracted (kms^{-1}). (10) Global scaleheight ($''$) (11) Global scaleheight (pc) 98
- 4.4 Basic statistics of the velocity difference maps. (1) Galaxy name. (2) Mean of the deviation velocities (kms^{-1}). (3) Standard deviation of the deviation velocities (kms^{-1}). (4) Minimal measured inclination in the galaxy. (4) σ_{v_d} corrected for i_{min} 107
- 4.5 Radially dependent best-fit parameters for the examined galaxies. (1) Radius ($''$). (2) Radius (kpc, according to Tab. 4.1). (3) Error of r_t (kpc) (4) Face-on surface brightness (Jy kms^{-1}). (5) Error of $I_{\text{tot,f}}$ (Jy kms^{-1}). (6) Face-on HI column density ($10^{19} \text{ atoms cm}^{-2}$). (7) Error of N_{HI} ($10^{19} \text{ atoms cm}^{-2}$). (8) Face-on surface density ($\text{M}_{\odot} \text{ pc}^{-2}$). (9) Error of σ ($\text{M}_{\odot} \text{ pc}^{-2}$). (10) Rotation velocity (kms^{-1}). (11) Error of v_{rot} (kms^{-1}). 130

4.5	(continued) NGC 2541. (12) Inclination ($^{\circ}$). (13) Error of i ($^{\circ}$). (14) Position angle ($^{\circ}$). (15) Error of pa ($^{\circ}$). (16) Inclination ($^{\circ}$). (17) - (23) are Cartesian components of the spin normal vector \mathbf{n} of the ring and their errors. (17) Spin normal vector component towards W (natural units). (18) Error of n_W (natural units). (19) Spin normal vector component towards N (natural units). (20) Error of n_N (natural units). (21) Spin normal vector component towards observer (natural units). (22) Error of n_{LOS} (natural units).	131
4.5	(continued) UGC 3580.	132
4.5	(continued) UGC 3580.	133
4.5	(continued) NGC 5204.	134
4.5	(continued) NGC 5204.	135
5.1	Observations and data reduction, summary. (1) Name of telescope. (2) Total on-source integration time (h). (3) Observation dates (4) Type of datacube, for the high-resolution cube no binning in velocity direction was applied and use of the full array information was made, for the low-resolution cube the data were binned 2 channels into one in the velocity regime and only visibilities inside a radius of $6.4k\lambda_{HI}$ ($\lambda_{HI} \approx 21.1$ cm) were used. (5) Applied weighting scheme. (6) Pixel size ($''$). (7) Channel width (km s^{-1}). (8) Half-power-beam-width along the beam major axis ($''$). (9) Half-power-beam-width along the beam minor axis ($''$). (10) Beam position angle ($^{\circ}$). (11) rms noise (mJy/beam) in the cubes. (12) rms noise per velocity resolution element (10^{19} atoms cm^{-2}). (13) rms noise per velocity resolution element ($M_{\odot} \text{pc}^{-2}$). (14) Maximal rms noise in the total intensity map (Jy/beam km s^{-1}). (15) Maximal rms noise in the total intensity map (10^{19} atoms cm^{-2}). (16) Maximal rms noise in the total intensity map ($M_{\odot} \text{pc}^{-2}$). (17) rms noise in the optical image (mag arcsec $^{-2}$). (18) rms noise in the optical image, $5\sigma_{\text{rms}}$ -level for a $2''$ aperture (mag).	144

5.2	Basic properties of NGC 2685. (1) Classification of galaxy (de Vaucouleurs et al. (1991)). (2) Right Ascension (J2000) (NED). (3) Declination (J2000) (NED). (4) Optical heliocentric systemic velocity (kms^{-1}). (5) Distance of object (Mpc, Freedman et al. 2001 and this work). (6) Scale between distance on sky and true distance ($''/\text{pc}$). (7) Apparent B-band magnitude (mag, LEDA). (8) Apparent I-band magnitude (mag, LEDA). (9) Apparent B-band magnitude corrected for dust extinction (mag, LEDA). (10) Apparent I-band magnitude corrected for dust extinction (mag). (11) Absolute B-band magnitude (mag). (12) Absolute I-band magnitude (mag). (13) B-band luminosity ($10^9 L_{\odot}$). (14) I-band luminosity ($10^9 L_{\odot}$). (15) Total HI flux (Jy km s^{-1}). (16) HI mass ($10^9 M_{\odot}$). (17) Blue optical radius ($''$, LEDA). (18) HI radius ($''$). (19) Terminal radius ($''$). (20) Blue optical radius (kpc, LEDA). (21) HI radius (kpc). (22) Terminal radius (kpc). (23) Rotation velocity at terminal radius (kms^{-1}). (24) Dynamical mass ($10^9 M_{\odot}$). (25) Ratio of HI mass and B-band luminosity ($M_{\odot} L_{\odot}^{-1}$). (26) Ratio of HI mass and I-band luminosity ($M_{\odot} L_{\odot}^{-1}$). (27) Ratio of dynamical mass and HI mass. (28) Ratio of dynamical mass and B-band luminosity ($M_{\odot} L_{\odot}^{-1}$). (29) Ratio of dynamical mass and I-band luminosity ($M_{\odot} L_{\odot}^{-1}$).	145
-----	--	-----

5.3	Basic properties of the detected dwarf galaxies in the vicinity of NGC 2685. The data show that these galaxies probably cannot account for the ring in NGC 2685 and are dynamically unimportant. (1) Name of galaxy. (2) Classification of galaxy (de Vaucouleurs et al. (1991)). (3) Right Ascension (J2000) (NED). (4) Declination (J2000) (NED). (5) Optical heliocentric systemic velocity (kms^{-1}). (6) Apparent B-band magnitude (mag, Paturel 1989). (7) Total HI flux (Jy km s^{-1}). (8) HI mass ($10^7 M_{\odot}$) at the same distance as NGC 2685. (9) Projected distance of object from NGC 2685 ($''$) at the same distance as NGC 2685. (10) Projected distance of object from NGC 2685 (kpc) at the same distance as NGC 2685. (11) Profile width at 20 percent of the peak flux density (kms^{-1}). (12) Inclination ($^{\circ}$). (13) Dynamical mass ($10^8 M_{\odot}$) at the same distance as NGC 2685.	147
-----	---	-----

5.4	Global best-fit tilted-ring parameters for the examined galaxies. (1) Right Ascension (J2000), fitting results. (2) Declination (J2000), fitting results. (3) Right Ascension (J2000) from NED. (4) Right Ascension (J2000) from NED. (5) Heliocentric optical systemic velocity (kms^{-1}). (6) Type of datacube used for analysis, high-resolution or low-resolution. (7) Velocity ispersion (kms^{-1}). (8) Internal dispersion, instrumental dispersion subtracted (kms^{-1}). (9) Global scaleheight ($''$) (10) Global scaleheight (pc)	159
5.5	Basic statistics of the velocity difference maps. (1) Mean of the deviation velocities (kms^{-1}). (2) Standard deviation of the deviation velocities (kms^{-1}). (3) Minimal measured inclination in the galaxy. (4) σ_{v_d} corrected for i_{\min}	163
5.6	Radially dependent best-fit parameters. (1) Radius ($''$). (2) Radius (kpc, according to Tab. 5.2). (3) Error of r_t (kpc) (4) Face-on surface brightness (Jy km s^{-1}). (5) Error of $I_{\text{tot,f}}$ (Jy km s^{-1}). (6) Face-on HI column-density ($10^{19} \text{ atoms cm}^{-2}$). (7) Error of N_{HI} ($10^{19} \text{ atoms cm}^{-2}$). (8) Face-on surface density ($\text{M}_{\odot} \text{ pc}^{-2}$). (9) Error of σ ($\text{M}_{\odot} \text{ pc}^{-2}$). (10) Rotation velocity (kms^{-1}). (11) Error of v_{rot} (kms^{-1}).	170
5.6	(continued) (12) Inclination ($^{\circ}$). (13) Error of i ($^{\circ}$). (14) Position angle ($^{\circ}$). (15) Error of pa ($^{\circ}$). (16) Inclination ($^{\circ}$). (17)-(23) are Cartesian components of the spin normal vector \mathbf{n} of the ring and their errors. (17) Spin normal vector component towards W (natural units). (18) Error of n_{W} (natural units). (19) Spin normal vector component towards N (natural units). (20) Error of n_{N} (natural units). (21) Spin normal vector component towards observer (natural units). (22) Error of n_{LOS} (natural units). . . .	171

Ich versichere, daß ich diese Arbeit selbständig verfaßt und keine anderen als die angegebenen Quellen und Hilfsmittel benutzt, sowie Zitate kenntlich gemacht habe.